

IMPERIAL COLLEGE OF SCIENCE, TECHNOLOGY AND MEDICINE
University of London

**THE NONDESTRUCTIVE TESTING OF PLATES USING
ULTRASONIC LAMB WAVES**

by

David N. Alleyne

A thesis submitted to the University of London for
the degree of Doctor of Philosophy and for the
Diploma of Imperial College

Department of Mechanical Engineering
Imperial College of Science, Technology and Medicine
London SW7

February 1991

Abstract

The major objective of this thesis is the development of quantitative methods of applying Lamb waves in industrial nondestructive testing (NDT). The key problem associated with the measurement of the characteristics of Lamb waves is that invariably more than one mode is excited at any given frequency. This has led to problems when interpreting the typically complicated Lamb wave signals which are commonly found in NDT applications.

The first two chapters of this thesis provide an introduction to the field of NDT using Lamb waves, reviewing past work and relevant theory. The review has shown that quantitative or qualitative time domain methods may be adopted in low frequency-thickness product regions where only two propagating modes are possible as they may be easily decoupled from one another by the orientation of the transducers. However, in higher frequency-thickness regions the multi-mode dispersive nature of Lamb waves makes this approach unreliable for most NDT applications. In chapter 3 a new method is presented for measuring the amplitudes and velocities of Lamb waves. The method involves a two-dimensional Fourier transformation (2-D FFT) of the time history of the signals received at a series of equally spaced positions along the propagation path. The output of this transform is a three-dimensional plot of the amplitude versus frequency and wavenumber, from which the amplitudes of the different propagating Lamb modes may be obtained.

In chapters 4 and 5 the 2-D FFT method is used to measure the characteristics of propagating Lamb waves in finite element modelling studies, where single Lamb modes have been launched. Numerical predictions of Lamb wave reflection from boundaries and interaction with straight sided notches are presented. In chapters 6 and 7 the numerical model is validated by experimental investigations carried out on a variety of plates with straight sided notches. The correlation between the experimental results and the numerical predictions is excellent and the results are presented in terms of Lamb wave amplitudes as a function of frequency-thickness product and Lamb wave amplitudes as a function of notch depth at particular frequency-thicknesses, this being the more useful format in NDT applications. The final two chapters discuss the practical implementation of quantitative and qualitative Lamb wave techniques in the NDT of plate-like structures and present the major conclusions of the thesis. Here, the emphasis is on practical problems such as signal-to-noise considerations, coupling requirements, excitation methods, and on methods of distinguishing the signals from defects from those produced by boundaries or other impedance changes.

The main conclusion of the thesis is that Lamb waves may be used very successfully for the quantitative NDT of plates. In localised, detailed NDT applications the detectability of a defect

may be optimised by choosing the most suitable mode at the appropriate frequency-thickness product. Since stresses are produced throughout the thickness of the plate by Lamb waves (in some cases there may be stress nodes which must be carefully considered), the entire thickness of the plate is interrogated, which means it is possible to find defects that are initiated at either surface or internal locations. Lamb waves may be propagated over considerable distances, so they are ideally suited to the long range NDT of plates and plate-like structures where a fast, coarse inspection may be carried out. The finite element predictions and experimental results have shown that Lamb wave techniques may be used to find defects when the wavelength to critical defect dimension is as high as 40. The computational requirements of the 2-D FFT method are fairly modest and can be handled by most IBM compatible micro-computers interfaced to a data capture system. The multi-element transducers which are now available make the implementation of the 2-D FFT method feasible in industrial NDT.

Acknowledgements

I would like to extend the warmest thanks to Dr. Peter Cawley for his guidance, support and encouragement throughout the course of my research. I would also like to take this opportunity to thank Tom Pialucha, Ningqun Guo, Paul Dewen, Mike Lowe and Denis Hitchings.

My deepest thanks are due to Valrie and all the rest of my family (you too Janet and Tony) for their help, support and understanding.

I would also like to thank The Welding Institute and the SERC for the financial support which has enabled this work to be undertaken. I would especially like to thank past and present member of the nondestructive testing section at the The Welding Institute, notably Alan Lank, Peter Mudge, Peter Bartle and John Turner.

Contents

Abstract	i
Acknowledgements.....	iii
Contents.....	iv
List of Tables.....	viii
List of Figures.....	ix
Nomenclature.....	xvii

CHAPTER 1

A review of the application of stress waves in nondestructive testing and monitoring

1.1	Introduction	1
1.2	General ultrasonic nondestructive testing.....	2
	1.3.1 General nondestructive testing using Rayleigh and Lamb waves.....	5
	1.3.2 Localised nondestructive testing using Rayleigh and Lamb waves.....	7
	1.3.3 Long range nondestructive testing using Lamb waves.....	8
1.4	Conclusions	9
1.5	Outline of the thesis	10

CHAPTER 2

Wave propagation and boundary interaction

2.1	Introduction	14
2.2	The plane wave model	14
2.3	Bulk waves.....	15
2.4	Reflection from a free elastic half space.....	18
	2.4.1 An incident longitudinal or shear wave	18
2.5	Reflection from a liquid-solid half space.....	19
	2.5.1 A longitudinal wave incident from the liquid.....	20
	2.5.2 A longitudinal or shear wave incident from the solid	21
2.6	Wave propagation characteristics in bounded media	21
	2.6.1 Shear horizontal waves in a free plate.....	21
	2.6.2 Longitudinal and shear waves in a free plates.....	22
	2.6.3 Reflection and transmission from a fluid loaded plate	23

2.7	Inhomogeneous waves.....	23
2.8	Energy considerations.....	25
2.9	Rayleigh waves.....	25
	2.9.1 Leaky Rayleigh waves.....	27
2.10	Lamb waves.....	28
	2.10.1 Dispersion curves and mode shapes.....	28
	2.10.2 The zig-zagging wave model of Lamb waves.....	32
	2.10.3 Leaky Lamb waves.....	34
2.11	The effect of bounded waves.....	35
2.12	The excitation of Rayleigh and Lamb waves.....	35
2.13	Discussion.....	37
2.14	Conclusions.....	39

CHAPTER 3

The measurement of the properties of propagating Lamb modes

3.1	General.....	50
3.2	Frequency domain methods.....	51
3.3	The two-dimensional Fourier transform method.....	52
3.4	Initial test of the spatial transform.....	53
3.5	Conclusions.....	56

CHAPTER 4

Numerical modelling of propagating stress waves

4.1	An introduction to numerical modelling.....	60
	4.1.1 The finite difference method.....	61
	4.1.2 The finite element method.....	63
	4.1.3 Method of temporal discretization.....	65
	4.1.4 Discussion.....	68
4.2	Initial test case modelling investigations.....	69
	4.2.1 Introduction.....	69
	4.2.2 Excitation signals.....	70
	4.2.3 Finite element results of initial test cases.....	71
4.3	Initial modelling of Lamb wave propagation.....	72
	4.3.1 Results of the initial modelling of propagating Lamb waves.....	73
4.4	Further modelling of propagating Lamb waves.....	76

4.5	The modelling of Lamb wave reflection from the free end of a plate.....	78
4.5.1	Results of Lamb wave reflection from the plane edge of a plate.....	78
4.5.2	Results of Lamb wave reflection from a stepped edge in a plate.....	80
4.6	Conclusions.....	81

CHAPTER 5

Finite element modelling of Lamb wave interaction with idealised defects

5.1	Objectives and introduction.....	104
5.2	Lamb wave interaction with straight sided notches.....	106
5.2.1	Modes and frequency-thickness regions used	106
5.2.2	Lamb waves a_0 and s_0 at 0.45 MHz	106
5.2.3	Discussion of transmission and reflection results	109
5.2.4	Lamb wave s_0 at 0.225 MHz	110
5.2.5	Lamb waves a_0 and a_1 at 0.75 MHz	111
5.3	Lamb wave interaction with notches of varying width.....	114
5.4	Lamb wave interaction with an inclined notch	115
5.5	Conclusions	116

CHAPTER 6

The measurement of propagating Lamb waves in plates

6.1	Introduction	143
6.2	Experimental procedure and equipment.....	143
6.3	Practical methods of exciting and receiving Lamb waves.....	144
6.3.1	Pulse excitation	148
6.3.2	Tone burst excitation.....	148
6.4	Time domain measurements of Lamb wave velocities	149
6.5	Frequency domain measurements of Lamb wave velocities.....	153
6.6	The measurement of propagating Lamb waves using the 2-D FFT method	154
6.7	Conclusions.....	157

CHAPTER 7

The measurement of Lamb wave interaction with notches

7.1	Introduction	188
-----	--------------------	-----

7.2	Measurements of Lamb wave interaction with straight sided notches.....	189
	7.2.1 Discussion.....	192
7.3	Defects in a butt welded plate	194
7.4	Conclusions	195

CHAPTER 8

The practical implementation of Lamb waves in standard NDT methods

8.1	General.....	206
8.2	Signal-to-noise considerations	207
	8.2.1 Standard techniques for maximising the signal-to-noise ratio.....	207
	8.2.2 Signal regeneration.....	208
8.3	Transducers, coupling and excitation signals	213
	8.3.1 Transducers	213
	8.3.2 Coupling.....	214
	8.3.3 Excitation signals.....	215
8.4	Decoupling boundaries and other impedance mismatches	215
8.5	The implementation of the 2-D FFT method	216
8.6	Choice of time or frequency domain methods or the 2-D FFT method	216

CHAPTER 9

Conclusions

9.1	General.....	222
9.2	Signal processing.....	223
9.3	Numerical modelling	223
9.4	Practical applications	224
	References	226

List of Tables

- Table 5.1 Predicted reflection (R) and transmission (T) ratios of a_0 .
- Table 5.2 Predicted transmission ratios of s_0 .
- Table 5.3 Predicted reflection (R) and transmission (T) ratios of a_0 .
- Table 5.4 Predicted transmission ratios of a_1 .
-
- Table 7.1 Measured properties of the steel plates used in the experiments.
- Table 7.2 Measured transmission ratios of s_0 at 1.35 MHzmm.
- Table 7.3 Measured transmission ratios of a_1 around 2.45 MHzmm.

List of Figures

- Figure 1.1 (a) Schematic representation of (a) pulse-echo mode, (b) pitch-catch mode and (c) through-transmission mode.
- Figure 1.2 Schematic representation of Lamb wave testing.
- Figure 2.1 Schematic representation of a plane wave approaching an interface.
- Figure 2.2 Schematic representation of the reflection of bulk waves from free boundaries.
- Figure 2.3 Schematic representation of the plate geometry and the coordinate system used.
- Figure 2.4 Lamb wave wavenumber dispersion curves for steel, where $c_1=5960$ m/s and $c_2=3260$ m/s.
- Figure 2.5 Lamb wave phase velocity dispersion curves for steel, where $c_1=5960$ m/s and $c_2=3260$ m/s.
- Figure 2.6 Lamb wave group velocity dispersion curves for steel, where $c_1=5960$ m/s and $c_2=3260$ m/s.
- Figure 2.7 The through-thickness deflected mode shapes of Lamb waves, where c_1 and c_2 are the same as in figure 2.4: ———.x direction displacements; ----- z direction displacements. (a) a_0 at 0.5 MHzmm (b) s_0 at 0.5 MHzmm (c) a_0 at 1.63 MHzmm (d) s_1 at 2.98 MHzmm (e) a_0 at 15 MHzmm (f) s_0 at 15 MHzmm.
- Figure 2.8 The through-thickness stress mode shapes of Lamb waves, where c_1 and c_2 are the same as in figure 2.4: ———. σ_{xx} ; ----- σ_{zz} ; - - - - σ_{xz} . (a) a_0 at 0.5 MHzmm (b) s_0 at 0.5 MHzmm (c) a_0 at 1.63 MHzmm (d) s_1 at 2.98 MHzmm (e) a_0 at 15 MHzmm (f) s_0 at 15 MHzmm.
- Figure 2.9 Lamb wave coincidence angle (water $c_L=1500$ m/s) dispersion curves for steel, where $c_1=5960$ m/s and $c_2=3260$ m/s.
- Figure 2.10 The theoretical pressure distribution generated by a one inch diameter transducer acting as a piston source.
- Figure 3.1 (a) Steady-state response of an infinite plate, at a single frequency as a function of time; (b) as a function of position in the x direction. (c) The steady-state response in (b) modified by the application of a Hanning window.
- Figure 3.2 (a) Analytically calculated spatial FFT of the s_0 mode in a 1.0 mm thick plate at 63.6 kHz, when the spatial record was related to s_0 at 63.6 kHz, which was sampled at 64 equally spaced points over 5 wavelengths. (b) as in (a) but when the spatial record extended from $x = 0$ to $x = 8.56$ m (100 whole wavelengths) and a 1024 point FFT was used. (c) When the spatial record extended from $x = 0$ to $x = 4.28$ m (100 whole wavelengths), the frequency was 127.2 kHz and a 1024 point FFT was used.

- Figure 3.3 (a) Spatial FFT of the s_0 mode in a 1.0 mm thick plate at 63 kHz, when the sampled spatial record was at 64 equally spaced points over 5.2 wavelengths and a 256 point FFT was carried out, by padding the end of the spatial record with 192 zeros. (b) spatial FFT when the simple sinusoidal spatial record used in (a) was modified by the application of a Hanning window function.
- Figure 4.1 (a) Time history of the 5 cycle 1 MHz tone burst used in the numerical tests. (b) Time history of the 5 μ s duration sine squared pulse used in the numerical test. (c) Amplitude spectrum of the time history shown in (a). (d) Amplitude spectrum of the time history shown in (b).
- Figure 4.2 Normalised 3-D plot of a snapshot of strain energy distribution in a steel block as a function of position 16 μ s after the application of the sine squared pulse at the origin. The vertical (energy) scale is linear and is not shown to improve the clarity of the plot.
- Figure 4.3 Predicted time history at $x = 100$ mm, when the input at $x = 0$ was designed to excite only the longitudinal wave c_1 .
- Figure 4.4 Predicted time history at $x = 100$ mm, when the input at $x = 0$ was designed to excite only the shear wave c_2 .
- Figure 4.5 (a) Predicted time history at $x = 100$ mm in a 0.5 mm thick plate when the input at $x = 0$ was designed to excite only s_0 . (b) Normalised 3-D plot of the 2-D FFT results of the case given in (a), showing a single propagating mode, s_0 .
- Figure 4.6 A comparison of the finite element predictions with the analytically generated dispersion curves for s_0 : ---- analytical predictions; \square finite element predictions.
- Figure 4.7 (a) Predicted time history at $x = 100$ mm in a 2.0 mm thick plate when the input at $x = 0$ was designed to excite only s_0 . (b) Normalised 3-D plot of the 2-D FFT results of the case given in (a), showing a single propagating mode, s_0 .
- Figure 4.8 The through-thickness deflected mode shapes of Lamb waves, where c_1 and c_2 are the same as in figure 2.4: — x direction displacements; - - - - - z direction displacements. (a) a_0 at 3.0 MHzmm (b) a_1 at 3.0 MHzmm.
- Figure 4.9 (a) Predicted time history at $x = 50$ mm in a 3.0 mm thick plate when the input at $x = 0$ was designed to excite only a_0 . (b) Normalised 3-D plot of the 2-D FFT results of the case given in (a).
- Figure 4.10 A comparison of the finite element predictions with the analytically generated dispersion curves for a_0 and a_1 : — analytical predictions; \odot finite element predictions for a_1 , \square finite element predictions for a_0 .
- Figure 4.11 (a) Predicted time history at $x = 50$ mm in a 3.0 mm thick plate when the input at $x = 0$ was designed to excite only a_1 . (b) Normalised 3-D plot of the 2-D FFT results of the case given in (a).
- Figure 4.12 (a) Predicted time history at $x = 50$ mm in a 3.0 mm thick plate when the input at $x = 0$ was designed to excite a_0 and a_1 . (b) Normalised 3-D plot of the 2-D FFT results of the case given in (a). (c) The relative surface amplitudes in the z direction of the two modes a_0 and a_1 , obtained from (b), as a function of the frequency-thickness product.
- Figure 4.13 The analytically calculated deflected shape time histories at $x = 0$ of the a_0 mode,

- Figure 4.13 The analytically calculated deflected shape time histories at $x = 0$ of the a_0 mode, in the x direction at (a) $z/2d = 0$, (b) $z/2d = 0.5$ and (c) $z/2d = 1.0$. In the z direction at (d) $z/2d = 0$, (e) $z/2d = 0.5$ and (f) $z/2d = 1.0$.
- Figure 4.14 (a) Predicted time history at $x = 50$ mm in a 3.0 mm thick plate when the input signal at $x = 0$ corresponded to the time histories shown in Fig. 4.13 and was designed to excite only a_0 . (b) Normalised 3-D plot of the 2-D FFT results of the case given in (a) showing a single propagating mode a_0 .
- Figure 4.15 Distribution of energy between a_0 and a_1 after reflection from the free end of the plate. — theoretical predictions using the method of Torvik (1967); \odot numerical results. (a) when only a_0 was incident, (b) when only a_1 was incident.
- Figure 4.16 (a) Predicted time history at $x = 50$ mm in a 3.0 mm thick plate, showing the first passage of the a_0 wave and the reflection containing both a_0 and a_1 from the free end of the plate, when the input signal at $x = 0$ was designed to excite only a_0 . (b) Normalised 3-D plot of the 2-D FFT results from the reflected wave packet shown in (a).
- Figure 4.17 (a) Predicted time history at $x = 50$ mm in a 3.0 mm thick plate, showing the first passage of the a_1 wave and the reflection containing both a_1 and a_0 from the free end of the plate, when the input signal at $x = 0$ was designed to excite only a_1 .
- Figure 4.18 Schematic representation of the geometry of the steps at the end plate. (a) symmetric step (with respect to the middle of the plate) and (b) non-symmetric step (with respect to the middle of the plate).
- Figure 4.19 Predicted time history of the 1.0 mm thick plate when the input signal at $x = 0$ was designed to excite only s_0 , showing the first passage of the s_0 wave and the wave packet reflected from the free symmetric step at the end of the plate. (a) at $x = 75$ mm and (b) at $x = 95$ mm.
- Figure 4.20 (a) Normalised 3-D plot of the 2-D FFT results of the case shown in Fig. 4.19 when the incident wave ($t \leq 26 \mu\text{s}$) was gated out. It shows that the signal reflected from the symmetric step contains only one propagating mode s_0 . (b) Predicted reflection ratio of the s_0 mode as a function of frequency-thickness in the 1.0 mm thick plate after reflection from the symmetric notch.
- Figure 4.21 Predicted time history of the 1.0 mm thick plate when the input signal at $x = 0$ was designed to excite only s_0 , showing the first passage of the s_0 wave and the wave packet reflected from the free non-symmetric step at the end of the plate. (a) at $x = 75$ mm and (b) at $x = 95$ mm.
- Figure 4.22 Normalised 3-D plot of the 2-D FFT results of the case shown in Fig. 4.21 when the incident wave ($t \leq 26 \mu\text{s}$) was gated out, showing that the signal reflected from the non-symmetric step contains two propagating modes s_0 and a_0 .
- Figure 5.1 Schematic diagram of the notch geometry used in the finite element models.
- Figure 5.2 Lamb wave group velocity dispersion curves for steel showing the frequency-thickness regions in which the finite element modelling was carried out.
- Figure 5.3 The through-thickness deflected mode shapes of Lamb waves, where c_1 and c_2 are the same as in figure 2.4: — x direction displacements; - - - - - z direction displacements. (a) a_0 at 1.35 MHzmm (b) s_0 at 1.35 MHzmm.

- Figure 5.4 (a) Predicted time history at $x = 150$ mm in a 3.0 mm thick plate showing the first passage of the a_0 mode and the reflection from the 0.5 mm deep notch, and (b) the predicted time history when the notch was 2.0 mm deep.
- Figure 5.5 Normalised 3-D plot of the 2-D FFT results of the case given in Fig. 5.4 when the signal reflected from the notch was gated out and shows a single propagating mode, a_0 .
- Figure 5.6 Normalised 3-D plot of the 2-D FFT results from the reflected wave shown in Fig. 5.4(b).
- Figure 5.7 (a) Normalised amplitude versus wavenumber at 1.26 MHzmm obtained from the results shown in Fig. 5.5 and (b) at 1.36 MHzmm.
- Figure 5.8 Predicted reflection ratio of the a_0 mode as a function of frequency-thickness in a 3.0 mm thick plate after interaction with (a) the 0.5 mm deep notch, (b) the 1.0 mm notch, (c) the 1.5 mm notch and (d) the 2.0 mm notch.
- Figure 5.9 Predicted normalised reflection ratio of the a_0 mode as a function of frequency-thickness after interaction with (a) the 0.5 mm deep notch, (b) the 1.0 mm notch, (c) the 1.5 mm notch and (d) the 2.0 mm notch.
- Figure 5.10 (a) Predicted time history in a 3.0 mm thick plate 50 mm after interaction with the 2.0 mm deep notch, when the input signal was designed to excite only a_0 . (b) Normalised 3-D plot of the 2-D FFT results for the case given in (a).
- Figure 5.11 Predicted transmission ratio of the a_0 mode as a function of frequency-thickness after interaction with (a) the 0.5 mm deep notch, (b) the 1.0 mm notch, (c) the 1.5 mm notch and (d) the 2.0 mm notch.
- Figure 5.12 Predicted normalised transmission ratio of the a_0 mode as a function of frequency-thickness after interaction with (a) the 0.5 mm deep notch, (b) the 1.0 mm notch, (c) the 1.5 mm notch and (d) the 2.0 mm notch.
- Figure 5.13 Predicted transmission ratio of the s_0 mode as a function of frequency-thickness after interaction with (a) the 0.5 mm deep notch, (b) the 1.0 mm notch, (c) the 1.5 mm notch and (d) the 2.0 mm notch.
- Figure 5.14 (a) Predicted time history in a 6.0 mm thick plate 5 mm after interaction with a 0.5 mm deep notch, when the input signal was designed to excite only s_0 . (b) at 55 mm after the notch.
- Figure 5.15 Predicted transmission ratio of the s_0 mode as a function of frequency-thickness in the 6.0 mm thick plate after interaction with (a) the 0.5 mm deep notch, (b) the 1.0 mm notch, (c) the 1.5 mm notch, (d) the 2.5 mm notch, (e) the 3.5 mm notch and (f) the 4.5 mm notch.
- Figure 5.16 Predicted transmission ratio as a function of $h/2d$ at 1.25, 1.35 and 1.45 MHzmm (a) for the s_0 mode and (b) for a_0 produced by mode conversion at the notch.
- Figure 5.17 (a) Predicted time history in a 3.0 mm thick plate 105 mm before the 0.5 mm deep notch, when the centre frequency of the input tone burst was 0.75 MHz and was designed to excite only a_0 . (b) at 65 mm after the notch.
- Figure 5.18 Normalised 3-D plot of the 2-D FFT results of the case given in Fig. 5.17(a) when the signal reflected from the notch was gated out, showing a single propagating mode, a_0 .

- Figure 5.19 Normalised 3-D plot of the 2-D FFT results of the case shown in Fig. 5.17(a) when the incident wave ($t \leq 70 \mu\text{s}$) was gated out. It shows that the signal reflected from the notch contains three propagating modes a_1 , s_0 and a_0 .
- Figure 5.20 Predicted reflection ratio of the a_0 mode as a function of frequency-thickness in the 3.0 mm thick plate after interaction with (a) the 0.5 mm deep notch, (b) the 1.0 mm notch, (c) the 1.5 mm notch, (d) the 2.0 mm notch.
- Figure 5.21 Predicted transmission ratio of the a_0 mode as a function of frequency-thickness in the 3.0 mm thick plate after interaction with (a) the 0.5 mm deep notch, (b) the 1.0 mm notch, (c) the 1.5 mm notch, (d) the 2.0 mm notch.
- Figure 5.22 (a) Predicted time history in a 3.0 mm thick plate 5 mm after the 0.5 mm deep notch, when the centre frequency of the input tone burst was 0.75 MHz and was designed to excite only a_1 . (b) at 70 mm after the notch.
- Figure 5.23 Predicted transmission ratio of the a_1 mode as a function of frequency-thickness in the 3.0 mm thick plate after interaction with (a) the 0.5 mm deep notch, (b) the 1.0 mm notch, (c) the 1.5 mm notch, (d) the 2.0 mm notch.
- Figure 5.24 Predicted transmission ratio of the s_0 mode as a function of frequency-thickness in the 3.0 mm thick plate after interaction with a 0.5 mm deep notch which was (a) 0.25 mm wide notch; (b) 0.5 mm wide, (c) 0.75 mm wide, (d) 1.0 mm wide, (e) 2.0 mm wide, (f) 4.0 mm wide notch.
- Figure 5.25 Predicted transmission ratio of the s_0 mode as a function of $w/2d$ at 1.25, 1.35 and 1.45 MHzmm.
- Figure 5.26 (a) Predicted time history in a 3.0 mm thick plate 60 mm after the angled (45° to the plate surface) 1.0 mm deep notch, when the centre frequency of the input tone burst was 0.45 MHz and was designed to excite only s_0 . (b) Predicted transmission ratio of the s_0 mode as a function of frequency-thickness for the case given in (a).
- Figure 6.1 Schematic representation of experimental setup.
- Figure 6.2 Schematic representation of (a) the direct 'wedge' method and (b) the indirect 'wedge' method.
- Figure 6.3 Schematic representation of (a) the variable angle probe and (b) the interfaces of the variable angle probe shown in (a).
- Figure 6.4 (a) Normalised time history of the response of the variable angle probe in air when excited by a broad band signal. (b) Amplitude spectrum of the time history shown in (a).
- Figure 6.5 Schematic representation of the Lamb wave test rig.
- Figure 6.6 Amplitude spectrum of the response of the 0.5 MHz immersion probe when excited by a broad band signal.
- Figure 6.7 Amplitude spectrum of the response of the 1.0 MHz immersion probe when excited by a broad band signal.

- Figure 6.8 Lamb wave coincidence angle dispersion curve for steel for a variable angle probe mounted in a perspex block (perspex $c_L = 2550$ m/s). The rectangle shows the region of excitation for the variable angle probes used in the initial experiments with pulse excitation.
- Figure 6.9 (a) Normalised time history of the measured response at $x = 100$ mm in a 1.0 mm thick plate when broad band pulsed excitation was used. (b) Amplitude spectrum of the time history shown in (a)
- Figure 6.10 (a) Normalised time history of a simple 5 cycle excitation tone burst at 1.2 MHz. (b) Measured response at $x = 200$ mm in a 0.5 mm thick plate when the excitation signal shown in (a) was appropriate for s_0 . (c) Amplitude spectrum of the time history shown in (b).
- Figure 6.11 Normalised time history of the measured response at $x = 200$ mm in a 2 mm thick plate when the frequency of the excitation signal shown in Fig. 6.10(a) was 1.0 MHz and was appropriate for s_0 .
- Figure 6.12 Normalised time history of the measured response at $x = 200$ mm in a 3 mm thick plate when the frequency of the excitation signal shown in Fig. 6.10(a) was 1.0 MHz and was appropriate for a_1 .
- Figure 6.13 (a) Normalised time history of the 5 cycle 1.2 MHz excitation tone burst modified by a Hanning window. (b) Measured response at $x = 200$ mm in a 0.5 mm thick plate when the excitation signal shown in (a) was appropriate for s_0 . (c) Amplitude spectrum of the time history shown in (b).
- Figure 6.14 (a) Normalised time history of the measured response at $x = 150$ mm in a 0.5 mm thick plate when the excitation signal was a 12 cycle 1.0 MHz tone burst in a Hanning window and the angle was appropriate for s_0 ; (b) at $x = 250$ mm and (c) the sum of the time histories shown in (a) and (b).
- Figure 6.15 (a) Normalised time history of the measured response at $x = 150$ mm in a 3.0 mm thick plate when the excitation signal was a 12 cycle 0.45 MHz tone burst in a Hanning window and the angle was appropriate for s_0 ; (b) at $x = 250$ mm.
- Figure 6.16 (a) Normalised time history of the measured response at $x = 150$ mm in a 3.0 mm thick plate when the excitation signal was a 12 cycle 0.6 MHz tone burst in a Hanning window and the angle was appropriate for s_0 ; (b) at $x = 250$ mm.
- Figure 6.17 (a) Normalised time history of the measured response at $x = 150$ mm in a 3.0 mm thick plate when the excitation signal was a 12 cycle 0.75 MHz tone burst in a Hanning window and the angle was appropriate for s_0 ; (b) at $x = 250$ mm.
- Figure 6.18 (a) Normalised time history of the measured response at $x = 150$ mm in a 3.0 mm thick plate when the excitation signal was a 12 cycle 1.0 MHz tone burst in a Hanning window and the angle was appropriate for s_1 , a_1 , and s_0 ; (b) at $x = 250$ mm.
- Figure 6.19 (a) Normalised time history of the measured summed responses at $x = 200$ mm and $x = 250$ mm in a 0.5 mm thick plate when the excitation signal was a 5 cycle 1 MHz tone burst in a Hanning window and the angle was appropriate for s_0 ; (b) Amplitude spectrum of the time history shown in (a).
- Figure 6.20 A comparison of the phase and amplitude spectrum results obtained from the time record shown in Fig. 6.19, where the amplitude spectrum results are denoted by squares.

- Figure 6.21 (a) Normalised time history of the measured summed responses at $x = 200$ mm and $x = 250$ mm in a 3.0 mm thick plate when the excitation signal was a 5 cycle 0.6 MHz tone burst in a Hanning window and the angle was appropriate for s_0 ; (b) Amplitude spectrum of the time history shown in (a).
- Figure 6.22 A comparison of the phase and amplitude spectrum results obtained from the time record shown in Fig. 6.21, where the amplitude spectrum results are denoted by squares.
- Figure 6.23 (a) Normalised time history of the measured summed responses at $x = 200$ mm and $x = 250$ mm in a 3.0 mm thick plate when the excitation signal was a 5 cycle 1.0 MHz tone burst in a Hanning window and the angle was appropriate for s_1 , a_1 , and s_0 ; (b) Amplitude spectrum of the time history shown in (a).
- Figure 6.24 Normalised 3-D plot of the 2-D FFT results for the case of Fig. 6.10(b).
- Figure 6.25 Normalised 3-D plot of the 2-D FFT results for the case of Fig. 6.11.
- Figure 6.26 Normalised 3-D plot of the 2-D FFT results for the case of Fig. 6.12.
- Figure 6.27 A comparison of the experimental results (\square) obtained from Fig. 6.24 with the analytically generated dispersion curve for s_0 .
- Figure 6.28 A comparison of the experimental results (Δ) obtained from Fig. 6.25 with the analytically generated dispersion curve s_0 .
- Figure 6.29 Normalised 3-D plot of the 2-D FFT results for the case of Fig. 6.13(b).
- Figure 7.1 Schematic representation of experimental procedure; (a) to obtain reference 2-D FFT; (b) to obtain 2-D FFT after interaction with a notch.
- Figure 7.2 (a) The time history of the measured response at $x = 350$ mm from the transmitter in a 3.0 mm thick steel plate, when the excitation was appropriate for s_0 . (b) Amplitude spectrum of the time history shown in (a).
- Figure 7.3 (a) The time history of the measured response at $x = 350$ mm from the transmitter in a 3.0 mm thick steel plate, when the excitation was appropriate for s_0 and a 0.5 mm deep notch was located at $x = 250$ mm; (b) a 1.0 mm notch; (c) a 1.5 mm notch; (d) a 2.0 mm notch.
- Figure 7.4 (a) Normalised 3-D plot of the reference 2-D FFT results for the case of Figure 7.2(a). (b) Normalised 3-D plot of the 2-D FFT results after the s_0 mode had interacted with the 2.0 mm deep notch.
- Figure 7.5 Normalised plot of the measured amplitude versus wavenumber information from the 2-D FFT results, obtained after the transmission of s_0 across notches of different depths; (a) at 1.35 MHzmm, (b) at 1.45 MHzmm and (c) 1.55 MHzmm.
- Figure 7.6 (a) The time history of the measured response at $x = 350$ mm from the transmitter in a 3.0 mm thick steel plate, when the excitation was appropriate for a_1 . (b) Amplitude spectrum of the time history shown in (a). (c) Time history of the response when a 1.0 mm deep notch was located at $x = 250$ mm and the excitation was the same as in (a).
- Figure 7.7 Normalised plot of the measured amplitude versus wavenumber information from the 2-D FFT results, obtained after the transmission of a_1 across notches of different depths at 2.5 MHzmm.

- Figure 7.8 Transmission ratio of the a_1 mode as a function of frequency-thickness after interaction with (a) the 0.5 deep notch, (b) the 1.0 mm notch, (c) the 1.5 mm notch and (d) the 2.0 mm notch.
- Figure 7.9 Schematic representation of a 3.12 mm thick 350 mm long butt welded steel plate.
- Figure 7.10 Normalised time history of the measured response at $x = 500$ mm from the transmitter in a 3.12 mm thick butt welded steel plate, when the excitation was appropriate for s_0 and the weld region was located at $x = 250$ mm. (a) good weld (b) poor weld (c) bad weld and (d) very bad weld.
- Figure 8.1 (a) Predicted time history at $x = 150$ mm in a 2.0 mm thick plate, when the excitation signal was a 3 cycle 60 kHz tone burst modified by a Hanning window and was designed to excite only a_0 and recombine at $x = 340$ mm to form the 3 cycle tone burst. (b) at 200 mm, (c) at 260 mm and (d) at 340 mm.
- Figure 8.2 (a) Time history of the 12 cycle 0.65 MHz tone burst in a Hanning window excitation signal applied to the transmitter. (b) Normalised time history of the measured response at $x = 200$ mm in a 3.0 mm thick plate when the excitation signal was shown in (a).
- Figure 8.3 (a) The reverse of the response signal shown in Fig. 8.2(b) used as the excitation signal. (b) The time history of the measured response at $x = 200$ mm from the transmitter in a 3.0 mm thick steel plate, when the excitation signal was shown in (a).
- Figure 8.4 (a) The time history of the measured response at 200 mm from the transmitter in a 3.0 mm thick steel plate, when the excitation was shown in Fig. 8.3(a) and a 1.0 mm deep and 0.5 mm wide notch was located at 100 mm from the transmitter.

Nomenclature

In some cases multiple definitions have been made due to the large number of parameters used, but they can be easily identified from the context.

1. Normal letters

A	Generalised amplitude constant
$a_{0,1,2,...etc}$	Antisymmetric Lamb wave (subscript refers to wave mode)
B	Generalised amplitude constant
C, C', C''	Constants
c	Generalised wave velocity
$c_{1,2}$	Bulk wave velocity (subscripts refer to wave mode 1-longitudinal 2- shear)
c_e	Theoretical velocity error
c_f	Free flexural wave velocity considering transverse shear and rotary inertia
c_g	Group wave velocity
c_L	Longitudinal wave velocity in a ideal fluid
c'	Leaky Lamb wave phase velocity respectively
c_R, c'_R	Rayleigh and leaky Rayleigh phase velocity respectively
c_o	Velocity of Longitudinal wave in an infinite plate
c_p	Generalised phase velocity
D	Constants
2d	Plate thickness
E	Modulus of elasticity
[E]	Normal (to the surface) energy flux of an acoustic wave
f	Function
F	Forcing vector; Generalised constant wave shape; Function
f	Generalised frequency
$f_{d_{co}}$	Cut-off frequency for non zero order dispersive wave modes
f_n	Resonant frequency
g	Function

G	Modulus of rigidity; function
h	Notch depth
H(k)	Spatial Fourier transform
H(k,t)	Two-dimensional Fourier transform
H(ω)	Transfer function
i	$\sqrt{-1}$
I	Function
K	Bulk modulus
k	Generalised wavenumber = ω/c
k_1, k_2, k_L	Wavenumbers (subscripts refer to wave type 1-longitudinal, 2-shear and L-longitudinal in a fluid)
k'	Inhomogeneous wave vector
k'	Leaky Lamb wavenumber
k_{ny}	Nyquist wavenumber
k_R, k'_R	Rayleigh and leaky Rayleigh wave number respectively
k_{sam}	Sampling wavenumber
k_{SH}	Wavenumber of dispersive shear horizontal waves = $\sqrt{[k_2 - (\pi n/2d)^2]}$
k_x, k_y, k_z	Complex wavenumbers
K	Global stiffness matrix
K_e	Element stiffness matrix
L	Distance in the x direction
M	Global mass matrix
M_e	Element mass matrix
M_{II}	Diagonalised consistent mass matrix
N	Number of nodes per wavelength; matrix of element shape functions
$N_{x,y,z}$	Direction cosines in cartesian directions
SH, SV	Horizontally and vertically polarized shear Waves
R	Generalised reflection coefficient
$s_{0,1,2,..etc}$	Symmetric Lamb wave (subscript refers to wave mode)

T	Generalised transmission coefficient
T	Kinetic energy
t	Time
t_c	Critical time step in numerical modelling
u, v, w	Displacement in x, y and z directions in cartesian coordinates
\mathbf{u}	Displacement vector of horizontally polarized waves
U	Strain energy
$u_{s,a}, w_{s,a}$	Lamb wave displacements Lamb wave in the x and z directions (subscripts refer to mode type s -symmetric and a -antisymmetric modes)
w	notch width
$u'_{s,a}, w'_{s,a}$	Leaky Lamb wave displacements in the x and z directions
x, y, z	Cartesian coordinates
Z	Generalised normal acoustic impedance = $\rho c / \cos\theta$

2. Greek letters

α	Modulus of imaginary part of complex angle
δ	Dirac delta function
Δ	Dilatation ($\epsilon_{xx} + \epsilon_{yy} + \epsilon_{zz}$)
∇^2	Laplace operator in cartesian coordinates ($\partial^2/\partial x^2 + \partial^2/\partial y^2 + \partial^2/\partial z^2$)
$\epsilon_{xx}, \epsilon_{yy}, \epsilon_{zz}$	Direct strains in cartesian directions
$\epsilon_{xy}, \epsilon_{yz}, \epsilon_{zx}$	Shear strains in cartesian directions
η_c	Ratio of Lamb wave phase and group velocity (c_p/c_g)
θ	Generalised incidence angle
$\theta_1, \theta_2, \theta_L$	Propagation direction of bulk waves (subscripts denote wave type 1-longitudinal 2-shear L-longitudinal in an fluid)
θ_{cr}	Critical angle at which the bulk waves travel parallel to a boundary
λ	Generalised wavelength

λ	Lame's constant
Λ	Mesh spacing
μ	Lame's constant
ν	Poisson's ratio
ρ	Generalised density
ρ_L	Density of fluid
$\sigma_{xx}, \sigma_{yy}, \sigma_{zz}$	Direct stresses in cartesian directions
$\sigma_{xy}, \sigma_{yz}, \sigma_{zx}$	Shear stresses in cartesian directions
ϕ	Longitudinal wave potential
$\Phi(z)$	Through-thickness mode shape
φ	Generalised Phase
$\Delta\varphi$	Difference in phase spectrum of two signals
ψ	Shear wave potential
ω	Angular frequency = $2\pi/f$
Ω	Frequency thickness product = $2fd$

CHAPTER 1

A review of the application of stress waves in nondestructive testing and monitoring

1.1 Introduction

The testing and monitoring of the state of manufactured items is so commonplace that we tend to take it for granted. For example, few would buy a bicycle without leaning or sitting on it to test its sturdiness. With the trend in the more industrialised nations to produce finished products which have an ever higher proportion of added value, nondestructive testing and process monitoring methods are becoming more important. In particular, the nuclear and aerospace industries, in which component reliability is crucial, have in many cases, developed new, specialised techniques. Ultrasonic inspection is one of the most commonly used techniques and its application has been increasing rapidly over the last few decades as the electronic equipment necessary has become cheaper and more readily available.

The aim of all nondestructive testing and monitoring methods is to identify and locate physical features which are unacceptable without causing any damage to the material structure or component under test. These features will be referred to henceforth as defects. Restricting our attention to industrial applications and disregarding qualitative audio and/or visual inspection carried out by humans (probably the most widely used forms of inspection), then the following methods are the most commonly used:

- Magnetic particle
- Dye penetrants
- Eddy currents
- Radiography
- Ultrasonics (standard)

The first three methods are generally used to detect surface breaking or near surface defects. Radiography and ultrasonics are used generally to detect buried features as well as surface breaking defects and may be employed where a quantitative analysis is required.

In the next section a brief introduction to standard ultrasonic NDT will be given. Experimental Rayleigh and Lamb wave NDT methods will then be discussed, the results and work of many of the leading researchers being used to illustrate particular applications. Finally, the advantages of using Lamb waves in applications, where coarse, fast, long range testing is adequate, and in situations where a more detailed localised interrogation is necessary will be discussed.

1.2 General ultrasonic nondestructive testing.

Standard ultrasonic testing in the 0.2-30 MHz range using bulk stress waves constitutes a substantial area of NDT. These waves may be excited in the majority of materials used in industrial applications, and systems using stress waves are flexible, versatile, cheap and safe. The resulting data may be interpreted in the time or frequency domain and can be stored and processed to operate sorting gates, or to give alarms. Standard ultrasonic testing may be separated into two major areas, resonance techniques in which the excitation is narrow band and pulse techniques in which the excitation is wide band.

Resonance techniques are principally employed to measure the thickness of walls and the depth of delaminated layers. Physically, this is achieved by locating the resonant frequencies of the component under investigation, the wall thickness being obtained from the relation

$$2d = \frac{c}{2(f_{n+1} - f_n)} \quad n = 0, 1, 2, \dots, n_{\max} \quad (1.1)$$

where f_n is a resonant frequency, c is the wave velocity, $2d$ is the wall thickness and n is an integer. Since the wave velocity is material dependant, instruments that use this method must be recalibrated for different materials. Provided that damping (or apparent damping due to, for example, acoustic transmission) is light these frequencies are well defined and may be located accurately. For more details on resonance techniques see standard NDT texts, for example, Szilard (1982) or Krautkrämer and Krautkrämer (1983).

Pulse excitation methods in which ultrasonic pulses are propagated through the area of interest, (see Fig. 1.1) are used far more extensively in industry. When ultrasonic pulses

interact with a defect, for example, air filled cracks, there will generally be almost total reflection. This enables the relative amplitudes and time of flight of the ultrasonic pulses to be used as a measure of the integrity of the material or component under investigation. The advantage of pulse methods is that the system under test may be decoupled easily from the measuring system and the rest of the world. Firestone (1940) and Firestone and Ling (1951) probably were the first to recognise the advantage of using pulsed methods in NDT applications

The pulse-echo mode, (see Fig. 1.1(a)) requires access to only one side of the testpiece and a single transducer acts as a transmitter and receiver. In pitch-catch mode, (see Fig. 1.1(b)) two transducers, one acting as transmitter one acting as receiver are located on the same side of the testpiece. In through-transmission mode, (see Fig. 1.1(c)) the transmitting and receiving transducers are located on either side of the testpiece. In each of the above cases the area interrogated is along a line joining the two transducers.

Because of the large impedance mismatch between air and solid material, it is difficult to propagate waves from a transducer through air into the structure to be tested. Therefore, a coupling media between the two is generally employed. The normal impedance Z , is the ratio of the acoustic pressure to the projection of the particle velocity on the normal of the surface and is given by

$$Z = \frac{\rho c}{\cos\theta} \quad (1.2)$$

where ρ is the density and θ is the angle of the wave front to the normal of the surface. Maximum energy transfer occurs if the impedances of the testpiece and the coupling medium are equal. In solid coupling, the transducer is bonded or fixed to the testpiece. In dry contact coupling a flexible membrane which is generally filled with oil and will deform to the shape of the testpiece surface is attached to the transducer. In thin film coupling a gel is applied to a small area where the transducer is to be positioned, and in immersion coupling the whole testpiece is immersed in a liquid (generally water). Thin film and immersion coupling are the most popular methods because only a longitudinal wave is incident at the liquid-testpiece interface.

The frequency and the wavelength of ultrasound are related by

$$\lambda = \frac{c}{f} \quad (1.3)$$

where λ is the wavelength. Hence, if the wave velocity is constant, the wavelength will become smaller with increasing frequency. It is shown by, for example, Ensminger (1973) that detectable defect size is related to wavelength, the higher the frequency the smaller the detectable defect. However, in real materials the wave amplitudes decrease or attenuate during propagation. Attenuation is a function of frequency, therefore, as the frequency of the wave is increased its penetrating power (propagation distance) will be reduced. At frequencies where the wavelength is reduced to the order of grain size, scattering from the grain boundaries will also result. Modern NDT techniques using high frequency ultrasonic stress waves (up to 50 MHz) are capable of detecting defects less than 0.1 mm in diameter. In order to detect ever smaller defects and increase the resolution, the trend has been to use ever higher frequencies with short duration pulses. However, in some cases, for instance in highly attenuating media or materials with a coarse grain structure (a good example being stainless steel), it is not possible or desirable to use high frequencies.

The sensitivity of ultrasonic methods is dependent on the properties of the transducer used. Transducers have near and far fields (see Krautkrämer and Krautkrämer 1983); in the near field it is difficult to determine the presence of defects as the amplitude of the reflected wave is affected by the diffraction pattern. Delay lines or immersion coupling may be used to alleviate this problem. Focussed transducers may also be used to reduce the extent of the near field and increase the intensity of the ultrasound at a particular point, thereby increasing sensitivity.

Resolution is the ability to distinguish between defects located very close to one another. To increase the resolution, short pulses are required, which require wide band, heavily damped transducers. Resolution and sensitivity are also functions of the properties of the testpiece. The testpiece geometry determines accessibility, and is also a factor when considering the choice of wave mode for inspection. When thin film coupling is used, the amplitude of the wave at the fluid-testpiece interface is also sensitive to the contact pressure between the testpiece and the transducer.

Other important factors include anisotropy, surface roughness, the presence of internal scatterers and their cross-section, and grain-size and grain-boundary conditions; for more details on these effects and ultrasonic NDT in general there are many good text books, for example, Szilard (1982).

1.3.1 General nondestructive testing using Rayleigh and Lamb waves

Rayleigh and Lamb waves are propagating two-dimensional vibrational modes (sometimes called guided waves). The Rayleigh wave exists on the boundary of a free half space and Lamb waves may propagate in free plates. In practice half spaces do not exist, but if the plate thickness is greater than $5\lambda_R$, where λ_R is the Rayleigh wavelength, Viktorov (1970) shows that the zero order Lamb modes a_0 and s_0 will combine to form a quasi-Rayleigh wave which is effectively indistinguishable from the Rayleigh wave, and henceforth will be referred to as the Rayleigh wave. Other types of guided waves also exist in tubes and cylinders and theoretical treatments of them may be found in many standard texts, for example, Graff (1975). When the radius of curvature of these sections is much less than the wavelength of the propagating mode(s), they may be approximated to plates.

In the last few decades Rayleigh, Lamb and other guided waves have been used increasingly in ultrasonic NDT applications where standard ultrasonic techniques using bulk waves cannot be applied; for example, to detect small cracks located near an interface or narrow cracks that run normal to an interface or free surface. As Rayleigh and Lamb waves are two-dimensional they may be propagated over considerable distances and therefore many workers have applied them in long range testing applications. However, more than one propagating mode is usually excited by real transducers and in the case of Lamb waves, dispersion is generally present. The last two points mean that Lamb wave signals are generally very complicated. Hence, a substantial part of the research work to date has been directed towards the interpretation of Lamb wave signals. Rayleigh and Lamb waves are usually excited using either thin film or immersion coupling; if immersion coupling is used then energy from these modes will be leaked continuously into the coupling fluid and their propagation distances will be reduced.

Rayleigh wave inspection is used predominantly to find small defects located near to or at boundaries, as the Rayleigh wavelength is always smaller than that of any other propagating mode and most of its energy is concentrated close to the surface. Reinhardt and Dally (1970) looked at the interaction of Rayleigh waves with slits and were able to obtain quantitative transmission and reflection coefficients using dynamic photoelasticity methods. Hall (1976) and Burger *et al* (1982) and many of his co-workers have also used photoelasticity methods to obtain quantitative measurements of Rayleigh wave defect interactions. Finch and Bray (1973) used quarter scale model railway wheels to study the interaction of surface and other guided waves with simulated thermal cracks. Derkacs and Matay (1979) have used high frequency (45 MHz) Rayleigh waves to detect defects with dimensions of the order of 0.1 mm. The frequency dependent amplitudes of reflected Rayleigh wave signals have been used by Singh and Singh (1981), Klein and Salzburger (1982), Fitting, Adler (1982) and Kinra and Vu

(1983) to determine the dimensions of surface defects. Bond *et al* (1984) have discussed the trends in ultrasonic NDT and highlighted the increasing emphasis on quantitative methods, in which detectable changes caused by mode conversion are used in the analysis. Bond and his co-workers, for example, Georgiou and Bond (1985) and Saffari and Bond (1983) have concentrated on the interaction of Rayleigh waves with different types of surface breaking defects. Cooper *et al* (1985) have used a laser to generate short duration Rayleigh wave pulses in order to investigate surface breaking slots. They report being able to detect slots from 0.3 mm to 3.0 mm deep and conclude that the technique may be developed to measure slot depth.

Viktorov has published extensively on the use of Rayleigh and Lamb waves in nondestructive testing and monitoring applications, and his book (Viktorov 1970) has become a standard text in the field. However, it was probably Worlton (1957) and (1961) who first recognised the advantages of using Lamb waves to nondestructively test plates. Since then there has been a great deal of interest in these and other guided waves in NDT applications. Worlton's work, and that of many other early investigators (for example, Lehfedt 1962) was qualitative, but they led many other workers to investigate the possibility of using the Lamb modes, a_0 and s_0 at frequency-thickness products below the cut-off of the first higher order mode, a_1 (approximately 1.63 MHzmm in steel).

Doyle (1978) reviewed guided wave NDT methods and gave suggestions for directions of future research. Much of the previous and subsequent work has shown that coarse, fast, long range qualitative NDT techniques using Lamb waves can be carried out on plates or plate-like structures, if the tolerable defect dimension is less than 25% of the section thickness. Rowland and Lichodziejewski (1973) have used Lamb waves in long range fast inspection of honeycomb panels and report reliably finding 25 mm long delaminations over propagation distances of 300 mm. Silk and Bainton (1979) carried out experiments to study the interaction of guided waves with artificial defects. The aim of the work was to locate defects in boiler and heat exchanger piping. Hayashi and Naoe (1986) have used Lamb waves, the s_0 mode, in a continuous automatic NDT method for testing thin metal sheets (thickness less than 0.8 mm), but report low sensitivity. Duncumb and Keighley (1987) reported using Lamb waves to detect simulated corrosion defects, where the defect depth was greater than a quarter of the plate thickness. Rose *et al* (1983) and Avioli (1988) tried to obtain quantitative results of defect detectability in large structures, by comparing Lamb wave signals in the frequency and time domain respectively, but they reported limited success because of the typically complicated nature of Lamb waves signals when more than one mode is present.

Zelik and Reinhardt (1972) used Lamb wave techniques to detect and locate small cracks and holes in space cabin wall panels of 1.5 mm thick aluminium. Lockett (1973) looked at the

interaction of Lamb waves with defects in tubes and reported limited success. Work in the Soviet Union by Burmistrov *et al* (1978) was carried out to develop methods of testing steel pipes with ribs for cracks and foreign inclusions using guided waves, and they report being able to detect defects with depths of less than 0.1 mm, when the thickness of the pipe wall was 0.6 mm. Boness (1981) reported experimental investigations carried out to determine the integrity of welded seals on nuclear material storage cans, in which they used the lowest order Lamb modes a_0 and s_0 . Chimenti and Bar-Cohen (1985) have analysed the spectra of Lamb waves in order to test fibre-reinforced composite laminates.

Ultrasonic NDT techniques using guided waves have concentrated on using pulsed methods. Most of the researchers have tried to correlate defect size to the scattered pulse amplitude using time domain methods or spectroscopic analysis. However, because of the difficulty of measuring Lamb wave amplitudes accurately using standard time or frequency domain methods, the reported quantitative experimental results have tended to be restricted to frequency-thickness regions where only a_0 and s_0 may propagate. Recently many workers have recognised that there are two distinct application areas of Rayleigh and Lamb waves; firstly in localised short range applications where sensitivity is important, and secondly in long range applications where speed is important. Hence, these two situations are discussed briefly below.

1.3.2 Localised nondestructive testing using Rayleigh and Lamb waves

When testing very thin plates or looking for defects on or very close to an interface, the resolution between two echoes, which is inversely proportional to the pulse length, is critical. Because of the finite duration of pulses from real probes a null zone below any interface will not be interrogated using standard ultrasonic bulk wave testing. This is of major importance in industrial NDT, where many potentially damaging defects are found near free surfaces or at material interfaces, for example, fatigue cracks in steel.

Lamb waves have been used to determine the elastic properties of materials, especially composites on which there is a great deal of published work. For example, Nayfeh and Chimenti (1988) and Mal and Bar-Cohen (1990) have carried out work to determine the elastic constants of composites and Okada (1986) has used Lamb waves techniques to measure anisotropy of cold rolled metals.

In localised detailed nondestructive testing or monitoring applications the detectability of a particular defect may be optimised when using Lamb waves by choosing the most appropriate

mode at the most suitable frequency-thickness product and not necessarily by using higher frequencies as in standard ultrasonic NDT using bulk waves. Furthermore, in these applications the dispersive nature of Lamb waves is not so problematic, as the propagation distances are relatively small and reasonable signal-to-noise ratios may be maintained in most frequency-thickness regions.

The major advantage of using Lamb waves in localised detailed NDT applications is that they produce stresses throughout the plate thickness (although there may be stress nodes which have to be carefully considered). Therefore, the entire thickness of the plate is interrogated. This point is of major importance as it means that it is possible to detect defects that are located at or very near interfaces, or at other internal locations. Many workers have investigated the possibility of using Lamb waves and/or other guided waves with similar properties to detect delaminations and defects in adhesively bonded joints. Kline and Hashemi (1987) have used guided waves to monitor fatigue cracks in bonded joints and Rokhlin (1986) has investigated using these modes to characterise the quality of adhesive bonds.

1.3.3 Long range nondestructive testing using Lamb waves

Standard ultrasonic methods using bulk waves for the nondestructive testing and monitoring of large plates or plate-like structures interrogate discrete points, or discrete points along a line as may be seen from Fig. 1.1, and are therefore essentially one-dimensional. In order to completely test a component or structure of any significant size reliably requires many point readings. The use of Lamb waves is a very attractive solution to this problem since they can be excited at one point on the structure and propagated over considerable distances. If a receiving transducer is positioned at a remote point on the structure, the received signal contains information about the integrity of the line between the transmitting transducer and the receiving transducer. This procedure therefore interrogates a two-dimensional area between two points (as can be seen from Fig. 1.2), rather than a line between two points. Hence we refer to this as two-dimensional inspection. The use of these modes would therefore greatly reduce testing time on large plates and plate-like structures where a thorough inspection is required.

Moreover, bulk waves are three-dimensional and will thus radiate energy three-dimensionally. Therefore, if excited from a point source their amplitude decreases inversely as a function of distance squared and at any instance after initiation the wavefront will describe a sphere in space. Because Lamb waves are free modes of plates (two-dimensional propagating vibrations), their amplitude will decrease only inversely with respect to the propagation

distance from the source, (see Fig. 2.1). Hence, Lamb waves may be propagated over considerably longer distances than bulk waves and still have a reasonable signal-to-noise ratio. The signal-to-noise ratio is usually further improved by using long duration tone burst excitation and exciting the Lamb wave required at a point of minimum velocity dispersion.

A very large number of workers in the field have recognised the advantages of using Lamb waves for fast inspection, where sensitivity and resolution in comparison to standard high frequency ultrasonic techniques is not so critical. Lamb waves have been used to carry out coarse, quick inspection on a variety of different strips and plates by, for example, by Conn and Jackson (1971), Ball and Shewring (1976) and Mansfield (1975). Rokhlin (1979) has reported many studies on the sensitivity of Lamb waves to elongated delaminations. Rokhlin and Bendec (1983) have also studied the interaction of Lamb waves with spot welds and have shown that the transmission of the first symmetric mode through a spot weld may be linearly related to the cube of the diameter of the spot weld. Rose *et al* (1983) have reported investigations using Lamb waves to globally inspect K-joints in off-shore structures. The Welding institute in the UK (see, for example, Bartle 1985) have been developing an acoustic pulsing technique to monitor crack growth in large plate-like structures.

1.4 Conclusions

During the last few decades a large number of researchers have investigated using Rayleigh and Lamb waves in industrial NDT applications, where standard ultrasonic methods may not be used or are difficult to apply.

Rayleigh waves are used to detect near surface defects where the defect size is of the order of the Rayleigh wavelength. Lamb waves produce stresses throughout the thickness of the plate (although there are stress nodes in many cases which have to be considered) and therefore allow two-dimensional interrogation of plates and plate-like structures, rather than the usual point by point investigation necessary when using standard ultrasonic methods. Also, because they are two-dimensional, their amplitudes decrease less rapidly with propagation distances than the three-dimensional bulk waves. Propagation distances for NDT purposes may therefore be increased. The last two points are of great importance in NDT applications where a quick coarse inspection is sufficient. It is also possible to optimise the detectability of a particular defect by choosing the most appropriate Lamb wave at the best frequency-thickness product.

The review of past experimental research has shown that qualitative or quantitative methods can be applied in low frequency-thickness product regions, where the only propagating modes are a_0 and s_0 , as they may be easily decoupled from one another. In higher frequency-thickness regions most researchers have been unable to report reliable and robust methods of obtaining quantitative experimental results and have in many cases reported qualitative results obtained using a variety of comparison techniques.

1.5 Outline of the thesis

The major objective of the thesis is the development of quantitative and qualitative methods of applying Lamb waves to industrial nondestructive testing and monitoring applications.

Chapter 1 provided an introduction, including a review of the use of guided waves in the NDT of plates and plate-like structures.

Chapter 2 will present all the stress wave theory necessary, paying attention to the physical significance of the analytical expressions. The way in which these waves may be excited and received more efficiently using transducers of finite size and excitation signals of finite duration will also be discussed.

The key problem of Lamb wave testing is that invariably more than one mode is excited by real transducers and in chapter 3 a new method of measuring the amplitudes and velocities of guided waves using a two-dimensional Fourier transformation will be presented.

In chapter 4 the results of initial numerical studies using the finite element numerical method are presented. The initial results are discussed and the advantages of the finite element method stated. Further numerical work is presented where single and multiple modes have been launched successfully using finite elements. The results have been processed using the time of flight method and the two-dimensional Fourier transform.

Chapter 5 presents a finite element study of the interaction of different Lamb waves with straight sided notches of varying depths, which are orientated normal to the plate surface. In all the finite element tests the 2-D FFT method was used to analyse the results quantitatively.

In chapter 6 the experimental procedures and equipment used are discussed and the practical methods of exciting and measuring propagating Lamb waves are presented. The velocities are

calculated using standard time domain and frequency domain methods and the 2-D FFT method, which also gives the relative amplitudes of the modes.

Chapter 7 reports the results of experiments carried out using a variety of plates with straight sided notches and weld defects. The results are correlated with those obtained in the finite element studies to validate the model and again the 2-D FFT method is used to analyse the results quantitatively.

Chapter 8 discusses the implementation of Lamb waves to the NDT of plates and plate-like structures, concentrating on ways of reducing or circumventing the practical limitations evident when trying to adopt quantitative or qualitative methods.

The major conclusions of the the thesis are given in chapter 9.

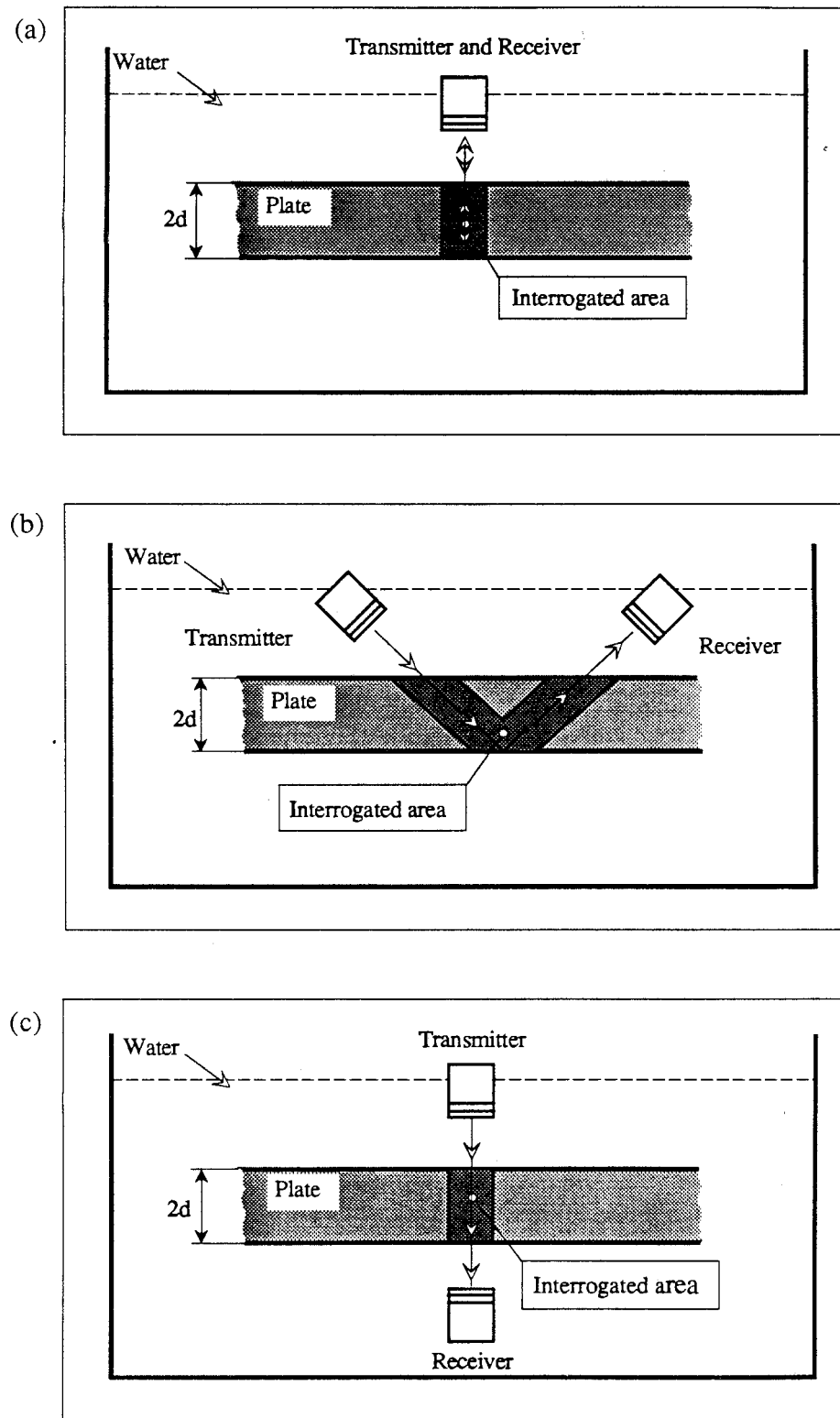


Figure 1.1 (a) Schematic representation of (a) pulse-echo mode, (b) pitch-catch mode and (c) through-transmission mode.

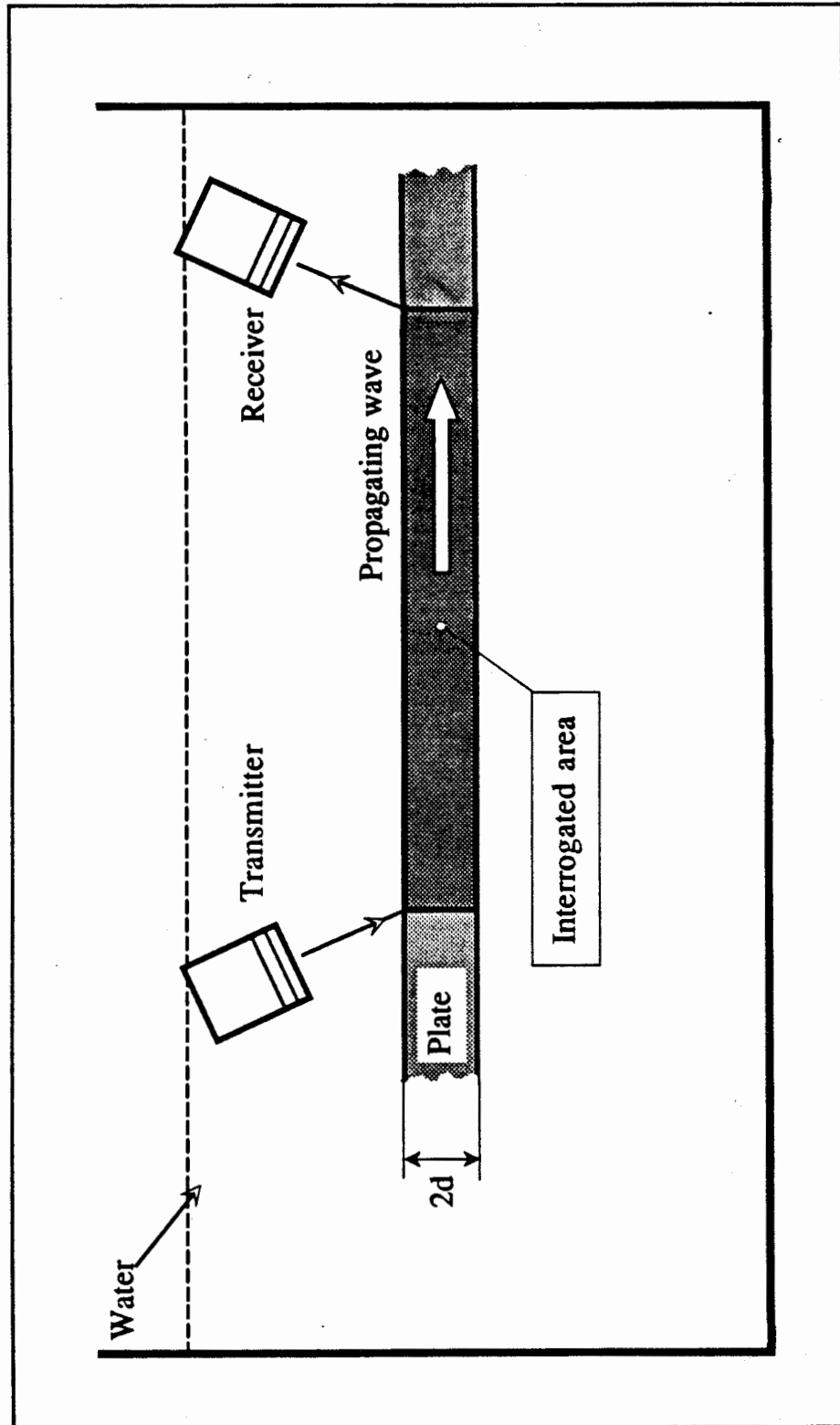


Figure 1.2 Schematic representation of Lamb wave testing.

CHAPTER 2

Wave propagation and boundary interaction

2.1 Introduction

Elastic waves can propagate in solid, liquid and gaseous media. However, the propagation of waves in solids and liquids is the major area of interest in ultrasonic NDT. This is because of the large impedance mismatch between solid materials, in which the ultrasonic waves are usually generated and gases such as air, which are sufficiently rarefied for them to be considered as a vacuum.

In this chapter, the theory used to describe the characteristics of stress waves in infinite and finite media will be briefly described, and a number of commonly used methods of efficiently exciting and receiving Rayleigh and Lamb waves will be discussed. In all the analysis, the material will be assumed to be homogeneous, isotropic, linear elastic, non-absorbing and non-piezoelectric.

2.2 The plane wave model

In most practical NDT applications simple plane wave models are sufficiently accurate to yield satisfactory results. This describes the simplest form of wave motion, and may be expressed by a general analytic expression given by Brekhovskikh (1980) as:

$$F\left[\frac{N_x x + N_y y + N_z z}{c} - t\right] = A \quad (2.1)$$

Where A is a constant and $N_{x,y,z}$ may be regarded as direction cosines of the line representing the direction of propagation, which satisfy the condition

$$N_x^2 + N_y^2 + N_z^2 = 1 \quad (2.2)$$

The function F is constant at any time over a plane normal to that line. It describes a wave travelling with velocity c , and the waveform defined by F remains constant during propagation.

2.3 Bulk waves

Rigid body dynamics assumes that a resultant force sets every point in a body in motion instantaneously, which is equivalent to assuming that the material of the body has infinite Young's modulus. In all real media Young's modulus will be finite, and wave equations may be developed from the concept of a series of infinitesimally small mass elements. If forces are applied to an element, the element will accelerate according to Newton's law. Therefore, a finite time is required for the element to change its position. To maintain the continuum (compatibility) neighbouring particles also undergo change of position. This causes stresses to be progressively transmitted through the media, and these propagating waves are simply termed stress waves.

Lamé's constants λ and μ completely define the elastic stress-strain behaviour of the material. In engineering applications Lamé's constants are usually replaced for convenience by four related elastic constants:

$$E = \frac{\mu[3\lambda + 2\mu]}{\lambda + \mu} \quad (2.3)$$

$$\nu = \frac{\lambda}{2[\lambda + \mu]} \quad (2.4)$$

$$K = \frac{\lambda + 2\mu}{3} \quad (2.5)$$

$$G = \mu \quad (2.6)$$

Where E is the modulus of elasticity, ν is Poisson's ratio, K is the bulk modulus and G is the modulus of rigidity.

The equations which describe motion in a solid may be obtained by considering stress variations across an element (see for example Timoshenko 1982), are applicable regardless of

the stress-strain behaviour of the solid, and expressed in terms of the stress strain relations are:

$$(\lambda + \mu) \frac{\partial \Delta}{\partial x} + \mu \nabla^2 u - \rho \frac{\partial^2 u}{\partial t^2} = 0 \quad (2.7)$$

$$(\lambda + \mu) \frac{\partial \Delta}{\partial y} + \mu \nabla^2 v - \rho \frac{\partial^2 v}{\partial t^2} = 0 \quad (2.8)$$

$$(\lambda + \mu) \frac{\partial \Delta}{\partial z} + \mu \nabla^2 w - \rho \frac{\partial^2 w}{\partial t^2} = 0 \quad (2.9)$$

where

$$\nabla^2 = \frac{\partial^2}{\partial x^2} + \frac{\partial^2}{\partial y^2} + \frac{\partial^2}{\partial z^2} \quad \text{and} \quad \Delta = \epsilon_{xx} + \epsilon_{yy} + \epsilon_{zz}$$

∇^2 is the Laplace operator in cartesian coordinates and Δ represents the change in volume, and is termed the dilatation. They are linear homogeneous partial differential equations for which the principle of superposition holds. It is shown by, for example, Kolsky (1963) that by integration and manipulation of the above three equations, two independent effects may be obtained.

Firstly, if it is assumed that any deformation produced is such that no volume changes take place, then in the x direction eqn 2.7 becomes:

$$\mu \nabla^2 u - \rho \frac{\partial^2 u}{\partial t^2} = 0 \quad (2.10)$$

This is a wave equation, which describes a disturbance of constant shape, travelling with constant velocity, in the positive x direction. Similar equations may be deduced in the y and z directions, the resultant propagating wave being termed shear or distortional, and may be shown to travel with constant velocity c_2 given by:

$$c_2 = \sqrt{\frac{\mu}{\rho}} = \sqrt{\frac{G}{\rho}} = \sqrt{\frac{E}{2\rho(1 + \nu)}} \quad (2.11)$$

If we consider the situation without rotation, in the x direction eqn 2.7 becomes:

$$(\lambda + \mu) \nabla^2 u - \rho \frac{\partial^2 u}{\partial t^2} = 0 \quad (2.12)$$

This equation is mathematically identical to eqn 2.10 and describes a propagating disturbance which may be either called a dilatational or longitudinal wave. This wave propagates with constant velocity c_1 given by:

$$c_1 = \sqrt{\frac{\lambda + 2\mu}{\rho}} = \sqrt{\frac{E(1 - \nu)}{\rho(1 + \nu)(1 - 2\nu)}} \quad (2.13)$$

The shear and longitudinal waves propagate independent of one another. Therefore, any plane wave propagating through an infinite medium must travel with a constant velocity (c_1 or c_2), which is a function of material properties only. The velocity c_1 is associated with displacement components parallel to the direction of propagation, while c_2 is associated with displacement components normal to the direction of propagation. Investigations of these uncoupled waves in infinite media were first carried out by seismologists.

A perfect liquid cannot sustain shear, therefore $\mu=0$ and only longitudinal waves may exist, their velocity being given by:

$$c_L = \sqrt{\frac{\lambda}{\rho}} = \sqrt{\frac{K}{\rho}} \quad (2.14)$$

A shear wave with an arbitrary polarisation vector may be considered as consisting of a combination of shear waves with polarisation vectors in the vertical and horizontal planes. The effects due to these waves are investigated separately and superposition is used to obtain the total effect. For vertically polarized waves the displacement vector \mathbf{u} may be completely defined in the xz plane (see Fig. 2.1), and expressed in terms of a scalar, ϕ , and vector, ψ , potential relation,

$$\mathbf{u} = \text{grad } \phi + \text{curl } \psi \quad (2.15)$$

where ϕ and ψ are the potentials associated with the longitudinal and shear waves respectively, which satisfy the wave eqns 2.12 and 2.10. The potentials may be written as follows:

$$\phi = A(\omega)e^{i[k_1(x\sin\theta_1 + z\cos\theta_1) - \omega t]} \quad (2.16)$$

and,

$$\psi = B(\omega)e^{i[k_2(x\sin\theta_2 + z\cos\theta_2) - \omega t]} \quad (2.17)$$

where $A(\omega)$ and $B(\omega)$ are the potential amplitudes, $i=\sqrt{-1}$, $k_1=\omega/c_1$ and $k_2=\omega/c_2$ are the angular wavenumbers of longitudinal and shear waves respectively and are proportional to the momentum of the wave, and $\omega=2\pi f$ is the angular frequency.

2.4 Reflection from a free elastic half space

In any real medium a propagating wave will interact with a boundary, where boundary stress and strain conditions must be satisfied. In the following, continuous wave propagation and infinite wave fronts in the x and y Cartesian directions shown schematically in Fig. 2.1 will be assumed. For details of the analysis when the wavefront is of finite dimension and duration see Pialucha (1991).

A solid-air interface is a very good approximation to the generally analysed case of a solid-vacuum interface. In this section we will consider the reflection of longitudinal and shear waves at a plane boundary parallel to the x axis. Shear horizontal waves are reflected from plane boundaries (see Fig. 2.2(a)), without a change of angle or amplitude.

2.4.1 An incident longitudinal or shear wave

If a longitudinal wave is incident at the boundary (Fig. 2.2(b)), two waves, a longitudinal wave and a shear wave are generally reflected, the shear wave being generated by mode conversion. The angles of reflection of the longitudinal and shear wave are given by Snell's law:

$$c_p = \frac{c_1}{\sin\theta_1} = \frac{c_2}{\sin\theta_2} \quad (2.18)$$

where c_p is the phase velocity, which is the rate at which points of constant phase travel along the boundary. Snell's law expresses the fact that the phase velocity of the longitudinal and shear waves must be the same if one is generated from the other. Rigorous proofs of the equality of the phase velocity of bulk waves, may be obtained in Brekhovskikh (1980).

The reflection coefficients of the longitudinal and mode converted shear waves are given by, for example, Graff (1975) and are dependent only on the Poisson's ratio of the solid,

$$v = \frac{\left[\frac{c_1}{c_2}\right]^2 - 2}{2\left\{\left[\frac{c_1}{c_2}\right]^2 - 1\right\}} \quad (2.19)$$

At normal incidence, no mode conversion takes place, and the reflected longitudinal wave is 180° out of phase with the incident one.

If only a shear wave is incident, as illustrated in Fig. 2.2(c), in general there will be mode conversion to a longitudinal wave to satisfy boundary conditions. Reflection coefficients of the shear and longitudinal waves are presented by Graff (1975), and are dependent only on Poisson's ratio. No mode conversion occurs at normal incidence, or when the shear wave is incident at 45° . Because c_1 is always greater than c_2 , Snell's law relates the angle of the reflected waves such that, $\theta_1 > \theta_2$, and there will be a critical angle of incidence $\theta_1 = \theta_{cr}$ at which $\theta_2 = 90^\circ$, as shown in Fig. 2.2(d). For $\theta_1 > \theta_{cr}$ total internal reflection of the shear wave takes place, θ_1 is replaced by a complex angle α_1 , and plane wave theory is not applicable to the non-uniform or inhomogeneous longitudinal wave reflected. The amplitude of the inhomogeneous longitudinal wave decays exponentially in the z direction with depth from the surface.

2.5 Reflection from a liquid-solid half space

It is necessary to model wave interaction at liquid solid interfaces as they are encountered frequently in ultrasonic NDT. An ideal liquid will always be assumed. At the interface, the relative amplitudes of the reflected and transmitted waves, will depend on the wave mode, the acoustic impedance of the liquid and the solid and the angle at which the incident wave approaches the interface; again, boundary conditions of stress and strain must be satisfied.

The general reflection and transmission equations given by, for example, Brekhovskikh (1980) in terms of impedance are derived by imposing the boundary conditions and using the elastic relations.

In fluids, only longitudinal waves can exist, but in the solid, longitudinal and shear waves may be present. Here, we will only consider waves of vertical polarization.

2.5.1 A longitudinal wave incident from the liquid

If a longitudinal wave is incident from the liquid, the reflection coefficient of the generated longitudinal wave in the liquid denoted by the suffix L, and the transmission coefficient of the longitudinal and shear wave generated in the solid by mode conversion may be computed from expressions given by, for example Brekhovskikh (1980). The angles of the respective waves to the normal to the interface are given by,

$$c_p = \frac{c_L}{\sin\theta_L} = \frac{c_1}{\sin\theta_1} = \frac{c_2}{\sin\theta_2}$$

At normal incidence all the angles are zero, no mode conversion takes place and we obtain the simple expressions for the reflection and transmission coefficients at normal incidence,

$$R = \frac{Z_L - Z}{Z_L + Z} \quad (2.20)$$

and

$$T = \frac{2Z}{Z_L + Z} \quad (2.21)$$

where Z and Z_L are the impedance in the solid and fluid respectively. In almost all practical NDT applications the longitudinal wave velocity in the fluid is less than the shear wave velocity in the solid so ($\theta_L < \theta_2 < \theta_1$). This causes θ_2 , θ_1 and hence their associated impedances to become complex over certain ranges of incident angle. In the range $0 < \sin\theta_L < (c_1/c_2)$ all the angles are real.

When $(c_1/c_2) > \sin\theta_L > (c_1/c_1)$, θ_2 is real and the shear wave in the solid will be plane. However, θ_1 will be complex, physically this means that the longitudinal wave in the solid will be inhomogeneous and travel along the surface. Plane wave concepts no longer apply to the longitudinal wave and the energy of the incident wave (normal to the surface component) is divided between the reflected longitudinal and transmitted shear wave in this angular region.

When shear waves are used for NDT inspection, angular regions where the longitudinal wave is inhomogeneous are preferable, as all the transmitted ultrasonic energy will be taken by the shear wave.

Finally, for $(\pi/2) \geq \sin\theta_L > (c_1/c_2)$ both θ_1 and θ_2 will be complex. This signifies that there are local surface disturbances in the solid (inhomogeneous waves). The boundary will present

a purely reactive impedance to the incident wave. The modulus of the reflection coefficient is unity in this range. Total internal reflection takes place and this phenomenon is analogous to the optical situation.

2.5.2 A longitudinal or shear wave incident from the solid

Longitudinal or shear waves may be incident on the boundary from the solid. Expressions for the reflection and transmission coefficients are given by Brekhovskikh (1980). For all incident angles of the longitudinal wave ($0 \leq \theta_1 \leq 90^\circ$), all the angles of the reflected or transmitted waves are real. When a shear wave is incident, if $(c_2/c_1) \leq \sin\theta_2 \leq 1$ the reflected longitudinal wave in the solid will be inhomogeneous.

2.6 Wave propagation characteristics in bounded media

If the elastic medium is made finite in the z direction then a plate or elastic layer results. Plates cause plane waves to be guided between their boundaries, and hence are sometimes called waveguides. The assumptions previously applied, relating to the properties of the medium, will also be employed here as will the coordinate system in Fig. 2.3, with the origin of the z -axis at the mid-plane of the plate. Both free and fluid loaded plates will be considered in this section.

2.6.1 Shear horizontal waves in a free plate

This is the simplest situation and hence will be analysed to illustrate some of the effects present in the more complex situations to follow. It is shown by Redwood (1960) that shear horizontal waves in plates or waveguides are analogous to longitudinal waves in a fluid waveguide.

The solution for this case is given in Graff (1975). Two particle displacement modes are observed, one symmetric and the other antisymmetric with respect to the middle plane of the plate. These two modes of propagation may be examined in terms of propagating plane waves. The phase velocity of a particular mode is a function of frequency, and this is called velocity dispersion.

Energy propagates at the group velocity c_g , which may be thought of in terms of the velocity of a small packet of waves of slightly differing phase velocities. Group and phase velocity are equal if the phase velocity is nondispersive. The group velocity is given by Redwood (1960) as:

$$c_g = \frac{\partial \omega}{\partial k_p} \quad (2.22)$$

A plane wave solution exists, which represents a shear horizontal wave travelling parallel to the boundaries with constant velocity c_2 . This is known as a Love wave. All other modes possess cut off frequencies which are observed when the phase velocity tends to infinity; for any mode this occurs when:

$$k_2 = \frac{2d}{\pi n} = 1 \quad f_{co} = \frac{nc_2}{4d} \quad (2.23)$$

where f_{co} is the cut off frequency of a particular mode, which happens when half wavelengths are an integer multiple of the plate thickness. This phenomenon may be understood by considering plane wave reflections. At f_{co} , $\theta_2=0$, and the wave no longer progresses in the x direction but simply reflects between the boundaries; the wavenumber $k_p=0$, therefore, at the cut off frequency for any propagating mode the momentum is zero. As $\theta_2 \rightarrow (\pi/2)$, the phase velocity tends to the shear wave velocity. This demonstrates that at the higher frequencies the plane waves that make up a particular mode tend asymptotically to propagate parallel to the boundaries. Another way of explaining this is to realize that as f tends to infinity the thickness/wavelength ratio tends to infinity.

2.6.2 Longitudinal and shear waves in a free plates

When either shear or longitudinal waves are incident on a free boundary of the plate, reflection and mode conversion will occur as detailed previously in the case of a free half space. The bulk waves will interact, their combined effect under certain conditions of frequency and incidence angle creating a system of plate waves.

In subsequent sections these free wave modes, first investigated by Lamb (1917), and subsequently referred to as Lamb waves, will be analysed in detail.

2.6.3 Reflection and transmission from a fluid loaded plate

If we assume a semi-infinite liquid lying on either side of an elastic plate of thickness $2d$ (see Fig. 2.3), then this situation is of practical interest because it models the ultrasonic immersion testing of plates.

Suppose that a longitudinal wave at an oblique angle to the plate normal is incident from the fluid. In general, there will be reflected and refracted waves in the fluid and the elastic layer, and a transmitted wave in the lower fluid. When the fluid on either side of the plate is the same the coefficients of reflection and transmission may be found from a solution due to Reissner (1938), and given by Brekhovskikh (1980). It is worthwhile noting an effect relating wavelength and thickness. For a thickness equal to an integral number of half wavelengths,

$$\frac{2d}{\cos\theta} = \frac{n\lambda}{2} \quad (2.24)$$

the reflection coefficient will be zero. Complete transmission will occur, the layer having no effect on the incident wave. This effect is frequently applied in transducer coupling and frequency filtering applications.

2.7 Inhomogeneous waves

The equations given previously describing reflection and refraction coefficients for various boundary conditions apply formally only in specific angular regions. As a consequence of Snell's law, substitutions are required when the incidence angle is greater than a critical angle, defined previously.

Graff (1975) and others describe the physical nature of the resultant refracted wave when the incident wave is at an angle greater than the critical angle, by looking at the assumptions in the original differential wave equations and making the necessary substitutions to the wave potentials.

An explanation by Brekhovskikh (1980) will be followed here. It is assumed that $k_{x,y,z}$ are three complex numbers,

$$k_x = k'_x + ik''_x \quad (2.25)$$

$$k_y = k'_y + ik''_y \quad (2.26)$$

$$k_z = k'_z + ik''_z \quad (2.27)$$

Substitution of these definitions into eqns 2.16 gives:

$$\phi = A(\omega)e^{i(k'_x x + k'_y y + k'_z z - \omega t) - k''_x x - k''_y y - k''_z z} \quad (2.28)$$

where $A(\omega)$ is an amplitude constant which is a function of frequency. A wave of this form is usually called an inhomogeneous or non-uniform wave, which propagates in the direction parallel to the boundary and its amplitude decays in the direction perpendicular to the boundary. Planes of constant phase (ie wave fronts) are given by the equation,

$$k'_x x + k'_y y + k'_z z = C' \quad (2.29)$$

and planes of constant amplitude are given by,

$$k''_x x + k''_y y + k''_z z = C'' \quad (2.30)$$

where C' and C'' are constants. If the coordinate system is chosen such that $k'_y = k''_y = 0$, as with plane waves we may set,

$$k_x = k \sin \theta \quad k_z = k \cos \theta \quad (2.31)$$

but since k_x and k_z are complex wavenumbers and k is real, the angle θ must be complex. From the above we may redefine $k_{x,z}$ as,

$$k_x = k \cosh \alpha \quad \text{and} \quad k_z = i k \sinh \alpha \quad (2.32)$$

The plane wave equation may then be expressed as,

$$\phi = A(\omega)e^{i(k \cosh \alpha x - k \sinh \alpha z - \omega t)} \quad (2.33)$$

This equation describes a wave propagating in the x direction with an amplitude which decays exponentially in the z direction. Since $k = \omega/c$ it may be seen from eqn 2.33 that the velocity of the wave in the x direction is reduced by $1/\cosh \alpha$. Therefore the greater α the greater the decay coefficient of the wave in the z direction and the greater the velocity reduction in the x direction.

It is worthwhile noting that on refraction at an interface, inhomogeneous waves may result from plane waves and vice versa.

2.8 Energy considerations

It is sometimes useful to consider energy relations as they can aid physical understanding of wave reflection and transmission at boundaries. They may also be used to calculate the coefficients of reflection or transmission.

An ideal material which does not dissipate energy is always assumed. For an arbitrary incident angle ($0 \leq \theta < 90^\circ$) there will be symmetry regarding the passage of energy or energy flux (normal to the boundary) from one medium to another and vice versa. For conservation of energy, the energy carried to the boundary by an incident wave must be equal to the energy carried away from the boundary by the reflected, refracted and transmitted waves, i.e.,

$$[E]_{\text{incident}} = [E]_{\text{reflected}} + [E]_{\text{refracted}} + [E]_{\text{transmitted}} \quad (2.34)$$

The energy relations between bulk waves may be deduced by expressing the particle velocities in terms of the scalar and vector potentials. The kinetic energy per unit volume is $0.5\rho[(\partial u/\partial t)^2 + (\partial w/\partial t)^2]$, and the total energy multiplied by the velocity of propagation gives the flow of energy in a plane perpendicular to the direction of propagation. For a unit area of the free surface the energy in all the waves must balance. The important characteristics of these relations may be seen from curves presented by Ergin (1952) describing the energy partition when bulk waves are incident on interfaces separating different materials.

2.9 Rayleigh waves

Rayleigh waves are free modes which can propagate on half spaces. In this section the theoretical derivation of these wave modes will be discussed.

It is shown by Viktorov (1970) that the scalar, ϕ , and vector, ψ , potentials describing propagation in the x direction may be given as:

$$\phi = Ae^{i[k_1x - qz - \omega t]} \quad (2.35)$$

$$\psi = BE^{i[k_1x - sz - \omega t]} \quad (2.36)$$

where, $q^2 = k^2 - k_1^2$ and $s^2 = k^2 - k_2^2$. Particle displacements and normal and shear stresses in Cartesian coordinates may be defined in terms of the potentials as follows:

$$u = \frac{\partial \phi}{\partial x} - \frac{\partial \psi}{\partial z} \quad (2.37)$$

$$w = \frac{\partial \phi}{\partial z} + \frac{\partial \psi}{\partial x} \quad (2.38)$$

$$\sigma_{xx} = \lambda \left[\frac{\partial^2 \phi}{\partial x^2} - \frac{\partial^2 \phi}{\partial z^2} \right] + 2\mu \left[\frac{\partial^2 \phi}{\partial x^2} - \frac{\partial^2 \psi}{\partial x \partial z} \right] \quad (2.39)$$

$$\sigma_{zz} = \lambda \left[\frac{\partial^2 \phi}{\partial x^2} - \frac{\partial^2 \phi}{\partial z^2} \right] + 2\mu \left[\frac{\partial^2 \phi}{\partial z^2} - \frac{\partial^2 \psi}{\partial x \partial z} \right] \quad (2.40)$$

$$\sigma_{xz} = \mu \left[\frac{2\partial^2 \phi}{\partial x \partial z} + \frac{\partial^2 \psi}{\partial x^2} - \frac{\partial^2 \psi}{\partial z^2} \right] \quad (2.41)$$

The scalar potential is associated with dilatation and the vector potential is associated with distortion. It may be seen that for q and s to be real then $k^2 > k_2^2 > k_1^2$, as for an isotropic elastic solid $c_1 \geq c_2$. A and B are arbitrary constants which may be determined from the boundary conditions.

The wavenumber k corresponding to a surface wave may be determined from the characteristic equation which is given by Viktorov (1970) as:

$$4k^2qs - (k^2 + s^2)^2 = 0 \quad (2.42)$$

This may be manipulated into the usually quoted form,

$$\left[\frac{k_2}{k} \right]^6 + 8 \left[\frac{k_2}{k} \right]^4 + 8 \left\{ 3 - 2 \left[\frac{c_2}{c_1} \right]^2 \right\} \left[\frac{k_2}{k} \right]^2 - 16 \left\{ 1 - \left[\frac{c_2}{c_1} \right]^2 \right\} = 0 \quad (2.43)$$

The roots of eqn 2.43 depend only on Poisson's ratio. The Rayleigh wave corresponds to one root, $(k_2/k)_R$, the suffix R denoting the Rayleigh wave. For solids, $0 < \nu < 0.5$, and only one root exists; the resultant Rayleigh velocity c_R is nondispersive and monotonically dependent

on Poisson's ratio. Rayleigh waves are composed of inhomogeneous longitudinal and shear waves, 90° out of phase, propagating along the surface at the same velocity, therefore,

$$c_R = \frac{c_1}{k \cosh \alpha_1} = \frac{c_2}{k \cosh \alpha_2} \quad (2.44)$$

where α is as defined in section [2.7]. An approximate expression given by, for example, Krautkrämer and Krautkrämer(1983) as,

$$\frac{k_2}{k} = \frac{0.87 + 1.12\nu}{1 + \nu} \quad (2.45)$$

is often used to calculate the phase velocity of Rayleigh waves. Eqn 2.45 computes k_2/k for solids to an accuracy of $\pm 0.5\%$.

The particle displacements of Rayleigh waves are elliptical and localized close to the surface, with amplitudes which decay exponentially in the z direction. The wave vector \mathbf{k}' of Rayleigh waves is parallel to the boundary surface. Expressions are given in for example, Viktorov (1970) for displacement and stress as a function of through-thickness position, which may be obtained by substituting eqns 2.35 and 2.36 into eqns 2.37 to 2.41. The normalised displacements of the Rayleigh wave in steel as a function of distance from the surface are given in Szilard (1982).

Investigations of these surface waves were first carried out by Rayleigh (1885) who was interested in describing seismic phenomena, where large amplitude surface waves are observed, remote from the epicentre of the earthquake, after the arrival of the bulk waves. He argued that because these waves were essentially two-dimensional, less of their energy was radiated into the body of the earth, causing their amplitudes to be greater than bulk waves at points distant from the earthquake source.

2.9.1 Leaky Rayleigh waves

When the elastic half space is bounded by an infinite fluid, surface waves similar to Rayleigh waves can exist. In this case their wave vectors \mathbf{k}' will not be parallel to the boundary, indicating a flow of energy from one medium to the other. The characteristic equation which determines the leaky Rayleigh wavenumber k'_R may be obtained in the same manner as in the previous section and is given by Plona *et al* (1975) as:

$$4k^2qs - (k^2 + s^2)^2 = i \frac{\rho_L}{\rho} qk^2 \frac{1}{\sqrt{k_L^2 + k^2}} \quad (2.46)$$

Given that $c'_R > c_L$ for almost all real media, the previous equation has two roots, one complex and one real. The real solution occurs when $c'_R/c_L > 1$ and strictly speaking is an undamped interface wave, the Stoneley wave, where most of the energy propagates through the fluid and therefore, in general is of no use in NDT. When the wavenumber k is complex, most of the energy propagates through the solid and the amplitude of the wave in the solid decreases as it travels along the boundary. This solution corresponds to a system of two inhomogeneous waves in the solid and a plane wave in the fluid. These waves are generally termed leaky Rayleigh waves and have velocity c'_R . The complex solution of k is related to the wavenumber of the wave by;

$$k'_R = \{\text{Re}(k)\} \quad (2.47)$$

The velocity of these waves tend to the Rayleigh wave velocity in the case when the impedance of the liquid approaches zero. Physically, this system of waves may be described in terms of energy being leaked to the liquid from the surface wave. The magnitude of the imaginary part of k depends on the density ratio of the liquid and the solid. Typical ratios of metal to liquid density vary between 0.1 and 0.2, and the difference between the Rayleigh and leaky Rayleigh velocities is less than 1%. However, for low density solids, for example, polymers this approximation is not applicable. The above phenomena may be described in terms of coupling between two systems, one fluid the other solid. For density ratios much less than one, the fundamental modes of each system are almost unaffected.

The liquid has a critical effect on the damping of the leaky Rayleigh wave in the x direction. The amplitude of the leaky wave decreases exponentially in the x direction due to the continual radiation of energy into the liquid. Even for small density ratios the attenuation in the x direction is considerable, significantly reducing propagation distances.

2.10 Lamb waves

2.10.1 Dispersion curves and mode shapes

Lamb (1917) proved theoretically that under certain conditions a finite number of vibrational wave modes could propagate independently in a plate. Lamb waves represent two-

dimensional propagating vibrations in plates. Sometimes they are referred to as normal or free modes, because they are the eigen solutions of characteristic equations.

The method of analysis followed here will be in keeping with the original paper by Lamb (1917) and subsequently adopted by Viktorov (1970).

If we consider a Lamb wave propagating in a plate of thickness $2d$, all particle displacements may be described by the vector \mathbf{u} , which by definition is zero in the y direction. As before we may define scalar and vector potentials, ϕ and ψ , respectively, which satisfy the boundary conditions. The potentials are given by Viktorov (1970) as,

$$\phi = A_s \cosh qz + B_a \sinh sz \, e^{i[kx - \omega t]} \quad (2.48)$$

$$\psi = D_s \cosh qz + C_a \sinh sz \, e^{i[kx - \omega t]} \quad (2.49)$$

where A_s , B_a , C_a and D_s are arbitrary constants. The characteristic equations are obtained by substituting the above equations into the stress relations (eqns 2.39, 2.40 and 2.41) and applying zero stress boundary conditions, and are given by Viktorov (1970) in the following form,

$$(k^2 + s^2)^2 \cosh qd \sinh sd + 4k^2 qs \sinh qd \cosh sd = 0 \quad (2.50)$$

$$(k^2 + s^2)^2 \sinh qd \cosh sd - 4k^2 qs \cosh qd \sinh sd = 0 \quad (2.51)$$

Phase velocity is the fundamental characteristic of the Lamb waves, as once it is calculated, the stresses, displacements and group velocity may also be found. The phase velocity is computed by numerically solving eqns 2.50 and 2.51, which are generally rewritten in a more appropriate dimensionless form, given by Viktorov (1970) as,

$$\frac{\tan k_2 d \sqrt{1 - \left[\frac{c_2}{c}\right]^2}}{\tan k_2 d \sqrt{\left[\frac{c_2}{c_1}\right]^2 - \left[\frac{c_2}{c}\right]^2}} + \left[4 \frac{\left[\frac{c_2}{c}\right]^2 \sqrt{1 - \left[\frac{c_2}{c}\right]^2} \sqrt{\left[\frac{c_2}{c_1}\right]^2 - \left[\frac{c_2}{c}\right]^2}}{\left\{2 \left[\frac{c}{c_2}\right]^2 - 1\right\}^2} \right]^{\pm 1} = 0 \quad (2.52)$$

The +ve and -ve signs in the above transcendental equation relate to symmetric and antisymmetric Lamb waves respectively. The velocities of all Lamb waves are a function of frequency and in any plate of thickness, $2d$, at a particular frequency, f , there will be a finite number of propagating modes, which may be determined from the number of real roots of eqn 2.52. The positive and negative real roots of eqn 2.52 correspond to propagating harmonic

waves in the +ve and -ve directions, while the imaginary or complex roots relate to non-propagating spatially varying vibrations, which are of importance in forced or transient wave motion. The group velocity, $c_g = \partial\omega/\partial k$, of Lamb waves is the velocity at which energy is propagated and may be calculated once the phase velocity or wavenumber as a function of frequency is known. Group velocity may be expressed in terms of phase velocity and frequency-thickness product ($\Omega = 2fd$) by,

$$c_g = \frac{c_p}{1 - \frac{\Omega}{c_p} \frac{\partial c_p}{\partial \Omega}} \quad (2.53)$$

Fig. 2.4 shows the predicted Lamb wavenumber dispersion curves for the first five symmetric and antisymmetric Lamb waves of a steel plate, where $c_1=5960$ m/s and $c_2=3260$ m/s. The predicted phase and group velocity curves are shown in Fig. 2.5 and 2.6 respectively. The phase and group velocity dispersion curves show pronounced velocity dispersion, which is typical for all solids.

The displacement components in the x and z directions and the direct and shear stresses may be calculated by substituting eqns 2.48 and 2.49 into eqns 2.37 to 2.41. The through thickness displacement components of the symmetric modes are obtained from the following equations,

$$u_s = Ak_s \left\{ \frac{\cosh q_s z}{\sinh q_s d} - \frac{2q_s s_s}{k_s^2 - s_s^2} \frac{\cosh s_s z}{\sinh s_s d} \right\} e^{i[k_s x - \omega t]} \quad (2.54)$$

and

$$w_s = Aq_s \left\{ \frac{\sinh q_s z}{\sinh q_s d} - \frac{2k_s^2}{k_s^2 + s_s^2} \frac{\sinh s_s z}{\sinh s_s d} \right\} e^{i[k_s x - \omega t]} \quad (2.55)$$

where u_s and w_s are the displacements in the x and z directions respectively and k_s is the wavenumber of the symmetric Lamb modes. The through thickness stress components of the symmetric modes are obtained from the following equations

$$\sigma_{xx(s)} = A\mu \left\{ (s_s^2 - k_s^2 - 2q_s^2) \frac{\cosh q_s z}{\cosh q_s d} - (k_s^2 + s_s^2) \frac{\cosh s_s z}{\cosh s_s d} \right\} e^{i[k_s x - \omega t]} \quad (2.56)$$

$$\sigma_{zz(s)} = A\mu \left\{ (k_s^2 + s_s^2) \frac{\cosh q_s z}{\cosh q_s d} - (k_s^2 + s_s^2) \frac{\cosh s_s z}{\cosh s_s d} \right\} e^{i[k_s x - \omega t]} \quad (2.57)$$

and

$$\sigma_{xz(s)} = A\mu_i \left\{ 2k_s q_s \frac{\sinh q_s z}{\sinh q_s d} - 2k_s q_s \frac{\sinh s_s z}{\sinh s_s d} \right\} e^{i[k_s x - \omega t]} \quad (2.58)$$

Similar relations for the displacement and stress components of the antisymmetric Lamb modes may be obtained by changing the subscripts s to a and replacing \sinh by \cosh and vice versa. Fig. 2.7(a-f) and Fig. 2.8(a-f) show the deflected displacement and stress mode shapes of a_0 , s_0 , a_1 and s_1 at a variety of frequency-thickness values. The displaced shape of a_0 and s_0 at 0.5 MHzmm are dominated by out of plane and inplane motion respectively, as may be seen from Fig. 2.7(a and b). At 15 MHzmm however, a_0 and s_0 combine to form the quasi-Rayleigh wave as can be seen from their displacement and stress mode shapes in Fig. 2.7(e and f) and Fig. 2.8(e and f) respectively. At the cut-off frequency-thickness product, for a_1 and s_1 , there is only one component of displacement (Fig. 2.7(c and d)), as these represent reflecting shear and longitudinal waves respectively.

The above relations describe two groups of waves, each of which independently satisfies the wave equation and free boundary conditions. These waves may thus propagate independently of one another. As for Rayleigh waves, the particle motion of Lamb waves is elliptical. The particle motion eccentricity depends on whether the mode is symmetric or antisymmetric, the order number of the mode, the position in the plate thickness and the Poisson's ratio of the solid.

When the frequency thickness product tends to zero, the characteristic equations each have only one root. These are called the zeroth order antisymmetric and symmetric modes, a_0 and s_0 , respectively. As the frequency thickness product increases the roots of a_0 and s_0 will vary until at specific frequency thickness products new roots will appear; these frequency thickness values are the cut-off values for the new modes a_n and s_n (higher frequency modes), n being a positive integer. At the cut-off frequencies assuming constant plate thickness the wavenumber of the Lamb waves will be zero (see Fig. 2.4). The new symmetric or antisymmetric Lamb waves describe non-propagating standing longitudinal or shear waves being reflected at normal incidence within the plate. If the frequency-thickness product is less than the cut-off value for any particular mode then the phase velocity of the mode will be imaginary. This may be physically interpreted as non-propagating particle vibration.

In the limit when $2d$ tends to infinity the plate becomes a half space, and the phase velocity of all non-zero order Lamb modes, tend to the shear wave velocity. Particle displacements of the a_0 and s_0 modes become localized near the free boundary and combine to form the Rayleigh wave.

The zero order modes are different from the other modes, in that they exist at the lowest frequencies. As the frequency-thickness product becomes small it is worthwhile looking at them in detail, because a great deal of Lamb wave NDT testing is carried out in this range.

The symmetric mode, s_0 , which possesses a finite phase velocity at low frequency-thicknesses, represents a longitudinal (or extensional) wave in a plate as may be seen from the displacement and stress mode shapes in Fig. 2.7(b) and Fig. 2.8(b). The phase velocity of the longitudinal plate wave may be derived by assuming that the stress σ_{xx} is constant over the plate thickness. Kolsky (1963) shows that as the frequency-thickness product tends to zero the phase velocity of s_0 tends to the velocity of the longitudinal plate wave c_0 , which is given by.

$$c_0 = \sqrt{\frac{E}{\rho(1-\nu^2)}} = 2c_2 \sqrt{1 - \left[\frac{c_2}{c_1}\right]^2} \quad (2.59)$$

At low frequency-thicknesses the zeroth antisymmetric mode may be interpreted as a flexural (ie bending) wave. The Timoshenko-Mindlin approximation takes into account the transverse shear and rotary inertia, the free flexural wave velocity c_f as a function of frequency, being given by Freedman (1978) as:

$$c_f^4 - \frac{4\pi^2}{3} (fd)^2 \left\{ 1 - \left[\frac{c_f}{c_R}\right]^2 \right\} \left\{ 4 \left[\frac{c_2}{c_1}\right]^2 (c_1^2 - c_2^2) - c_f^2 \right\} = 0 \quad (2.60)$$

The lower of the two roots of c_f represents the a_0 mode almost exactly and the other root represents the a_1 mode.

2.10.2 The zig-zagging wave model of Lamb waves

A great deal is known about transmission and reflection coefficients of incident waves at boundaries. Therefore, it is sometimes useful from a practical NDT viewpoint to consider Lamb waves as the resultant of bulk waves interacting with the plate boundaries.

The standard method of exciting Lamb waves is by an incident longitudinal wave on one of the plate boundaries. This causes longitudinal and shear waves to propagate in the plate along zig-zagging paths. Lehfeldt (1962) and Krautkrämer and Krautkrämer (1983) consider Lamb waves in terms of bounded zig-zagging waves propagating within a plate. Assuming the bulk waves are of infinite extent in the x and y directions Graff (1975) and Auld (1973) showed

that Lamb waves may be derived by considering the reflection of longitudinal and shear waves.

In section [2.6.1], shear horizontal dispersion curves were considered in terms of a combination of plane shear horizontal waves travelling in a zigzag path within the plate. However, in the case of vertically polarized waves, the waves within the plate will not always be plane.

Consider for simplicity the situation when the Lamb wave phase velocity is always greater than the longitudinal velocity. The resultant bulk waves within the plate will travel at either c_1 or c_2 , their phase velocities being equal. The combined effect of incident and reflected waves throughout the plate thickness will be a sinusoidal stress variation typical of Lamb modes. The incident angles (θ_1, θ_2) of the longitudinal and shear waves have to be such that in combination the boundary conditions are satisfied. As the frequency-thickness product is increased from the critical value, the Lamb wave phase velocity (Fig. 2.5) will decrease from infinity for all modes. In order to satisfy boundary conditions for a particular mode the angles of incidence of the reflected bulk waves must increase, to satisfy Snell's law. At some frequency-thickness value different for each Lamb mode, the incident angle of the longitudinal wave will be 90° and the Lamb wave phase velocity will be equal to c_1 .

If the frequency-thickness product is further increased the longitudinal wave will become inhomogeneous. This causes the particle displacements of the inhomogeneous longitudinal wave to be localized near the surface. The effect is more pronounced the greater the phase velocity retardation of the longitudinal wave, as described in section [2.7]. Displacements through the depth of the plate will become almost entirely a function of the shear wave. As the frequency-thickness product is further increased, the propagation direction of the shear wave will rotate until in the limit of a half space, the shear wave will be travelling parallel to the boundary. The displacement components of the symmetric and antisymmetric modes are a function of the shear wave. In the body of the material the displacements will be parallel to the z axis and the Lamb wave phase velocity will be equal to c_2 .

If $c_p = \sqrt{2} c_2$, for a particular material, the shear waves will travel at 45° to the z axis, the Lamb waves for this case are pure shear waves, and are called Lamé wave.

Only the a_0 and s_0 Lamb modes have phase velocities which may be less than the bulk shear velocity. The phase velocity of a_0 increases monotonically from zero to the Rayleigh velocity as the frequency-thickness product is varied from zero to infinity. The wavenumbers of the bulk waves that combine to form a_0 are imaginary in the low frequency-thickness limit, but as the frequency-thickness product increases, the imaginary components of the wavenumber

decrease. In the low frequency-thickness range, the phase velocity of s_0 is greater than the bulk shear wave velocity, and as the frequency-thickness product increases the phase velocity of s_0 will decrease monotonically to c_R .

2.10.3 Leaky Lamb waves

A Lamb wave propagating in a plate which is bounded by a liquid will leak some of its energy into the liquid under steady-state conditions, in an analogous way to leaky Rayleigh waves. NDT using Lamb waves, where immersion coupling is employed, makes this situation of considerable practical importance.

As in the case of leaky Rayleigh waves, it is possible to compare the free plate with a plate loaded by a liquid. For a fluid loaded plate the velocities of the leaky Lamb waves may be deduced from characteristic equations given by Plona *et al* (1975). These relations are different from eqns 2.50 and 2.51 in that they have a term on the right-hand side, which accounts for the liquid, where the influence of the liquid is a function of the liquid-solid density ratio.

Assuming the density ratio to be small (less than 0.2), Viktorov (1970) shows that the phase velocity of the leaky Lamb waves will be effectively the same as the Lamb wave velocity.

The attenuation of the leaky Lamb modes, due to energy leaking to the liquid is far more pronounced than the velocity change, the attenuation being heavily dependent on the ratio of vertical and horizontal surface displacements. For example, Viktorov (1970) shows that for an aluminium plate at 1.02 MHzmm, s'_0 is attenuated by 77% over a distance of approximately $5\lambda_2$, where λ_2 is the shear wavelength, while the change in phase velocity is minimal. The attenuation is greatest for those modes which have significant vertical displacement (w'_s and w'_a) components.

In free plates the Lamb wave phase velocity is either real or imaginary. This follows from energy considerations since no energy may be radiated to or from the surrounding space (vacuum). The energy flux along the plate must be either constant or zero, which relates to real or imaginary phase velocity. When the plate is bounded by a liquid then waves propagating in the plate will generally leak energy to the fluid, which corresponds to complex phase velocities.

Therefore, if a free half space or plate is bounded by a fluid, the effect on the Rayleigh or Lamb wave velocity is minimal and it will be assumed throughout the rest of the thesis that the solutions derived for the wave velocity in a vacuum are applicable when fluid loading is applied.

2.11 The effect of bounded waves

Hitherto the wave fronts have been assumed to be of infinite extent in both the x and y directions, which implicitly allows steady-state conditions to be assumed. If we retain the assumption of plane wave fronts, in real situations the wave will be bounded in the x and y directions and be of a finite duration.

The amplitude of spatially bounded Lamb waves will decrease as the wave propagates in the x direction, as energy is distributed spatially by the wavefront spreading out. As the wave dimensions are increased from zero to infinity, the amplitude of the Lamb wave monotonically increases from zero to infinity for a free plate, and to a steady-state amplitude for a fluid loaded plate. Using the zig-zagging bulk wave model the amplitude of the Lamb wave in the plate is finite because it will not be reinforced by the incident wave continuously in the x direction, as is the case if a wave of infinite extent is assumed.

2.12 The excitation of Rayleigh and Lamb waves

In many NDT applications, Rayleigh or Lamb waves are produced by mode conversion of a longitudinal wave incident at the boundary of the testpiece, piezoelectric transducers being used to both excite and receive the waves.

A detailed account of resonant and nonresonant methods of exciting Rayleigh waves is given by Viktorov (1970). Nonresonant methods excite all wave modes, while resonant methods are discriminating and will theoretically only excite the Rayleigh wave. Resonance methods are thus preferred in practical applications. The principles of exciting Rayleigh and Lamb wave are analogous and will be dealt with together below.

It is shown by Viktorov (1970) that Lamb waves may be excited in a plate by the introduction of a stress system on the plate surface. The stresses on the plate may be induced by a transducer in physical contact with the plate (solid coupling) or indirectly by an ultrasonic

wave from a transducer which is not in contact with the plate (thin film and immersion coupling).

The most commonly used technique to excite Lamb waves is by a longitudinal wave incident on the plate surface at an oblique angle, as was used by Worlton (1961) to experimentally confirm the existence ultrasonic Lamb waves by measuring their velocity. Maximum transmission will occur at an angle of incidence such that the phase velocities of the incident longitudinal wave and a Lamb wave coincide. Cremer (1942) called this the coincidence rule and it is expressed by Freedman (1981) for immersion coupling as:

$$\theta_p = \sin^{-1}\left(\frac{c_L}{c_p}\right) \quad (2.61)$$

where θ_p is the coincidence angle of the required Lamb wave, c_p is the Lamb wave velocity and c_L is longitudinal velocity in water. This allows Lamb waves to be selectively excited, by varying frequency and θ_p .

The dispersion curves of Fig. 2.5 in terms of phase velocity may be replotted in terms of incidence angle for water coupling, and this is shown in Fig. 2.9. The angle at which maximum transmission and reception of acoustic energy will occur at a particular frequency-thickness may be obtained from Fig. 2.9.

The excitation of Lamb waves by a finite sized transducer using the coincidence principle is one example of the general method of the excitation of Lamb waves by a localised surface driving force. This was first investigated theoretically by Lyon (1955) and subsequently adopted by Viktorov (1970). Scalar and vector potentials which satisfy the wave equations may be separated into symmetric and antisymmetric components, and expressed as Fourier integrals. Expressing the driving stresses in terms of these potentials and applying the boundary conditions allows the integrals to be determined by the calculus of residues. The motion of the plate in the z and x directions is shown by Lyon (1955) to be the sum of eigenmodes. These modes represent the symmetric and antisymmetric motion of the plate, ie Lamb waves.

In NDT applications it is the surface motion which is important as this is detected by transducers. Viktorov (1970) expresses the surface motion of the plate in the z and x direction when subjected to a driving force as a function of three dimensionless factors. The first term represents the dependence of the Lamb wave amplitude on the normal stresses. The second factor demonstrates the coincidence requirement and its effect on the amplitude of the excited Lamb waves. The surface amplitudes are a maximum when the coincidence rule (eqn 2.61) is satisfied, and one Lamb mode is then predominantly excited. The last factor demonstrates the

linear dependence of the maximum amplitude, on the spatial extent of the excitation zone. As the spatial extent of the excitation zone increases the situation tends to that of an infinite wave incident on the plate boundary.

Excitation at a point by a Dirac function of force will have a continuous and constant spectrum both in the spatial and frequency domains and will excite all possible Lamb waves. However, the spatial and frequency domain bandwidths of real signals is always finite. Long tone bursts may be used to reduce the frequency domain bandwidth, but the spatial or angular bandwidth is generally dependent solely on the properties of the transducer. An expression for the pressure field in the far field of a round ultrasonic transducer acting as a piston source is given in Krautkrämer and Krautkrämer (1983) The angular pressure distribution is shown in Fig. 2.10, from which it will be seen that the angular bandwidth may be reduced by increasing the frequency or diameter of the transducer. Therefore, the acoustic energy will be distributed over a finite region in Fig. 2.9, the position and dimensions of which are dependent on the excitation signal and the properties and orientation of the transducer.

The ratio of the phase to group velocity η_c of Lamb waves,

$$\eta_c = \frac{c_p}{c_g} \quad (2.62)$$

is a measure of the degree of dispersion of a particular Lamb mode. The different frequencies of a Lamb wave signature will travel at different velocities. In order to reduce the spread of energy it is best to use of frequency-thickness values where η_c is a maximum (ie a point of maximum or minimum group velocity), as dispersion is then in general a minimum.

2.13 Discussion

Rayleigh (1885) and Lamb (1917) first showed that propagating vibrational modes existed in free elastic half spaces and plates respectively. In the last 30 years, Rayleigh and Lamb waves have been applied increasingly to ultrasonic NDT applications.

Rayleigh waves are non-dispersive; their phase velocities are a function of Poisson's ratio of the solid and, strictly speaking, they exist only on a free half space. The amplitude of their particle displacements decays exponentially in the z direction and is only significant at depths of less than λ_R , and may be considered in terms of longitudinal and shear inhomogeneous waves, propagating at equal phase velocities along the boundary.

In practice, half spaces do not exist, and in many NDT applications a solid of finite thickness is bounded by a fluid, on at least one surface. However, if the thickness of the solid is greater than $5\lambda_R$, Viktorov (1970) shows that the zero order Lamb modes, a_0 and s_0 , will combine to form a quasi-Rayleigh wave which is almost indistinguishable from the Rayleigh wave. It was also shown that for liquid-solid density ratios of less than 0.2 the velocity of the leaky Rayleigh wave does not differ by more than 1% higher than the Rayleigh wave velocity.

Lamb waves have dispersive phase velocities, which may be calculated as a function of the frequency-thickness product from two characteristic equations given in section [2.10]. Lamb (and Rayleigh) waves represent the eigen solution (eigenvalue and eigenvector solution) of characteristic equations and for this reason they are sometimes referred to as normal modes.

The particle displacements of Lamb waves may be symmetric or antisymmetric with respect to the middle plane of the plate and Lamb waves are identified as being symmetric or antisymmetric. The strain field within the plate may be considered in terms of the superposition of longitudinal waves of equal amplitudes propagating at angles θ_1 and $(\pi - \theta_1)$ to the plate normal, and shear waves propagating at θ_2 and $(\pi - \theta_2)$ to the plate normal, as shown by Graff (1975). The resultant of all the waves interacting with the boundary must satisfy the boundary conditions of zero stress.

Assuming a harmonic force of infinite extent in the x and y directions, equivalent to an incident longitudinal wave incident at the boundary of the plate, when the coincidence rule is satisfied, a free mode will be excited and its amplitude will tend to infinity if the amplitude of the incident wave is finite. If the plate is bounded by a fluid then the Lamb wave amplitude will be finite as energy will be continuously leaked to the fluid. However, it should be noted that two conditions must be satisfied in order to excite only one Lamb wave by the coincidence (resonant) method. Firstly, the frequency of the harmonic force must be identical to the Lamb wave frequency being excited (assuming a plate of constant thickness). Secondly, the spatial distribution of the amplitude of the force input, and hence stress on the plate surface, must match the spatial distribution of the stress amplitude on the plate surface of a particular Lamb mode. Therefore it is not possible to excite a pure Lamb wave with a finite sized transducer. In practice the strain distribution on the surface of the testpiece produced by the longitudinal wave from the transducer will not be identical to that of the Lamb wave required in the plate, and all the Lamb waves that can be excited by the incident wave will in general be excited simultaneously. However, in general if the excitation signal is applied for sufficient time the response of the plate will be dominated by a single mode

It is extremely difficult to obtain the coincidence effect, as frequency and incidence angle have to be absolutely correct and transducers have finite bandwidths in the angular and frequency

domains. More importantly the pressure field produced by the transducer will not be plane (see Krautkrämer and Krautkrämer 1983), and it will not exactly match the surface strain distribution of one Lamb wave, which is a function of the frequency-thickness product. Therefore, the mismatch of the the spatial distribution of the strain amplitudes (between that produced by transducer and that of a Lamb mode) on the plate surface will cause other modes to be excited. This may be considered in terms of the response of the plate to an arbitrary forcing function, which will be the modal summation of all the propagating and nonpropagating Lamb waves.

2.14 Conclusions

Rayleigh and Lamb waves represent resonance conditions in a half space and plates, and as they are the solution to characteristic equations they are generally termed normal modes. There are basically two methods of deriving the Rayleigh and Lamb wave equations. Firstly, as special cases when bulk waves interact at the boundary of a half space or plate (Brekhovskikh, 1980), or in terms of potentials associated with dilatation and distortion as shown by Viktorov (1970).

Rayleigh waves are the limiting case of Lamb waves, and when $2d > 5\lambda_R$, a_0 and s_0 , will have almost identical velocities and will be indistinguishable from the Rayleigh wave.

Strictly speaking Rayleigh waves exist on a free half spaces, and Lamb waves exist in free plates. However, if the acoustic impedance of a loading fluid is small compared to the acoustic impedance of the solid, than the leaky Rayleigh and Lamb wave velocities can be approximated by the Rayleigh and Lamb wave velocities respectively.

Leaky Lamb or Rayleigh waves will not generally propagate over large distances as most of their acoustic energy will be leaked to the surrounding fluid.

In order to excite one Lamb mode using the coincidence method (assuming constant plate thickness), the frequency and the phase velocity of the incidence wave must match the frequency and phase velocity of the Lamb wave required. The through-thickness mode shape caused by the application of the excitation signal must also match the through-thickness mode shape of the Lamb mode to be excited.

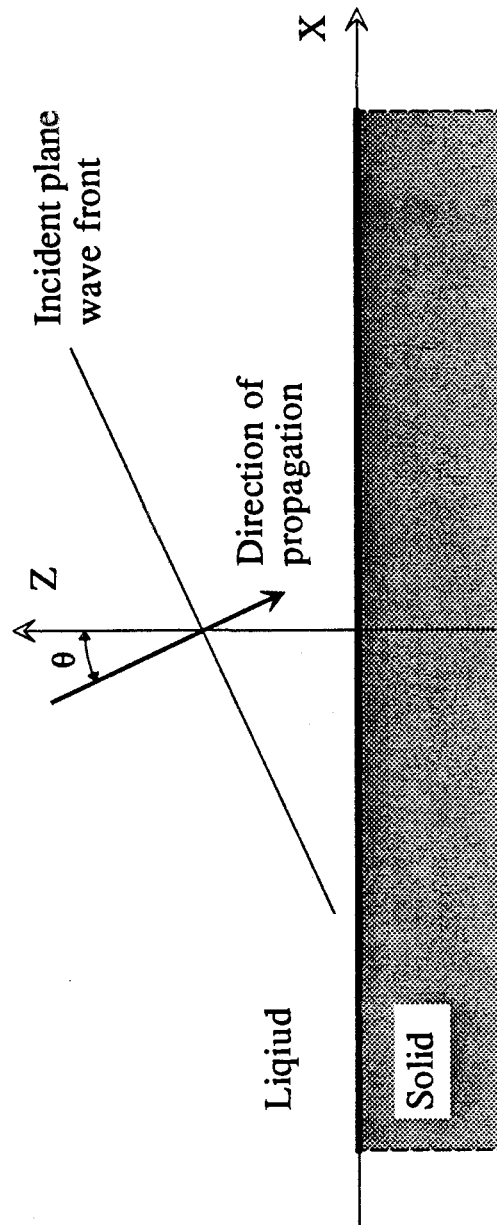


Figure 2.1 Schematic representation of a plane wave approaching an interface.

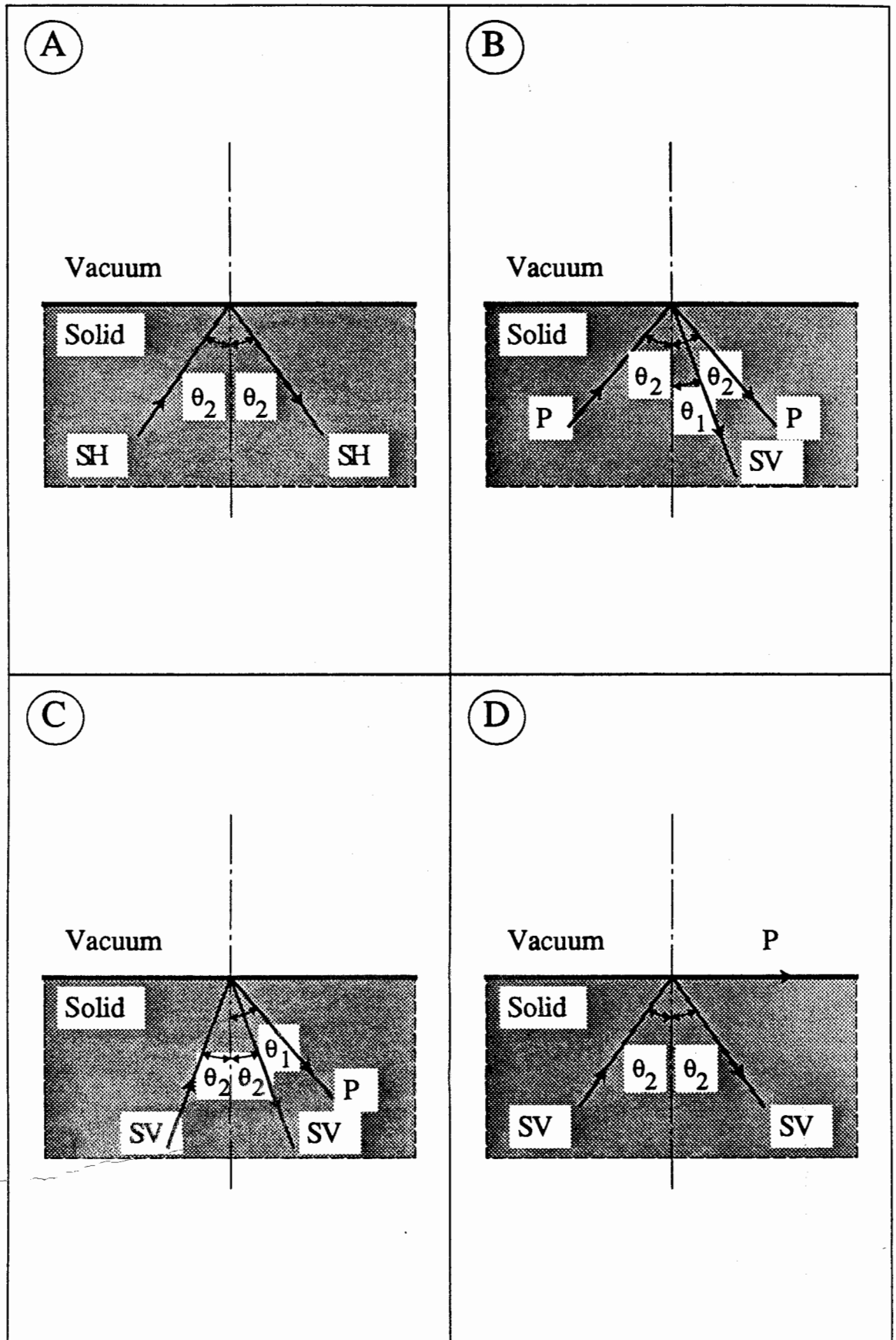


Figure 2.2 Schematic representation of the reflection of bulk waves from free boundaries.

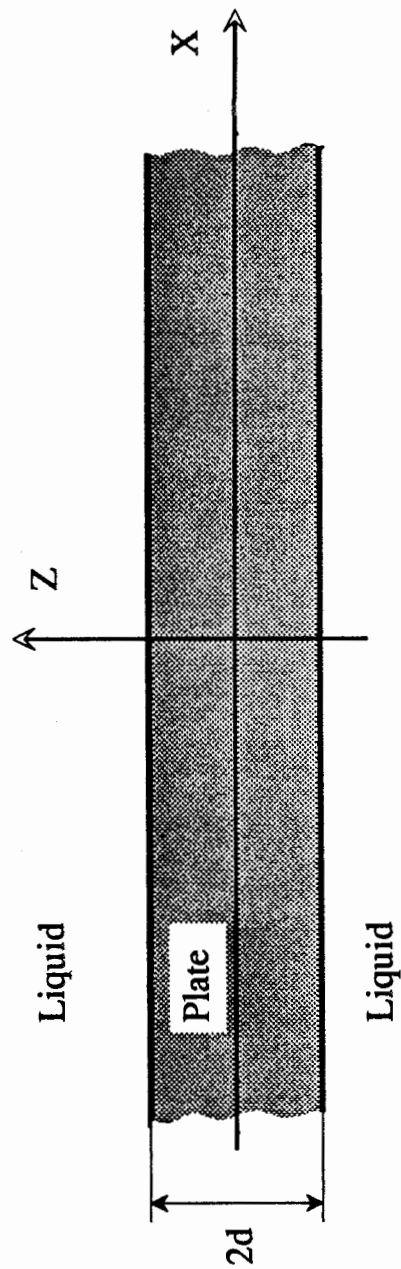


Figure 2.3 Schematic representation of the plate geometry and the coordinate system used.

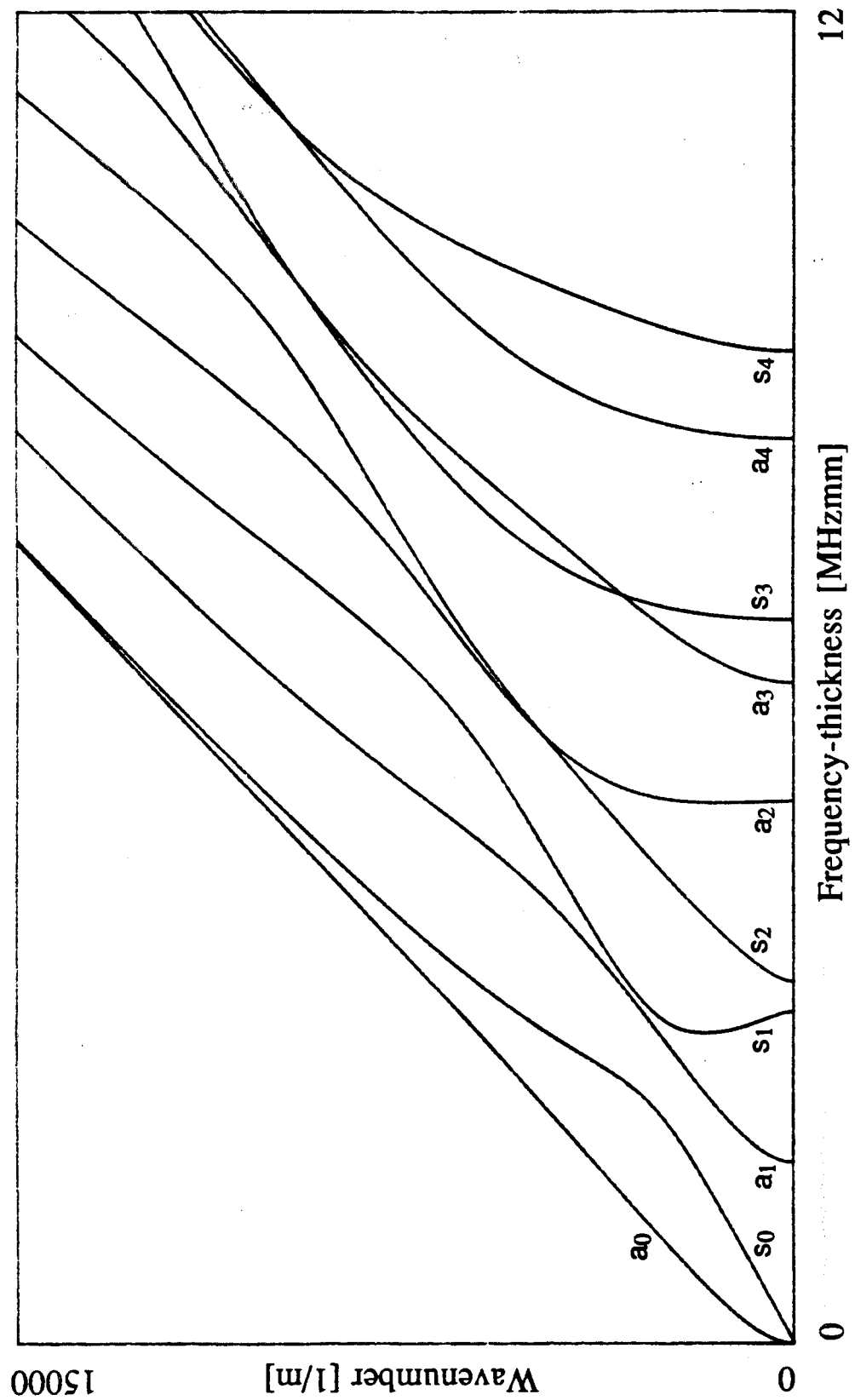


Figure 2.4 Lamb wave wavenumber dispersion curves for steel, where $c_1=5960$ m/s and $c_2=3260$ m/s.

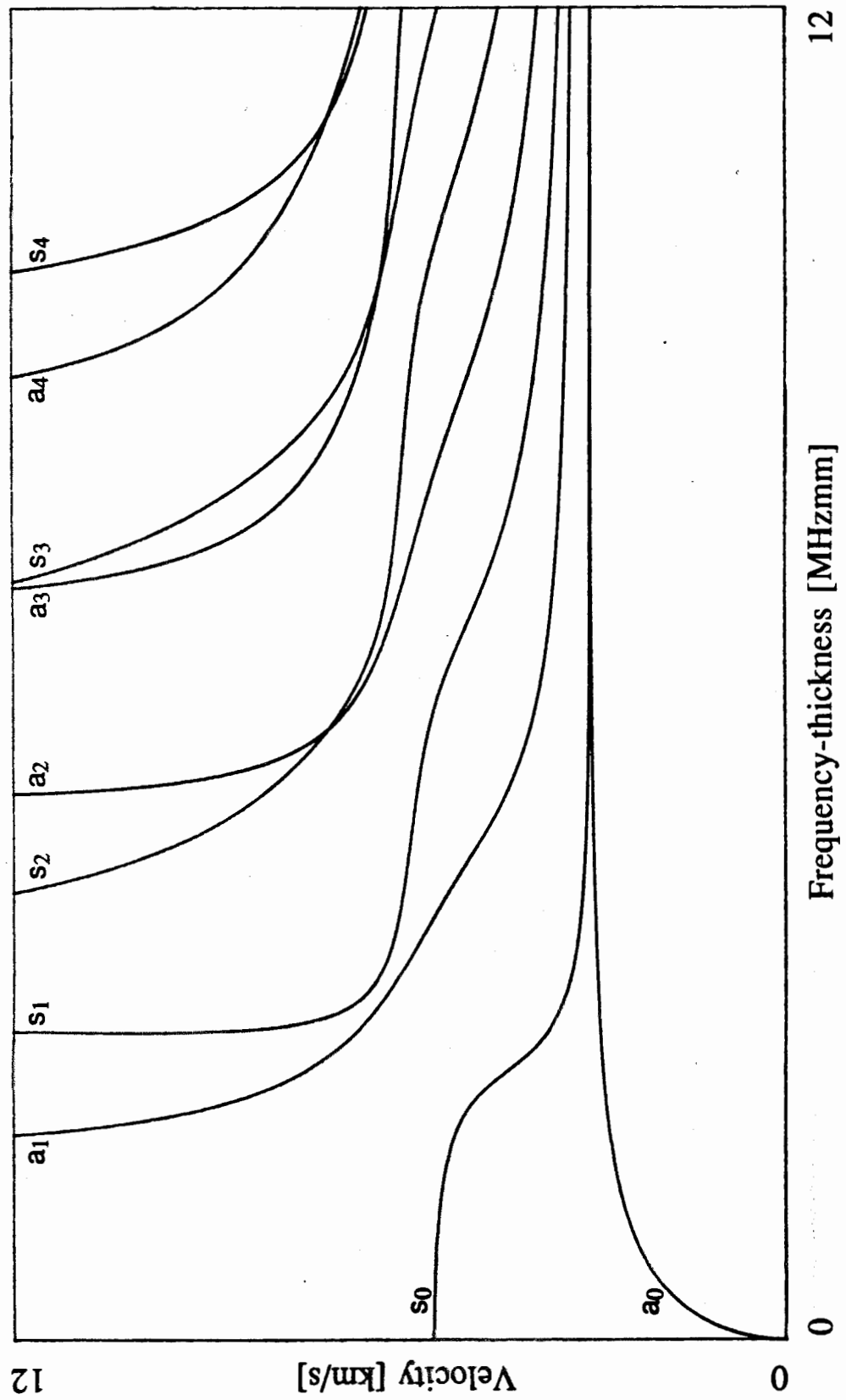


Figure 2.5 Lamb wave phase velocity dispersion curves for steel, where $c_1=5960$ m/s and $c_2=3260$ m/s.

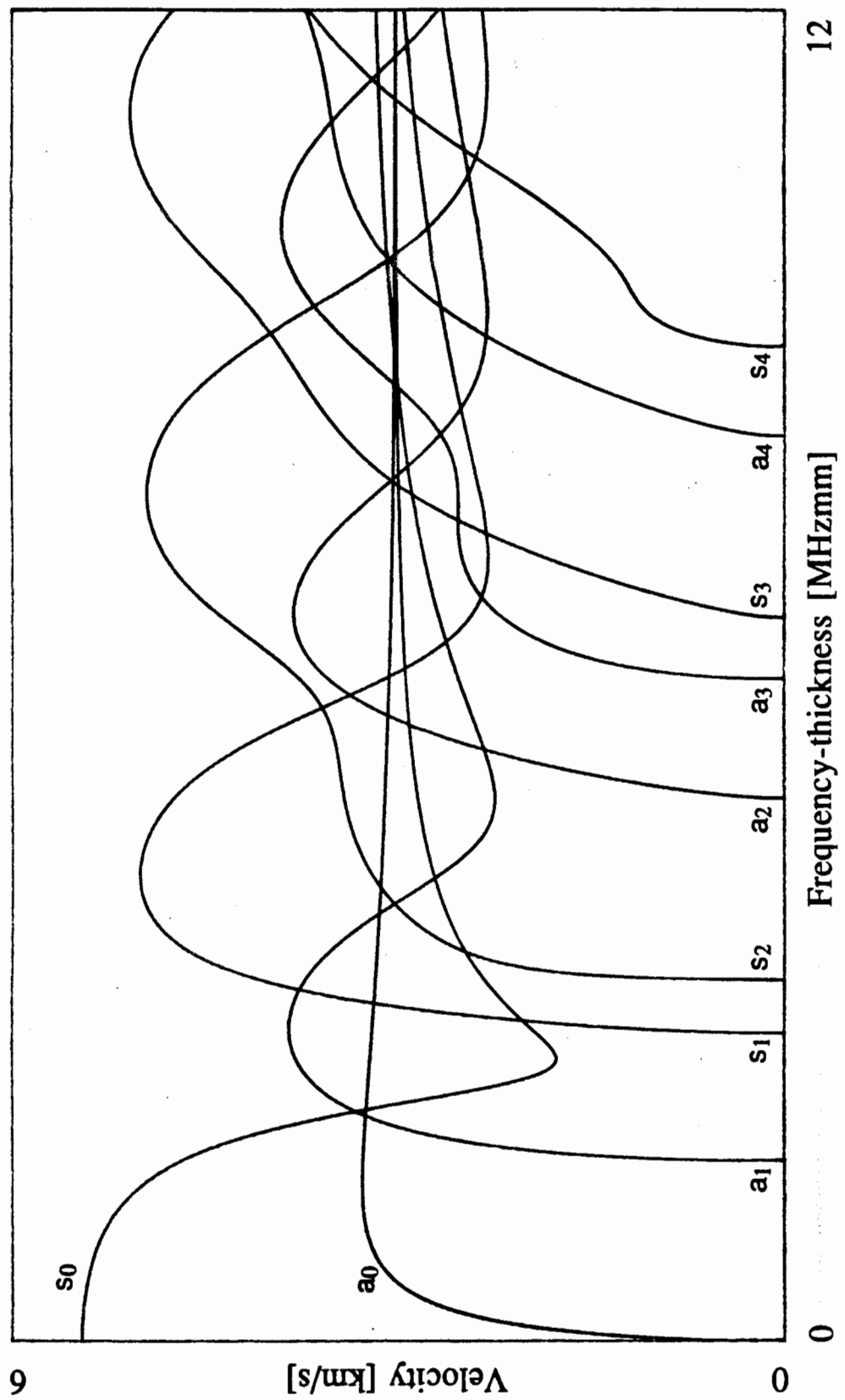


Figure 2.6 Lamb wave group velocity dispersion curves for steel, where $c_1=5960$ m/s and $c_2=3260$ m/s.

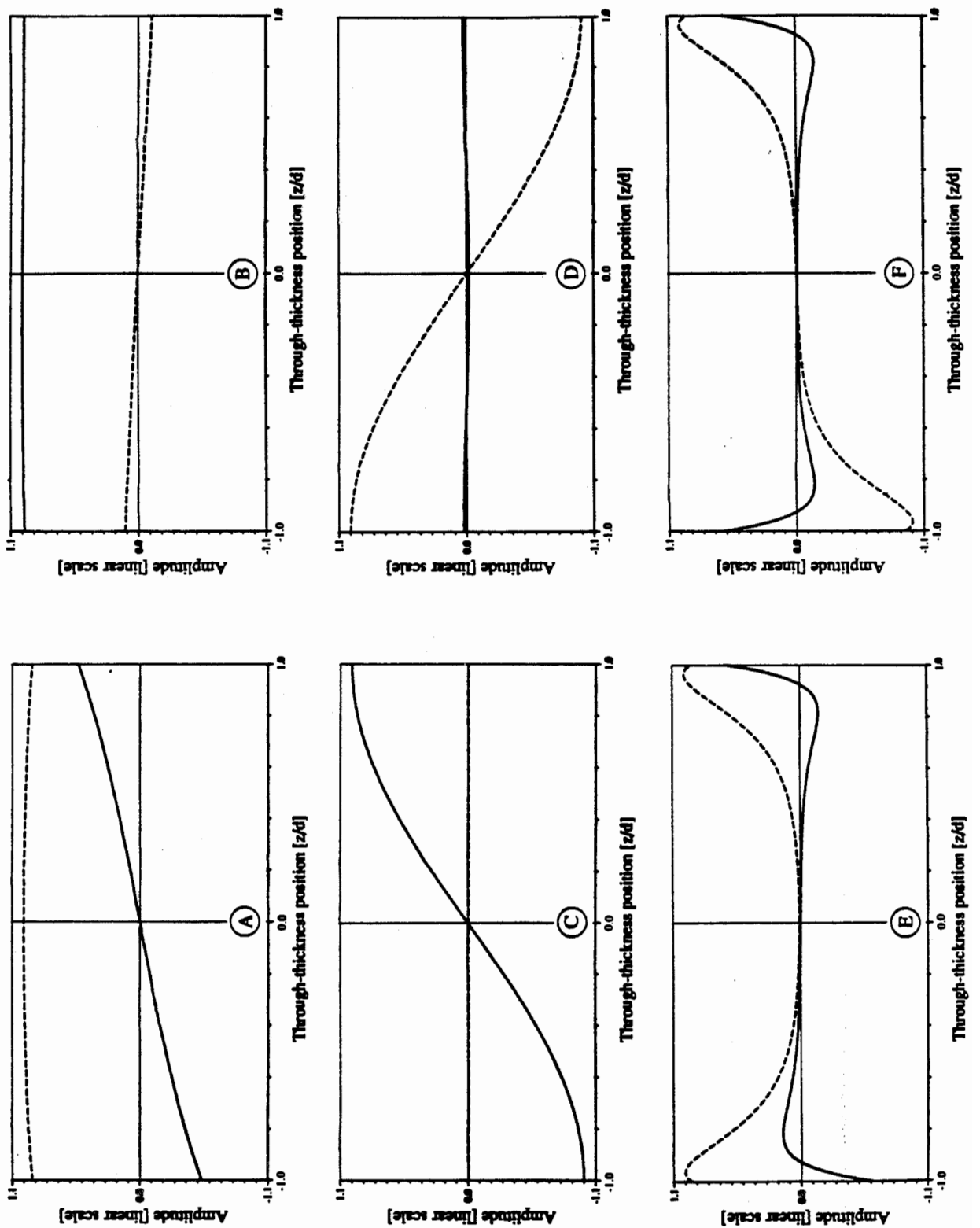


Figure 2.7 The through-thickness deflected mode shapes of Lamb waves, where c_1 and c_2 are the same as in figure 2.4: —.x direction displacements; ----- z direction displacements. (a) a_0 at 0.5 MHzmm (b) s_0 at 0.5 MHzmm (c) a_0 at 1.63 MHzmm (d) s_1 at 2.98 MHzmm (e) a_0 at 15 MHzmm (f) s_0 at 15 MHzmm.

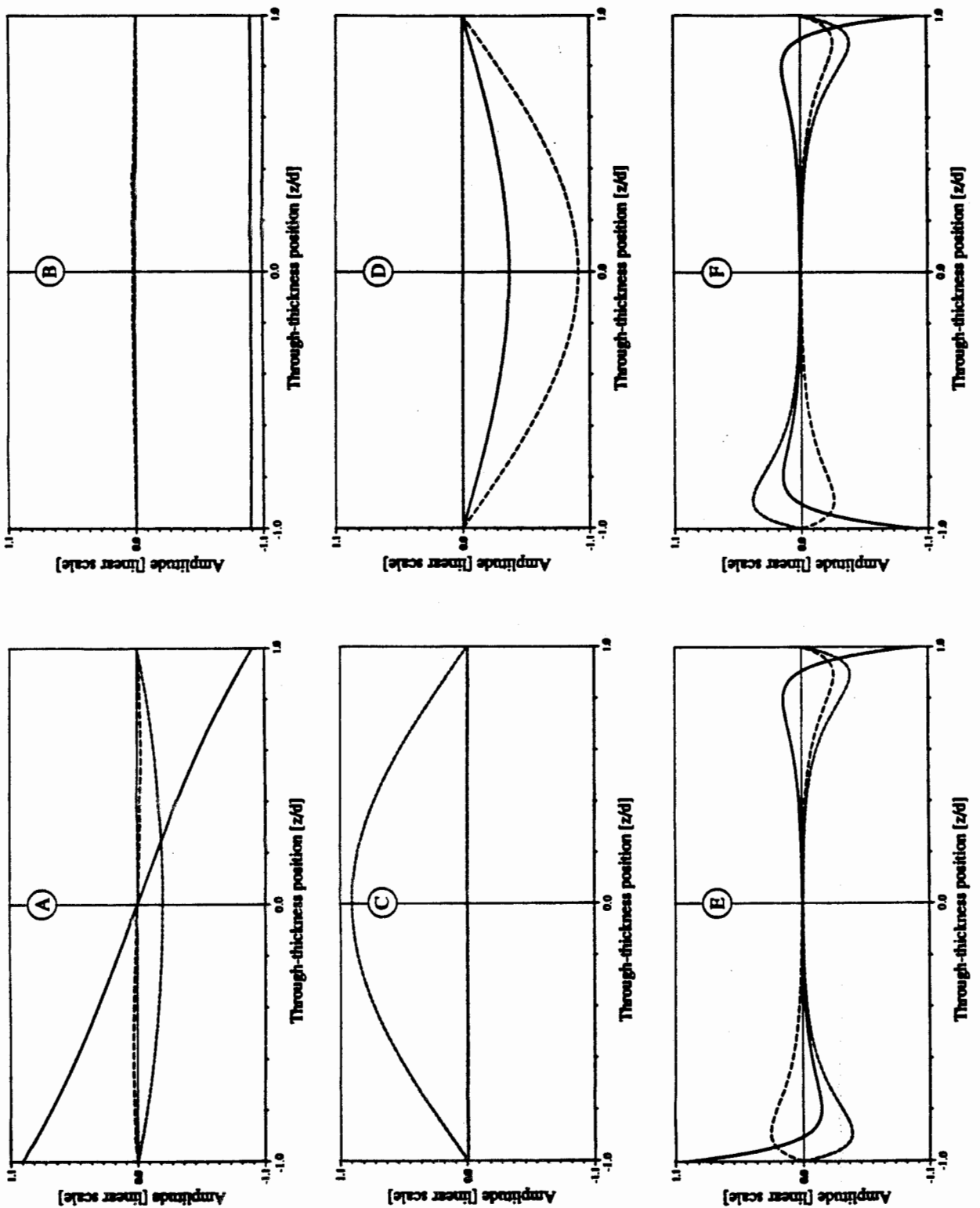


Figure 2.8 The through-thickness stress mode shapes of Lamb waves, where c_1 and c_2 are the same as in figure 2.4: — σ_{xx} ; - - - σ_{zz} ; - · - σ_{xz} . (a) a_0 at 0.5 MHzmm (b) s_0 at 0.5 MHzmm (c) a_0 at 1.63 MHzmm (d) s_1 at 2.98 MHzmm (e) a_0 at 15 MHzmm (f) s_0 at 15 MHzmm.

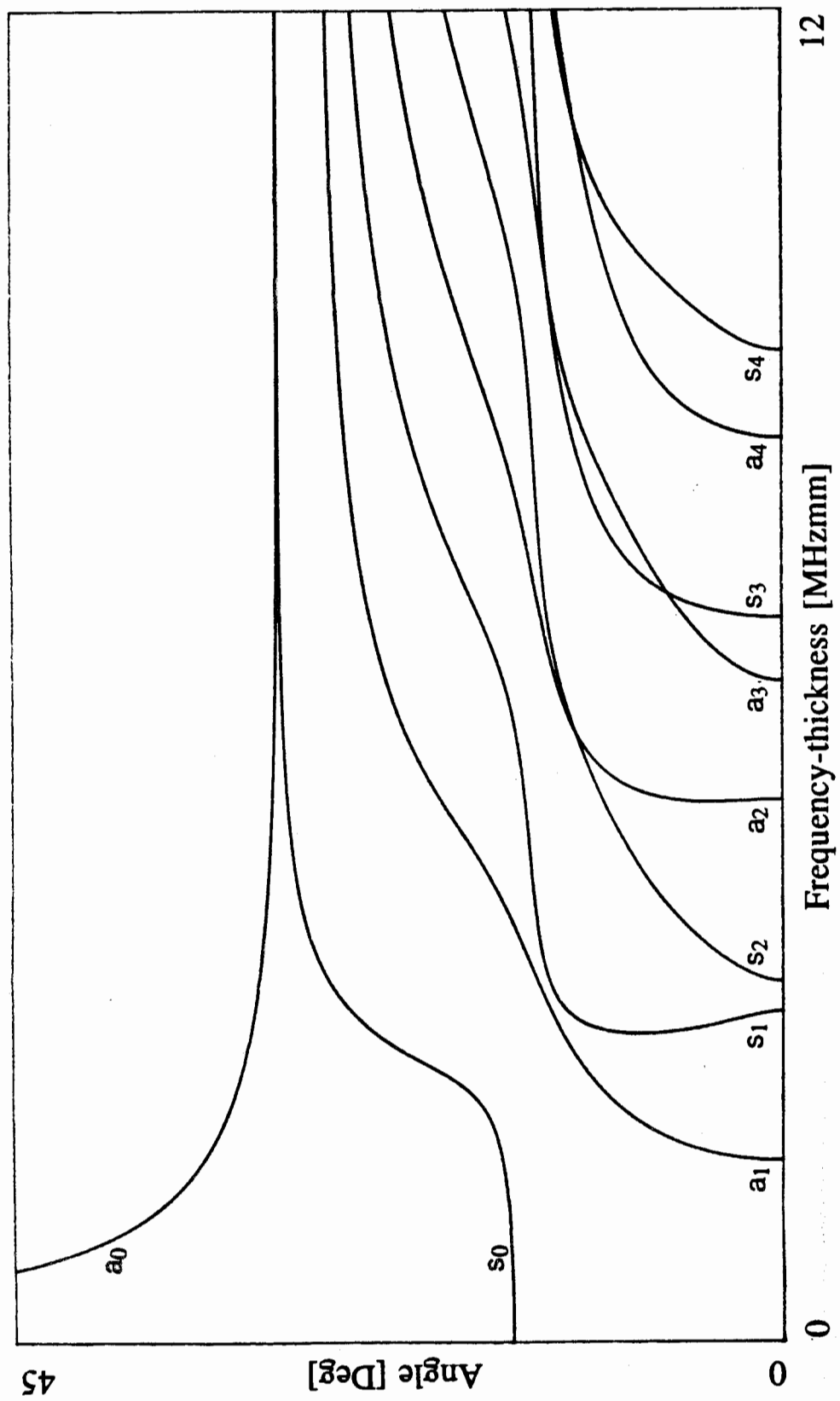


Figure 2.9 Lamb wave coincidence angle (water $c_L=1500$ m/s) dispersion curves for steel, where $c_1=5960$ m/s and $c_2=3260$ m/s.

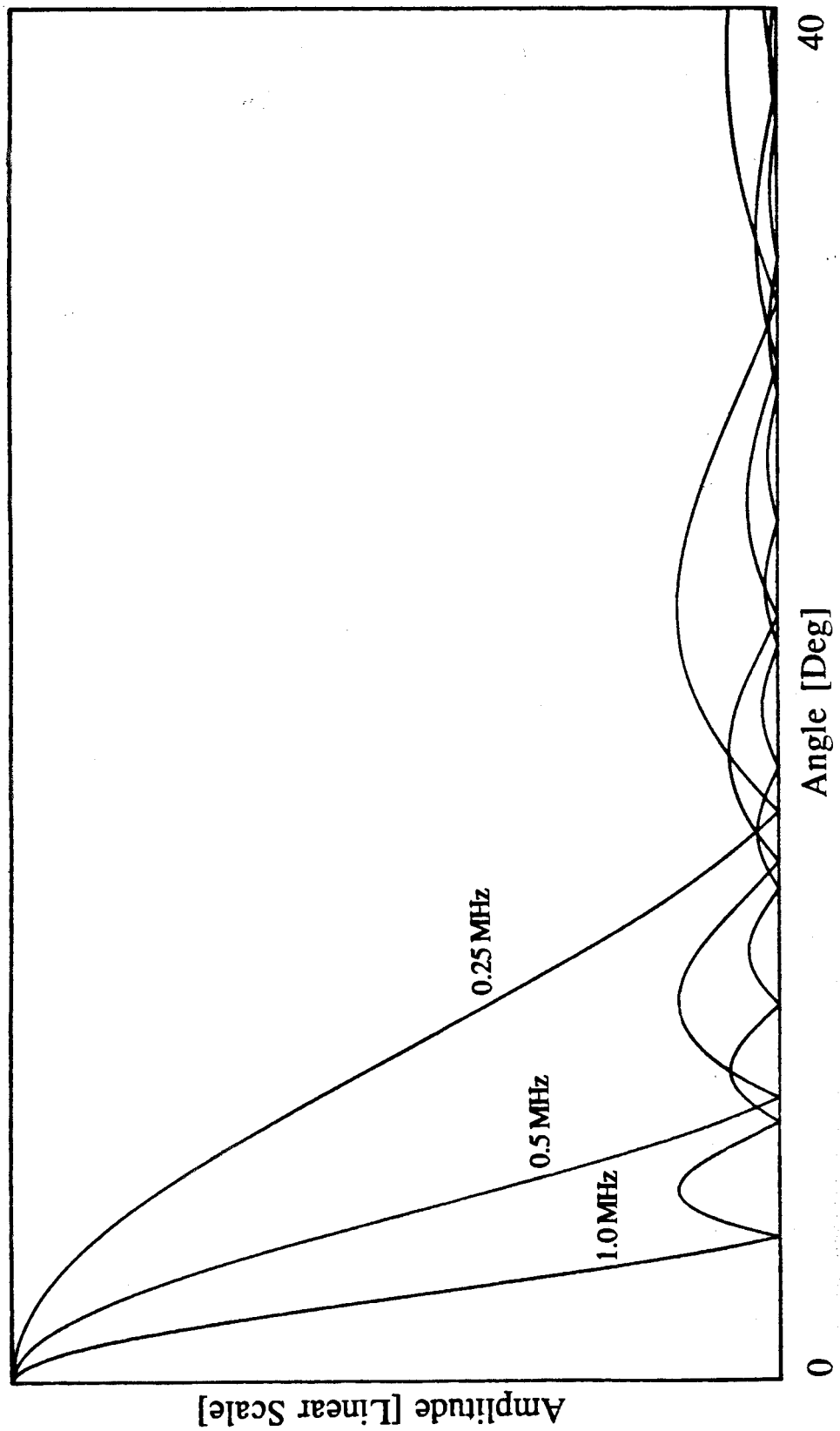


Figure 2.10 The theoretical pressure distribution generated by a one inch diameter transducer acting as a piston source.

CHAPTER 3

The measurement of the properties of propagating Lamb modes

3.1 General

The key problem associated with the quantitative measurement of the characteristics of propagating Lamb modes is that more than one mode can exist at any given frequency. Excitation via transducers of finite dimensions inevitably means that all the modes possible at any particular frequency of excitation are produced so it is not possible to separate the modes simply by transforming from the time domain to the frequency domain. Also, since the excitation will not be single frequency, dispersion will also be present leading to complicated time domain signals. Therefore, the time history of the response of the plate is usually multi-mode and dispersive. In such cases the shape of the Lamb wave response wave packet is strongly dependent on propagation distance.

Conventional time domain methods of measuring the amplitudes and velocities of Lamb waves generally require minimal signal processing and are often the easiest to apply. If the time history of a wave packet consisting of a single mode can be resolved separately from other wave packets in the time domain then its amplitude may be measured, and its group velocity may be determined by measuring the time it takes to propagate between two positions a known distance apart. Time domain techniques may be adopted to measure the amplitude and velocities of a_0 and s_0 in low frequency-thickness regions (see Fig. 2.6) where only these two propagating modes are possible and since their phase velocities are very different they may be easily decoupled from one another by the orientation of the transducer.

When the time record is composed of a number of superimposed wave packets, it is not usually possible to measure the amplitude or group velocity of individual Lamb waves. Hence, many workers have used time domain correlation methods (for example Bartle 1987 and Avioli 1988), where the received signal is processed to obtain a signal envelope. Rose *et al* (1983) have developed a method using a similarity coefficient, where the spectrum of received signals is compared with a reference or good spectrum. However, none of these

methods have been able to obtain reliable results at frequency-thickness products above the cut-off value for the a_1 mode (1.63 MHzmm in steel).

Mal *et al.* (1988), Chimenti and Nayfeh (1985) and others have used a reflection coefficient technique to measure the dispersion curves of leaky Lamb waves to determine material properties. However, the relative amplitudes of the Lamb waves present (mode purity) cannot easily be determined.

The first part of this chapter will briefly introduce standard spectral methods of measuring the velocities of Lamb waves, when only one mode is present. Then a two-dimensional Fourier transformation method will be presented, which can be used to measure the amplitudes and velocities of Lamb waves when many propagating modes are present.

3.2 Frequency domain methods

Early investigations to detect different echoes in seismic signals deconvolved the time record using a cepstrum analysis, which is a logarithmic conversion of the spectrum of the time record (see, for example, Randall 1987). More recently, spectral methods developed by Sachse and Pao (1978) have been used by, for example, Pialucha *et al.* (1989) to measure phase and group velocity by transforming the time domain data to the frequency domain, where data interpretation may be easier. To measure the dispersion curve of an individual Lamb wave we may Fourier transform the time record containing a series of echoes, from a single position. Alternatively, the time records of the response of a plate at two or more positions a known distance apart may be summed and Fourier transformed. The resulting amplitude spectrum will have resonance peaks, from which the phase velocity of the Lamb wave at discrete frequencies may be calculated using a relation given by Pialucha *et al.* (1989) as,

$$c = \frac{Lf}{n}, \quad n = 1, 2 \dots \quad (3.1)$$

where c is the Lamb wave phase velocity and L is the distance between the measurement positions. If the echoes may be separated in the time domain, a phase spectrum method may be used in which two time records or echoes are Fourier transformed separately and a relation given by, for example, Pialucha (1989) as

$$c = \frac{L\omega}{\Delta\phi} \quad (3.2)$$

may be used to calculate the phase velocity, where $\Delta\phi$ is the difference in the phase spectrum of the two signals. Pialucha *et al* (1989) have measured the phase velocity of the longitudinal wave in steel to an accuracy of better than 0.1% using spectral methods. The result of carrying out a discrete temporal Fourier transform of a time history of the response of the plate is that a plot of amplitude versus frequency is obtained but there is no information about which Lamb modes are present. Because of the multi-mode dispersive nature of Lamb waves, and the probability of more than one propagating mode being excited by broad band excitation signals, amplitude and phase spectrum methods of measuring the dispersion curves are not usually applied in frequency-thickness regions above 1.63 MHzmm.

3.3 The two-dimensional Fourier transform method

The two-dimensional Fourier transformation method (2-D FFT) discussed in this section is an extension of the one-dimensional Fourier transformation method developed by Sachse and Pao (1978) and is an alternative method of measuring the properties of Lamb waves. It overcomes the problems of multiple modes and dispersion by transforming the received amplitude-time records to amplitude-wavenumber records at discrete frequencies, where individual Lamb waves may be resolved and their amplitudes measured. The major advantage of the 2-D FFT method, which is of great importance in NDT applications, is that Lamb wave amplitudes *and* velocities are measured. Propagation distances may be large and are limited only by the signal-to-noise ratio.

Assuming a harmonic wave propagating in a plate with the coordinate system shown in Fig. 2.3, the displacement on the surface, $\mathbf{u}(x,t)$, from section [2.10] may be described by a general analytic expression,

$$\mathbf{u}(x,t) = \mathbf{A}(\omega) e^{i(kx - \omega t - \phi)} \quad (3.3)$$

where $\mathbf{A}(\omega)$ is a frequency dependent amplitude constant and ϕ denotes the phase.

From eqn 3.3 it may be seen that propagating Lamb waves are sinusoidal in both the time and spatial domains. Therefore, the normalised amplitude of the steady-state response of a plate at a given point on the plate surface as a function of time, for an individual Lamb wave would be a single sinusoid as shown in Fig. 3.1(a), where $T = 1/f$, is the period of the wave. The normalised amplitude of the steady-state response of a plate at a given instant in time as a function of position on the plate surface would, again, be a single sinusoid, shown in Fig.

3.1(b) for a single propagating mode, where λ is the wavelength of the mode. Therefore, a temporal Fourier transform may be carried out to go from the time to frequency domain, then a spatial Fourier transform may be carried out to go to the frequency-wavenumber domain, where the amplitudes and wavenumbers of individual modes may be measured.

Applying spatial Fourier methods in practice to data gained experimentally or numerically requires us to carry out a two-dimensional Fourier transform of eqn 3.3 giving

$$H(k,f) = \int_{-\infty}^{+\infty} \int_{-\infty}^{+\infty} \mathbf{u}(x,t) e^{-i(kx + \omega t)} dx dt \quad (3.4)$$

The discrete two-dimensional Fourier transform may be defined in a similar way to the one-dimensional DFT given in, for example, Newland (1984). The result of this transformation will be a two-dimensional array of amplitudes at discrete frequencies and wavenumbers. As in the one-dimensional case, aliasing must be avoided by sampling the data at a sufficiently high frequency in time, and wavenumber in space. Window functions such as the Hanning window may be used to reduce leakage, and zeros may be padded to the end of the signal to enable the frequency and wavenumber of the maximum amplitude to be determined more accurately. Details of the fast Fourier transform algorithm, aliasing, leakage, zero padding and other effects associated with discrete Fourier transforms may be found in standard texts (see for example, Press *et al* 1988).

The two-dimensional Fourier transform method is applied by carrying out a Fourier transform of the time history of the response at each position monitored to obtain a frequency spectrum for each position. At this stage, an array with the spectral information for each position in its respective column is obtained. A spatial Fourier transform of the vector (row) formed by the components at a given frequency then gives the amplitude-wavenumber-frequency information. In practice a two-dimensional fast Fourier transform algorithm (2-D FFT) may be used. In contrast to the method developed by Sachse and Pao (1978) this method enables the amplitude and velocity of different modes propagating at the same frequency to be determined.

3.4 Initial test of the spatial transform

The use of temporal transforms are well established but spatial transforms are less well known in ultrasonics so it was decided to check the operation of the spatial transform to determine the wavenumber content of signals. This was done using theoretically computed data of the

essentially non-dispersive s_0 mode at 63.6 and 127.2 kHz in a 1.0 mm thick plate, where the phase velocity was 5.45 km/s (see Fig. 2.5).

Let $g(x)$ be the displacement of the surface of an infinite plate as a function of position due to a harmonic travelling wave of phase velocity c , frequency ω and unit amplitude. Then

$$g(x) = e^{\frac{i\omega}{c}x} \quad (3.5)$$

and a spatial Fourier transform of $g(x)$ may be defined as

$$H(k) = \int_{-\infty}^{+\infty} g(x)e^{-ikx} dx \quad (3.6)$$

or

$$H(k) = \int_{-\infty}^{+\infty} e^{-i(k-\Omega)x} dx, \quad -\infty \leq x \leq \infty \quad (3.7)$$

where $\Omega = \omega/c$. Therefore,

$$H(k) = \int_{-\infty}^{+\infty} e^{-i\zeta x} dx \quad (3.8)$$

where $\zeta = k - \Omega$, and

$$H(k) = \delta(\zeta) = \delta(k - \Omega) \quad (3.9)$$

where δ is the Dirac delta function. In practice, $g(x)$ is in the form of sampled data and is known at N points x_m where,

where,

$$x_m = m \delta x \quad m = 0, 1, 2, \dots, N-1$$

and δx is the sampling interval, the amplitude at point m being g_m . Therefore, the discrete transform corresponding to the continuous transform of eqn 3.6 is

$$H_m = \sum_{n=0}^{N-1} g_n e^{-i2\pi mn/N} \quad (3.10)$$

The sampling wavenumber, k_{sam} , and Δk , the resolution in wavenumber, are defined as

$$k_{\text{sam}} = \frac{2\pi}{\delta x} \quad \text{and} \quad \Delta k = \frac{k_{\text{sam}}}{N} \quad (3.11)$$

The DFT produces estimates of the continuous Fourier transform at discrete wavenumbers k_m , where

$$k_m = \frac{k_{\text{sam}} \cdot m}{N} \quad m = 0, 1, 2, \dots, N/2 \quad (3.11)$$

A consequence of sampling continuous data at discrete intervals is that spatial aliasing may occur if a sufficiently high spatial sampling rate is not chosen. The Nyquist wavenumber

$$k_{\text{ny}} = \frac{k_{\text{sam}}}{2} \quad (3.12)$$

defines the critical sampling wavenumber. Another potential pitfall of DFTs is leakage, which occurs if the amplitudes and slopes of the sampled signal are not the same at the start and end of the sampled data. This may be reduced by windowing the data using, for example, a Hanning window.

In the first example, the steady-state response of the s_0 mode, at 63.6 kHz was calculated at 64 equally spaced discrete positions within the spatial window $0 \leq x \leq 5\lambda$ shown in Fig. 3.1(b), where λ was 85.6 mm. Fig. 3.2(a) shows the result of carrying out a 64 point spatial Fourier transformation of the resulting spatial record, where $\delta x = 6.8$ mm, $k_{\text{ny}} = 462 \text{ m}^{-1}$ and $\Delta k = 14.4 \text{ m}^{-1}$. In Fig. 3.2(a) the result of the spatial FFT is plotted in terms of amplitude versus wavenumber at the single frequency (63.6 kHz) and is correct with a single peak at $k = 71 \text{ m}^{-1}$, the points relating to different wavenumbers being joined by straight lines. Fig. 3.2(b) shows the result of carrying out a spatial FFT, when the steady-state response of the s_0 mode was calculated at 1024 equally spaced discrete positions within the spatial window $0 \leq x \leq 100\lambda$, where the frequency was 63.6 kHz and $100\lambda = 8.56$ m. Fig. 3.2(c) shows the result of carrying out a 1024 point spatial FFT at 127.2 kHz, where the spatial record extended from $x = 0$ to $x = 4.28$ m (ie over 100 wavelengths). In both Fig. 3.2(b) and (c) there is a single peak at the correct wavenumbers of 73 m^{-1} and 147 m^{-1} respectively. Fig. 3.2(b) also shows that increasing the spatial extent of the record by twenty has increased the resolution (the ability to identify different peaks close to one another) by twenty and confirms that resolution

between closely spaced peaks is inversely proportional to the spatial extent of the sampled records.

In practice the spatial extent of the sampled signal will not be an integer number of wavelengths and leakage occurs, which cause sidelobes around the maximum value as shown in Fig. 3.3(a), which was obtained by carrying out a discrete 256 point spatial FFT of 64 equally spaced positions within the spatial window $0 \leq x \leq 5.2\lambda$, where the frequency and number of computed points used was as in Fig. 3.2(a), and 192 zeros were padded to the end of the spatial record. Again the correct wavenumber of 73 m^{-1} was obtained, but the sidelobes present could obscure the presence of other wavenumber components in the signal. The leakage evident in Fig. 3.3(a) may be reduced by using a Hanning window function to smooth the data as shown in Fig. 3.1(c). Fig. 3.3(b) shows the result of performing a spatial FFT on the data used to produce Fig. 3.3(a), after applying a Hanning window to reduce the effect of leakage. The Hanning window has reduced the amplitude of the sidelobes, but has also broadened the peak significantly.

3.5 Conclusions

The tests on the spatial transform have shown that it can be successfully used to determine the wavenumber content of signals and they have shown that standard techniques such as windowing and zero padding are applicable.

The initial tests described in this chapter have only concerned the spatial Fourier transform at a single frequency. In practice, many frequencies will be present so the full two-dimensional transform will be required. This has been applied to the results of numerical modelling in chapter 4 and 5 and to experimental data in chapters 6 and 7.

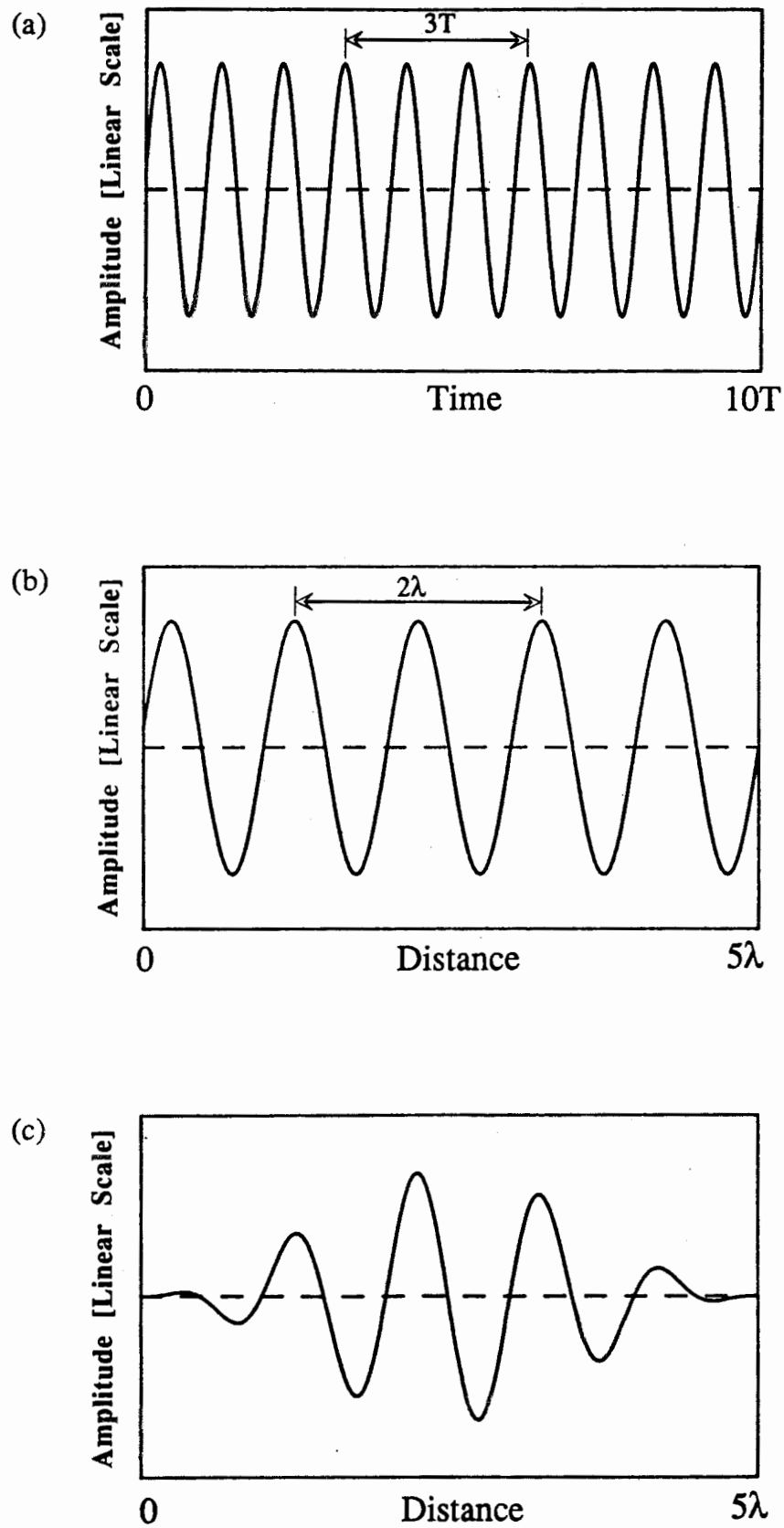


Figure 3.1 (a) Steady-state response of an infinite plate, at a single frequency as a function of time; (b) as a function of position in the x direction. (c) The steady-state response in (b) modified by the application of a Hanning window.

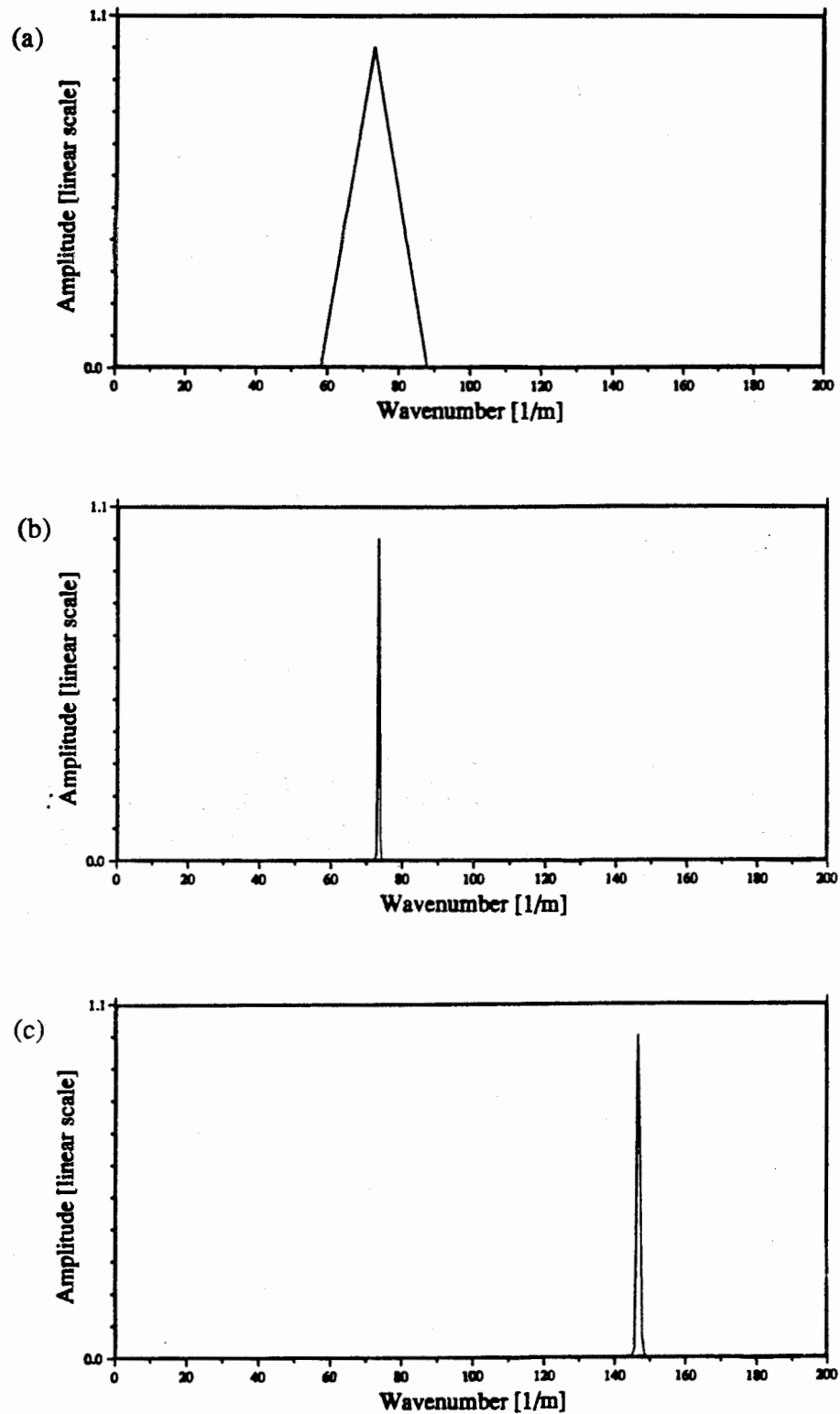


Figure 3.2 (a) Analytically calculated spatial FFT of the s_0 mode in a 1.0 mm thick plate at 63.6 kHz, when the spatial record was related to s_0 at 63.6 kHz, which was sampled at 64 equally spaced points over 5 wavelengths. (b) as in (a) but when the spatial record extended from $x = 0$ to $x = 8.56$ m (100 whole wavelengths) and a 1024 point FFT was used. (c) When the spatial record extended from $x = 0$ to $x = 4.28$ m (100 whole wavelengths), the frequency was 127.2 kHz and a 1024 point FFT was used.

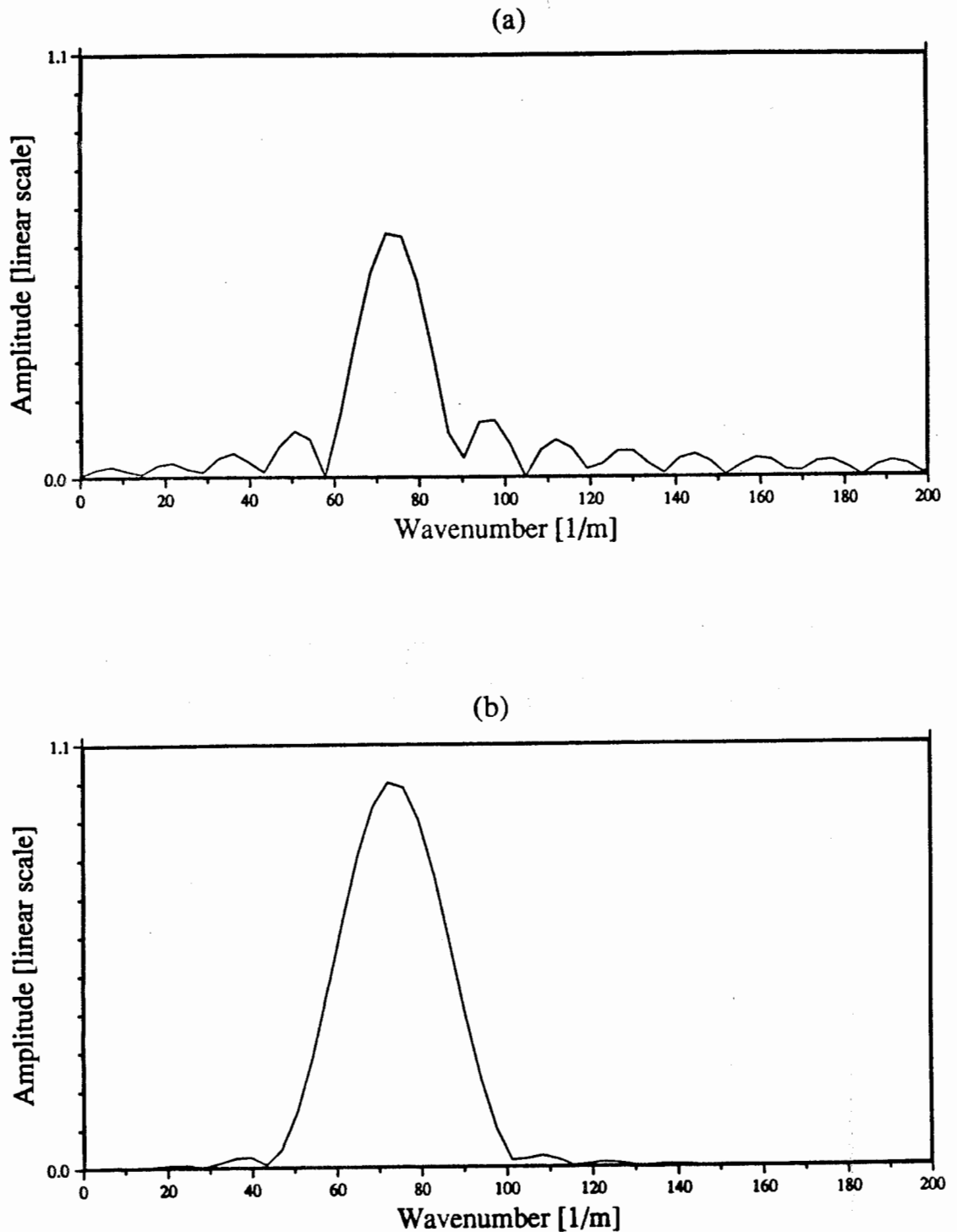


Figure 3.3 (a) Spatial FFT of the s_0 mode in a 1.0 mm thick plate at 63.6 kHz, when the sampled spatial record was at 64 equally spaced points over 5.2 wavelengths and a 256 point FFT was carried out, by padding the end of the spatial record with 192 zeros. (b) spatial FFT when the simple sinusoidal spatial record used in (a) was modified by the application of a Hanning window function.

CHAPTER 4

Numerical modelling of propagating stress waves

4.1 An introduction to numerical modelling

For all but the simplest boundary conditions, analytical solutions of the partial differential wave equations are at best very complicated, and at worst impossible. Therefore, rather than carry out tedious and complicated analysis an approximate numerical approach may be applied. Two numerical methods well known to engineers are the finite difference and finite element schemes. These numerical modelling methods have become very attractive methods of obtaining predictions of the behaviour of stress waves in a variety of situations of importance in NDT, particularly with the advent of cheap and fast digital computers. These methods offer idealized controlled conditions under which wave propagation tests may be carried out. It is also possible to obtain information which cannot be measured in experimental situations, for example, through-thickness stresses, strains and displacements. Consequently, numerical methods have become very popular over the last few decades.

Both the finite difference and the finite element schemes transform the partial differential equations which describe motion into a set of coupled ordinary differential equations of the form

$$M \frac{\partial^2 u}{\partial t^2} + K u = F \quad (4.1)$$

in the absence of damping, where M is the mass matrix, K is the stiffness matrix, u is the displacement vector and F is a forcing vector.

In this chapter theory relating to the finite difference and finite element numerical methods is presented. The results of an initial numerical investigation to validate the finite element approach are presented, and the merits of the finite element and finite difference methods are discussed. Finally, the results of finite element modelling of Lamb wave propagation and

reflection from the end of plates are presented together with conclusions concerning the usefulness of the numerical models.

In all of the numerical investigations reported here, plane strain conditions are assumed, the material properties and coordinate system previously defined apply and temporal discretization is carried out using a central difference scheme. In all the numerical modelling investigations, free boundaries will be assumed unless otherwise stated.

4.1.1 The finite difference method

Explicit finite difference (FD) schemes were the first numerical methods to be applied to solve propagating stress wave problems, for example, by Bertholf (1967) and Alterman (1968). However, finite difference schemes were not applied to NDT problems until the early 1970's when investigators such as Harumi *et al* (1973) modelled the pressure fields created by real transducers in the near field. More recently FD schemes have been used to model ultrasonic wave scattering from impedance mismatches, by for example, Bond (1982), Saffari and Bond (1983) and Harker (1985); and to study wave propagation in inhomogeneous material by Temple (1988). Kriz and Gary (1989) have used FD methods to study wave propagation in composites. Many standard texts are available which give detailed theoretical descriptions of FD methods, for example and Smith (1985). Here only the essential aspects of the FD methods will be discussed.

Finite difference methods work by transforming the differential form of the wave equations for a continuum into a discrete set of algebraic equations in which the field variable (usually displacement in the body node formulations used by most investigators) are defined at points of intersection of the grid. The partial derivatives in the wave equations are approximated by combining Taylor expansions (to a given accuracy, depending on the number of terms taken) of a function defined over the grid. Most workers in the field who use FD schemes (for example, Bond and his co-workers and Harker) employ algorithms which are derived from the wave equations in their second order form (eqn 2.7 to 2.9). It is also possible to express the problem in terms of coupled first order equations, using velocity and stress as the field quantities (see, for example, Duncan 1985).

The wave equations for a homogeneous, isotropic medium were given in eqn 2.7 to 2.9, and assuming plane strain conditions reduce to

$$\frac{\partial^2 u}{\partial t^2} = c_1^2 \frac{\partial^2 u}{\partial x^2} + (c_1^2 - c_2^2) \frac{\partial^2 u}{\partial x \partial z} + c_2^2 \frac{\partial^2 u}{\partial z^2} \quad (4.2)$$

$$\frac{\partial^2 w}{\partial t^2} = c_1^2 \frac{\partial^2 u}{\partial z^2} + (c_1^2 - c_2^2) \frac{\partial^2 u}{\partial x \partial z} + c_2^2 \frac{\partial^2 u}{\partial x^2} \quad (4.3)$$

The partial derivatives in the differential equations can be approximated by Taylor series expansions. The forward Taylor expansion of the longitudinal component of the displacement is

$$u(i+1,j,k) = u(i,j,k) + \Lambda \frac{\partial u}{\partial x} + \frac{\Lambda^2}{2!} \frac{\partial^2 u}{\partial x^2} + \frac{\Lambda^3}{3!} \frac{\partial^3 u}{\partial x^3} + \dots + \frac{\Lambda^n}{n!} \frac{\partial^n u}{\partial x^n} \quad (4.4)$$

where i,j,k are node indices, which have been dropped from the differential terms for clarity, Λ is the mesh spacing and n is an integer. Rearranging terms and combining the above expression with the backward Taylor series obtained in the same manner, gives the central difference quotient

$$\frac{\partial u}{\partial x} = \frac{u(i+1,j,k) - u(i-1,j,k)}{2\Lambda} + o(\Lambda^2) \quad (4.5)$$

where the term $o(\Lambda^2)$ represents the truncation error, ie the terms neglected in the Taylor series expansion. It may be seen that the truncation error in the central difference quotient is of the order of the grid spacing squared. Quotients for higher order and mixed derivatives may be obtained in a similar manner, for example,

$$\frac{\partial^2 u}{\partial x^2} = \frac{u(i+1,j,k) - 2u(i,j,k) + u(i-1,j,k)}{\Lambda^2} + o(\Lambda^2) \quad (4.6)$$

In most FD schemes employed to solve propagating stress wave problems the partial differential equations are replaced by their central difference quotients resulting in a body node formulation (in the form of eqn 4.1). However, in these formulations stress free boundaries may not be modelled and in order to cater for boundary nodes in these schemes special surface node formulations have to be developed. One example is the pseudo-node scheme (for details see Blake, 1988) in which a row of imaginary nodes are placed just outside the free boundary, the displacements of these nodes being altered to achieve a stress free boundary.

The spatial discretization error is a function of the mesh spacing and as the mesh spacing is refined, the FD solution converges to the exact solution in the absence of rounding errors. However, in transient wave propagation problems the solution must also converge temporally. To avoid spatial aliasing a single sinusoidal wave requires at least 2 nodes per

wavelength to be represented. The theoretical percentage velocity error c_e of the FD method for a wave of velocity c , propagating in the x direction is given by Harker (1989) as,

$$c_e = \left\{ \frac{N}{\pi} \frac{\Lambda}{c\Delta t} \sin^{-1} \left(\frac{c\Delta t}{h} \sin \frac{\pi}{N} \right) - 1 \right\} 100 \quad (4.7)$$

where N is the number of nodes per wavelength. If N is greater than eight, c_e will be less than 0.5%, therefore, for an accurate solution more than eight nodes per wavelength is required. Using a very refined mesh where N is very large only increases the computational cost excessively.

Central difference quotients, derived in the same manner as eqn 4.6 are generally used to obtain the temporal discretization in FD schemes. As the procedures are essentially the same for FD and FE schemes their details will be presented later (see section 4.1.3).

4.1.2 The finite element method

The advent of cheap and fast digital computers has made finite element (FE) methods very attractive for solving difficult and/or tedious engineering problems. It seems that FE methods were first employed by Courant in 1945. Since then they have become remarkably popular and over the last few decades they have been used to solve a variety of problems where there are, for example, discontinuities in the boundary conditions, the system is geometrically complicated or the the applied loading is complicated. In the FE method the system is first divided into a finite number of elements of finite size, which are connected to one another at nodal points, which are generally situated at the boundary of the element. A hypothesis of the displacement field is made, enabling the kinetic and potential (strain) energies to be calculated as a function of the nodal point displacements (assuming that there is no dissipation of energy). The energy is then summed through all the elements and the generalized forces are calculated using virtual work. Finally, Lagrange's equations are applied, which allow the differential equation of motion of the assembly to be obtained. More details on the theoretical basis of FE methods may be obtained in standard text books, for example Zienkiewicz (1971) and Bathe (1982).

The finite element method reduces a problem of an infinite number of unknowns to one of a finite number of unknowns by dividing the continuum (solution region) into finite elements and expressing the unknown field variables (usually displacements for solid mechanics problems) in terms of an assumed interpolation (shape) function within each element. This is

generally a polynomial expression which may be easily differentiated. The interpolation function is defined in terms of the field variables at the nodal points. The discrete nodal values of the field variables can be used to express the continuous behaviour within each element, and the full problem for the continuum is formulated by summing the contributions from each element.

Early investigators who used FE techniques for NDT applications include Alsop and Goodman (1972) who investigated Rayleigh wave scattering and Smith (1975) who modelled compression wave scattering. At present many investigators who employ numerical methods to predict the characteristics of propagating stress waves are using FE methods. Indeed many workers who previously used FD techniques are now turning to FE methods (for example, Bond and his co-workers). Blake and Bond (1989) and You and Lord (1988) have used FE methods to model the propagation and interaction of stress waves with impedance changes. Ludwig *et al* (1988) have carried out tests to compare FE and analytical results. Recently some workers in the field, for example, Datta and Shah (1987) have used a combination of FE and analytical models, where a finite elements approach is used in discontinuous regions and is coupled to an analytical model which applies in regions with constant geometries. These coupled FE analytical models have been used to predict effect that defects (cracks) have on propagating Rayleigh and Lamb waves.

The general expression for the strain energy of an element is

$$U = \frac{1}{2} \int_v \epsilon^t \sigma \, d v \quad (4.8)$$

where ϵ and σ are the strain and the stress matrices respectively and the integral is over the volume v of the element. The element stiffness matrix K_e , may be obtained by equating the (internal) strain energy to the work done on the element by external forces.

$$K_e = \int_v B^t D B \, d v \quad (4.9)$$

where B is a matrix relating strain and nodal displacements, D is a square symmetric matrix which represents the material stiffness of the continuum, and the superscript t indicates the transpose of the matrix.

The general expression for the kinetic energy of an element is

$$T = \frac{1}{2} \int_v \rho \, v^2 \, d v \quad (4.10)$$

where V is a velocity vector. This may be related to the nodal displacement vector of the element by means of the shape function matrix N . By substituting these expressions into the above equation the following expression for the consistent mass matrix M_e , is obtained,

$$M_e = \int_V \rho N^t N d v \quad (4.11)$$

The assembled global stiffness and mass matrices are the sum of all the element stiffness and mass matrices, and are defined as

$$K = \sum_{i=1}^Q K_e \quad (4.12)$$

and

$$M = \sum_{i=1}^Q M_e \quad (4.13)$$

respectively and Q is the number of elements.

The FE scheme employed in the work reported here used a central difference approximation, which is explained in the following section, to obtain a time marching solution.

4.1.3 Method of temporal discretization

The finite element and finite difference spatial discretization procedures both result in a set of coupled differential equations in the time variable (see eqn 4.1). The temporal discretization or time marching may be achieved by using a finite difference approximation. Implicit or explicit schemes may be employed, and details of various methods are given in, for example, Bathe (1982). Some investigators have used a mixture of both in their work, notably Bond and co-workers (see for example, Georgiou and Bond, 1985).

In implicit schemes the modelled system is assumed to be in equilibrium at a given time in the future and the displacements are obtained by solving the simultaneous equations. For more details see Bathe (1982). The major drawback of implicit schemes is that a matrix of the order of the number of displacements has to be inverted. This is a very restrictive condition when the model is large. However, there is no critical time step when implicit methods are applied, and the time step can in general be much larger than in explicit methods.

Explicit central difference schemes are attractive because they enable numerical integration to be performed with a minimum of information. They also have the largest stability region of any second order algorithm, (Nickell, 1973). Explicit schemes do not require any matrix inversions provided that a diagonal mass matrix is employed. In the work reported here only explicit time marching methods were used as the models were too large for implicit methods to be employed efficiently with the available computing resources. Explicit schemes assume that the system is in equilibrium at the present time interval or step and use this and information from the previous time step to compute the state of the system at the next time step. However, the major disadvantage of this method is that it is only conditionally stable. Stability may be defined in both FD and FE methods as the requirement that the growth of an initial disturbance be bounded. Lax's equivalence theorem (see Smith, 1985) states that if a solution is stable, this is generally a sufficient condition for convergence. Physically the restriction is that no energy may be propagated through a mesh spacing in under a time step. The critical time t_c step may be defined for a regular mesh in FD schemes by a relation given by Alterman and Loewenthal (1972) as,

$$t_c = \frac{\Lambda}{\sqrt{c_1^2 + c_2^2}} \quad (4.14)$$

Therefore the time step Δt , must always be less than or equal to t_c . This is a statement of the Courant-Fredrichs-Lewy condition (Courant *et al*, 1967).

Blake (1988) showed that the critical time step for a regular FE mesh of two-dimensional elements is

$$t_c = \frac{\Lambda}{c_1} \quad (4.15)$$

These stability limits apply to square spatial grids and the critical time step for FE schemes is greater than for FD schemes. Blake (1988) has shown that this is because the 'domain of dependence' in the FE method (effective Λ) is greater than in FD method. Physically, this is so because the shape function in FE schemes relates the displacement of position (i,j) to the displacement of position $(i+1,j)$ and $(i,j+1)$, which is not the case in FD schemes.

In FE schemes the acceleration derivative terms in eqn 4.1 are replaced with a central difference time approximation similar to eqn 4.6 to obtain the following explicit algorithm

$$\frac{1}{\Delta t^2} M u(t) = F(t-\Delta t) - \left\{ K - \frac{2M}{\Delta t^2} \right\} u(t-\Delta t) - \frac{M}{\Delta t^2} u(t-2\Delta t) \quad (4.16)$$

by using the explicit central difference quotient

$$\frac{\partial^2 u}{\partial t^2} = \frac{u(t+\Delta t) - 2u(t) + u(t-\Delta t)}{\Delta t^2} + o(\Delta t^2) \quad (4.17)$$

where the error in the expansion is of the order of Δt^2 . Because M has to be inverted before solving for $u(t)$ in eqn 4.16 and the consistent mass matrix is not diagonal, the computation requirement for problems with many degrees of freedom becomes very large. Alternatively the consistent mass matrix may be diagonalised and its diagonal elements multiplied by a factor such that

$$M_{II} = \begin{cases} \alpha M_{ij} & \text{if } i=j \\ 0 & \text{if } i \neq j \end{cases} \quad (4.18)$$

where

$$\alpha = \frac{\sum_{i=1}^P \sum_{j=1}^P M_{ij}}{\sum_{i=1}^P M_{ij}} \quad (4.19)$$

and P is the number of element nodes. This produces a diagonal mass matrix such that,

$$[M_{II}]^{-1} = \left[\frac{1}{M_{II}} \right] \quad (4.20)$$

where M_{II} is the diagonalised consistent mass matrix, which replaces the consistent mass terms M_{ij} with its scaled nodal values. Using a consistent mass matrix M_{II} it may readily be shown that eqn 4.16 reduces to

$$u(t) = \mathbf{R} \left\{ \frac{\Delta t^2}{M_{II}} \right\} \quad (4.21)$$

where \mathbf{R} is the effective load vector and is equal to the right hand side of eqn 4.16. The computation can be started with initial conditions $u(0) = 0$ and $u(-\Delta t) = 0$, which implies that the system is dormant before zero time. The disadvantage that only a diagonal mass matrix may be used is generally not of importance because the accuracy of the solution may be improved by refining the finite element mesh. In wave propagation problems the mesh is

generally very refined to ensure that $c_e \geq 0.5\%$ for the slowest wave possible, therefore diagonal mass matrices are almost always applied.

In practice, it is found (see Krieg and Key, 1973) that the lumped mass approximation works well with the finite difference quotient used for the temporal discretization because errors in the temporal and spatial approximations tend to cancel one another out. The advantage of incrementing the FE solution temporally is that the computations may be calculated on an element level. Although more numerical computations are carried using an element by element approach this method is still much more efficient than using the global mass and stiffness matrices if they cannot be held in RAM memory because the model has a large number of degrees of freedom. This is because input-output operation are very slow, typical 20-30 times slower than numerical operations; hence, slow input and output operations should be minimised when the number of degrees of freedom of the problem are large. When all the elements in the mesh are identical, it is more efficient to retain the element mass and stiffness matrices in memory throughout the computations. Using the lumped consistent mass matrix with a central difference temporal scheme thus enables very large FE models to be analysed (see Moore *et al* 1988). In the FE tests reported in this thesis the analysis was carried out at the element level by summing the force contributed from each element to obtain the effective load vector. An explicit time marching procedure was used in all the tests.

4.1.4 Discussion

The FE and FD numerical methods may be used to model stress wave propagation problems. Finite difference algorithms require less storage space than FE algorithms and are considerably faster (in general more than ten times faster). However, the FE methods are more flexible and will easily cope with stress free boundaries, which are common in almost all NDT investigations.

Blake (1988) carried out an extensive comparison study between FE and FD techniques to solve wave propagation problems and showed that the displacement errors when using FE schemes were smaller than when a FD scheme was employed for the same mesh refinement. Intuitively this could be deduced by recognising that the displacement functions in the FD schemes are linear (therefore stress is constant between adjacent nodes), whereas in FE methods the shape function usually is a higher order polynomial; most popular two-dimensional elements used in FE analysis include terms which are a function of the square of the node spacing. This results in linear stress variation throughout the element and the truncation error is hence of the order of the node spacing cubed. Blake also showed that the

critical time step for a regular mesh of two-dimensional elements is greater than in FD schemes, therefore, the solution can be advanced more rapidly (ie the time step is increased); this results in less computation, which reduces rounding errors.

In order to obtain an accurate solution the wavelength per node spacing ratio should be greater than eight. However, too fine a mesh increases the number of arithmetic operations necessary (Δt is reduced and to get to a particular future time there are more intermediate time intervals). This increases the run time unnecessarily while only marginally reducing the predicted velocity error. Excessively refined meshes also increase rounding errors significantly, bearing in mind that the spatial and temporal truncation errors are of the order of the discretization the intervals squared. Therefore, for most applications it is best to use mesh spacing where $8 \leq N \leq 20$ and time steps close to the critical time step t_c .

4.2 Initial test case modelling investigations

4.2.1 Introduction

Initially since in the past most workers have used FD schemes for wave propagation problems the numerical work was attempted using **PR2D**, a commercially available finite difference package. However these results were not satisfactory and following the publication of Blake's thesis, (Blake (1988) which reported detailed comparison tests of the FE and FD methods for bulk and Rayleigh wave propagation and reflection it was decided to carry out a comparison study to verify his results. Crucially, Blake could not obtain stable Rayleigh wave propagation along sloping boundaries using any FD scheme. This led to concern that it might not be possible to obtain satisfactory results with the **PR2D** finite difference code as a high proportion of the nodes in plates are at free boundaries.

Several test cases were run using both **PR2D** and **Finel**, a finite element package developed at Imperial college (Hitchings 1987), where the propagation of pulses and sinusoidal tone bursts in bars and plates, using plane strain models were used as verification and comparison tests of the finite element and finite difference schemes. In each test case the correct velocities were predicted. However, in the FD results there was considerable boundary node instability, whereas the FE results were excellent and indicated that boundary node stability was not a problem when using FE methods. In this respect the results were in agreement with those of Blake's and showed that the surface displacement errors of the FD methods are greater than those of the FE method. Moreover, the source of **PR2D** was not available at Imperial college

and therefore, the implementation of new ideas into the program was not convenient. In contrast, the **Finel** source code was available and this allowed for great flexibility and program development, for example in the method of data input and output. The finite element program **Finel**, was therefore used in all the following numerical studies, principally because of the flexibility of FE methods to deal with different boundary conditions.

In all the FE modelling studies, c_1 and c_2 were the same values used to calculate the dispersion curves of Fig. 2.4 and the density, $\rho = 8000 \text{ kg/m}^3$. Square meshes with a constant distance Λ between nodes were used throughout to avoid spurious reflection from the boundaries between adjoining elements. The time step $\Delta t = \beta(\Lambda/c)$, where $0.8 \leq \beta \leq 0.9$ was used. In order to obtain a phase velocity error c_e of less than 0.5% meshes in which the wavelength per node spacing ratio was kept between 10 and 25 were used throughout.

In the following sections the results of finite element modelling investigations on a 0.5 mm thick steel plate 200 mm long and a 50 mm thick steel block, which was 100 mm long will be presented. These results were used to validate the FE model. Eight noded quadrilateral elements were used, with a 0.5 mm square mesh and the FE predictions of the velocities of propagating waves will be measured by using the time of flight between two points a known distance apart.

4.2.2 Excitation signals

Two excitation signals were used in the initial tests a 5 cycle, 1.0 MHz sinusoidal tone burst modulated temporally by a Hanning window function to limit the bandwidth and a 5 μs duration sine squared pulse. These are shown in Fig. 4.1(a) and (b) respectively. The amplitude spectra derived from (a) and (b) are shown in (c) and (d) respectively, from which it may be seen that smoothly varying the amplitude of the excitation signal in the time domain limits the signal bandwidth.

4.2.3 Finite element results of initial test cases

Steel block results

The steel block extended from $0 \leq x \leq 100$ mm and from $-50 \leq z \leq 50$ mm and a plane strain model was used so it was effectively infinite in the y direction. It was excited by applying the input signal shown in Fig. 4.1(b) in the x direction at the single node at $z = 0$, $x = 0$. The problem was therefore symmetrical about the z axis so only the region $z \geq 0$ was analysed, the nodes at $z = 0$ being fixed in the z direction. A square 0.5 mm mesh was employed. Fig. 4.2 shows the amplitude of strain energy as a function of position 16 μ s after the application of the excitation signal the amplitude being plotted vertically on the 3-D plot. This scale is linear and is not shown for clarity. In Fig. 4.2 the longitudinal, shear and Rayleigh are clearly visible and are marked L, S, and R respectively. Using the position of the wavefronts after a known time interval the group velocities of the longitudinal, shear and Rayleigh wave were calculated as 5.98, 3.28 and 3.03 km/s respectively. In the 3-D plot it may be seen that the amplitude of the Rayleigh wave is greater than the bulk waves, since the energy of the bulk waves spreads out two-dimensionally away from the source. This fact is of importance in seismology where most of the damage caused by earthquakes is caused by the Rayleigh wave.

Steel 'plate' results

A further set of tests was carried out to check the velocity predictions obtained using the FE program on an extremely simple system. This was a 0.5 mm thick steel plate with all the surface nodes pinned in the z direction, the coordinate system being as defined in Fig. 2.3. The 'plate' was therefore effectively infinite in the y and z directions, so simple plane wave propagation could be expected. A 0.5 mm square mesh was used and the plate was excited by applying the signal shown in Fig. 4.1(a) in the x direction to all the nodes at $x = 0$. This should excite the bulk longitudinal wave. Fig. 4.3 shows the response of the top surface of the plate in the x direction at $x = 100$ mm. The shape of the waveform is the same as the input shown in Fig. 4.1(a) indicating that the numerical scheme has not introduced dispersion. Using the time of flight between the two monitored points the group velocity was calculated as 5.98 km/s.

The model was then amended by releasing the surface nodes in the z direction and pinning them in the x direction. This should allow a pure shear wave to propagate along the 'plate'. A

z direction displacement of the form shown in Fig. 4.1(a) was applied to each of the nodes at $x = 0$ and the resulting predicted waveform at $x = 100$ mm is shown in Fig. 4.4. Again, no dispersion is evident and using the time of flight between the two monitored points the group velocity was calculated as 3.28 km/s.

In all the above cases, the FE predictions are excellent and the velocities differed from the theoretically predicted ones by less than 0.5% confirming the applicability of the finite element program FINEL.

4.3 Initial modelling of Lamb wave propagation

The modelling ultrasonic Lamb waves is problematic because,

- Dispersion is always present
- Gross dispersion is present near cut-off frequencies
- More than one mode always exists
- The velocity of a_0 may be less than the Rayleigh wave velocity
- The through-thickness deflected shape is a function of the frequency-thickness product (see, Fig. 2.7(a) to (f))

The velocity of the longitudinal velocity (c_1), which is the fastest wave that can be propagated in the plate, controls the computational time step that must be chosen so that a disturbance cannot propagate through a grid spacing in under one time step, while the lowest phase velocity, and hence the shortest wavelength, sets the maximum permissible grid spacing that must be chosen so that spatial aliasing due to the finite element discretization does not occur. It is adequate to keep the nodes per wavelength ratio between 10 and 25 to obtain errors in the predicted velocity of less than 0.5%

Selective excitation of a single Lamb wave is in general not straightforward, because of the reasons given above. In the results reported in this section an individual Lamb wave was launched from the edge of the plate at $x = 0$ by applying the 5 cycle 1.0 MHz tone burst, modulated by a Hanning window function to limit the bandwidth, which was shown in Fig. 4.1(a). The amplitude of the x and z displacement components at each node on the plate edge was given by the through thickness deflected shape calculated for the required mode from eqns 2.54 and 2.55, at the frequency-thickness product corresponding to the plate thickness and the centre frequency of the tone burst. When the 2-D FFT method was used to compute the properties of the propagating Lamb waves the time history of the response in the z

direction on the plate surface at 64 equally spaced points in the x direction was recorded. In all the studies the sampling frequency was 10 MHz.

In this section the results of finite element modelling investigations on 0.5 mm, 2.0 mm and 3.0 mm steel plates will be presented. These results will be used in particular to show how the 2-D FFT method may be used to quantitatively analyze Lamb wave signals. In all the following FE investigations the boundary nodes were free.

4.3.1 Results of the initial modelling of propagating Lamb waves

Fig. 4.5(a) shows the normalised time histories of the response of the top surface of the 0.5 mm thick plate in the x direction at $x = 100$ mm, when the form of the input signal at $x = 0$ was shown in Fig. 4.1(a) and was appropriate to excite only the s_0 mode. The shape of response signal indicates that the propagating wave is almost nondispersive, and the group velocity was calculated as 5.44 km/s using the time of flight between the two monitored points. Fig. 4.5(b) shows the result of carrying out a two-dimensional Fourier transform on the 64 monitored time histories between $x = 100$ mm and $x = 163$ mm when the spatial sampling interval was 1.0 mm. The 2-D FFT results are presented in the form of a three-dimensional plot of amplitude versus frequency and wavenumber. The amplitude scale is linear and the units are arbitrary. (This scale is not shown to improve the clarity of the plot.) At each frequency, the amplitude is only significant at a single wavenumber, indicating that only one mode, in this case, s_0 , is present. The amplitude reaches a maximum at a frequency of 1.0 MHz which is the centre frequency of the excitation tone burst. A comparison of the 2-D FFT results and the theoretically predicted wavenumber dispersion curve for s_0 is shown in Fig. 4.6. The numerical results are represented by squares and are the wavenumber-frequency points at which the amplitudes in Fig. 4.5(b) are a maximum. The agreement is seen to be very good, the maximum error in wavenumber being less than 0.5%.

Fig. 4.7(a) shows the normalised time history of the response of the top surface of the 2.0 mm thick plate in the x direction at $x = 100$ mm, when the form of the input signal at $x = 0$ was shown in Fig. 4.1(a) and was appropriate to excite only s_0 . The response of the plate at $x = 100$ mm shows that the propagating wave is grossly dispersive. Using the time of flight of the arrival of the leading edge of Fig. 4.7(a) the maximum group velocity was calculated as 5.1 km/s. It may be seen that the duration of the response signal has been increased significantly by dispersion and it is difficult to determine if more than one propagating mode is present. However it may be seen that the lower frequency components of the response are at the front of the signal, indicating that their group velocities are higher (see Fig. 2.6 s_0 curve).

Fig. 4.7(b) shows the normalised three-dimensional view of the amplitude wavenumber-frequency information, which was obtained by carrying out a two-dimensional Fourier transformation of the time histories of 64 equally spaced points from $x = 0$ to $x = 63$ mm for the case shown in Fig. 4.7(a). The maximum amplitude of the response of the plate is at 1.0 MHz, which is the centre frequency of the excitation tone burst. At each discrete frequency in Fig. 4.6(b) the amplitude reaches a maximum at only one wavenumber which corresponds to the s_0 mode, showing that it is the only propagating Lamb wave.

The FE model of the 3.0 mm plate was 125 mm long. The input at $x = 0$ was of the form shown in Fig. 4.1(a), and was appropriate to excite a_0 . Fig. 4.8(a) shows the amplitudes of the applied displacements used to launch a_0 . The normalised time history of the response at $x = 50$ mm is shown in Fig. 4.9(a). The shape of the response is very similar to the excitation signal shown in Fig. 4.1(a). This indicates that a_0 is essentially nondispersive at this frequency-thickness value and the maximum group velocity measured from the leading edge of the signal was 3.27 km/s. Fig. 4.9(b) shows the normalised three-dimensional view of the amplitude wavenumber-frequency information, which was obtained by carrying out a two-dimensional Fourier transformation of the time histories of 64 equally spaced points from $x = 30$ mm to $x = 67.8$ mm. The maximum amplitude of the response of the plate is at 1.0 MHz, which is the centre frequency of the excitation tone burst. At each discrete frequency in Fig. 4.9(b) the amplitude reaches a maximum at the wavenumber corresponding to a_1 and a_0 . However, at the centre frequency of the excitation the response is almost pure a_0 and throughout the frequency-thickness range the amplitude of the a_0 mode dominates the response of the plate, the amplitude of the a_1 mode being less than 2% of the a_0 mode. Fig. 4.10 shows a comparison of the 2-D FFT results and the theoretically predicted wavenumber dispersion curve, where the numerical results obtained from Fig. 4.9(b) relating to the a_0 mode are represented by circles (the points relating to a_1 were obtained in a later test). The agreement with the theoretical curve is excellent, the maximum error in wavenumber being less than 0.5%.

The finite element model of the 3.0 mm thick plate when a_1 was launched at $x = 0$ was 125 mm long and the spatial sampling interval was 0.6 mm. Fig. 4.8(b) shows the amplitudes of the applied displacements used to launch a_1 at $x = 0$. Again the input at $x = 0$ was a 5 cycle 1.0 MHz tone burst of the form shown in Fig. 4.1(a). The normalised time history of the response at $x = 50$ mm is shown in Fig. 4.11(a), from which the maximum group velocity measured from the leading edge of the signal is 3.84 km/s. The time history of the response of the plate to the excitation at $x = 0$ changes shape as the wave packet propagates from $x = 0$ to $x = 50$ mm (see Fig. 4.1(a)), indicating that if the only propagating mode is a_1 , then it is dispersive. Fig. 4.11(b) shows the results of carrying out a two-dimensional Fourier transform on the time histories of 64 equally spaced points between $x = 30$ mm and $x = 67.8$

mm. Again, the maximum amplitude of the response of the plate is at 1.0 MHz, the centre frequency of the excitation tone burst. At each discrete frequency in Fig. 4.11(b), the maximum amplitude is seen at the wavenumbers corresponding to a_1 and a_0 , but in this case the response is dominated by the a_1 mode, the amplitude of the a_0 mode being always less than 2% of a_1 . Fig. 4.10 shows the comparison between the 2-D FFT results and the theoretically predicted wavenumber dispersion curve, where the numerical results obtained from Fig. 4.11(b) relating to the a_1 mode are represented by squares. Again the agreement with the theoretical curve is excellent, the maximum error in wavenumber being less than 0.5%.

The finite element model of the 3.0 mm thick plate when a_0 and a_1 were launched at $x = 0$ was 125 mm long and the spatial sampling interval was 0.6 mm. The modes were launched by superposing the displacement components shown in Fig. 4.8(a) and (b), and using the method of excitation discussed above. Fig. 4.12(a) shows the normalised time history in the z direction of the response at the surface of the plate at $x = 50$ mm. Again the input at $x = 0$ was a 5 cycle 1.0 MHz tone burst of the form shown in Fig. 4.1(a). The maximum group velocity measured from the leading edge of Fig. 4.12(a) was 3.84 km/s, the group velocity of a_1 . Fig. 4.12(b) shows the results of carrying out a two-dimensional Fourier transform on the time histories of 64 equally spaced points between $x = 30$ mm and $x = 67.8$ mm. Again, the maximum amplitude of the response of the plate is at 1.0 MHz, the centre frequency of the excitation tone burst. At each discrete frequency in Fig. 4.12(b) there are two distinct wavenumbers at which the amplitude is a maximum. These correspond to a_0 and a_1 . Hence, there are two propagating modes and their relative amplitudes on the surface in the z direction at 3.0 MHzmm was 1:0.65, the ratio of the two components of the displacements on the surface of the a_0 and a_1 modes respectively. Fig. 4.12(c) was obtained from Fig. 4.12(b) and shows the relative surface amplitudes in the z direction of the two modes a_0 and a_1 as a function of the frequency-thickness product, from which it may be seen that the relative amplitudes are a strong function of the frequency-thickness product. At each frequency-thickness value in Fig. 4.12(c) the ratio of the two amplitudes is in good agreement (less than 2% difference) with the theoretically predicted ratios calculated using eqns 2.54 and 2.55.

The FE results have shown that the 2-D FFT method may be used to measure both the velocity *and* the amplitude of propagating Lamb waves when more than one mode is present and the 2-D FFT method has been used to determine mode purity very accurately in FE modelling studies.

4.4 Further modelling of propagating Lamb waves

Careful inspection of the three-dimensional plots shown in Fig. 4.9(b) and Fig. 4.11(b) reveals that the modes were only pure at the centre frequency of the imposed excitation signal. This is to be expected as the imposed displacement deflected shapes shown in Fig. 4.8(a) and (b) were correct only at 3.0 MHzmm and as may be deduced from eqns 2.54 and 2.55 the mode shapes are slightly different either side of this frequency-thickness product. Hence, the frequency dependence of the mode shapes means that excitation signals of the form shown in Fig. 4.1(a) will generally excite more than one mode away from their centre frequencies. Pure a_0 and s_0 modes may be excited at frequency-thickness products below the frequency thickness products of the first non-zero propagating modes a_1 and s_1 respectively if the input signal is symmetric in the x direction and antisymmetric in the z direction for s_0 and vice versa for a_0 .

In order to excite a pure Lamb wave two conditions have to be simultaneously satisfied. Firstly, the frequency of the harmonic excitation signal must be identical to the Lamb wave frequency being excited and secondly, the variation of the excitation with z at the excitation position ($x = 0$ in the tests reported here) must correspond to the exact mode shape of the Lamb wave being excited. Assuming a single frequency input, the required excitation $f(z,t)$ is of the form

$$f(z,t) = \Phi(z) e^{i\omega t} \quad (4.22)$$

and $\Phi(z) = [u,w]^t$ may be calculated from eqns 2.54 and 2.55.

However, in almost all modelling applications single frequency excitation is not desirable or possible, for example in explicit time marching FE methods the duration of the input signal has to be finite. It is therefore very advantageous to be able to excite single modes with a wideband excitation signal $f(t)$. This can be achieved by summing the required inputs over a range of frequencies. For a single frequency component ω_j , the required input is

$$f_j(z,t) = \Phi_j(z) e^{i\omega_j t} \quad (4.23)$$

If all the significant energy components in the excitation signal are over a range of frequencies from $j = 1$ to k then

$$f(z,t) = \sum_{j=1}^{j=k} \Phi_j(z) A_j e^{i\omega_j t} \quad (4.24)$$

where,

$$\sum_{j=1}^{j=k} A_j = A(\omega) = \int_{-\infty}^{\infty} f(t) e^{-i\omega t} dt \quad (4.25)$$

Here, $A(\omega)$ is the complex amplitude of the Fourier transformation of the excitation signal $f(t)$, where in the tests reported here $f(t)$ was a tone burst modified by a Hanning window. Fig. 4.13(a) to (f) were calculated using eqn 2.24 and show the x and z direction deflected shape time histories of the a_0 mode, when $f(t)$ was the 5 cycle 1.0 MHz tone burst shown in Fig. 4.1(a), and the time histories are for $z/2d = 0, 0.5, \text{ and } 1.0$ respectively.

The finite element model of the 3.0 mm thick plate was 125 mm long, the spatial sampling interval was 0.6 mm and the input signal corresponded to the time histories shown in Fig. 4.13. The time history of the response at the surface of the plate in the z direction at $x = 50$ mm is shown in Fig. 4.14(a), from which the maximum group velocity was 3.27 km/s. The time history of the response of the plate to the excitation at $x = 0$ is almost the same as the response shown in Fig. 4.9(a) apart from the fact that in this case the amplitude has not been normalised to a maximum of 1.0. It may be seen that shape of the wave packet is almost unchanged from $x = 0$ to $x = 50$ mm (see Fig. 4.13(d)), indicating that if the only propagating mode is a_0 , then it is nondispersive. Fig. 4.14(b) shows the results of carrying out a two-dimensional Fourier transform on the time histories of 64 equally spaced points between $x = 30$ mm and $x = 67.8$ mm. Again, the maximum amplitude of the response of the plate is at 1.0 MHz, the centre frequency of the excitation tone burst. At each discrete frequency in Fig. 4.14(b), the maximum amplitude is seen at the wavenumber corresponding to a_0 , and in contrast to Fig. 4.9(b) no other maximum is seen, indicating that a_0 is the only propagating mode. The amplitude of the a_0 mode is over 40 dB above the 'noise floor' in Fig. 4.14(b) over the full bandwidth of the excitation signal, which was from 0.65 to 1.35 MHz (20 dB down points from the centre frequency of 1.0 MHz). Since no other modes are present in Fig. 4.14(b), it shows that in numerical studies, pure Lamb waves may be launched successfully in frequency-thickness regions where many modes with complicated mode shapes exist. This is of great importance in NDT, where for example, the sensitivity of individual Lamb waves to different defects may be studied separately. This method of exciting Lamb waves in the numerical investigation was hence adopted in all the FE investigations that follow.

4.5 The modelling of Lamb wave reflection from the free end of a plate

The finite element models used in the investigation of Lamb wave reflection from the free end of the plate were 3.0 mm thick and the material properties were the same as in the previous finite element studies. In the results reported below the 2-D FFT method will be used to quantitatively measure the amplitudes of Lamb waves after reflection from plane and stepped edges of plates.

4.5.1 Results of Lamb wave reflection from the plane edge of a plate

In any real plate a propagating wave will strike an edge, where the boundary conditions must be satisfied. The simplest case is that of a single Lamb wave propagating in a semi-infinite plate incident on the free end of the plate, the end being normal to the upper and lower plate surfaces. From eqns 2.56 and 2.57, σ_{xx} and σ_{zz} are even functions of k_s whereas σ_{xz} is an odd function; therefore, a simple reflection of the incident wave (corresponding to a change in sign of k_s) will not satisfy the zero stress boundary conditions. Therefore, all the propagating (real roots of the Rayleigh-Lamb equation) and the nonpropagating modes (imaginary or complex roots of the Rayleigh-Lamb equation) have to be considered and the acoustic energy of the incident mode will in general be divided between all the possible propagating modes. From the displacement equations, w_s is an odd function of z and w_a is an even function, therefore on reflection a symmetric mode cannot be mode converted to an antisymmetric mode and vice versa. For all modes, when $c = 2\sqrt{c_2}$, the Lamb wave degenerates to the Lamé wave, which only has one component of stress, and is therefore totally reflected at the free edge.

Gazis and Mindlin (1960) were the first to consider the nonpropagating modes in their theoretical analysis of the reflection of the first propagating symmetric mode. Auld and Tsao (1977) used the variational principle to obtain upper and lower bound solutions and more recently Zhang *et al* (1988) have used the principle of least squares in a series expansion to calculate the reflection coefficients of Lamb waves from the edge of a plate.

The theoretical analysis derived by Torvik (1967) was used to calculate the theoretical results presented here. In his analysis, solutions to the Rayleigh-Lamb equations (propagating and nonpropagating Lamb modes) are used as elements of an expansion, in which the modes are combined to satisfy the normal and shear stress boundary conditions. This allows the stress and displacements within the plate to be determined.

It was decided to study the reflection of the a_0 and a_1 modes from the free end of a plate when the frequency-thickness value was between the cut-off values of a_1 and a_2 . Fig. 4.15(a) shows the ratio of the energy in a_0 and a_1 in the signal reflected from the end of the plate to that of the energy in the incident wave when this was a pure a_0 mode. Fig. 4.15(b) shows the corresponding plot when the incident wave was a pure a_1 mode. The theoretically calculated points are represented by a continuous line and illustrate the reciprocal nature of the energy reflection coefficients of propagating Lamb waves.

Fig. 4.16(a) shows the normalised time history of the response of a 125 mm long finite element model at $x = 50$ mm, when the input at $x = 0$ was appropriate to excite only a_0 . The duration of the test was long enough to include the response of the plate after reflection from the end of the plate. When $t \leq 40 \mu\text{s}$ the response is identical to that of Fig. 4.14(a), a_0 is essentially nondispersive and the maximum group velocity is 3.27 km/s. On reflection from the end of the plate ($t \geq 40 \mu\text{s}$) more than one propagating mode is present (a_0 is mode converted), but the modes are superimposed and their amplitudes cannot be determined from the time history of the response of the plate. Fig. 4.16(b) shows the result of carrying out a two-dimensional Fourier transform on the time histories of the 64 equally spaced positions from $x = 30$ mm to $x = 67.8$ mm, when the incident signal ($t \leq 40 \mu\text{s}$) was gated out. The maximum amplitude of the response of the plate is at 1.0 MHz, which is the centre frequency of the excitation tone burst. However, at each discrete frequency in Fig. 4.16(b) there are two distinct wavenumbers at which the amplitude is a maximum. These correspond to a_0 and a_1 . Hence, there are two propagating modes and the amplitudes of the two modes are a function of frequency.

The amplitudes of a_0 and a_1 , seen in Fig. 4.16(b) depend not only on the reflection coefficients of the waves at the end of the plate, but also on the frequency content of the excitation tone burst and on the amplitude of the z component of the deflected shape compared with the x component (only the z component is monitored). In order to be able to compare these results with analytically calculated reflection coefficients, it is necessary to normalise the amplitudes by dividing by the theoretically calculated z component at the surface. The reflection coefficients are then obtained in the normal way by dividing the response by the input. In Fig. 4.15(a) the amplitude of the relative energies in the two modes calculated from the data of Fig. 4.16(b) is represented by squares. The agreement between the numerical results and theoretical predictions obtained using the theoretical approach described by Torvik (1967) are excellent, the maximum difference being less than 2%.

Fig. 4.17 shows the normalised time history of the response of a 125 mm long finite element model at $x = 50$ mm, when the input at $x = 0$ was appropriate to excite only a_1 . The duration

of the test was long enough to include the response of the plate after reflection from the end of the plate. When $t \leq 40 \mu\text{s}$ the response is almost identical to that of Fig. 4.11(a), a_1 being dispersive with a maximum group velocity of 3.84 km/s. On reflection from the end of the plate ($t \geq 40 \mu\text{s}$) a_1 is mode converted and more than one propagating mode is present after reflection. Again the modes are superimposed and their amplitudes cannot be determined from the time history of the response of the plate. The amplitude of the relative energies in the two modes represented in Fig. 4.15(b) by squares was calculated by carrying out a two-dimensional Fourier transformation of the time histories of the 64 equally spaced positions from $x = 30 \text{ mm}$ and $x = 67.8 \text{ mm}$, when the incident signal ($t \leq 40 \mu\text{s}$ in Fig. 4.17) was gated out. Again, the agreement with the theoretical curve is excellent.

The FE and theoretical results illustrate the reciprocal nature of the energy partition of propagating Lamb waves on reflection from a plane edge. For example, when a_0 is incident at a frequency-thickness product of 2.5 MHzmm the fraction of energy in the a_0 mode after reflection is 0.18 and that in a_1 is 0.82; If a_1 is incident, the fraction of the energy in a_0 and a_1 is 0.82 and 0.18 respectively.

4.5.2 Results of Lamb wave reflection from a stepped edge in a plate

A 1.0 mm thick plate 126 mm long was used in all the finite element tests reported in this section. The geometry of the symmetric and non-symmetric (with respect to the middle of the plate), steps at the end of the plate at $x = 120 \text{ mm}$ are shown in Fig. 4.18(a) and (b), where the length of the step $L = 6 \text{ mm} \approx \lambda_1$, the wavelength of the longitudinal wave, c_1 . In all the tests reported in this section the input at $x = 0$ was appropriate to excite only s_0 , the sampling frequency was 10 MHz and the sampling interval was 0.625 mm.

Fig. 4.19(a) and (b) show the normalised time history of the response of the plate in the x direction at $x = 75 \text{ mm}$ and 95 mm respectively, The duration of the test was long enough to include the response of the plate after reflection from the symmetrical step shown in Fig. 4.18(a) located at the end of the plate. When $t \leq 26 \mu\text{s}$ the response is that of s_0 only. On reflection from the end of the plate, $t \geq 26 \mu\text{s}$, the signal is complicated and the identity of the mode(s) present cannot be determined solely from the time history of the response of the plate at one position. Fig. 4.20(a) shows the result of carrying out a two-dimensional Fourier transform of the time histories of 32 equally spaced positions from $x = 75 \text{ mm}$ to $x = 95 \text{ mm}$, when the incident signal ($t \leq 26 \mu\text{s}$) was gated out. The maximum amplitude of the response of the plate is at 1.0 MHz, which is the centre frequency of the excitation tone burst and at each discrete frequency in Fig. 4.20(a) there is one wavenumber at which the amplitude is a

maximum. This corresponds to s_0 , confirming that, as expected, on reflection from a symmetric step, no mode conversion between s_0 and a_0 occurs. Therefore, from Fig. 4.19(a) and (b) it may be seen that the two superimposed disturbances, are travelling at the same velocity because the shape of the reflected wave packet does not change, and are both the s_0 mode, reflected from the shoulder of the step and the free end. Fig. 4.20(b) shows the reflection coefficient of the s_0 mode, plotted as a function of the frequency-thickness product and was obtained in the normal way by dividing the response 2-D FFT by the input 2-D FFT. This is unity at all frequencies confirming that the signal is totally reflected and no mode conversion has occurred.

Fig. 4.21(a) and (b) shows the normalised time history of the response of the plate in the x direction at $x = 75$ mm and 90 mm respectively, when the input at $x = 0$ was appropriate to excite only s_0 . The duration of the test was long enough to include the response of the plate after reflection from the step shown in Fig. 4.18(b), located at the end of the plate. When $t \leq 26 \mu\text{s}$ the response is that of s_0 only. On reflection from the end of the plate, $t \geq 26 \mu\text{s}$, the signal is again more complicated. By comparing the responses shown in Fig. 4.21(a) and (b) it may be seen that the two superimposed disturbances are travelling at different velocities because the shape of the reflected wave packet changes, and are therefore s_0 and a_0 , a_0 being caused by mode conversion at the end of the plate when s_0 interacted with the step. Fig. 4.22 shows the result of carrying out a two-dimensional Fourier transform of the time histories of 64 equally spaced positions from $x = 75$ mm to $x = 95$ mm, when the incident signal ($t \leq 26 \mu\text{s}$) was gated out. The maximum amplitude of the response of the plate is at 1.0 MHz, which is the centre frequency of the excitation tone burst and at each discrete frequency in Fig. 4.22 there are two wavenumbers at which the amplitude is a maximum. This correspond to s_0 and a_0 hence, on reflection from a non-symmetric step, there is in general mode conversion between s_0 and a_0 , in which the relative amplitudes of the two modes is strongly frequency-thickness dependent.

4.6 Conclusions

Both FD and FE schemes may be used to model stress wave propagation problems accurately. However, FE methods are more accurate and flexible and most importantly free boundaries are readily accommodated by FE schemes, whereas in the FD 'body node' formulations special boundary node routines have to be incorporated to deal with free surfaces. Blake (1988) has shown that even with some of the most sophisticated boundary node routines FD schemes still exhibited numerical stability problems coping with models of Rayleigh waves

propagating along sloping boundaries. As numerical models of plates have a high proportion of surface nodes FE schemes are preferred.

A finite element scheme using an explicit central difference temporal discretization scheme and a diagonal mass matrix was employed in all the numerical tests, enabling large FE models to be solved using an element by element approach. Wavelength per node spacing ratios of between 8 and 20 gave results in which the predicted velocity error was always less than 0.5%, which was accurate enough for the purposes of this investigation.

The 2-D FFT method can be used to measure the amplitudes and velocities of Lamb waves over a wide range of frequencies and phase velocities in a single test. It has been shown in a number of FE tests that this technique may be used when there is multi-mode propagation and/or dispersion.

A method has been developed to excite a single Lamb mode in FE investigations using broadband input signals. This is important as it will facilitate the modelling of the interaction of individual modes with defects in NDT application. This will allow Lamb wave interactions with defects to be investigated quantitatively.

The reflection of Lamb waves reflected from plane and stepped edge was modelled successfully using the finite element method. Quantitative results of the amplitude of the reflected waves were obtained using the 2-D FFT method.

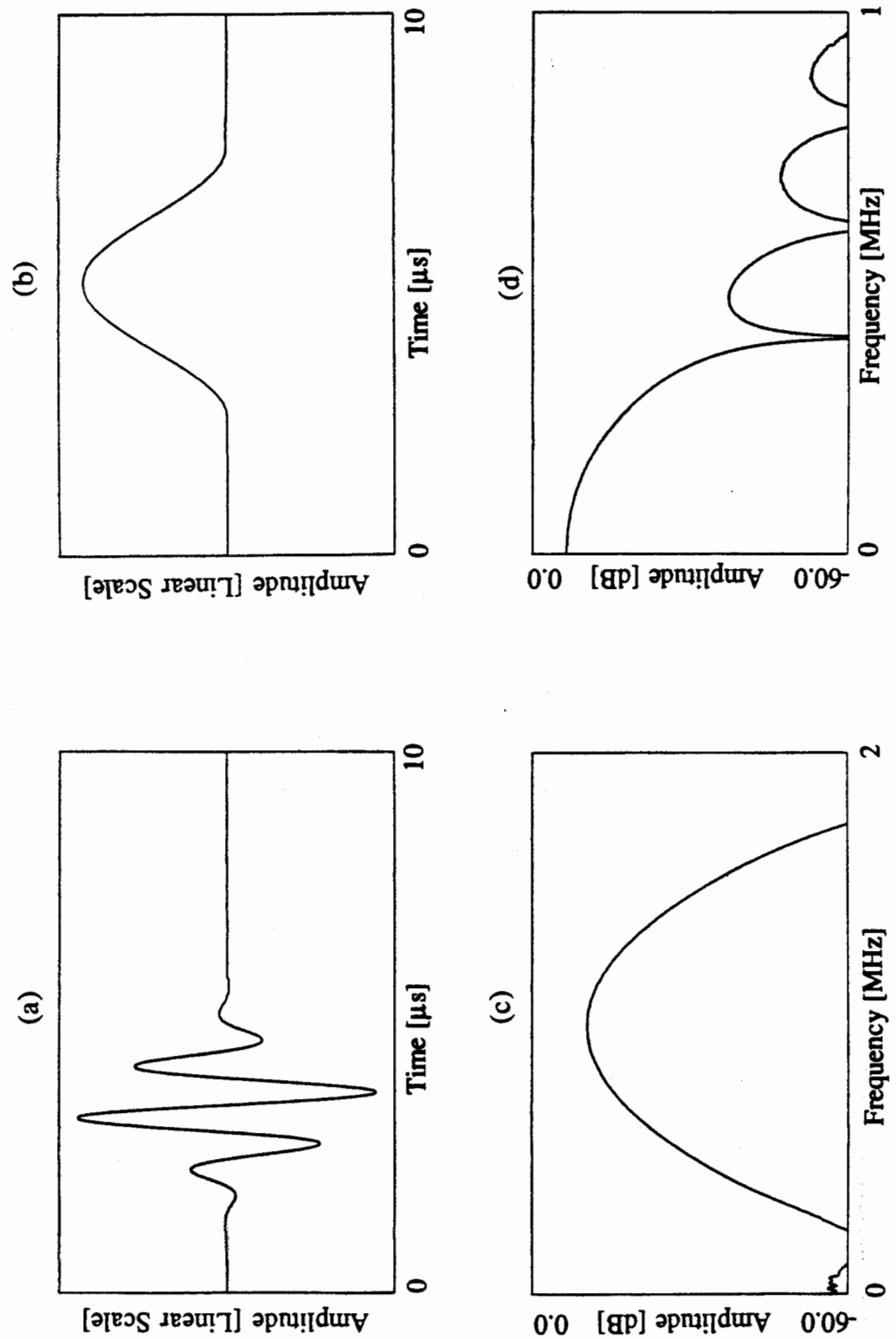


Figure 4.1 (a) Time history of the 5 cycle 1 MHz tone burst used in the numerical tests. (b) Time history of the 5 μs duration sine squared pulse used in the numerical test. (c) Amplitude spectrum of the time history shown in (a). (d) Amplitude spectrum of the time history shown in (b).

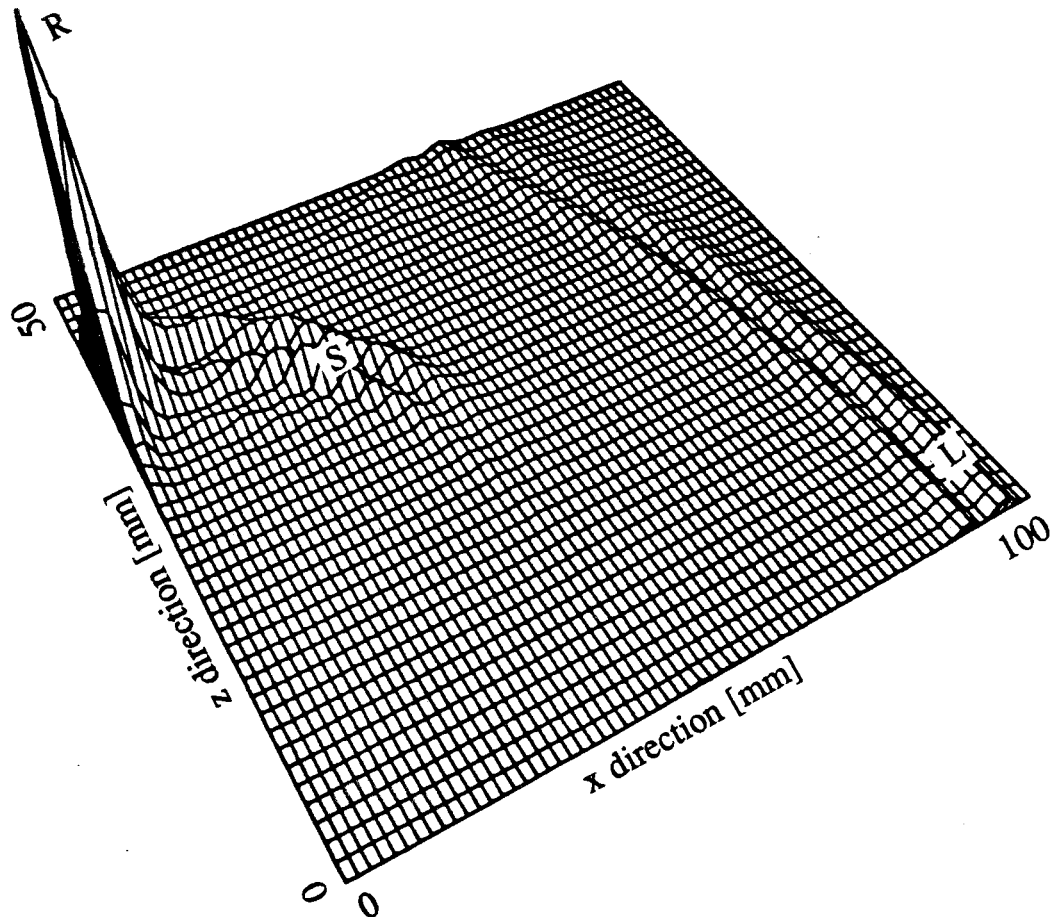


Figure 4.2 Normalised 3-D plot of a snapshot of strain energy distribution in a steel block as a function of position $16 \mu\text{s}$ after the application of the sine squared pulse at the origin. The vertical (energy) scale is linear and is not shown to improve the clarity of the plot.

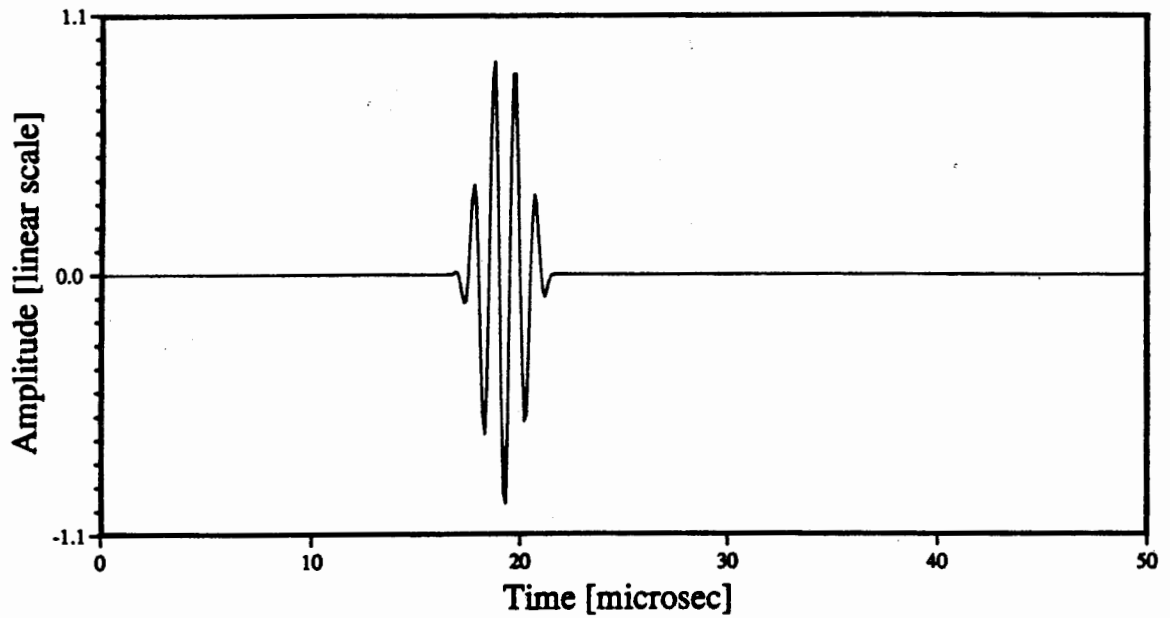


Figure 4.3 Predicted time history at $x = 100$ mm, when the input at $x = 0$ was designed to excite only the longitudinal wave c_1 .

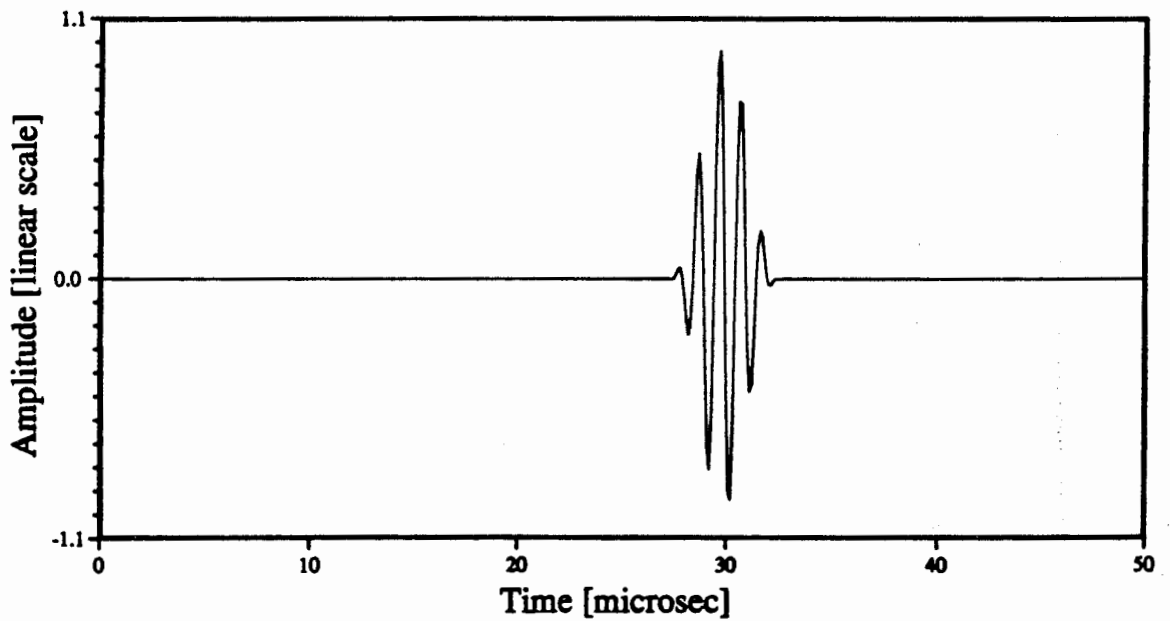


Figure 4.4 Predicted time history at $x = 100$ mm, when the input at $x = 0$ was designed to excite only the shear wave c_2 .

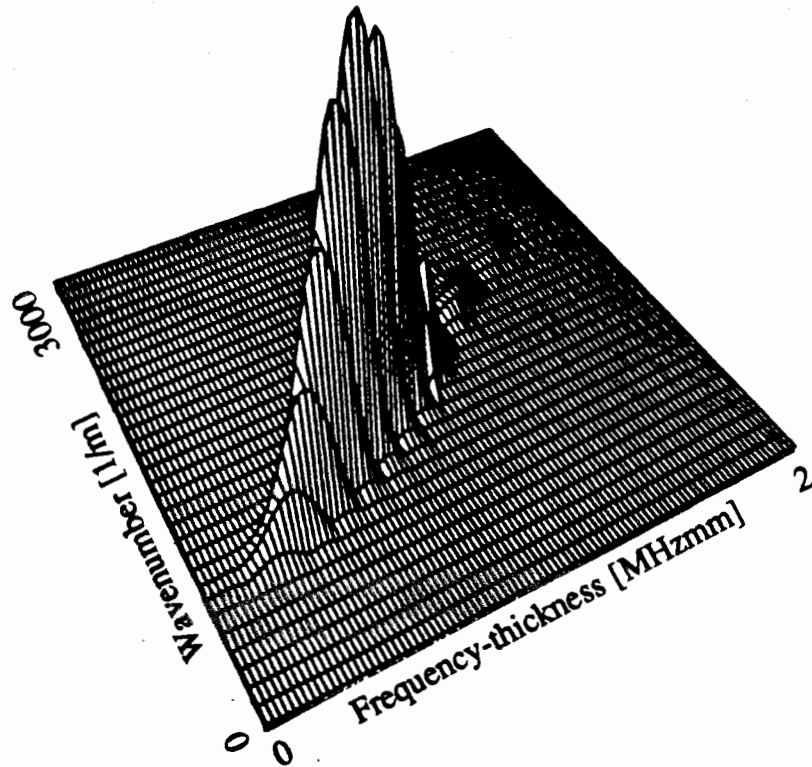
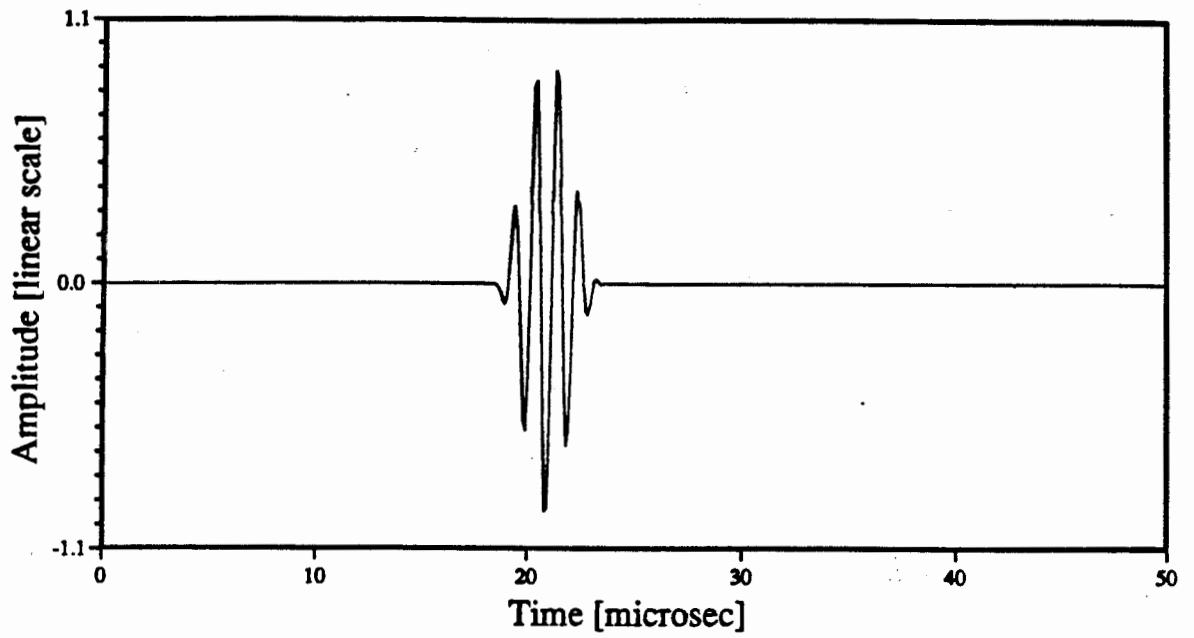


Figure 4.5 (a) Predicted time history at $x = 100$ mm in a 0.5 mm thick plate when the input at $x = 0$ was designed to excite only s_0 . (b) Normalised 3-D plot of the 2-D FFT results of the case given in (a), showing a single propagating mode, s_0 .

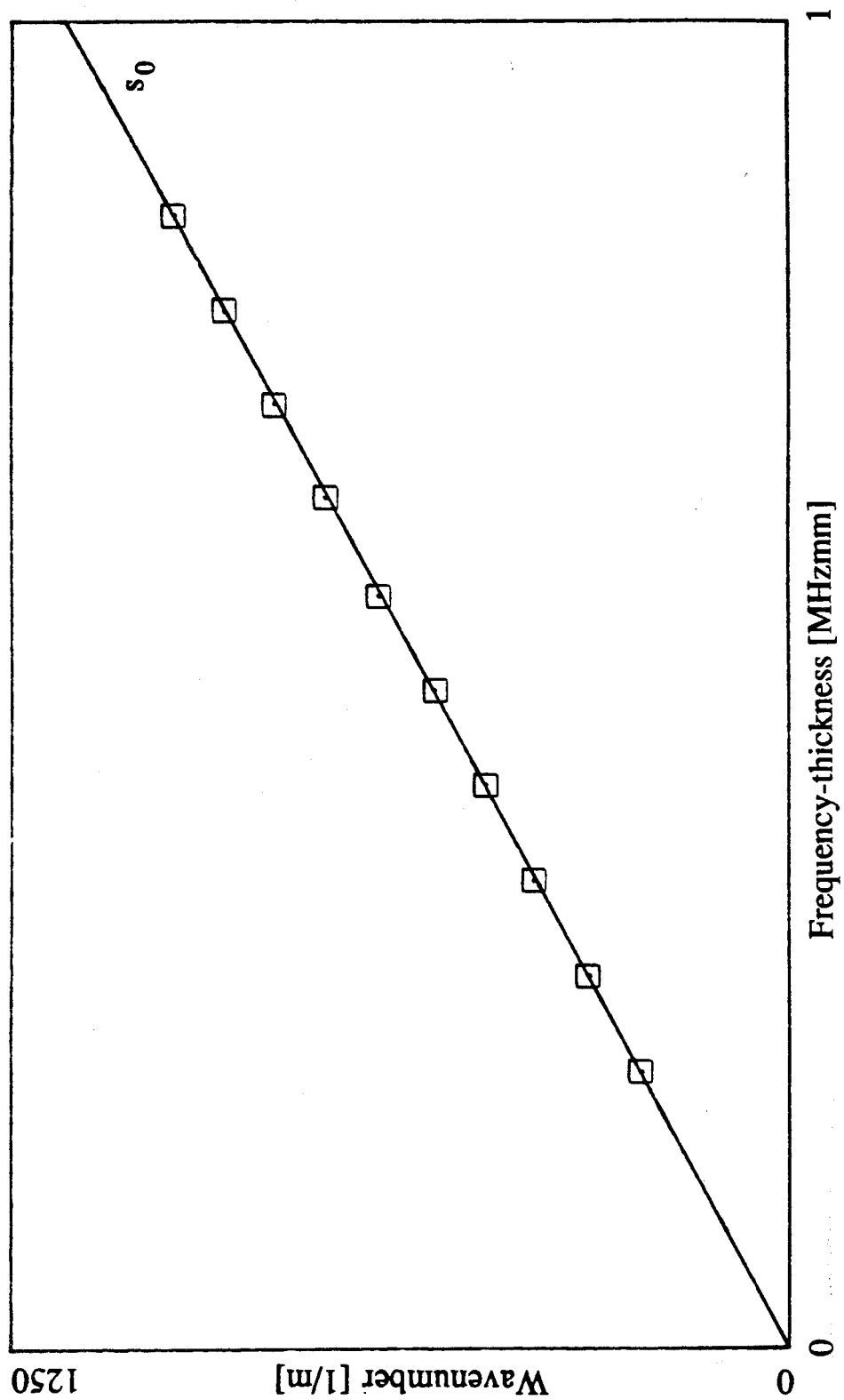


Figure 4.6 A comparison of the finite element predictions with the analytically generated dispersion curves for s_0 : — analytical predictions; \square finite element predictions.

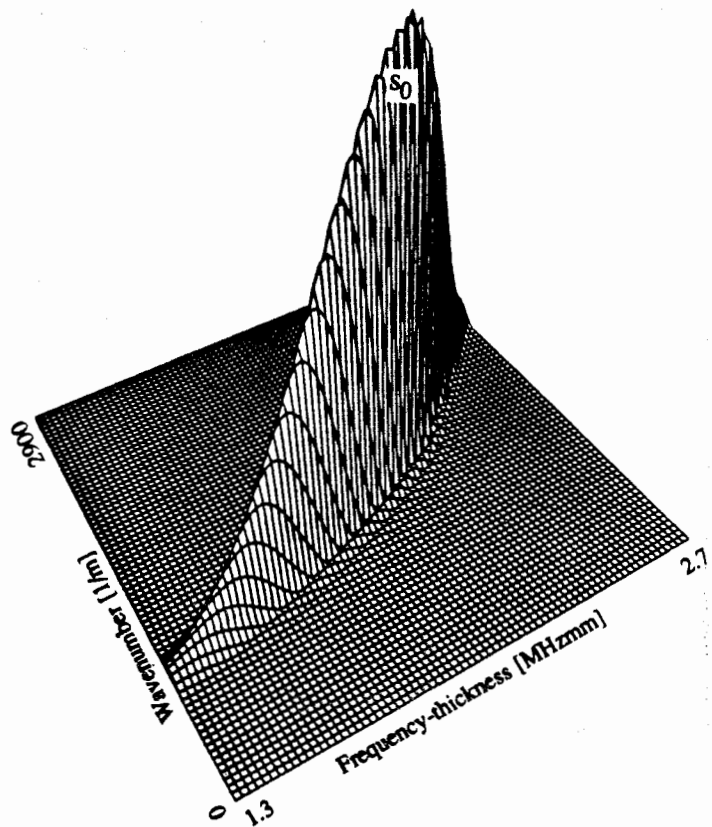
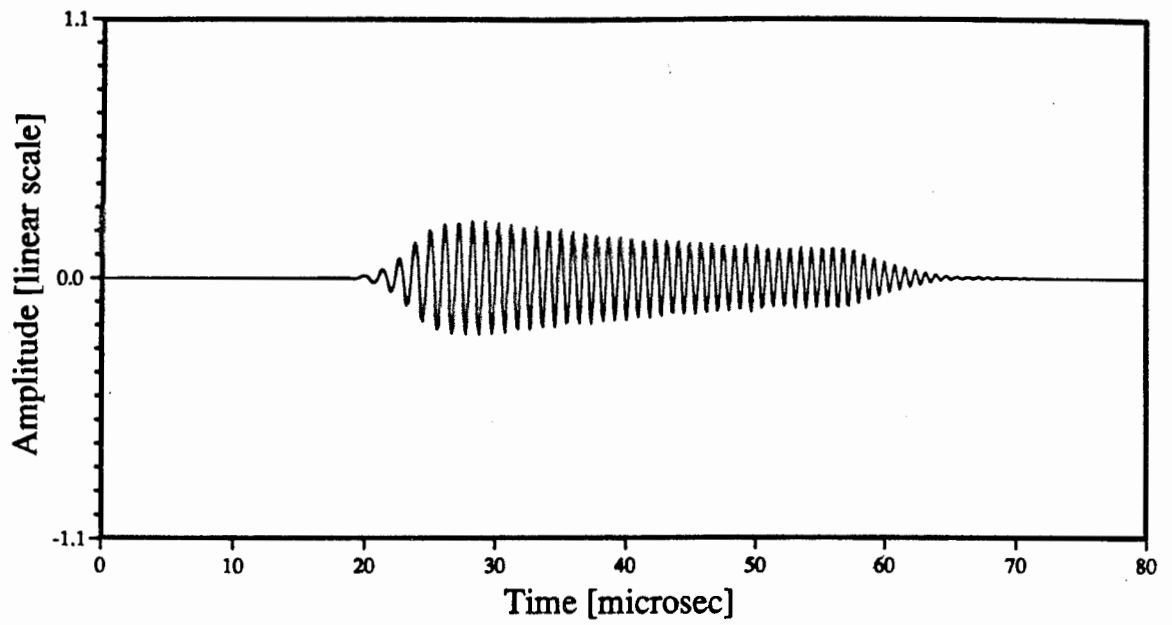


Figure 4.7 (a) Predicted time history at $x = 100$ mm in a 2.0 mm thick plate when the input at $x = 0$ was designed to excite only s_0 . (b) Normalised 3-D plot of the 2-D FFT results of the case given in (a), showing a single propagating mode, s_0 .

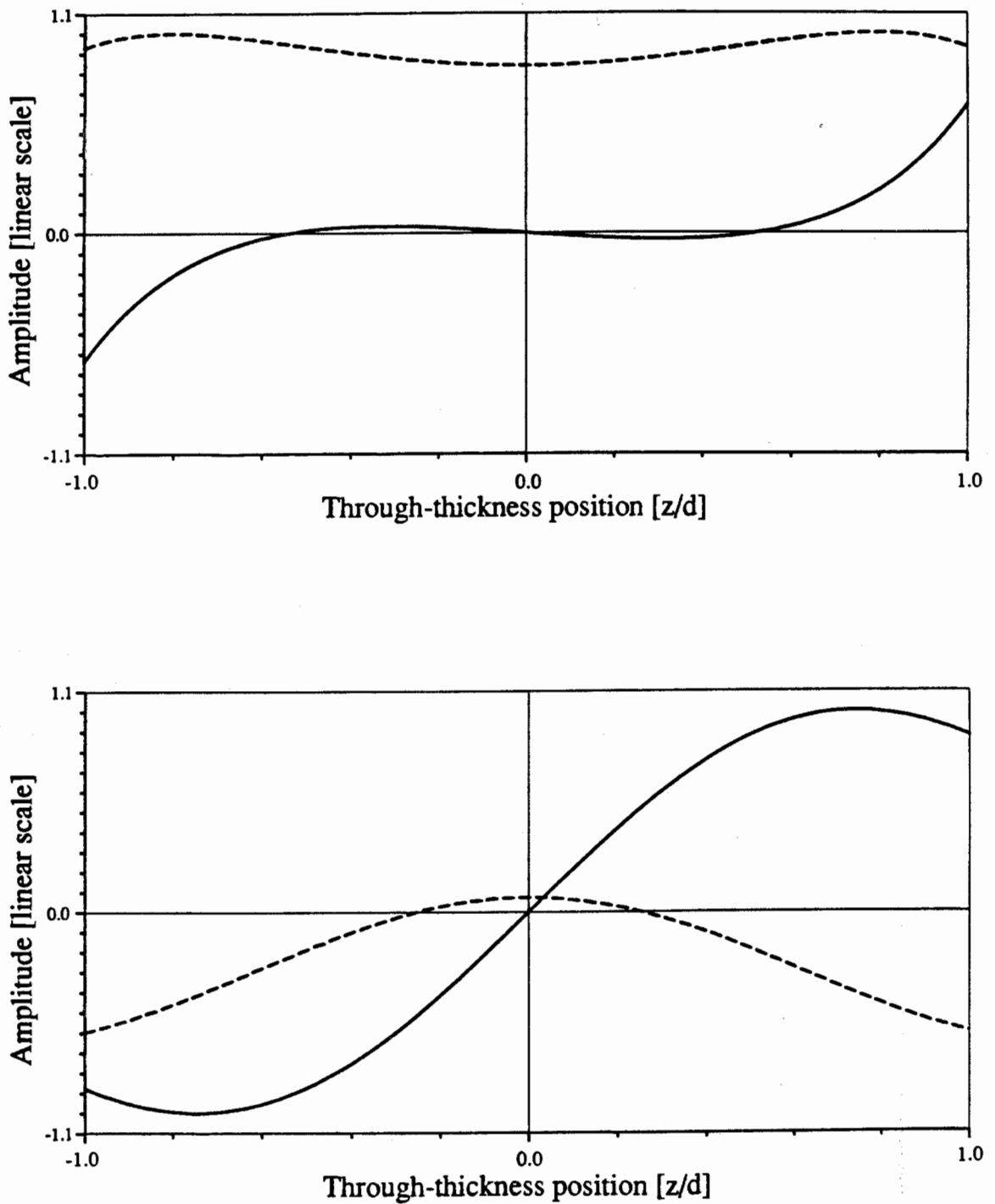


Figure 4.8 The through-thickness deflected mode shapes of Lamb waves, where c_1 and c_2 are the same as in figure 2.4: — x direction displacements; - - - - z direction displacements. (a) a_0 at 3.0 MHzmm (b) a_1 at 3.0 MHzmm.

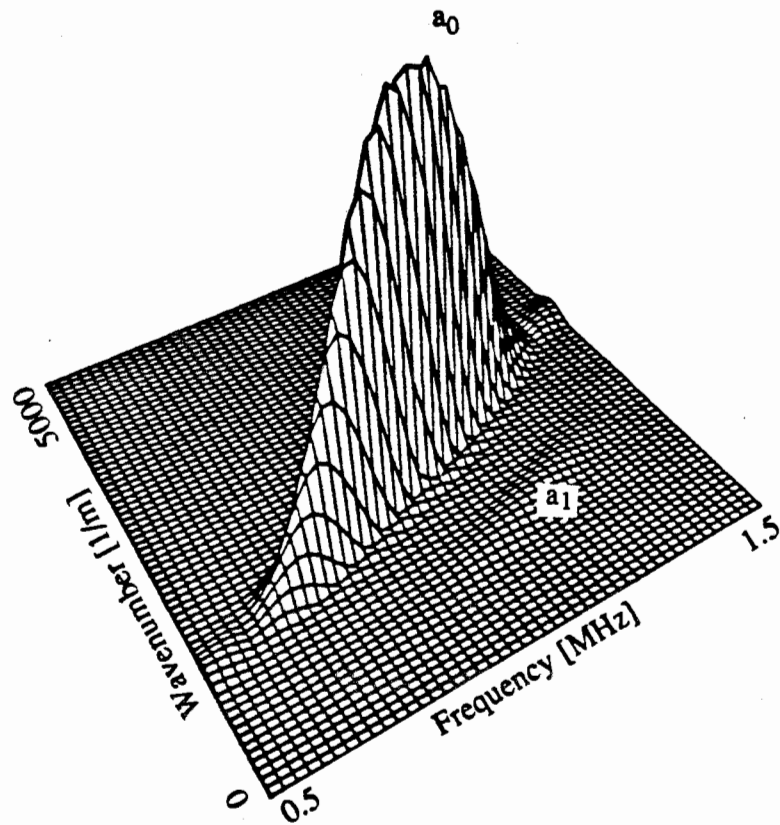
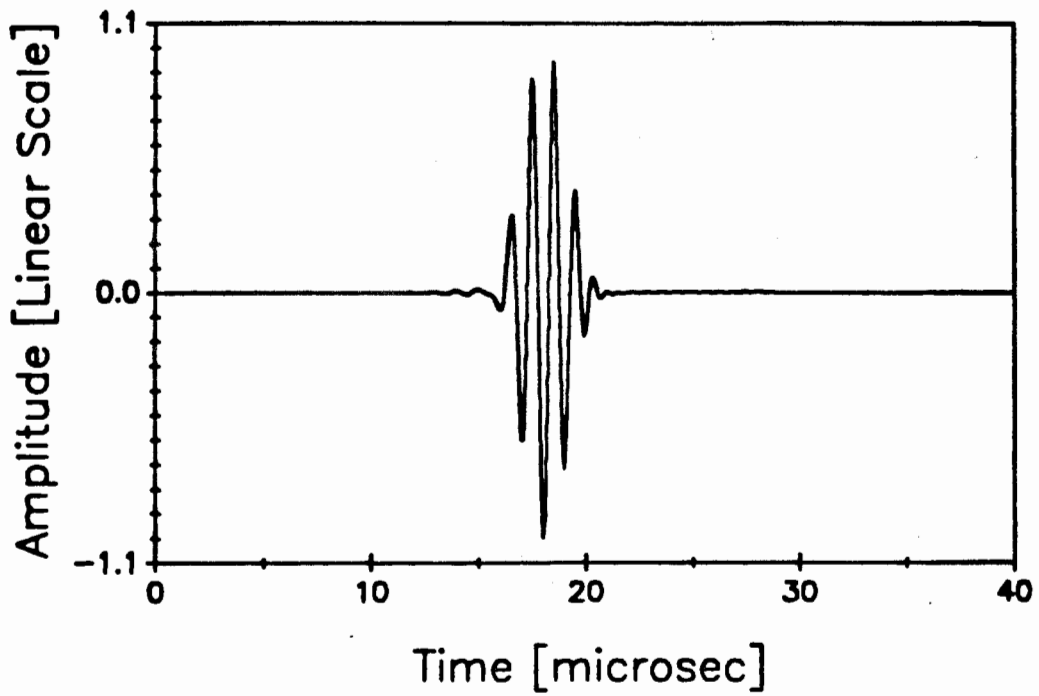


Figure 4.9 (a) Predicted time history at $x = 50$ mm in a 3.0 mm thick plate when the input at $x = 0$ was designed to excite only a_0 . (b) Normalised 3-D plot of the 2-D FFT results of the case given in (a).

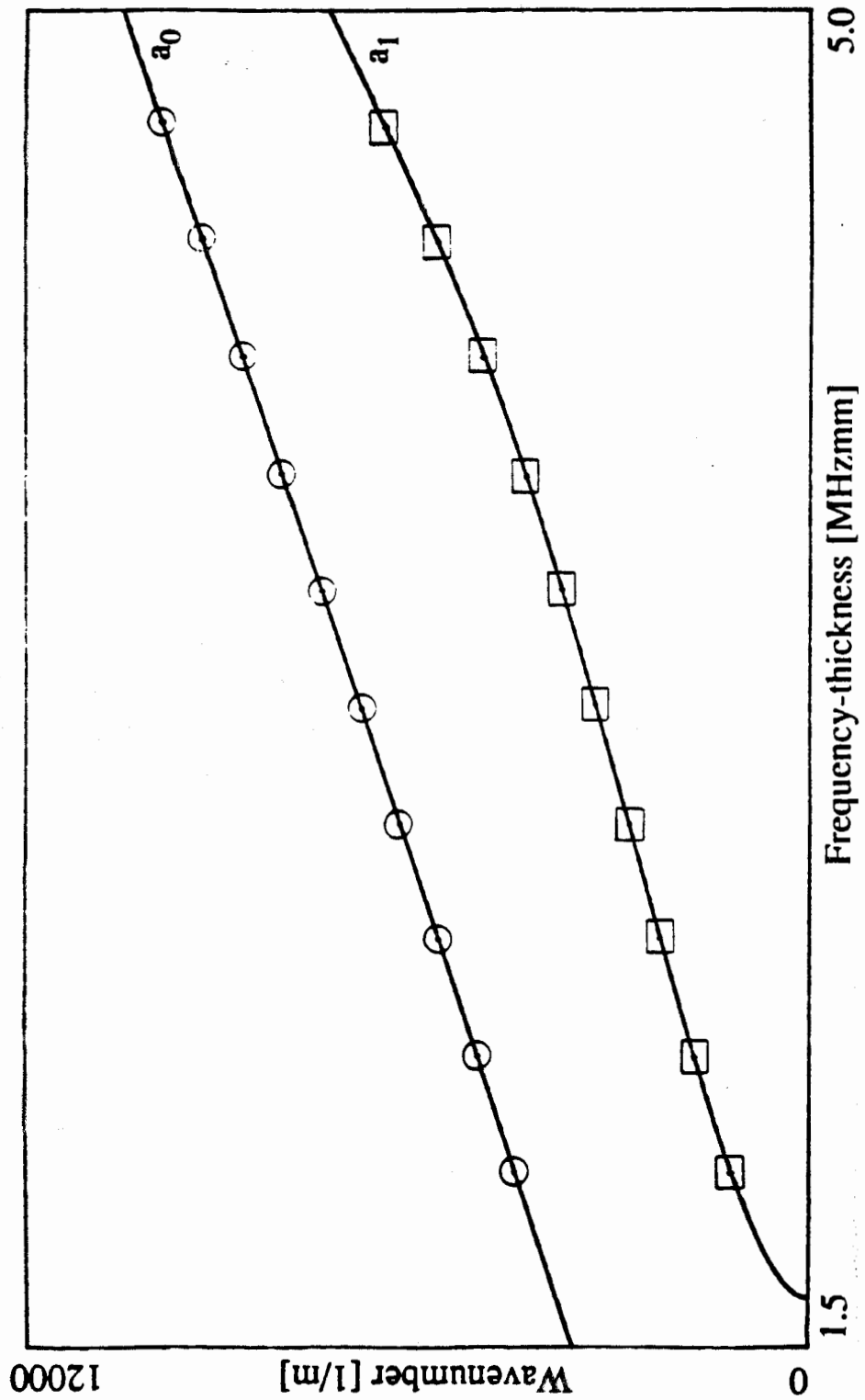


Figure 4.10 A comparison of the finite element predictions with the analytically generated dispersion curves for a_0 and a_1 : — analytical predictions; \odot finite element predictions for a_0 ; \square finite element predictions for a_1 .

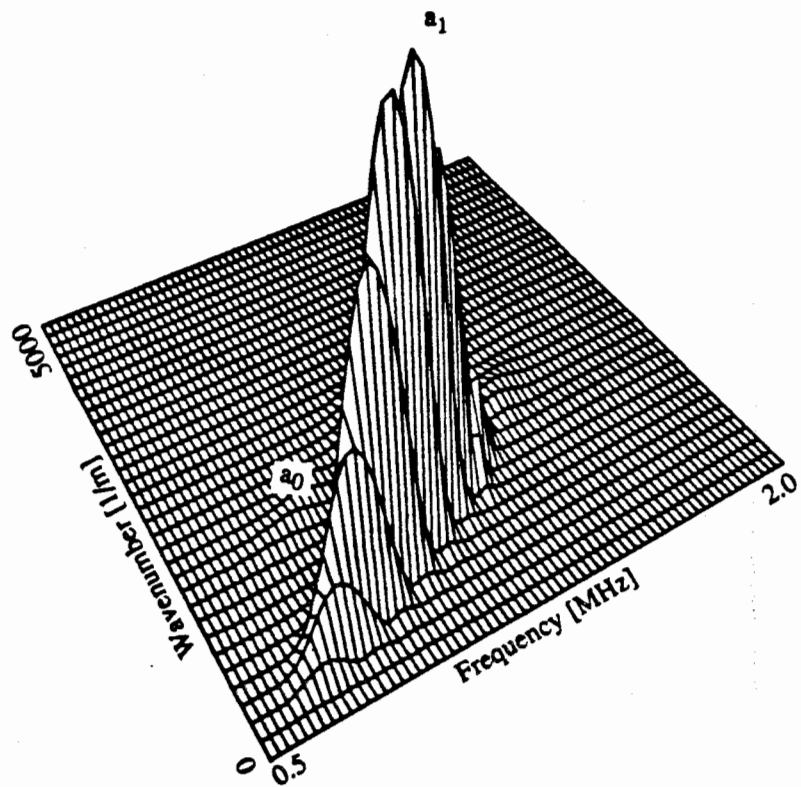
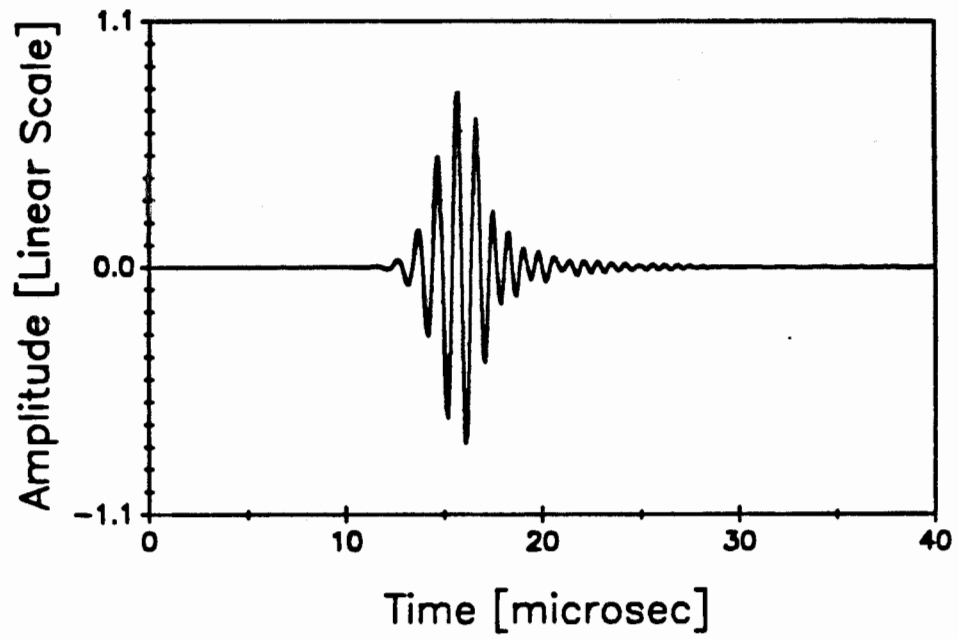


Figure 4.11 (a) Predicted time history at $x = 50$ mm in a 3.0 mm thick plate when the input at $x = 0$ was designed to excite only a_1 . (b) Normalised 3-D plot of the 2-D FFT results of the case given in (a).

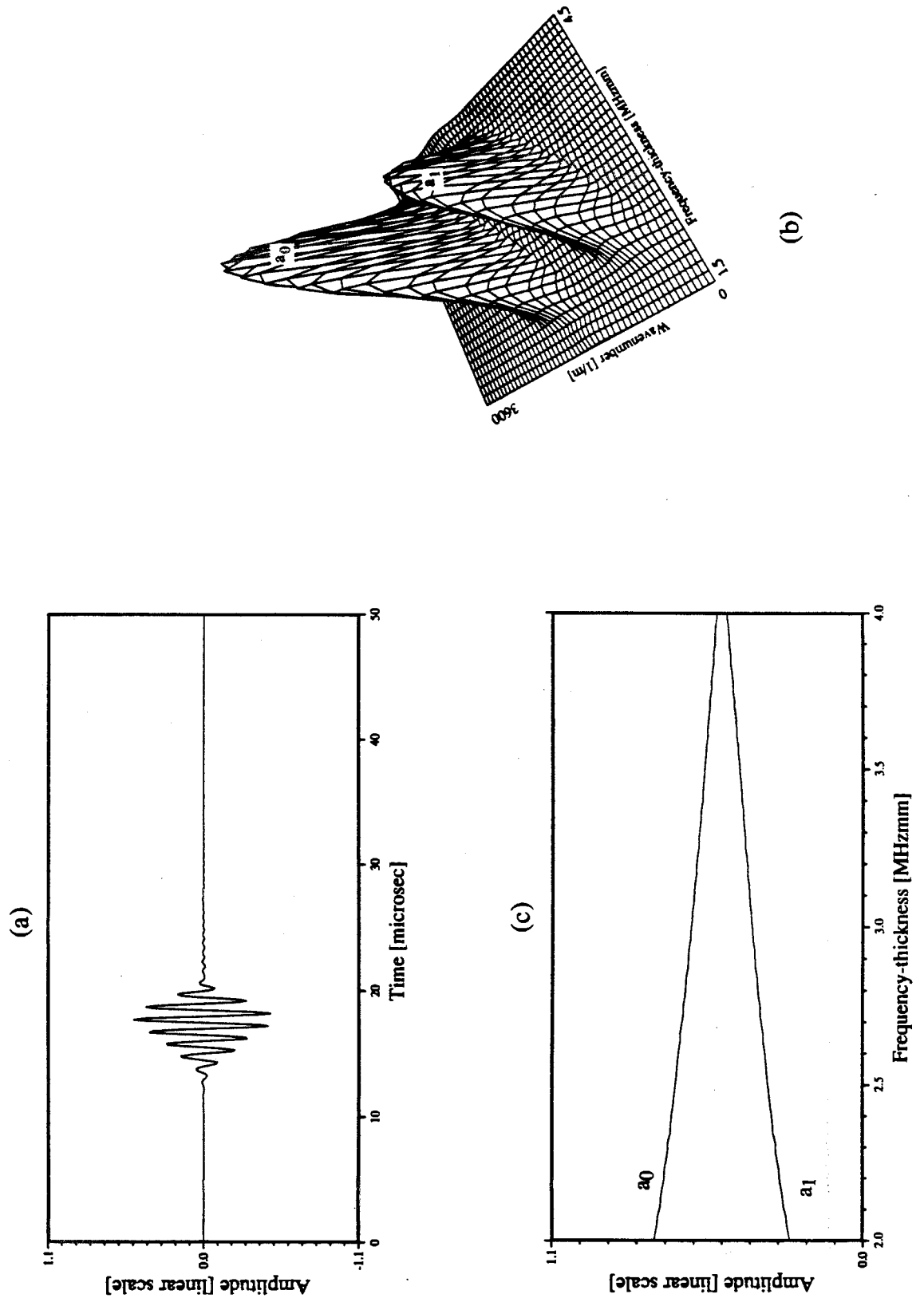


Figure 4.12 (a) Predicted time history at $x = 50$ mm in a 3.0 mm thick plate when the input at $x = 0$ was designed to excite a_0 and a_1 . (b) Normalised 3-D plot of the 2-D FFT results of the case given in (a). (c) The relative surface amplitudes in the z direction of the two modes a_0 and a_1 , obtained from (b), as a function of the frequency-thickness product.

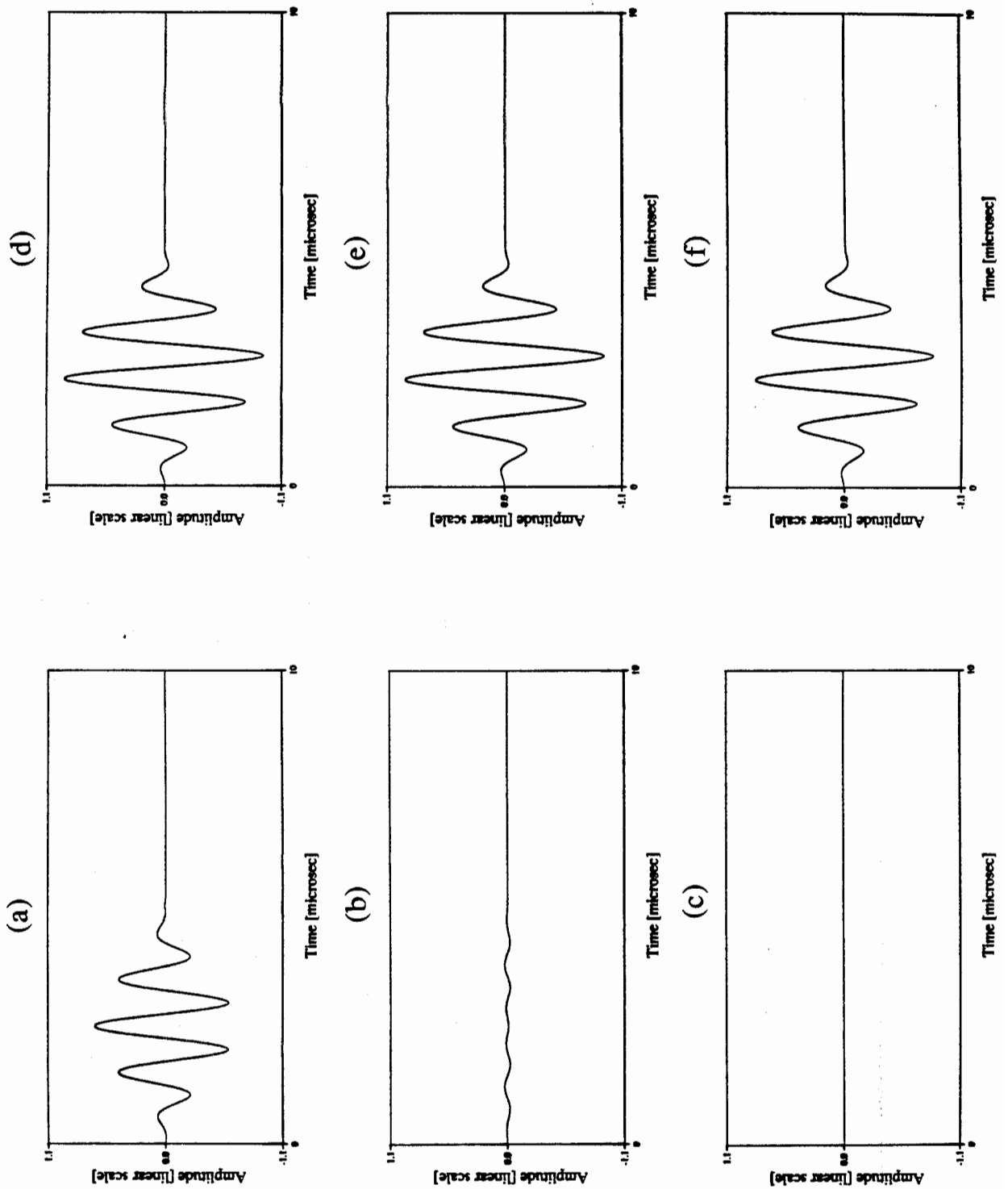


Figure 4.13 The analytically calculated deflected shape time histories at $x = 0$ of the a_0 mode, in the x direction at (a) $z/2d = 0$, (b) $z/2d = 0.5$ and (c) $z/2d = 1.0$. In the z direction at (d) $z/2d = 0$, (e) $z/2d = 0.5$ and (f) $z/2d = 1.0$.

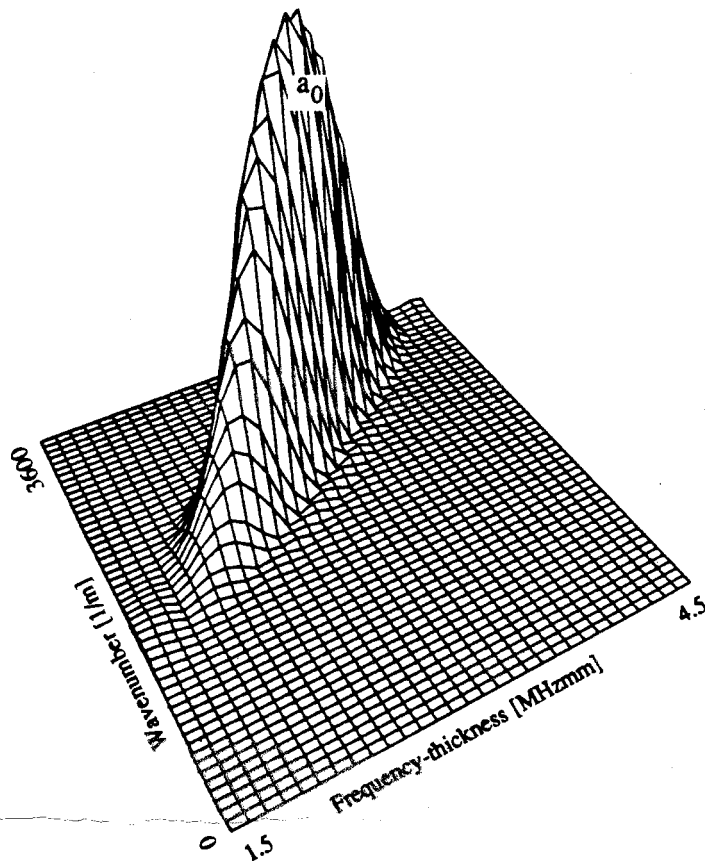
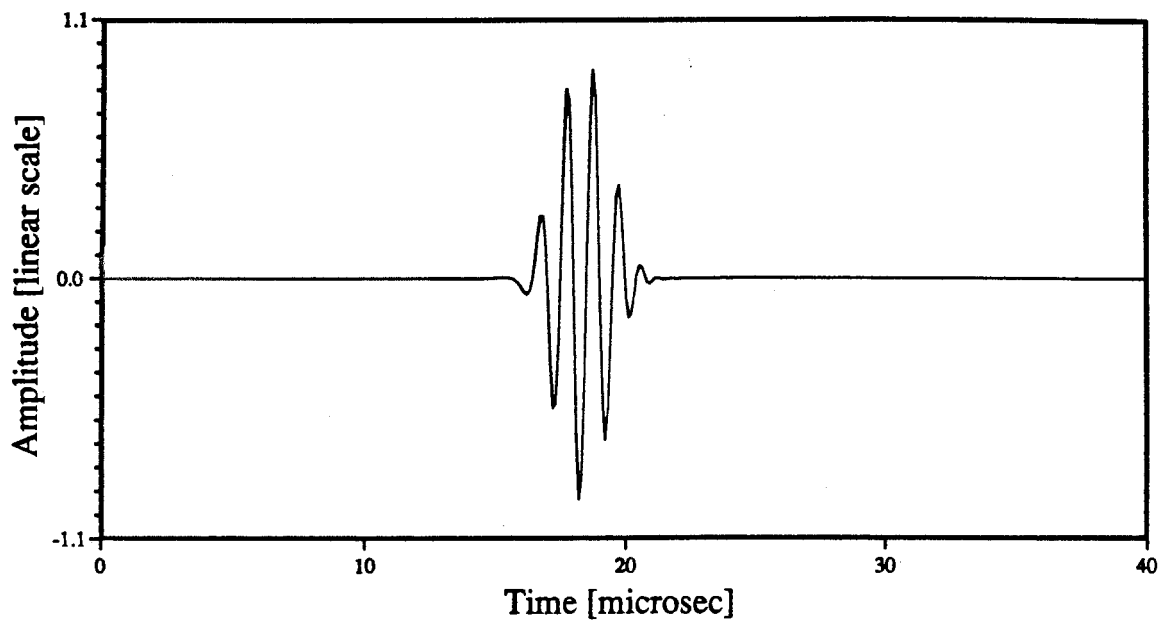


Figure 4.14 (a) Predicted time history at $x = 50$ mm in a 3.0 mm thick plate when the input signal at $x = 0$ corresponded to the time histories shown in Fig. 4.13 and was designed to excite only a_0 . (b) Normalised 3-D plot of the 2-D FFT results of the case given in (a) showing a single propagating mode a_0 .

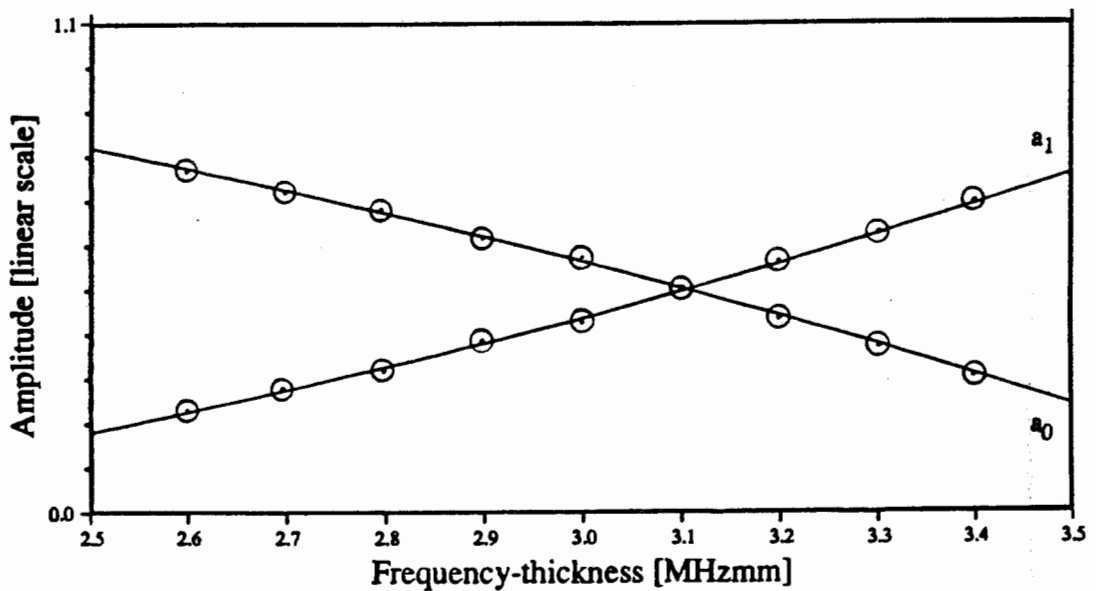
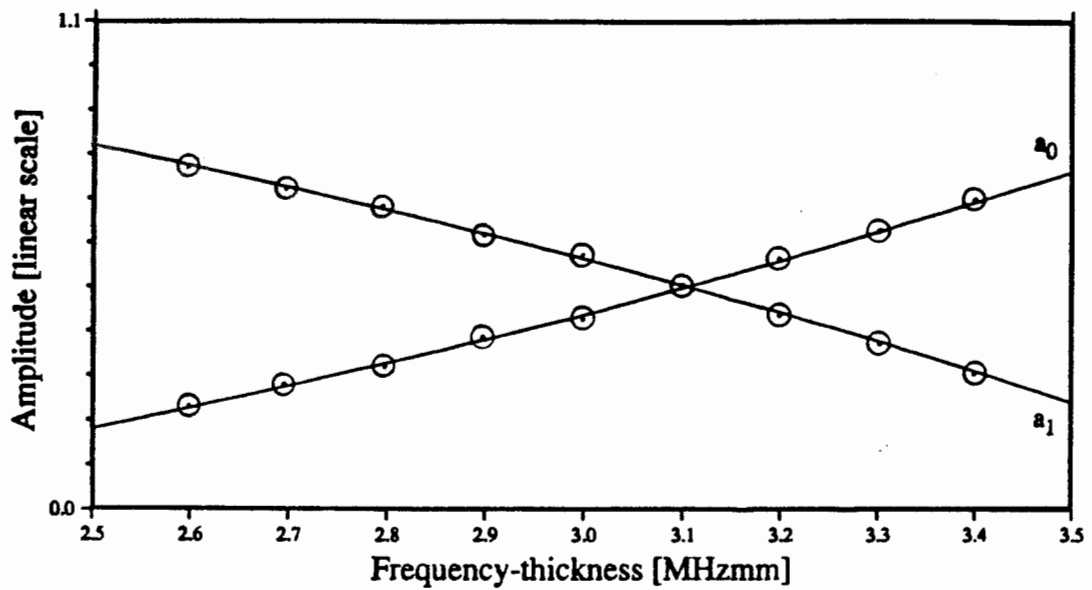


Figure 4.15 Distribution of energy between a_0 and a_1 after reflection from the free end of the plate. — theoretical predictions using the method of Torvik (1967); \odot numerical results. (a) when only a_0 was incident, (b) when only a_1 was incident.

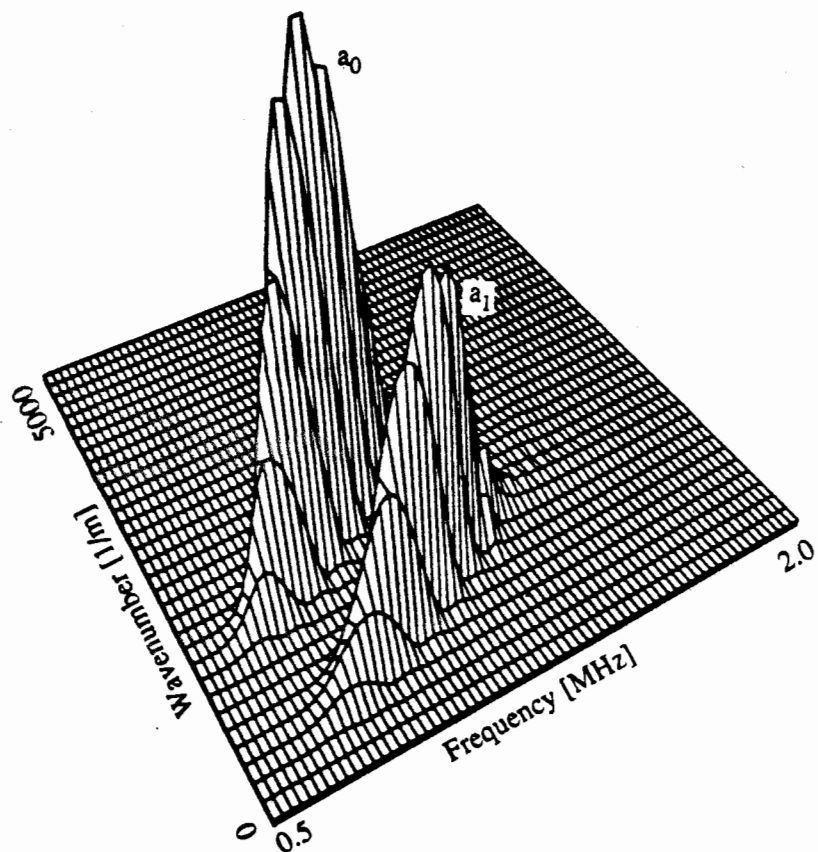
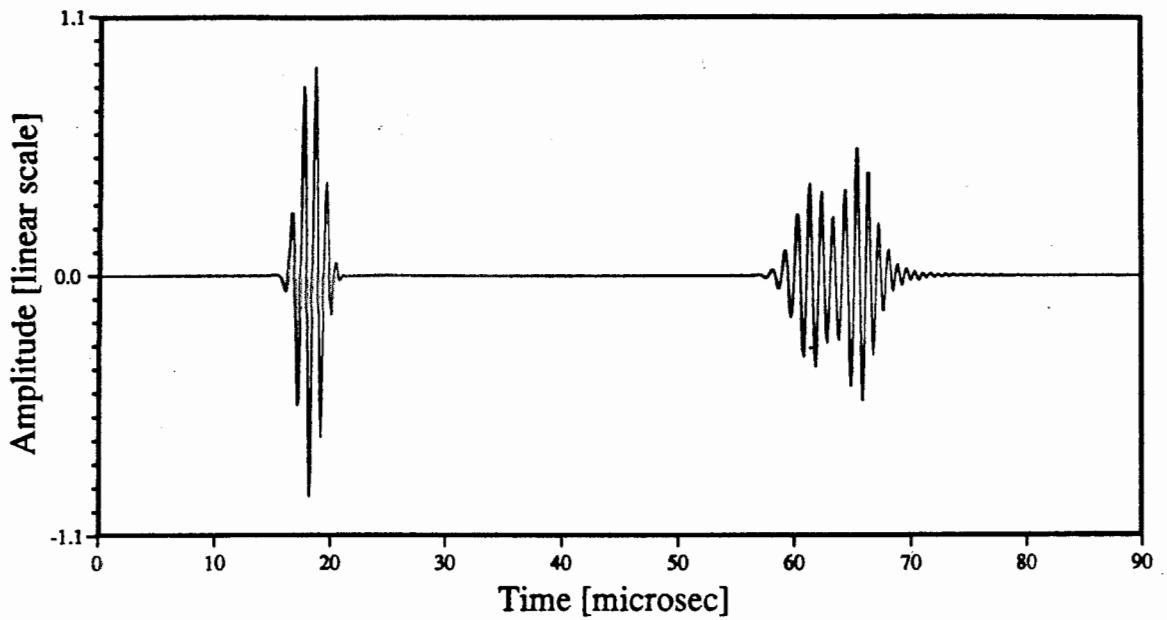


Figure 4.16 (a) Predicted time history at $x = 50$ mm in a 3.0 mm thick plate, showing the first passage of the a_0 wave and the reflection containing both a_0 and a_1 from the free end of the plate, when the input signal at $x = 0$ was designed to excite only a_0 . (b) Normalised 3-D plot of the 2-D FFT results from the reflected wave packet shown in (a).

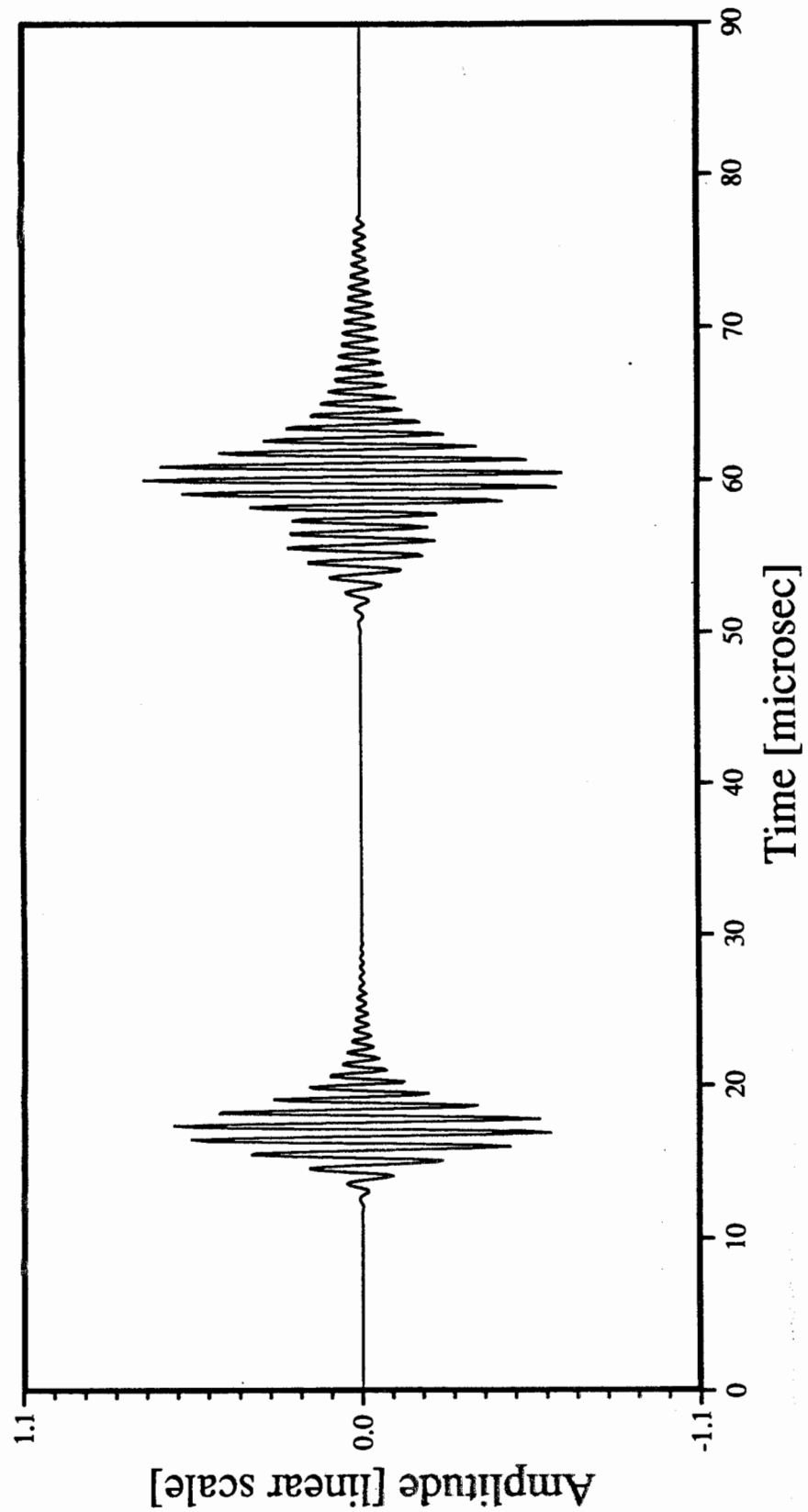


Figure 4.17 (a) Predicted time history at $x = 50$ mm in a 3.0 mm thick plate, showing the first passage of the a_1 wave and the reflection containing both a_1 and a_0 from the free end of the plate, when the input signal at $x = 0$ was designed to excite only a_1 .

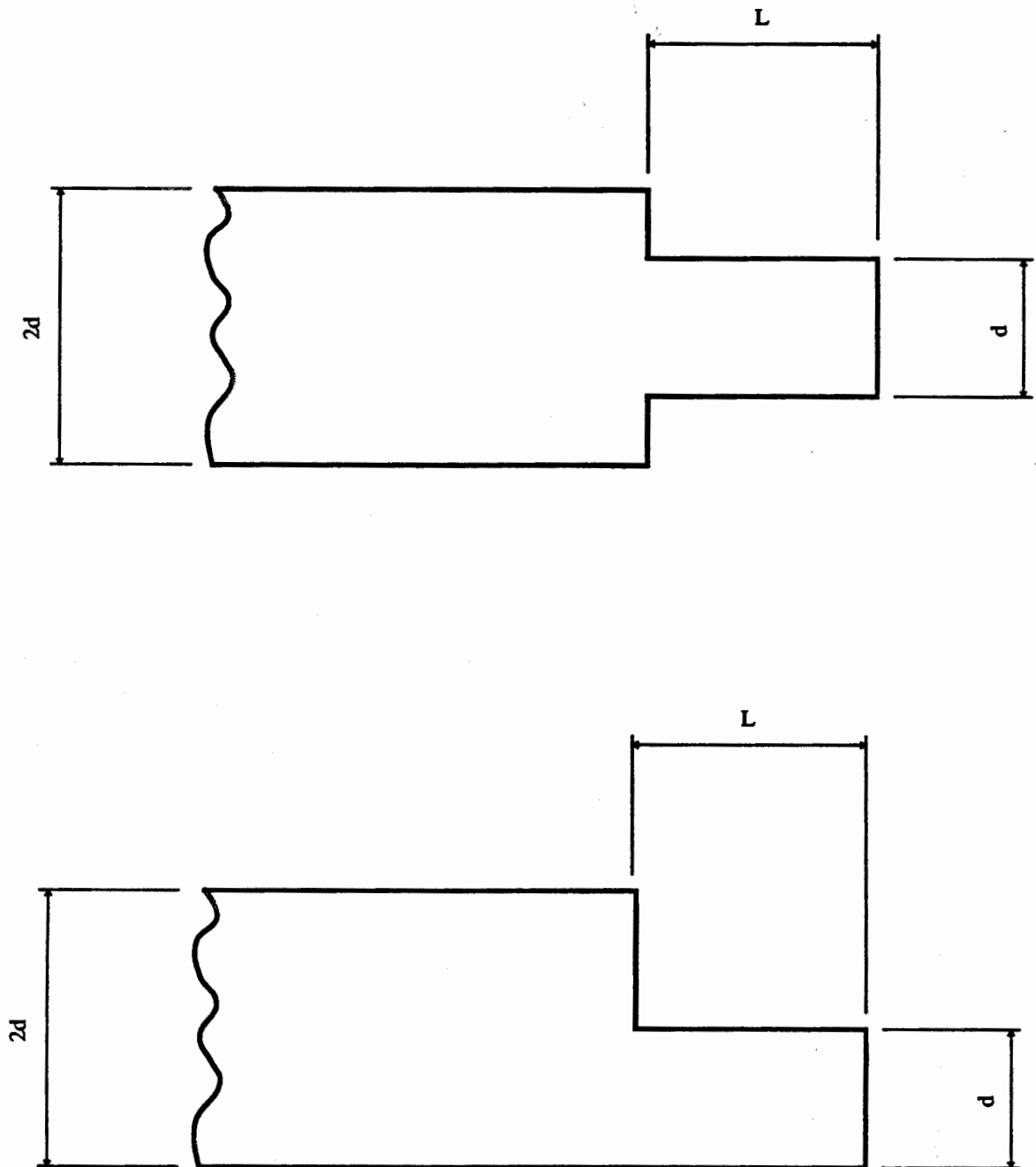


Figure 4.18 Schematic representation of the geometry of the steps at the end plate. (a) symmetric step (with respect to the middle of the plate) and (b) non-symmetric step (with respect to the middle of the plate).

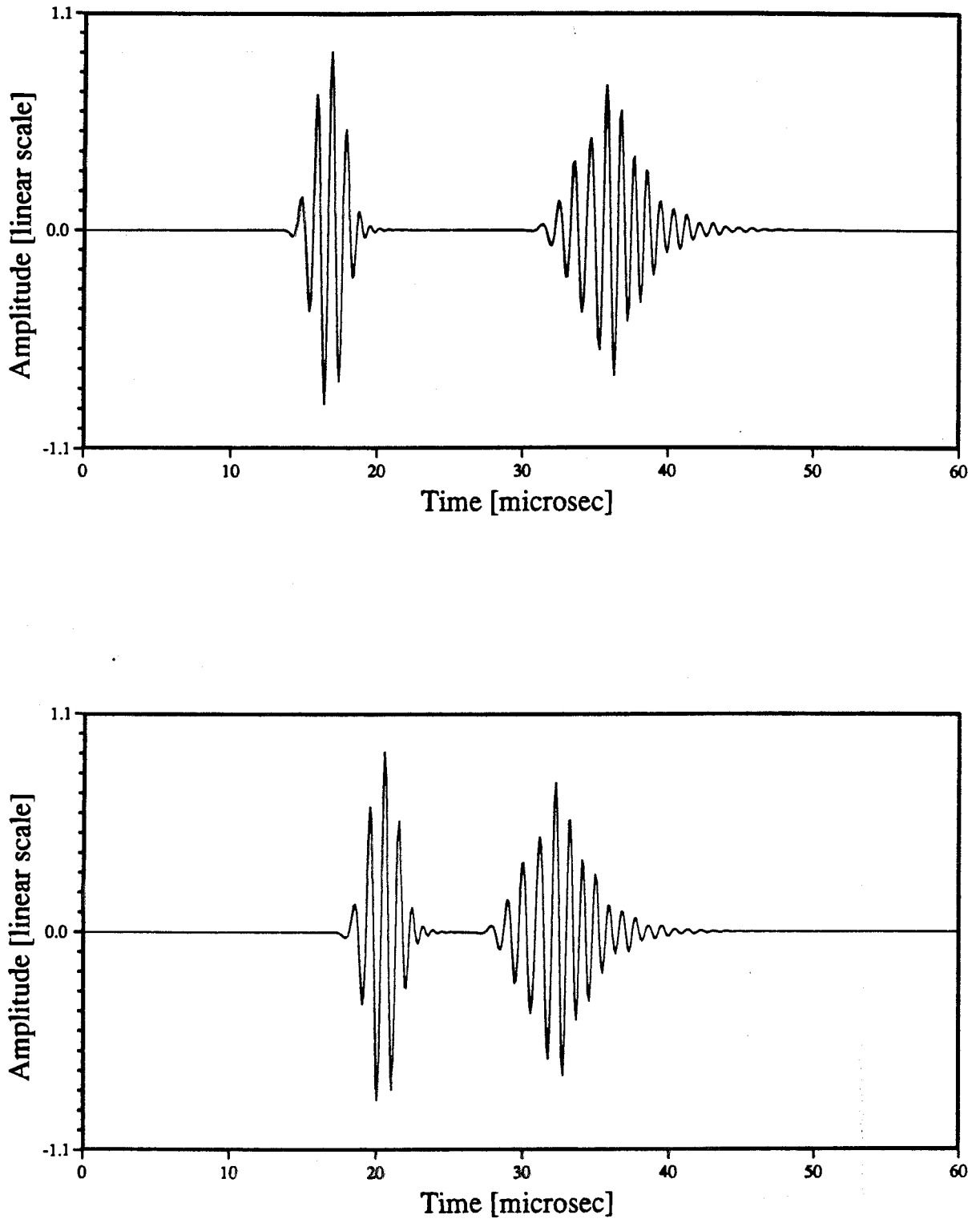


Figure 4.19 Predicted time history of the 1.0 mm thick plate when the input signal at $x = 0$ was designed to excite only s_0 , showing the first passage of the s_0 wave and the wave packet reflected from the free symmetric step at the end of the plate. (a) at $x = 75$ mm and (b) at $x = 95$ mm.

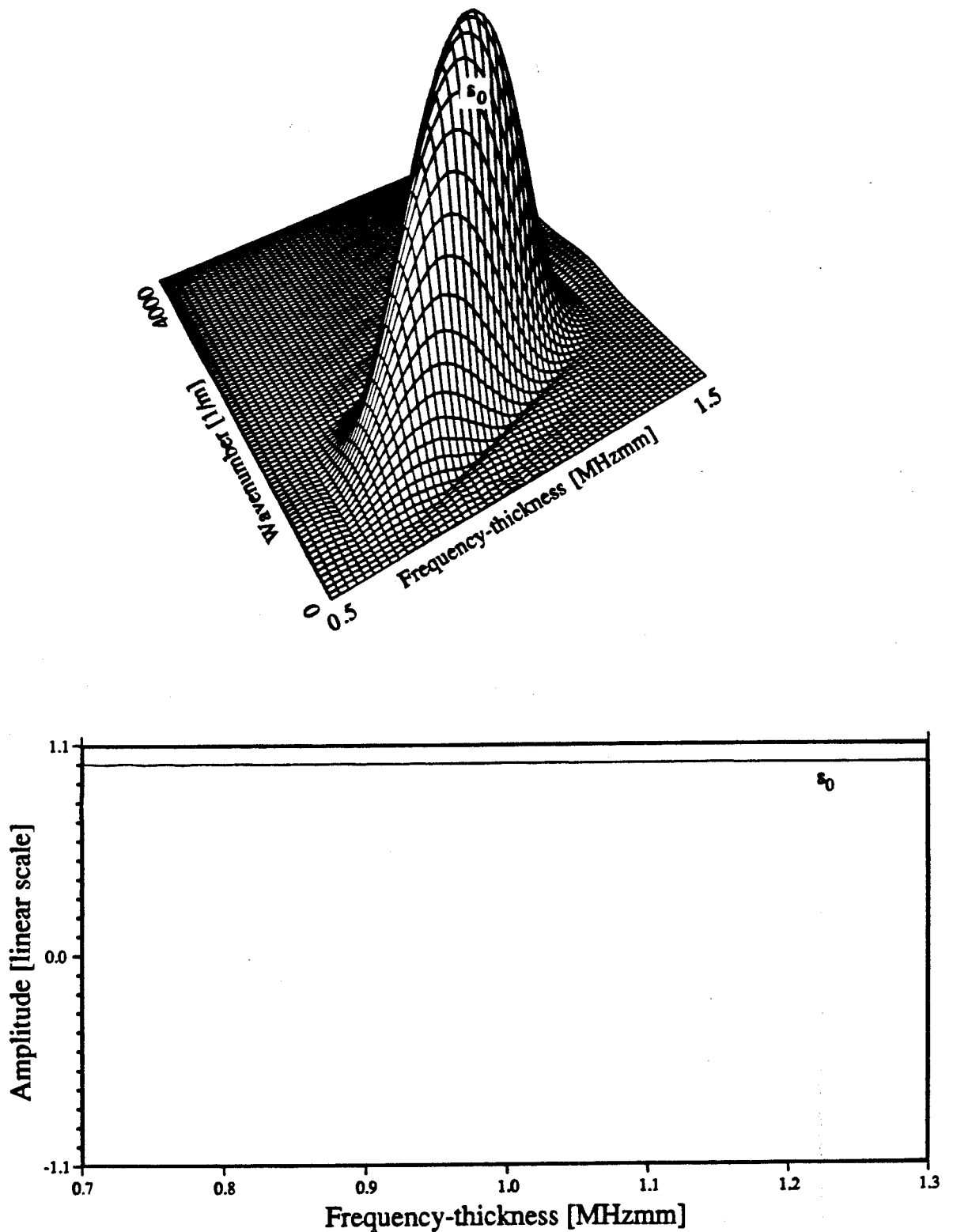


Figure 4.20 (a) Normalised 3-D plot of the 2-D FFT results of the case shown in Fig. 4.19 when the incident wave ($t \leq 26 \mu\text{s}$) was gated out. It shows that the signal reflected from the symmetric step contains only one propagating mode s_0 . (b) Predicted reflection ratio of the s_0 mode as a function of frequency-thickness in the 1.0 mm thick plate after reflection from the symmetric notch.

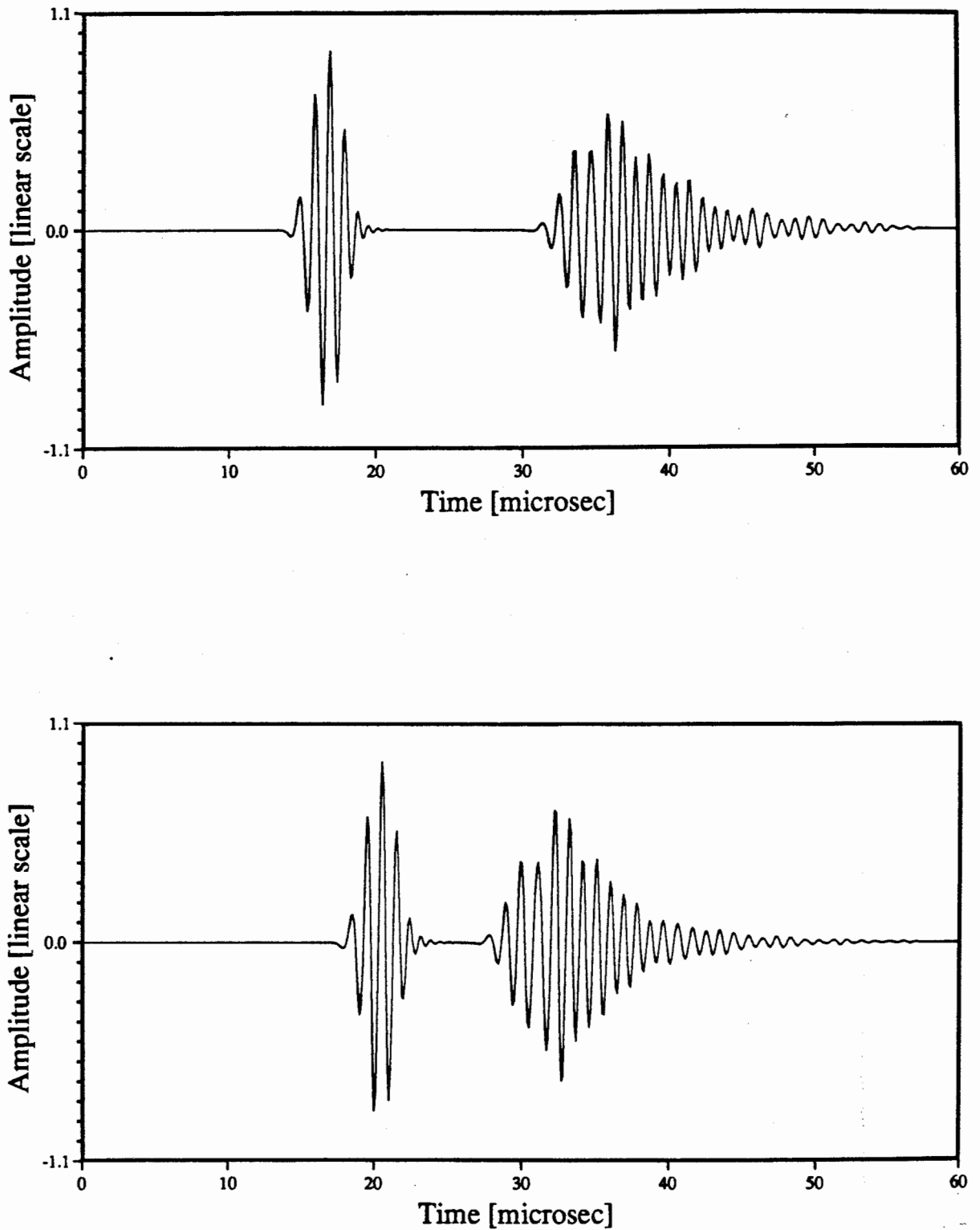


Figure 4.21 Predicted time history of the 1.0 mm thick plate when the input signal at $x = 0$ was designed to excite only s_0 , showing the first passage of the s_0 wave and the wave packet reflected from the free non-symmetric step at the end of the plate. (a) at $x = 75$ mm and (b) at $x = 95$ mm.

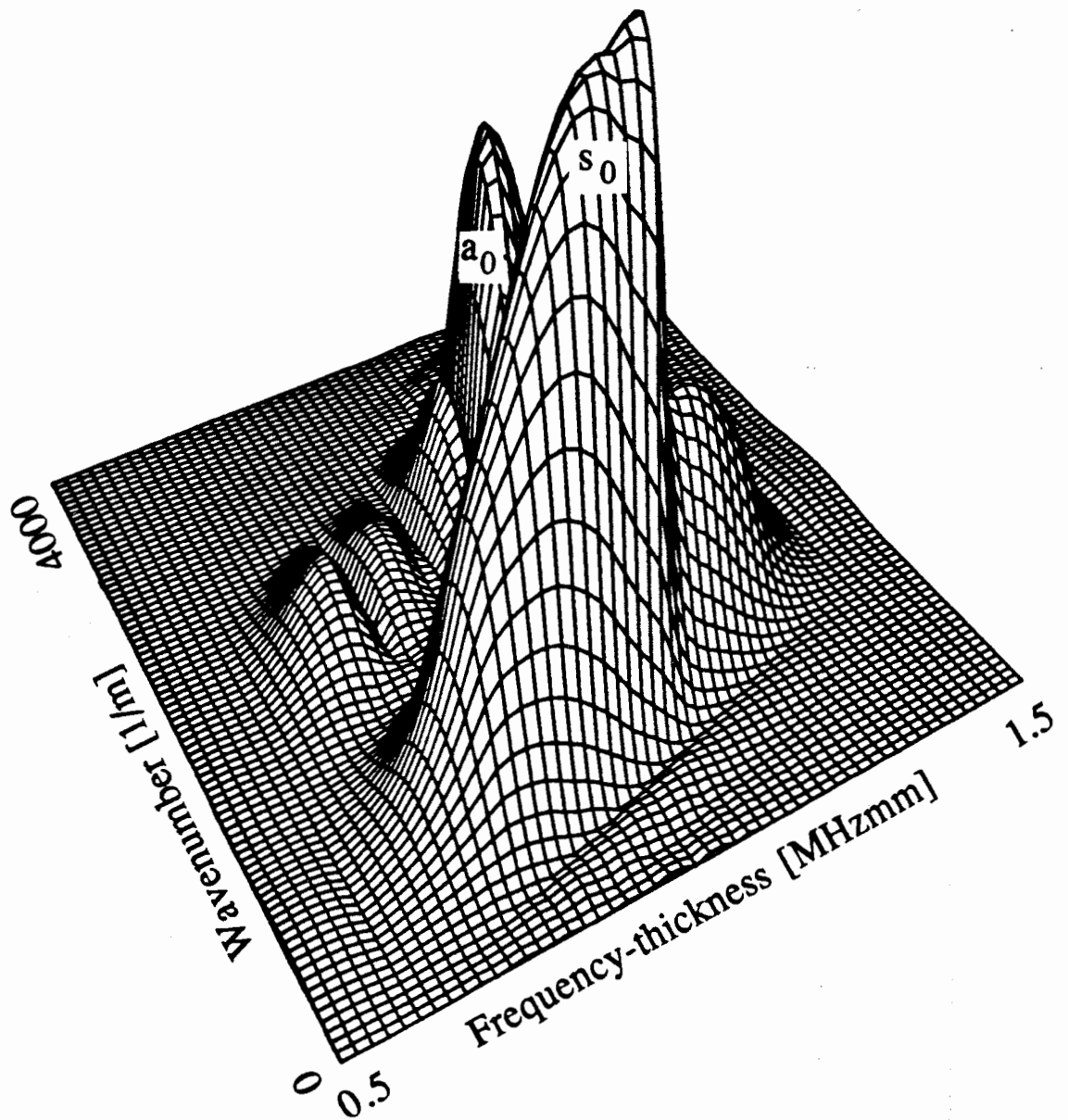


Figure 4.22 Normalised 3-D plot of the 2-D FFT results of the case shown in Fig. 4.21 when the incident wave ($t \leq 26 \mu\text{s}$) was gated out, showing that the signal reflected from the non-symmetric step contains two propagating modes s_0 and a_0 .

CHAPTER 5

Finite element modelling of Lamb wave interaction with idealised defects

5.1 Objectives and introduction

The problem of Lamb wave interaction with arbitrary defects is extremely complicated and for all but the simplest boundary conditions analytical solutions are not feasible. For details on the application of analytical methods to solve wave scattering problems, see Merkulov and Rokhlin (1970), Auld and Tsao (1977) and Harker (1989). In the majority of cases in nondestructive testing and monitoring of plates we are interested in defects above a critical dimension, which in many situations is of the order of 10 to 50% of the plate thickness. It has been pointed out by, for example, Bond *et al* (1984) that in the frequency-thickness regions where defect dimensions and wavelength are comparable, analytical methods break down altogether, or are extremely restrictive. Therefore, most of the work to predict Lamb wave defect interaction has been carried out numerically. For example, Al-Nasser and Datta (1990) have presented numerical predictions of Lamb wave scattering from surface breaking cracks in plates using a combination of finite element and analytical models while Harker (1985) and Georgiou and Bond (1985) have modelled Lamb wave interacting with cracks in plates using finite difference methods.

The finite element (FE) modelling investigations reported in this chapter were undertaken to predict the sensitivity of symmetric and antisymmetric Lamb waves to simulated defects. The aim of the FE modelling studies was to quantitatively characterise Lamb wave defect interactions in terms of the wave mode, (symmetric or antisymmetric), mode order and frequency-thickness product.

In real structures or components defects are arbitrary in geometry, size, orientation and position within the plate. However, in the finite element studies reported here, straight sided notches in steel plates will be investigated as they are a reasonable idealisation of a type of defect (cracks) commonly found in engineering structures. Schematic diagrams of the FE model used and details of the notch geometry are shown in Fig. 5.1. The model allows

variation of depth, width, position and angle with respect to the normal to the plate surface. However, in a large number of applications very thin cracks, for example, fatigue cracks, which are initiated at free surfaces and grow in a direction normal to the surface are of primary importance. Therefore, surface breaking, straight sided notches of a constant width running normal to the plate surface were used in most of the FE predictions reported here. This was also the simplest simulated defect to machine in the 3.0 mm thick steel plates used in the experimental investigations that will be reported later, so the predictions could readily be verified experimentally.

All the modelling was carried out using 4 noded quadrilateral elements and a uniform square mesh with more than 10 nodes per wavelength, which proved to be adequate. The bulk wave velocities, c_1 and c_2 used in the FE models were the same values as used in the Lamb wave dispersion curves for steel presented in chapter 2 (see Fig. 2.4 to 2.6) and the density, ρ was 8000 kg/m³. The two-dimensional Fourier transformation method (2-D FFT) developed during the project and presented in chapter 3 was used to analyse the response of the plate. The sensitivity of individual Lamb modes to different defects was studied separately, by launching individual modes from the edge of the plate using a method developed during this thesis, and described previously in section [4.4].

A 10 cycle tone burst modified by a Hanning window was used in all the tests reported in this section, and in each case energy was available over a narrow range of frequencies $0.8f_0 \leq f \leq 1.2f_0$ (40 dB down points), where f_0 was the centre frequency of the tone burst.

Most of the results presented in this chapter are of Lamb wave interaction with straight sided notches in steel plate, where the width of the crack was 0.5 mm. However, predictions showing the effect of varying the width, and orientation of the notch are also presented. The FE studies concentrated on the prediction of the transmission amplitudes of Lamb waves after interaction with a defect, as only transmission experiments were undertaken, though, in several cases the reflection amplitude ratios of Lamb waves are presented for completeness. Conclusions based on the FE predictions and relating to the best way of utilising Lamb waves in NDT and monitoring are also presented.

5.2 Lamb wave interaction with straight sided notches

5.2.1 Modes and frequency-thickness regions used

Since thin cracks are the defects which are of most interest in NDT, the critical dimension in Fig. 5.1(a) is the depth (h) of the notch. The majority of the tests reported below were carried out to investigate the sensitivity of the antisymmetric and symmetric modes a_1 , a_0 and s_0 to notches of varying depths. The principal reason for using the a_0 and s_0 modes was that they can be readily excited and received experimentally at low frequency-thickness products, where their group velocities are a maximum. The a_1 mode was chosen in order to obtain predictions for a non-zero order mode in a dispersive region. The FE studies were conducted in two frequency-thickness regions, which are labelled on the group velocity dispersion curves for steel shown in Fig. 5.2, from which it may be seen that the modelling was carried out away from the cut-off frequency-thickness value of a_1 where dispersion is a maximum. The FE predictions are presented in terms of the Lamb wave amplitudes as a function of the frequency-thickness product and the Lamb wave amplitudes as a function of notch depth at particular frequency-thicknesses, this being the more useful format in NDT applications. Here, the emphasis is on the practical applications of Lamb waves in NDT, therefore, the time histories of the response of the FE models in the z direction on the plate surface are recorded, as this is the component of displacement measured when immersion or grease coupling is used.

5.2.2 Lamb waves a_0 and s_0 at 0.45 MHz

a_0 incident

The tests reported in this section were carried out to determine the sensitivity of the first symmetric and antisymmetric modes, a_0 and s_0 , respectively, to notches of varying depths in region 1 of the dispersion curves shown in Fig. 5.2. All the FE models were 395 mm long and 3.0 mm thick, the spatial sampling interval was 1 mm and the sampling frequency was 3.125 MHz. In the reflection tests the notch was located at $x = 250$ mm and in the transmission tests the notch was located at $x = 150$ mm. The deflected mode shapes of a_0 and s_0 at 1.35 MHzmm are shown in Fig. 5.3 and it may be seen that at low frequency-thickness

products the a_0 and s_0 modes are essentially plane flexural and extensional waves with simple mode shapes.

Fig. 5.4(a) and (b) show the time histories of the response of the top surface in the z direction at $x = 150$ mm, when the signal applied at $x = 0$ was appropriate to excite only a_0 , where the duration of the test was long enough to include the response of the plate after reflection from the 0.5 mm deep and 2.0 mm deep notches respectively, but not from either end of the plate. Fig 5.5 shows that a single mode, a_0 , was launched at $x = 0$ and was obtained by carrying out a two-dimensional Fourier transform on the time histories of 64 equally spaced positions from $x = 120$ to $x = 183$ mm, when the reflected signal ($t \geq 80 \mu\text{s}$) was gated out. The maximum amplitude of the response is at 0.45 MHz, the centre frequency of the input signal. On reflection from the notch (Fig. 5.4(b)) more than one mode is present. Fig. 5.6 shows the result of carrying out a two-dimensional Fourier transform on the time histories of the same positions, when h was 2.0 mm, see Fig. 5.4(b), and the incident signal ($t \leq 80 \mu\text{s}$) was gated out. Again the maximum amplitude of the response is at 0.45 MHz. However, at each discrete frequency in Fig. 5.6 there are two distinct wavenumbers, relating to a_0 and s_0 , at which the amplitude is a maximum. Fig. 5.7 shows sections of Fig. 5.6 at 1.26 MHzmm and 1.36 MHzmm. From the two-dimensional plots the variation of amplitude with wavenumber is clearly shown and it is easily possible to measure the relative amplitude of the two modes. It can be seen that, as expected from the dispersion curves, the wavenumber at which the amplitude is a maximum changes with frequency and in this particular case, the relative amplitude of the two modes is not a strong function of frequency.

Fig. 5.8(a) to (d) show the reflection ratios of a_0 and s_0 for $h = 0.5, 1.0, 1.5$ and 2.0 mm respectively, and were obtained by dividing the 2-D FFT results from the reflected response signals by the input 2-D FFT shown in Fig. 5.5. Fig. 5.8 therefore shows the ratio of the amplitude of the surface motion in the z direction in the two modes in the signal reflected from the defect to the amplitude of the z direction surface motion in the a_0 mode in the incident signal. It should be noted that the vertical scales on Fig. 5.8(a) and (b) are different from those used in (c) and (d).

Fig. 5.9 shows normalised reflection ratios, Q_n , which were obtained from

$$Q_n = \frac{Q}{u_n} u_i \quad (5.1)$$

where Q is the un-normalised reflection ratio and u_n and u_i are the z direction displacement components on the plate surface in the mode being normalised and the incident mode respectively. Hence, for the incident mode Q_n and Q are equal. From Fig. 5.9 it may be seen that the normalisation increases the apparent amplitude of s_0 because in region 1 (see Fig. 5.2)

the surface motion in the z direction is only around 37% of the maximum motion (which occurs in the x direction at the middle of the plate), whereas in a_0 , the motion in the z direction at the surface is close to the maximum motion in this mode. It may be seen that with the 0.5 mm deep notch, there is little variation of the modal amplitude with frequency but significant variation with frequency is observed with the deeper defects, indicating that by measuring over a wide frequency range, it may be possible to size the defects. However, this has not yet been investigated.

Fig. 5.10(a) shows the FE prediction of the time history of the response of a 3.0 mm thick plate at $x = 215$ mm, when the input at $x = 0$ was appropriate to excite only a_0 , h was 2.0 mm and the defect was located at $x = 150$ mm; the duration of the test was not long enough to include reflections from either end of the plate. After interaction with the notch, more than one propagating mode is present (a_0 is mode converted), but in the time domain the modes are superimposed and their amplitudes may not be determined from the time histories of the responses of the plate. Fig. 5.10(b) shows the result of carrying out a two dimensional Fourier transform on 64 equally spaced signals from $x = 152$ to $x = 215$ mm (ie from 2 to 65 mm beyond the notch), from which the two propagating modes a_0 and s_0 (s_0 is caused by mode conversion at the 2.0 mm deep notch), may be identified and measured. Fig. 5.11(a) to (d) show the transmission amplitudes of a_0 and s_0 , when h was 0.5, 1.0, 1.5 and 2.0 mm respectively, and were obtained from results corresponding to the those of Fig. 5.10(b) and dividing by the input 2-D FFT shown in Fig. 5.5. The normalised transmission amplitudes are presented in Fig. 5.12(a) to (d), from which it may be seen that the relative amplitude of the s_0 mode is again increased if normalised ratios are considered.

Frequency-thickness [MHzmm]	h/2d			
	1/6	1/3	1/2	2/3
1.25 (R)	0.11	0.11	0.51	0.81
1.35 (R)	0.11	0.11	0.63	0.81
1.45 (R)	0.10	0.14	0.74	0.76
1.25 (T)	0.98	0.90	0.66	0.18
1.35 (T)	0.98	0.89	0.54	0.22
1.45 (T)	0.97	0.88	0.33	0.35

Table 5.1 Predicted reflection (R) and transmission (T) ratios of a_0 .

The data of Fig. 5.8 may be presented in the form of a relation between reflection amplitude and notch depth at particular frequencies. This shown in table 5.1 at 1.25, 1.35 and 1.45

MHzmm. It can be seen that the relation between reflection amplitude and notch depth is complicated and is a strong function of frequency. For example, the reflected amplitude of a_0 at notch depths of 0.5 mm and 1 mm ($h/2d = 1/6$ and $1/3$) is the same at 1.25 and 1.35 MHzmm, while at 1.45 MHzmm there is a 40% difference between the two.

s_0 incident

Fig. 5.13 shows the transmission ratios of the a_0 and s_0 modes when only s_0 was launched from the end of a 310 mm long plate. Again a reference 2-D FFT of the input signal was taken and the transmission ratios were obtained in the usual way by dividing the 2-D FFT of the transmitted signals after the notch by the reference 2-D FFT. The transmission amplitude ratios are given as a function of $h/2d$ in Table 5.2. In this case, at all notch depths the results are very similar.

Frequency-thickness [MHzmm]	$h/2d$			
	1/6	1/3	1/2	2/3
1.25	0.98	0.84	0.63	0.42
1.35	0.98	0.83	0.61	0.40
1.45	0.97	0.81	0.57	0.36

Table 5.2 Predicted transmission ratios of s_0 .

5.2.3 Discussion of transmission and reflection results

The reflection and transmission ratios shown in Fig. 5.8 and Fig. 5.11 respectively when a_0 was incident show that for notches where $h/2d$ is bigger than around 0.5 the ratios are not monotonic functions of frequency but there are minima and corresponding maxima, which are a function of the incident mode, the frequency-thickness product and the notch dimensions (and geometry); these local minima and maxima could potentially be used for defect sizing. However, the transmission ratios shown in Fig. 5.13 when s_0 was incident are not a strong function of frequency and are monotonic. The results indicate that the wavelength (velocity) of the Lamb waves is not the only factor which affecting sensitivity. For example, at 1.35 MHzmm the wavelengths of s_0 and a_0 are around 12 mm and 5.7 mm respectively, but the amplitude of their transmission ratio across a 0.5 mm deep notch was the same.

The time domain responses shown previously (see Fig. 5.4) indicate that when the group velocities of the modes are very different, it is possible to measure the relative amplitudes in the time domain since the wave packets will separate after a relatively short distance past the notch. The FE predictions have also shown that the amplitudes of the Lamb waves caused by mode conversion at the notch is measurable (greater than 5% of the amplitude of the incident wave) when the notch depth is greater than about one sixth of the plate thickness (see Fig. 5.8, 5.11 and 5.13). However, the monitored amplitude in the z direction of a_0 when s_0 was launched is greater than that of s_0 when a_0 was launched. This effect is due to the relative amplitudes of the z and x components of displacement in the deflected mode shapes at the surface, see Fig. 5.3, and would have been reversed if x direction displacements had been monitored. This shows the importance of monitoring modes which have a large proportion of their deflections at the surface in the z direction, as in most NDT applications it is the z direction surface displacement which is measured.

5.2.4 Lamb wave s_0 at 0.225 MHz

In order to verify that the interaction of individual Lamb modes with defects is frequency-thickness dependent, tests were carried out with s_0 incident on a 6.0 mm thick plate at 0.225 MHz, rather than the 3.0 mm thick plate at 0.45 MHz shown previously. The plate was 650 mm long and notches 0.5, 1.0, 1.5, 2.5, 3.5 and 5.0 mm deep were investigated, the notches being located at $x = 325$ mm. The 1.0 mm deep notch giving $h/2d = 1/6$ corresponding to the 0.5 mm deep notch in the 3.0 mm thick plate discussed earlier. The spatial sampling interval was 2 mm and the sampling frequency was 3.125 MHz.

Fig. 5.14(a) and (b) show the predicted time history of the response of the 6.0 mm thick plate 5 mm and 55 mm respectively, beyond a 0.5 mm deep notch.

The amplitude of the transmission ratios as a function of the frequency-thickness product are shown in Fig. 5.15. The results of Fig. 5.15(b) and 5.13(a), at $h/2d = 1/6$ are the same, demonstrating that for a given defect and Lamb mode, the sensitivity is dependent on the frequency-thickness product. Fig. 5.16 gives the transmission amplitude ratios as a function of $h/2d$ at three discrete frequencies over the bandwidth of the input signal. Here, the results obtained previously at $h/2d = 1/3, 1/2$ and $2/3$ shown in Fig. 5.13 are also included. It may be seen that they fall on a smooth curve giving further confirmation that the sensitivity is frequency-thickness dependent. The wavelength of the s_0 mode in this frequency-thickness region is about 24 mm and from Fig. 5.15(a) a 1.5 mm deep notch produces a reduction of

over 5% in its transmission ratio, indicating that it is possible to detect defects of dimensions greater than 1/16 of the wavelength if changes in amplitude of this order can reliably be measured. However, from Fig. 5.15(b) for a 0.5 mm deep notch the amplitude of the a_0 mode produced at the notch over 10% of the incident s_0 mode. This indicates that in this case it is possible to detect defects of dimensions less than 1/40 of the wavelength of the incident wave if the change in amplitude of the wave caused by mode conversion at the notch is measured.

5.2.5 Lamb waves a_0 and a_1 at 0.75 MHz

The tests reported in this section were carried out to determine the sensitivity of antisymmetric modes in region 2 of Fig. 5.2 to notches of varying depths. In this frequency-thickness region, a_0 is essentially nondispersive, but a_1 is grossly dispersive. The FE models were 410 mm long and the notches, where w was 0.5 mm and h was 0.5, 1.0, 1.5 and 2.0 mm were located at $x = 210$ mm in the reflection tests and at $x = 180$ mm in the transmission tests. In all the tests the spatial sampling interval was 1 mm and the sampling frequency was 4.167 MHz.

Fig. 5.17(a) shows the predicted time history of the response of the plate in a reflection test at $x = 105$ and Fig. 5.17(b) shows the predicted time history of the response of the plate in a transmission test at $x = 275$ mm. In each case the excitation at $x = 0$ was appropriate to launch only a_0 and the duration of the test was long enough to include the response of the plate after interaction with the 0.5 mm deep notch. The first wave packet seen in Fig. 5.17(a) is the a_0 mode which was launched at $x = 0$ and its shape has hardly changed from the input 10 cycle tone burst in a Hanning window, indicating that the wave is essentially nondispersive in this frequency-thickness region. After interaction with the notch a_0 is mode converted and the response shown in Fig. 5.17(a) for $t > 80 \mu\text{s}$ and in Fig. 5.17(b) beyond the notch indicate the presence of more than one mode, the increased duration of the signal indicating velocity dispersion.

The reference 2-D FFT of the a_0 mode shown in Fig. 5.18 was the result of carrying out a two-dimensional Fourier transform on the time histories of 64 equally spaced positions from $x = 105$ to 168 mm, when the signal due to reflection from the slot seen in Fig. 5.17(a) for $t \geq 80 \mu\text{s}$ was gated out. Fig. 5.19 shows the amplitude versus wavenumber and frequency-thickness product information obtained by carrying out a two-dimensional Fourier transform of the response of 64 spatial positions from $x = 212$ mm to $x = 275$ mm in a transmission test, when h was 1.5 mm. Three propagating modes, a_1 and a_0 and s_0 are present, the a_1 and s_0 modes being caused by mode conversion at the notch.

The reflection and transmission ratios as a function of frequency-thickness are shown in Fig. 5.20 and 5.21 respectively and in Table 5.3 the reflection and transmission amplitude ratios for the incident mode, a_0 , are given as a function of $h/2d$ at 2.25 and 2.55 MHzmm.

Frequency-thickness [MHzmm]	$h/2d$			
	1/6	1/3	1/2	2/3
2.25 (R)	0.06	0.41	0.52	0.52
2.55 (R)	0.08	0.66	0.74	0.76
2.25 (T)	0.93	0.59	0.29	0.25
2.55 (T)	0.92	0.23	0.20	0.24

Table 5.3 Predicted reflection (R) and transmission (T) ratios of a_0 .

Comparing the results presented here with those obtained in section 5.2.2 it may be seen that as expected at this higher frequency-thickness product, the sensitivity of a_0 to defects is improved. For example, after interaction with the 1.0 mm deep notch the amplitudes of the reflected and transmitted a_0 mode at 1.35 MHzmm were 0.11 and 0.89 respectively, whereas at 2.25 MHzmm the corresponding amplitudes were 0.41 and 0.59 respectively. However, the wavelength of the Lamb waves does not appear to be the only factor affecting sensitivity. For example, at 1.35 MHzmm the wavelength of a_0 is around 5.7 mm and the amplitude of its transmission ratio across a 2.0 mm deep notch ($h/2d = 1/2$) was 0.22, whereas the transmission ratio for a_0 at 2.25 MHzmm where its wavelength is 3.7 mm was 0.25. Therefore, the smaller wavelength has not produced a significant shift in the transmission ratio indicating that appropriate mode selection can sometimes remove the need to go to higher frequencies where the waveform could be more complicated.

Fig. 5.22(a) and (b) show the predicted time histories of the response of the plate at $x = 182$ and 245 mm respectively, after interaction with the 0.5 mm deep notch, when the excitation at $x = 0$ was appropriate to launch only the a_1 mode. The shape of the response is radically different from the input 10 cycle tone burst in a Hanning window, indicating that the response signal is multi-mode and/or dispersive. From Fig. 5.22 it may be seen that the amplitude at $x = 182$ mm is smaller than at $x = 245$ mm. This is due to the destructive and constructive superposition of the individual modes in the response wave packet produced after the incident a_1 mode has interacted with the notch. This plot shows clearly why it is not reliable to use time domain methods to measure the amplitudes of Lamb waves at frequency-thickness products above the cut-off value of the a_1 mode. The amplitudes of the transmission ratios as

a function of the frequency-thickness product are presented in Fig. 5.23 and the transmission ratios are given as a function of $h/2d$, at 2.25 and 2.55 MHzmm in Table 5.4.

Frequency-thickness [MHzmm]	$h/2d$			
	1/6	1/3	1/2	2/3
2.25	0.91	0.58	0.35	0.23
2.55	0.82	0.03	0.61	0.75

Table 5.4 Predicted transmission ratios of a_1 .

Again, when a_0 or a_1 is incident the transmission ratios vary with frequency with maximum and minimum values located at distinct frequency-thickness products, which are dependent on the size of the notch and the modal properties of the Lamb waves. However, comparing Fig. 5.21 with 5.23 it may be seen that the transmission amplitude of the all the response mode when a_1 was incident (Fig. 5.23) is far more oscillatory especially for notches where $h/2d$ is bigger than 0.5 than when the a_0 mode was incident (see Fig. 5.21). This effect has not been studied further here but is probably due to the dispersive nature of the a_1 mode in this frequency-thickness region, where its wavelength and mode shape are changing rapidly. It may also be seen from Table 5.3 and 5.4 that at 2.25 MHzmm and notch depths of 0.5 and 1.0 mm ($h/2d = 1/6$ and $1/3$) the sensitivity of the a_0 and a_1 modes are comparable, the higher order mode being slightly more sensitive. For example, at 2.25 MHzmm the transmission ratios of the a_1 and a_0 modes after interaction with a 1.0 mm notch are 0.58 and 0.59 respectively. However, the wavelength of the a_1 mode is more than twice that of the a_0 mode. The transmission amplitudes of the modes differ markedly at 2.55 MHzmm and it may be seen from Fig. 5.23 and 5.21 that this is due to the pronounced dips and peaks of the transmission curves in Fig. 5.23.

The results indicate that at higher frequency-thicknesses the transmission ratios are not related to the wavelength in a simple manner, but are dependent on mode type, order and frequency-thickness product. Therefore, appropriate mode selection can sometimes remove the need to go to higher frequencies where the waveform could be more complicated. For example, after interaction with the 0.5 mm notch the amplitude of the transmitted a_0 mode at 2.55 MHzmm was 0.92, whereas at the same frequency-thickness the transmitted amplitude of the a_1 mode was 0.82. Hence the change in the transmission amplitude has been more than doubled by mode selection.

It should be noted that the amplitudes of the mode converted Lamb waves a_0 and s_0 , when a_1 was incident were large when $h/2d$ was bigger than around one sixth, and therefore in many practical NDT applications it may be beneficial to focus the receiving transducer on one of these modes. Comparing Fig. 5.23 with 5.21 it may be seen that the amplitudes of the mode converted waves is larger when the a_1 mode was incident.

5.3 Lamb wave interaction with notches of varying width

One set of tests was carried out to check the effect of notch width on Lamb wave propagation. The incident wave was the s_0 mode in a 3.0 mm thick plate in region 1 of the dispersion curves shown in Fig. 5.2. The notch was 1.0 mm deep and the tests were carried out using 5 different notch widths (see Fig. 5.1(a), $w = 0.25, 0.75, 1.0, 2.0$ and 4.0 mm). Again 4 noded quadrilateral elements were used, the spatial sampling interval was 1 mm and the sampling frequency was 3.125 MHz. The plate was 350 mm long, the notch was located at $x = 150$ mm and time history of the response of the plate at 64 equally spaced positions from $x = 170$ to 233 mm was captured in order to perform the 2-D FFT analysis.

Fig. 5.24 shows the transmission amplitude ratios of the two modes for the different notch widths as a function of the frequency-thickness product. The amplitude ratios of a_0 and s_0 seen in Fig. 5.24(a)-(f) were obtained by dividing the 2-D FFT results from the transmitted response signals by a reference 2-D FFT computed before interaction with the notch when only the s_0 mode was propagating. Here, the transmission amplitude ratio relating to $w = 0.5$ mm, previously presented in Fig. 5.13(b) was included for completeness and comparison purposes. Fig. 5.25 shows the transmission ratios as a function of $w/2d$, at three frequency-thickness values. The results indicate that in this case the amplitudes of the transmitted s_0 mode is not sensitive to the notch width. The wavelength of s_0 in this frequency-thickness region is about 12 mm and the maximum defect width investigated was 4 mm. Therefore, the lack of sensitivity to notch width in test tests is not unexpected. However, the wavelength of a_0 in this frequency-thickness region is about 5.7 mm and significant frequency dependence of the transmitted amplitude of the a_0 is seen at the higher widths in Fig. 5.24. The main focus of this thesis is on crack like defects and these results confirm that when the notch width is small compared to the wavelength, as is usually the case with real cracks, the important parameter is the defect depth.

5.4 Lamb wave interaction with an inclined notch

In many practical situations notch like defects are oriented at an arbitrary angle to the surface of the plate see, Fig. 5.1(b). The tests reported in this section were carried out to determine the sensitivity of the symmetric Lamb mode s_0 in region 1 of the dispersion curve shown in Fig. 5.2 to a 1.0 mm deep surface breaking notch lying at an angle of 45° relative to the plate surface (ie $h = 1.0$ mm and $\theta = 45^\circ$). The plate was 3.0 mm thick and 350 mm long and a 4 noded 0.25 mm square element was used. The centre frequency of the 10 cycle tone burst used was 0.45 MHz, the spatial sampling interval was 1 mm and the sampling frequency was 3.125 MHz.

Modelling a notch inclined at an angle using finite elements represents a problem if wave propagation is to be modelled accurately, as a propagating wave will be reflected from any boundary across which there is a change in impedance, and any changes in shape or size of the element will cause a change in the effective impedance of the element and result in spurious reflections from the element boundaries. Hence, the 45° inclined notch was modelled by removing pairs of elements in a 'staircase' pattern which was not shown in Fig. 5.1(b) for clarity. However, this created an angled notch with stepped edges, the width of the step being one element.

The time history of the response of the top surface of the plate in the z direction at $x = 210$ mm, when the inclined notch was located at $x = 150$ mm is shown in Fig. 5.26(a). Fig. 5.26(b) shows the transmission ratios of the a_0 and s_0 modes as a function of the frequency-thickness product. The trend of the transmission ratio of the s_0 mode in Fig. 5.26(b) has slightly changed from the transmission ratio for the 1.0 mm deep slot normal to the plate surface (see Fig. 5.13(b)); the amplitude in this case increases slightly at higher frequency thickness values. However, the average transmission ratio of s_0 in region 1 is approximately 0.85 in both cases.

However, there are significant changes in the amplitude of the a_0 mode produced by mode conversion at the notch (Fig. 5.2(b)), the transmission at 1.1 MHzmm is larger than that with the notch normal to the surface (Fig. 5.13(b)), but at higher frequencies the transmission is significantly reduced. The reasons for this have not been investigated although it may be connected with the length of plate over which the notch runs which may be thought of as an effective notch width and this width is of the same order as the wavelength of a_0 in this frequency-thickness region.

5.5 Conclusions

The interaction of individual Lamb waves with a variety of simulated defects has been modelled successfully using finite elements. The results of the finite element study have been quantitatively analysed using the 2-D FFT method; in all cases the z direction displacements were recorded as this is the displacement measured in experimental tests when grease or immersion coupling is employed.

The FE results have shown that the sensitivity of individual Lamb waves to particular notches is dependent on the frequency-thickness product, the mode type (symmetric or antisymmetric), the mode order, and the geometry of the notch. The sensitivity of the Lamb modes a_1 , a_0 and s_0 to simulated defects in different frequency-thickness regions has been determined as a function of the defect depth and plate thickness ratio ($h/2d$). The results have indicated that Lamb waves may be used to find notches when the wavelength to notch depth ratio is of the order of 40.

The tests with an inclined notch have indicated that the reflection and transmission of Lamb waves is largely dependent on the notch depth (ie distance of penetration normal to the plate surface) rather than overall notch length.

The tests on notches of different widths have indicated that provided the width is small compared to the wavelength the transmission and reflection amplitudes are insensitive to changes in width so the depth of the notch is the major parameter.

The amplitude ratios of the Lamb wave after interaction with notches are not monotonic functions of frequency-thickness and have indicated that the frequency of the minimum or maximum in the amplitude ratios may be used as the basis of a defect sizing technique.

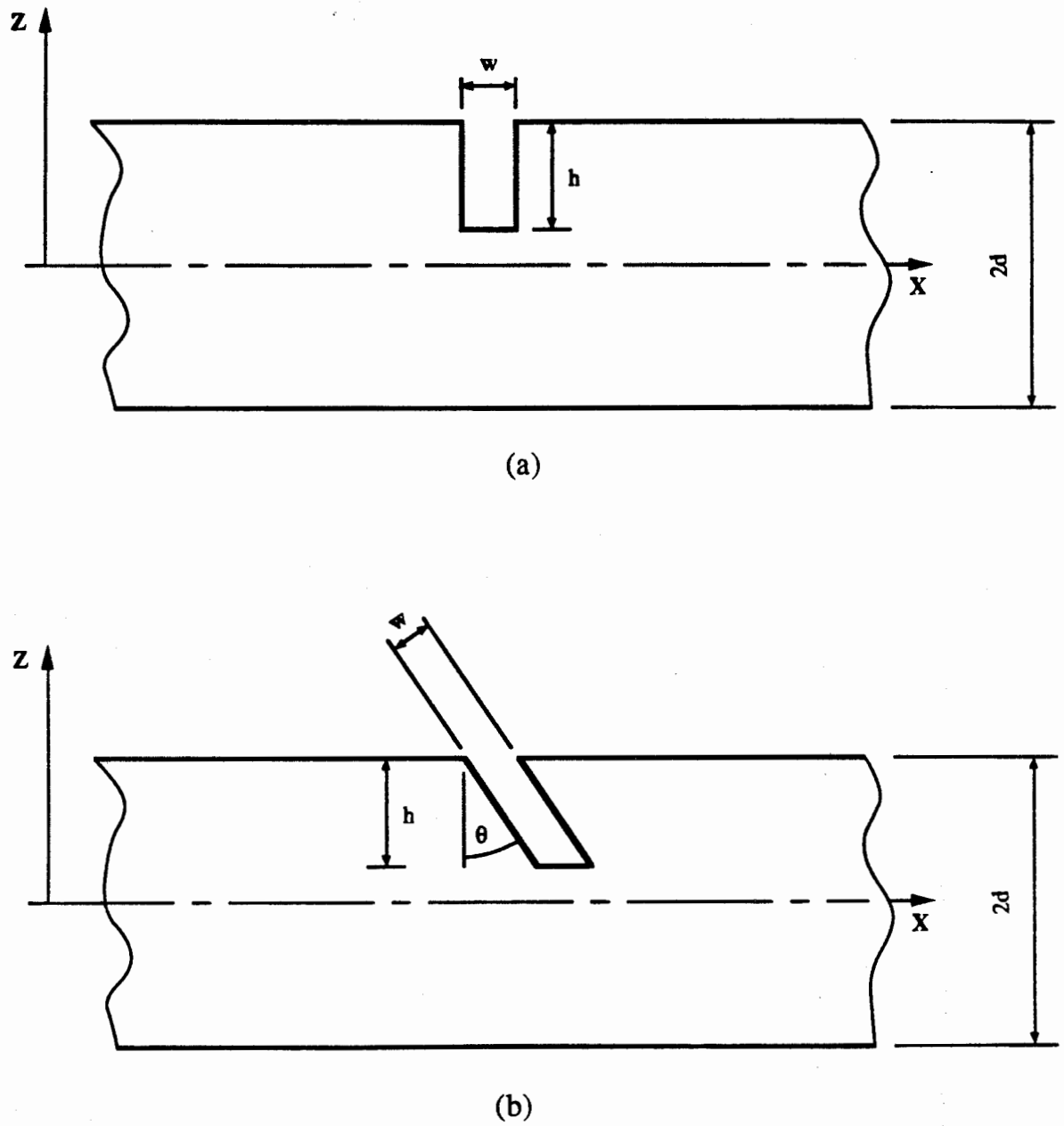


Figure 5.1 Schematic diagram of the notch geometry used in the finite element models.

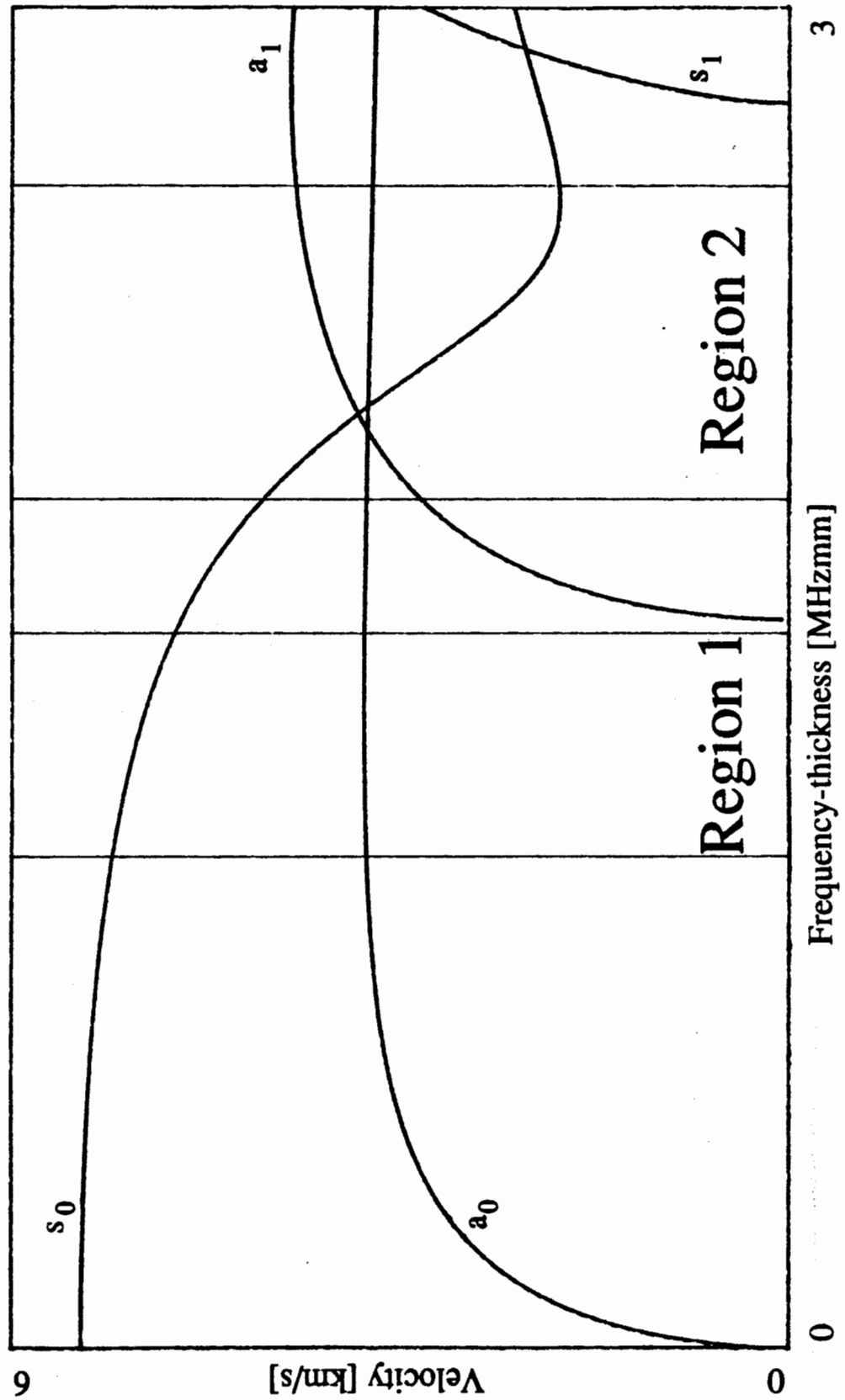


Figure 5.2 Lamb wave group velocity dispersion curves for steel showing the frequency-thickness regions in which the finite element modelling was carried out.

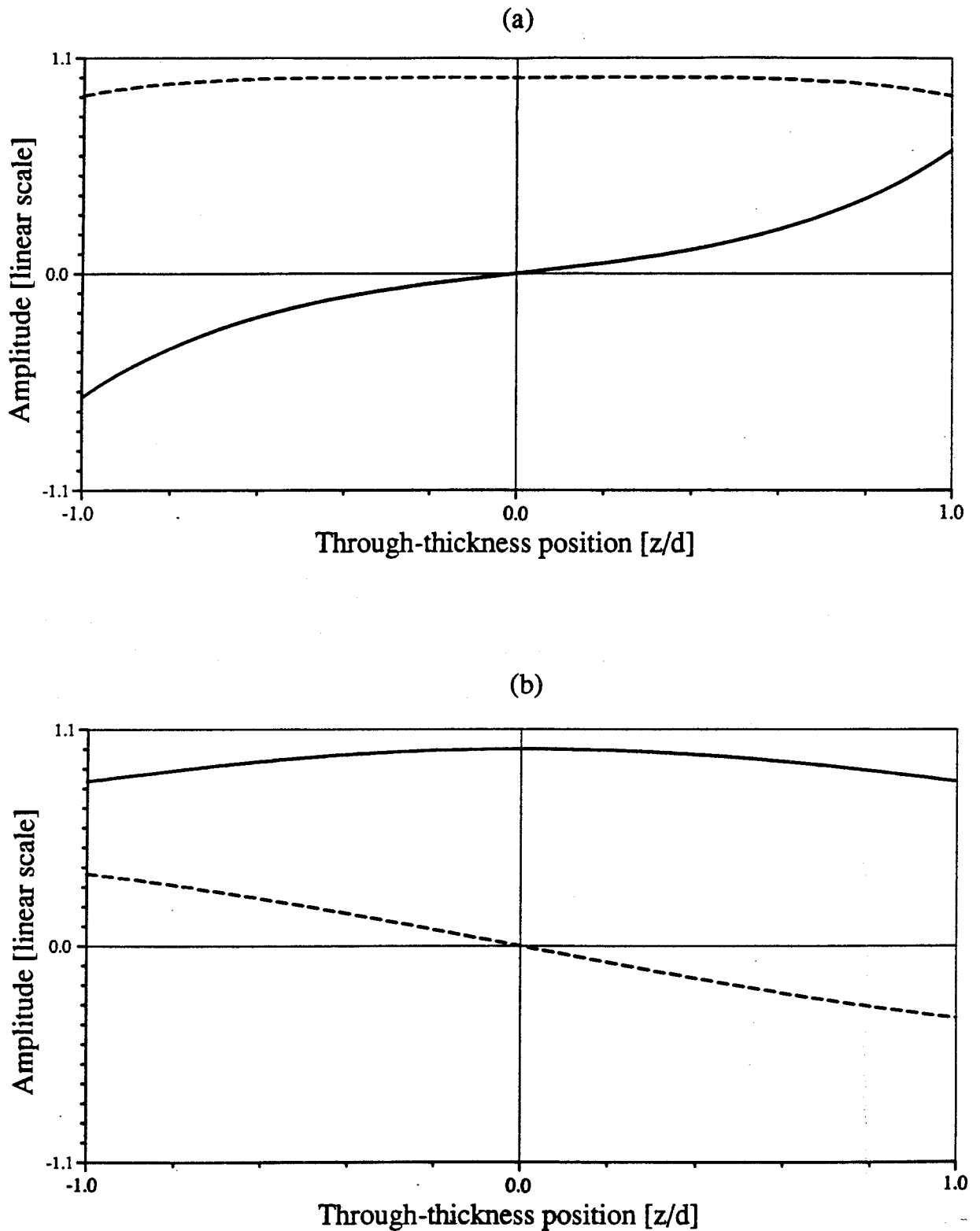


Figure 5.3 The through-thickness deflected mode shapes of Lamb waves, where c_1 and c_2 are the same as in figure 2.4: — x-direction displacements; - - - z-direction displacements. (a) a_0 at 1.35 MHzmm (b) s_0 at 1.35 MHzmm.

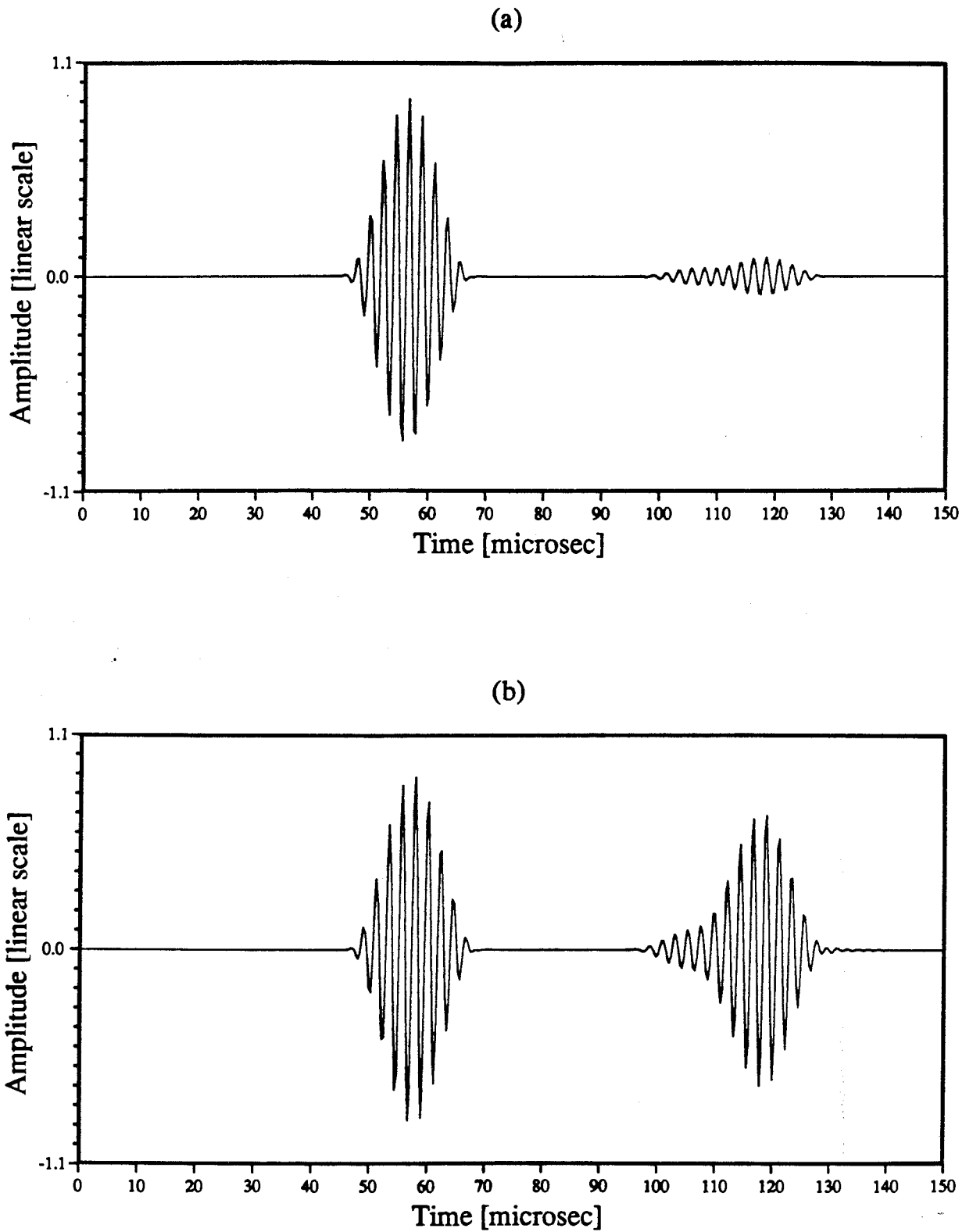


Figure 5.4 (a) Predicted time history at $x = 150$ mm in a 3.0 mm thick plate showing the first passage of the a_0 mode and the reflection from the 0.5 mm deep notch, and (b) the predicted time history when the notch was 2.0 mm deep.

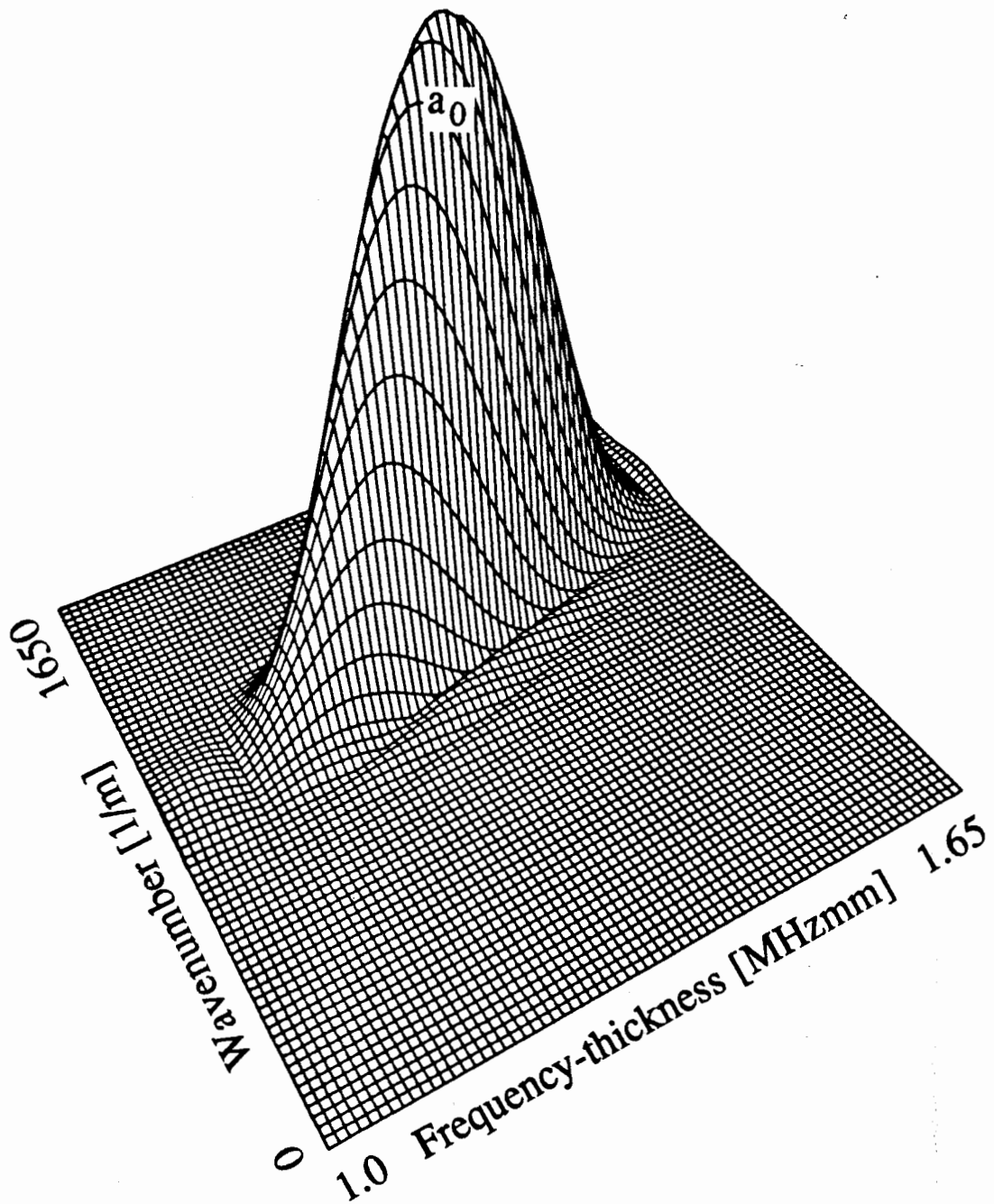


Figure 5.5 Normalised 3-D plot of the 2-D FFT results of the case given in Fig. 5.4 when the signal reflected from the notch was gated out and shows a single propagating mode, a_0 .

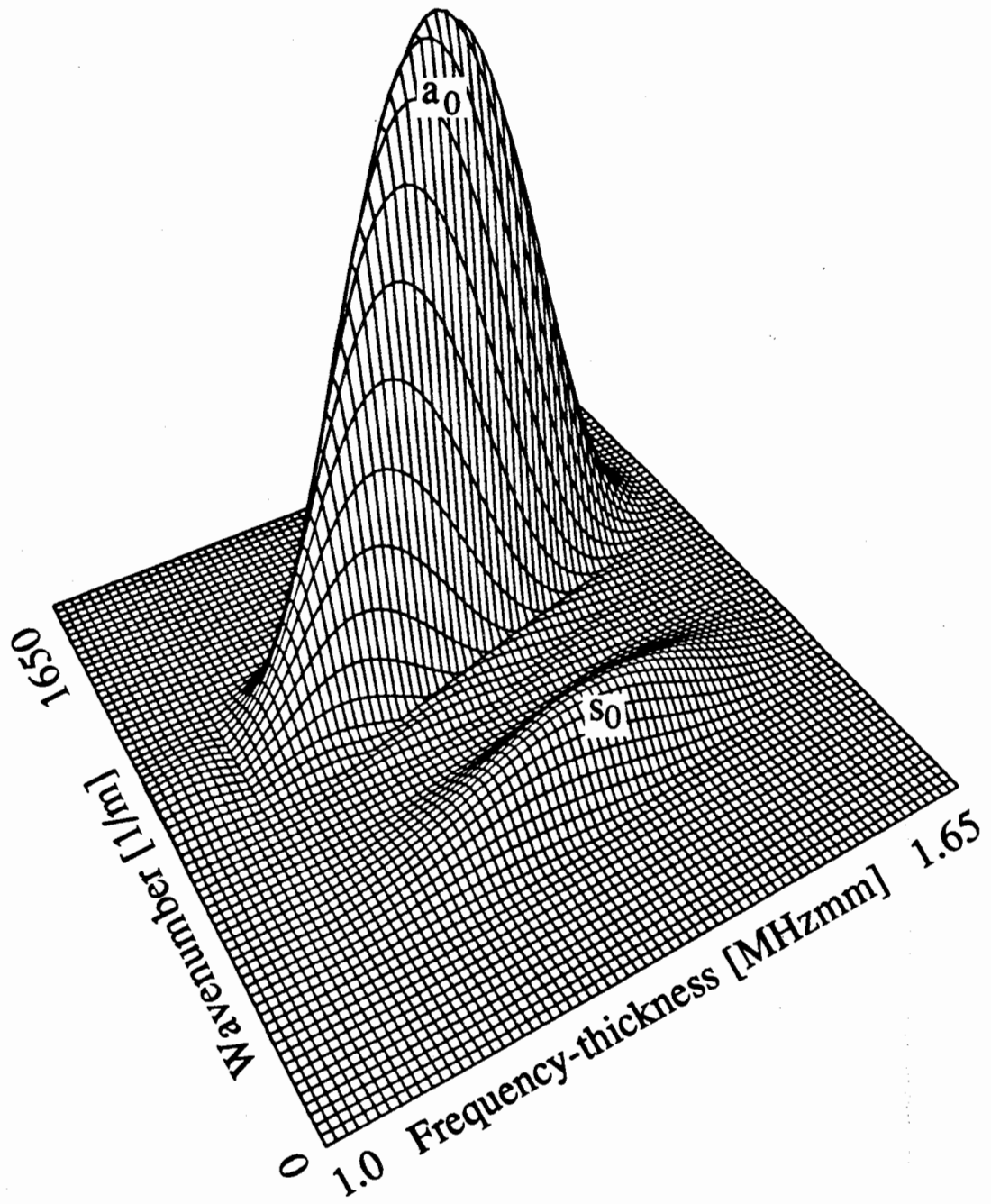


Figure 5.6 Normalised 3-D plot of the 2-D FFT results from the reflected wave shown in Fig. 5.4(b).

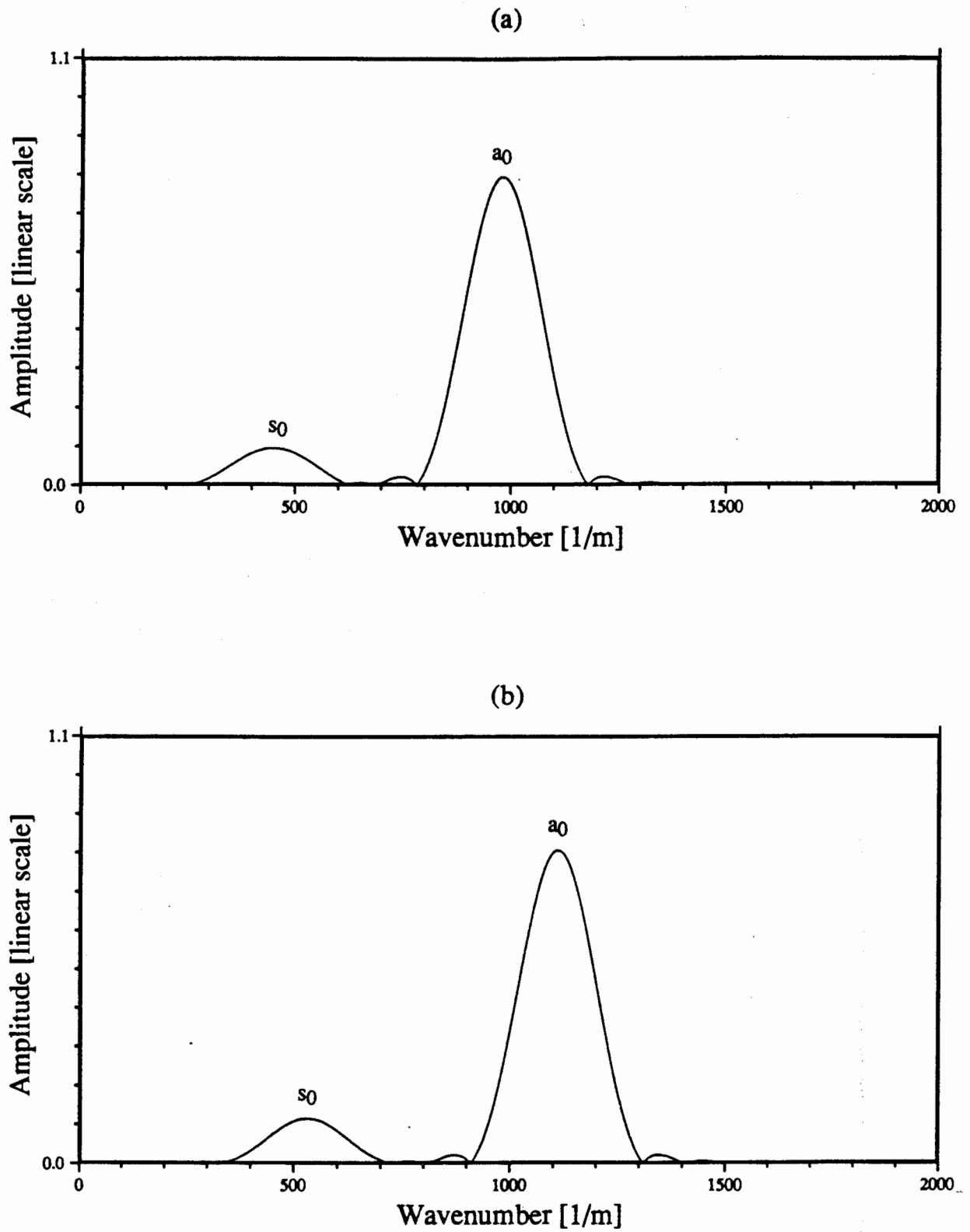


Figure 5.7 (a) Normalised amplitude versus wavenumber at 1.26 MHzmm obtained from the results shown in Fig. 5.5 and (b) at 1.36 MHzmm.

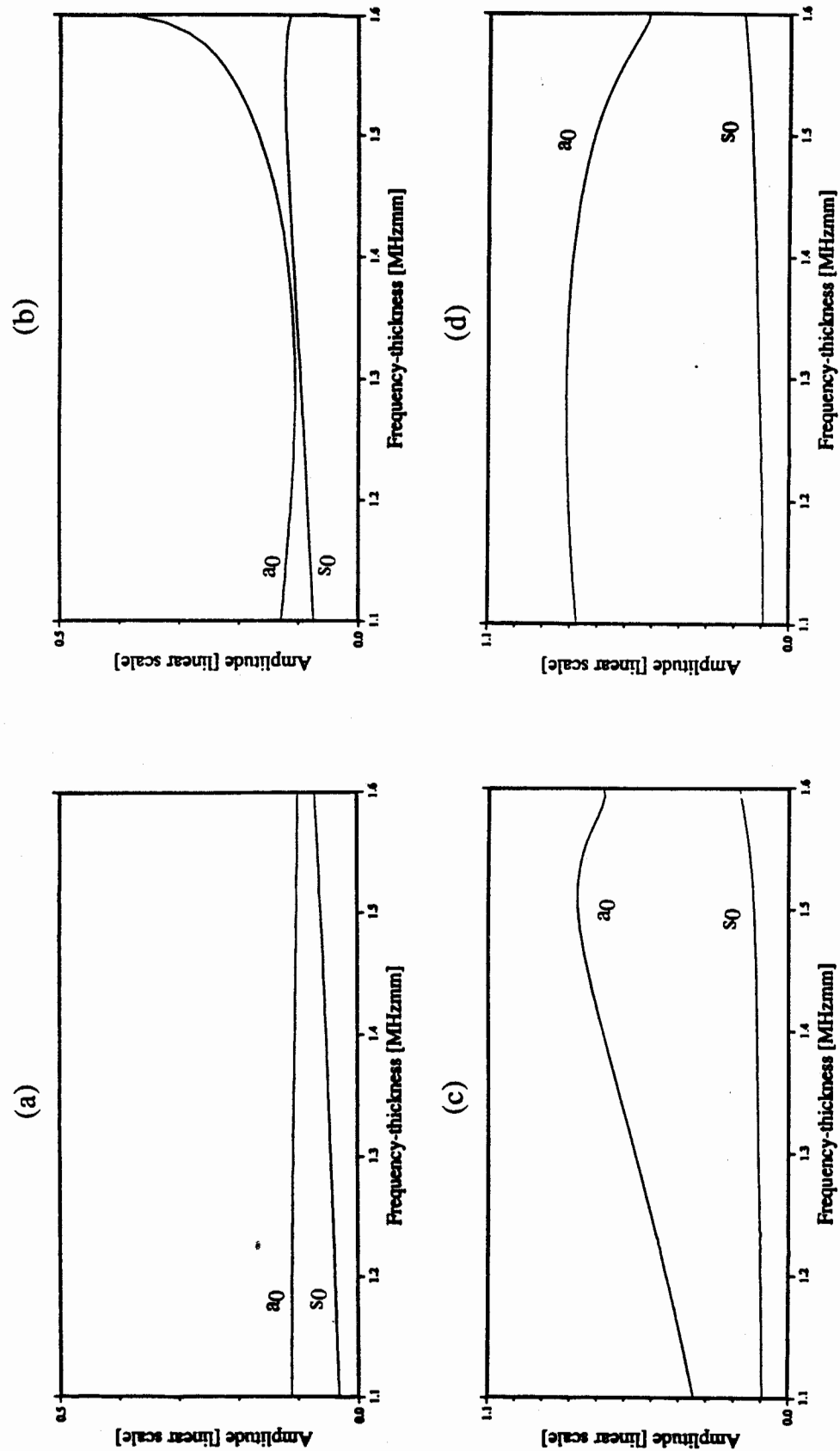


Figure 5.8 Predicted reflection ratio of the a_0 mode as a function of frequency-thickness in a 3.0 mm thick plate after interaction with (a) the 0.5 mm deep notch, (b) the 1.0 mm notch, (c) the 1.5 mm notch and (d) the 2.0 mm notch.

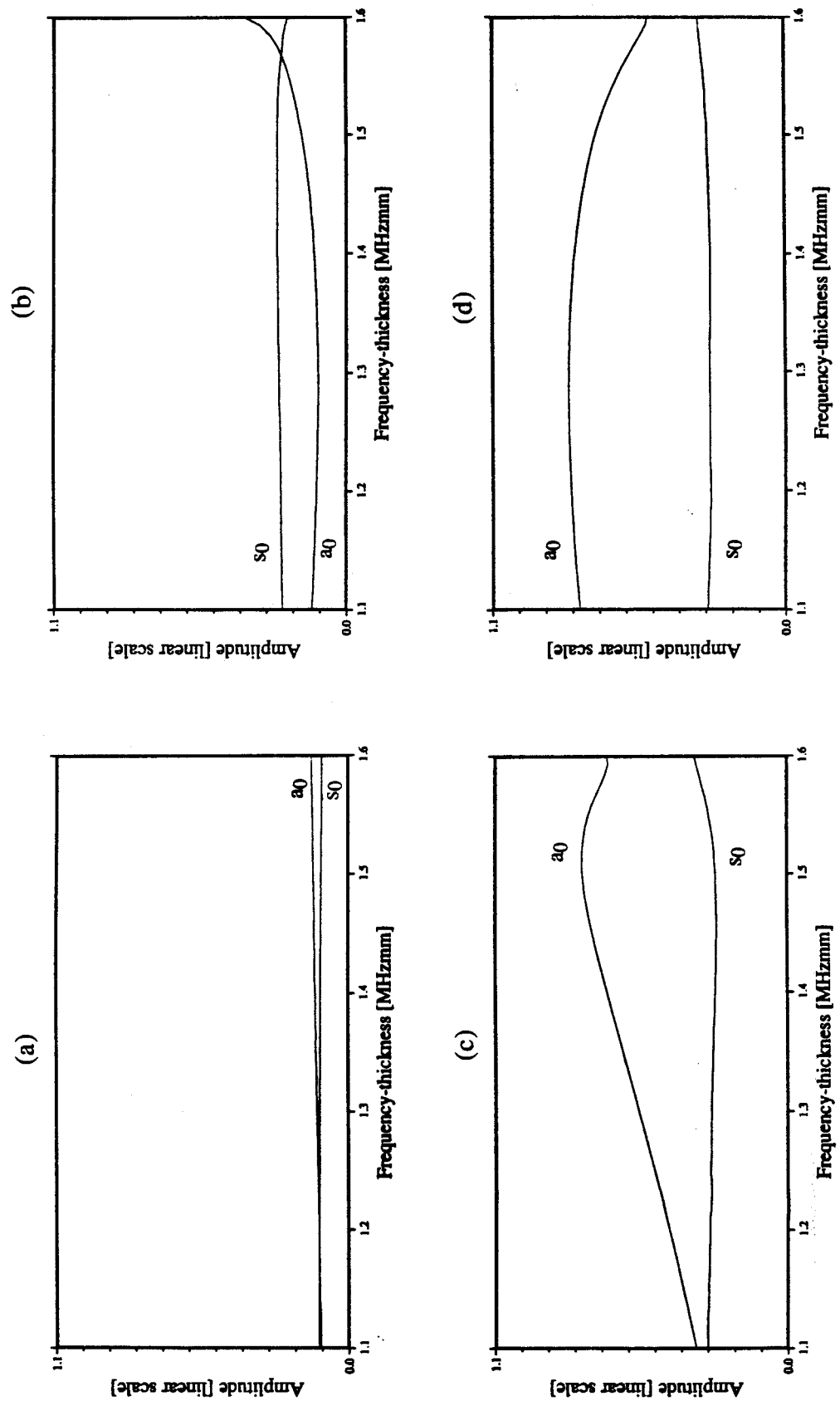


Figure 5.9 Predicted normalised reflection ratio of the a_0 mode as a function of frequency-thickness after interaction with (a) the 0.5 mm deep notch, (b) the 1.0 mm notch, (c) the 1.5 mm notch and (d) the 2.0 mm notch.

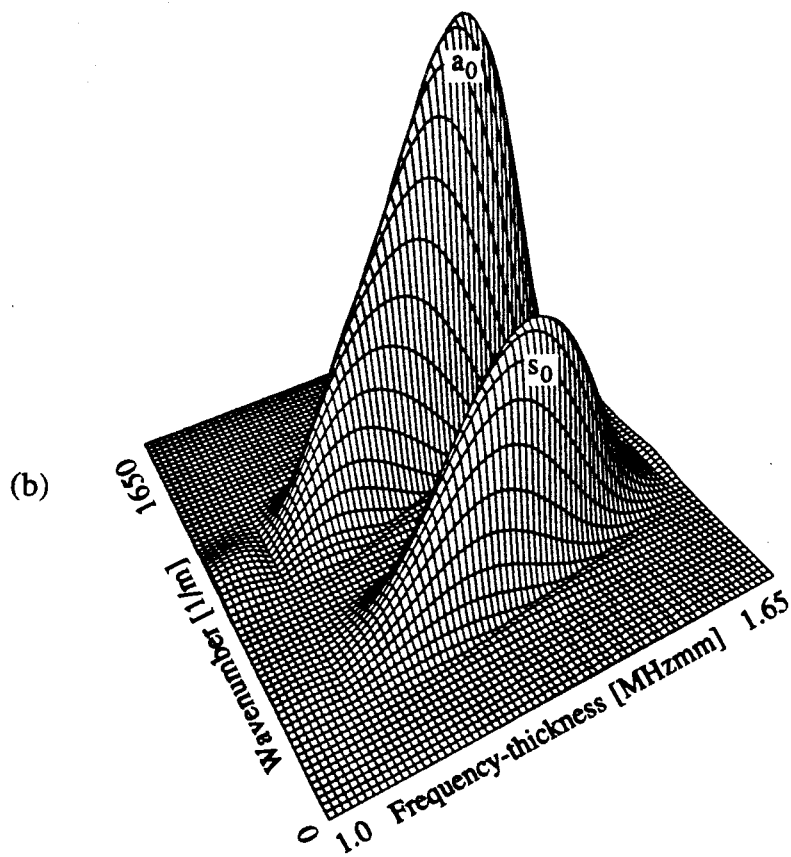
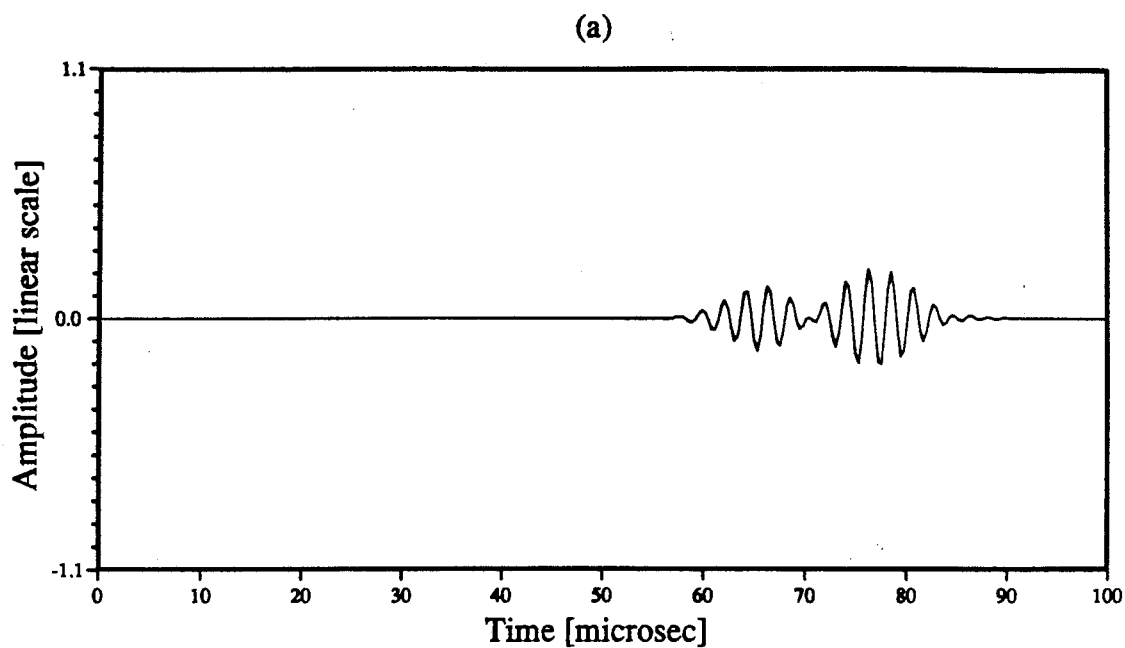


Figure 5.10 (a) Predicted time history in a 3.0 mm thick plate 50 mm after interaction with the 2.0 mm deep notch, when the input signal was designed to excite only a_0 . (b) Normalised 3-D plot of the 2-D FFT results for the case given in (a).

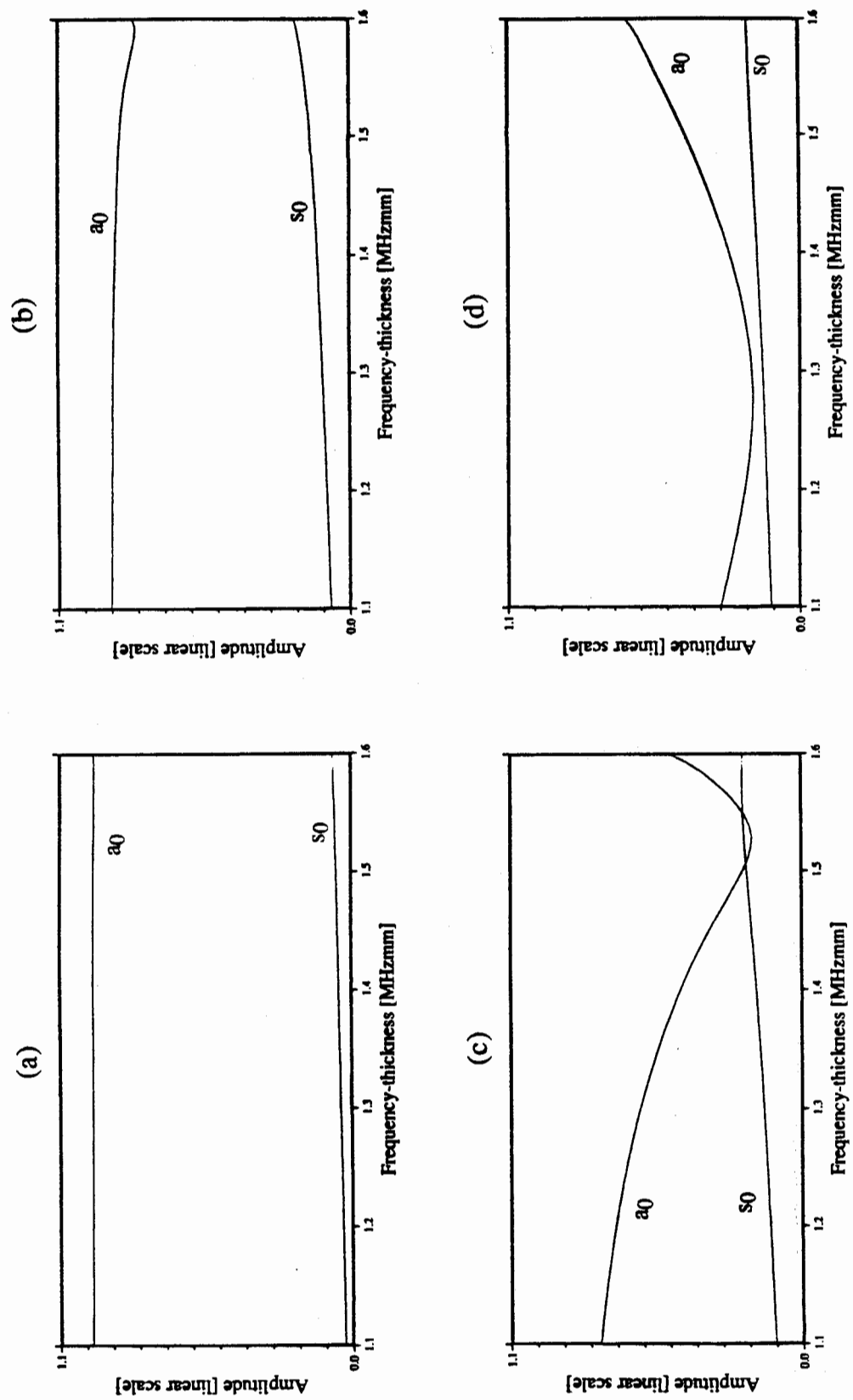


Figure 5.11 Predicted transmission ratio of the a_0 mode as a function of frequency-thickness after interaction with (a) the 0.5 mm deep notch, (b) the 1.0 mm notch, (c) the 1.5 mm notch and (d) the 2.0 mm notch.

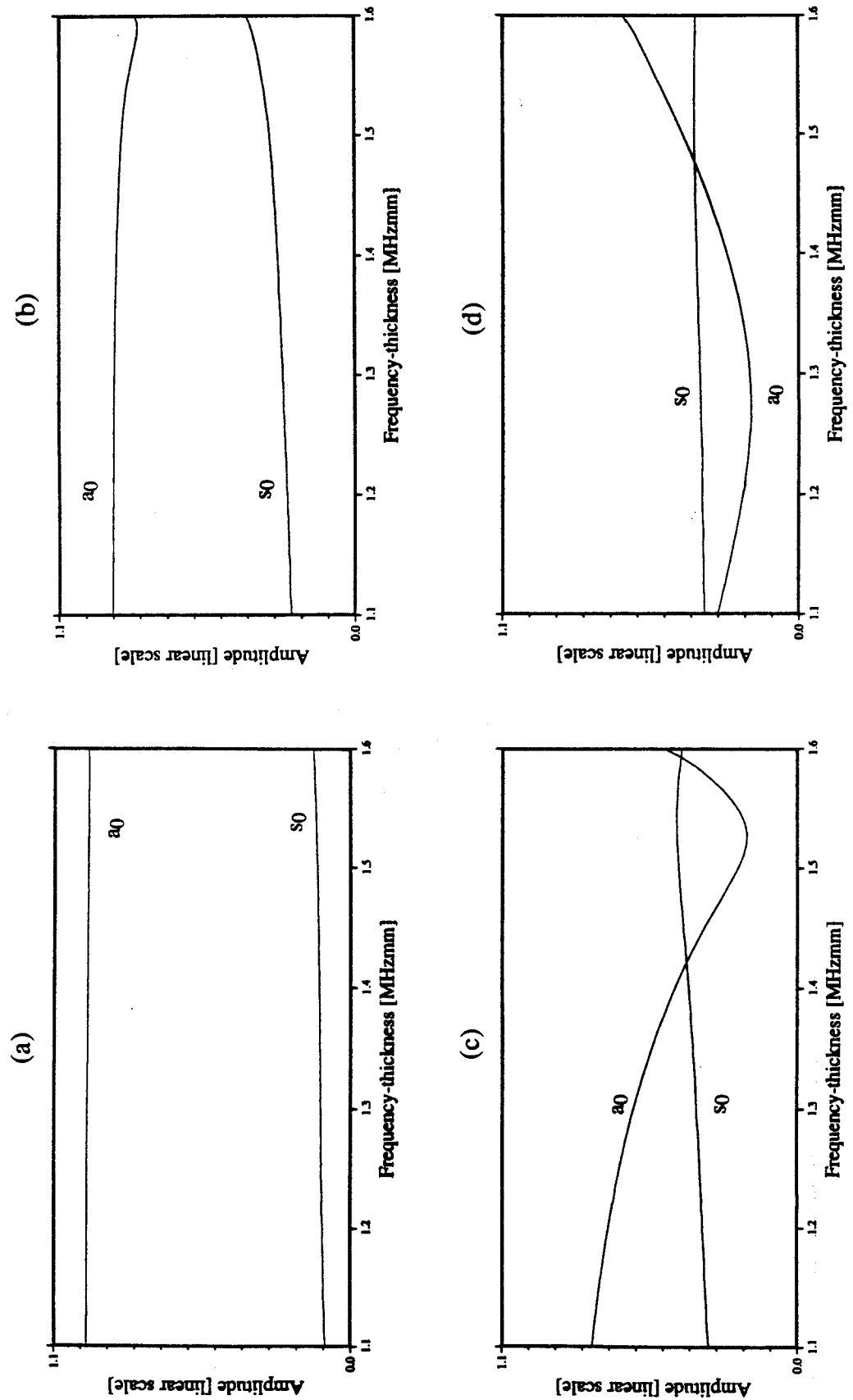


Figure 5.12 Predicted normalised transmission ratio of the a_0 mode as a function of frequency-thickness after interaction with (a) the 0.5 mm deep notch, (b) the 1.0 mm notch, (c) the 1.5 mm notch and (d) the 2.0 mm notch.

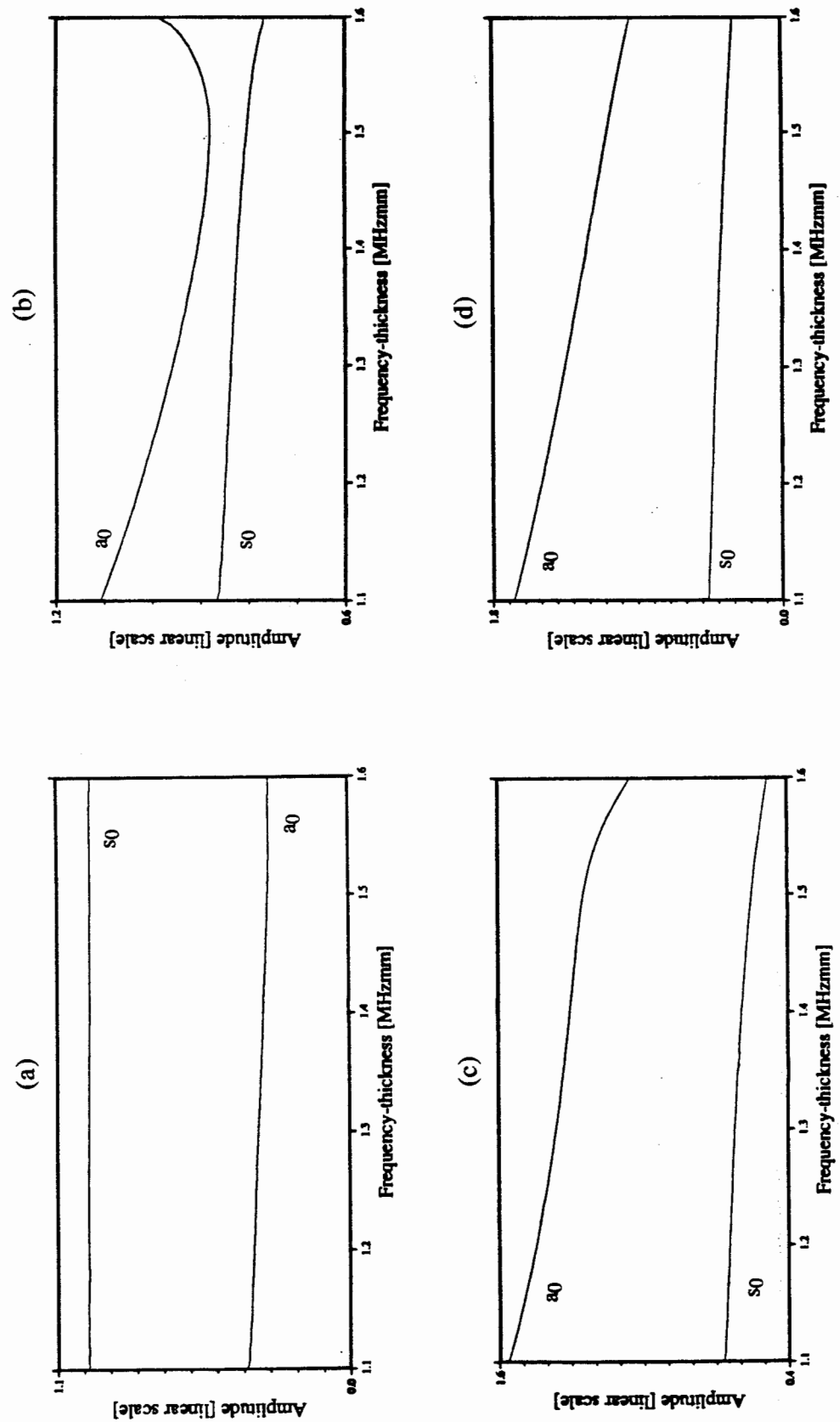


Figure 5.13 Predicted transmission ratio of the s_0 mode as a function of frequency-thickness after interaction with (a) the 0.5 mm deep notch, (b) the 1.0 mm notch, (c) the 1.5 mm notch and (d) the 2.0 mm notch.

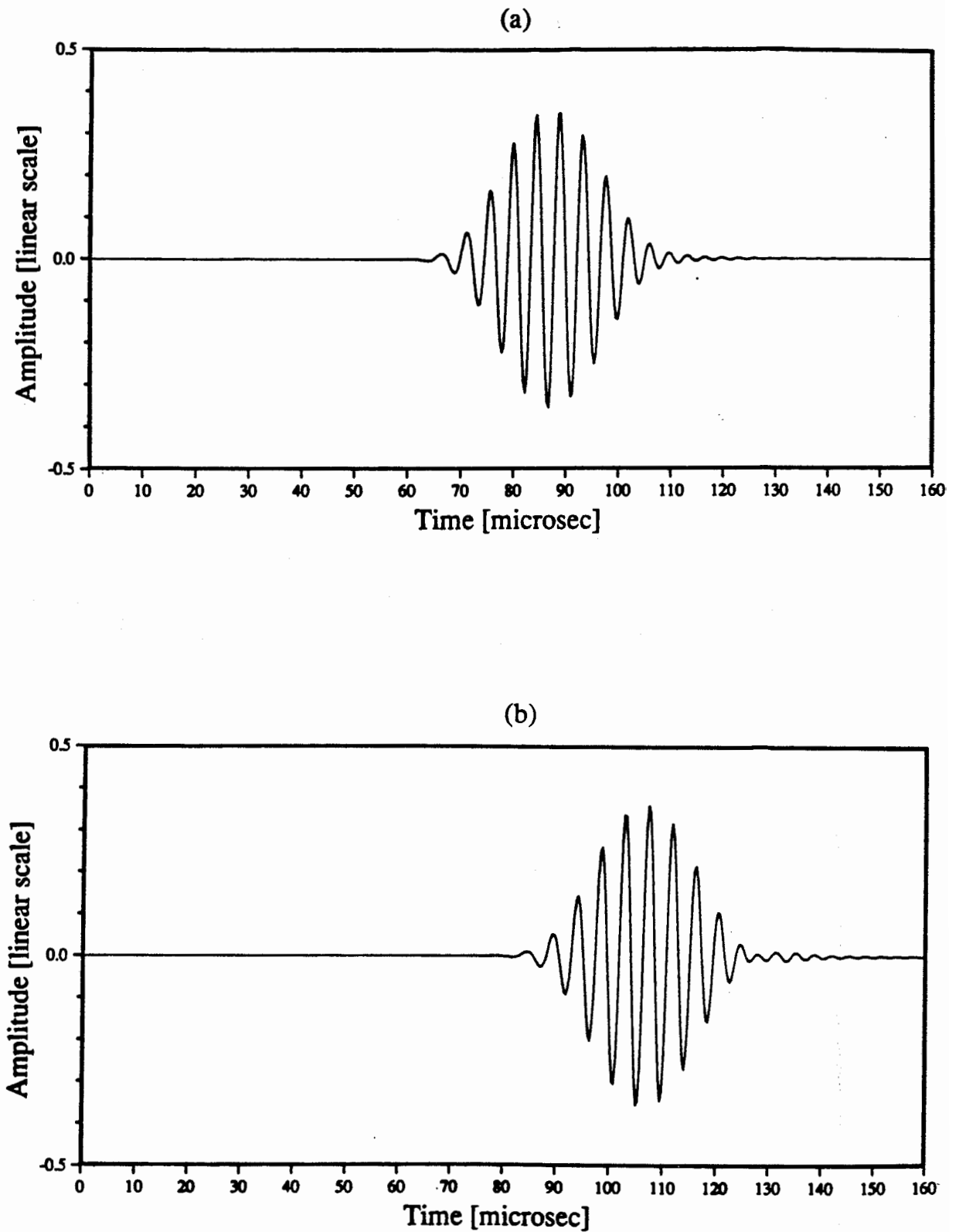


Figure 5.14 (a) Predicted time history in a 6.0 mm thick plate 5 mm after interaction with a 0.5 mm deep notch, when the input signal was designed to excite only s_0 . (b) at 55 mm after the notch.

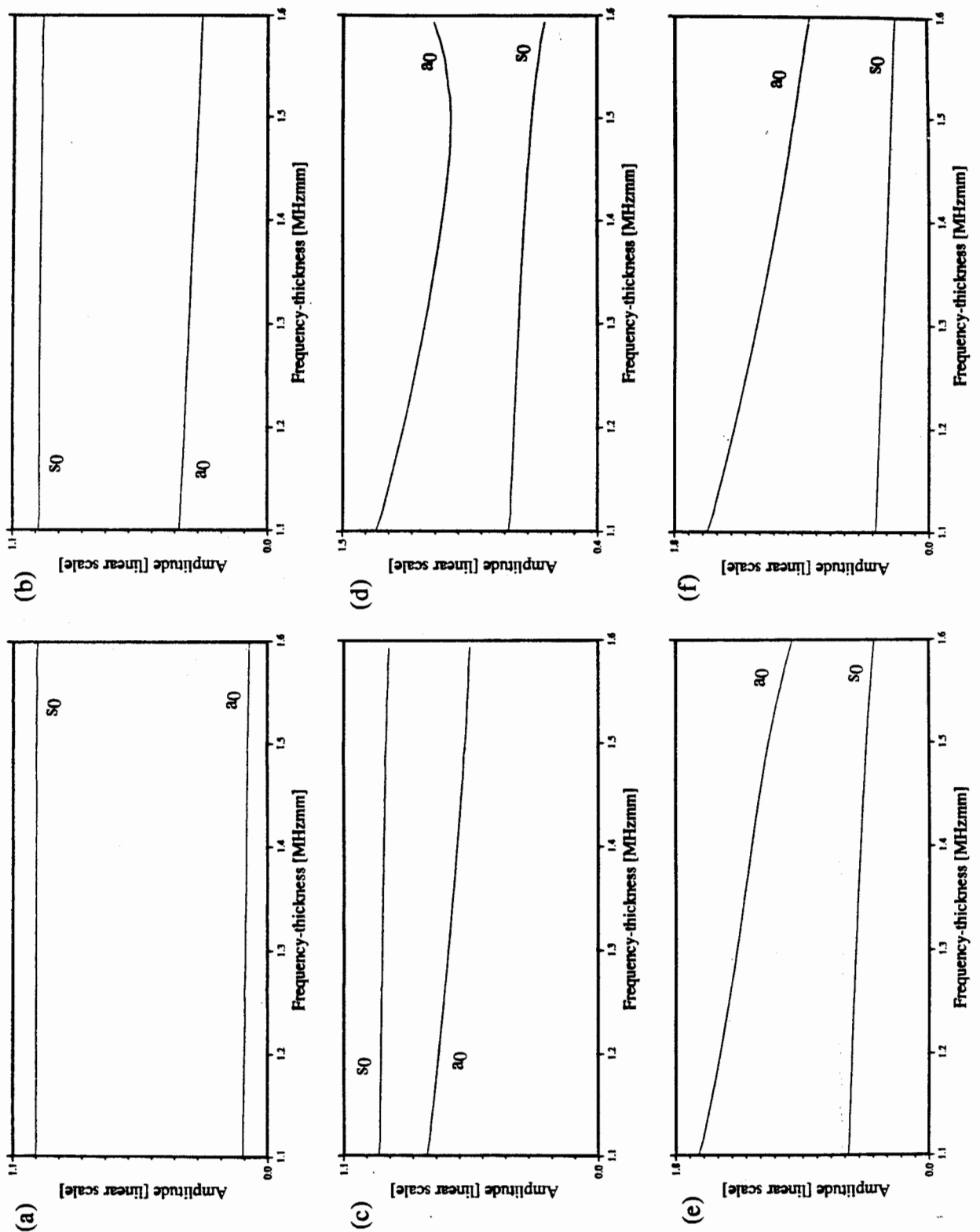


Figure 5.15 Predicted transmission ratio of the s_0 mode as a function of frequency-thickness in the 6.0 mm thick plate after interaction with (a) the 0.5 mm deep notch, (b) the 1.0 mm notch, (c) the 1.5 mm notch, (d) the 2.5 mm notch, (e) the 3.5 mm notch and (f) the 4.5 mm notch.

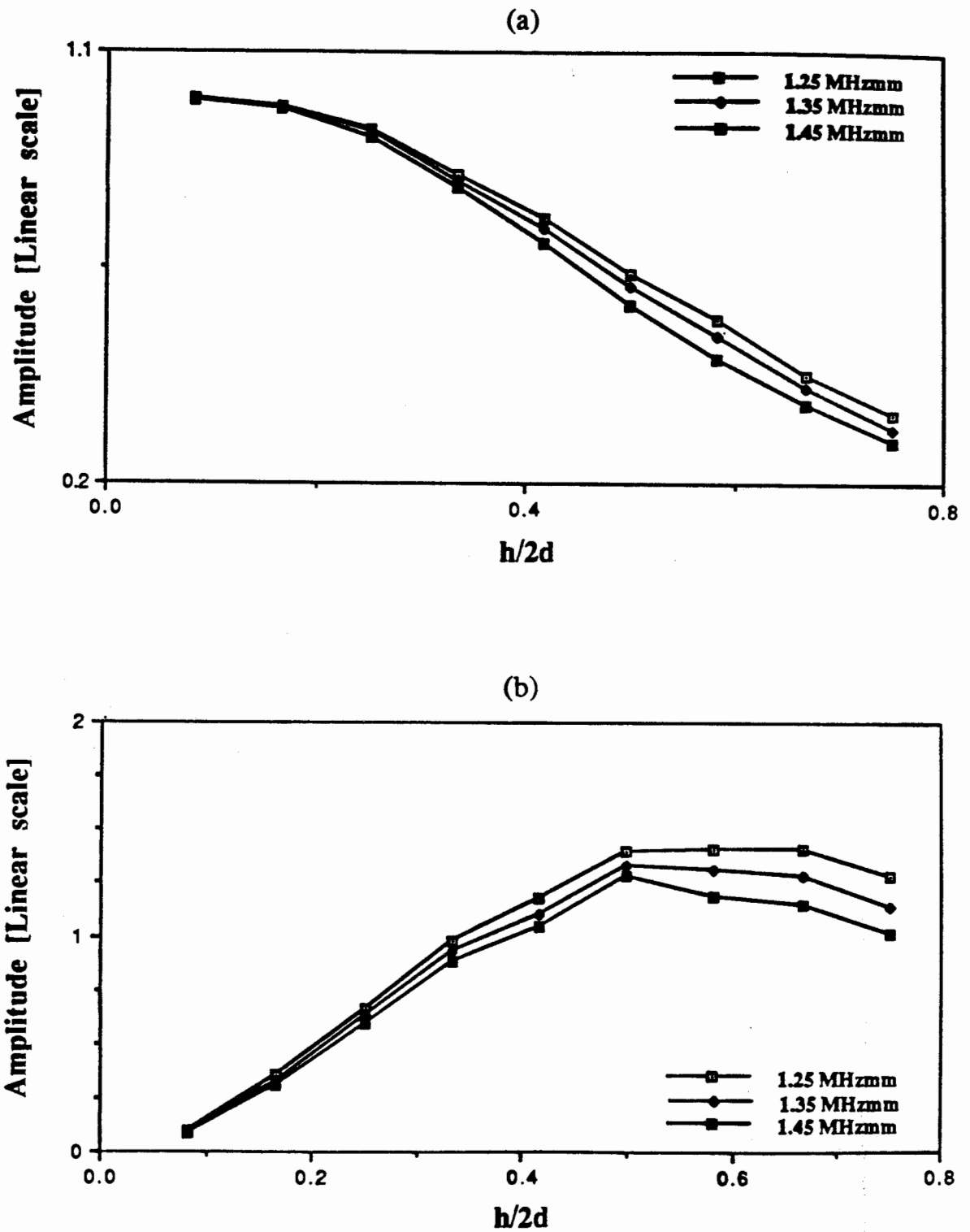


Figure 5.16 Predicted transmission ratio as a function of $h/2d$ at 1.25, 1.35 and 1.45 MHzmm (a) for the s_0 mode and (b) for a_0 produced by mode conversion at the notch.

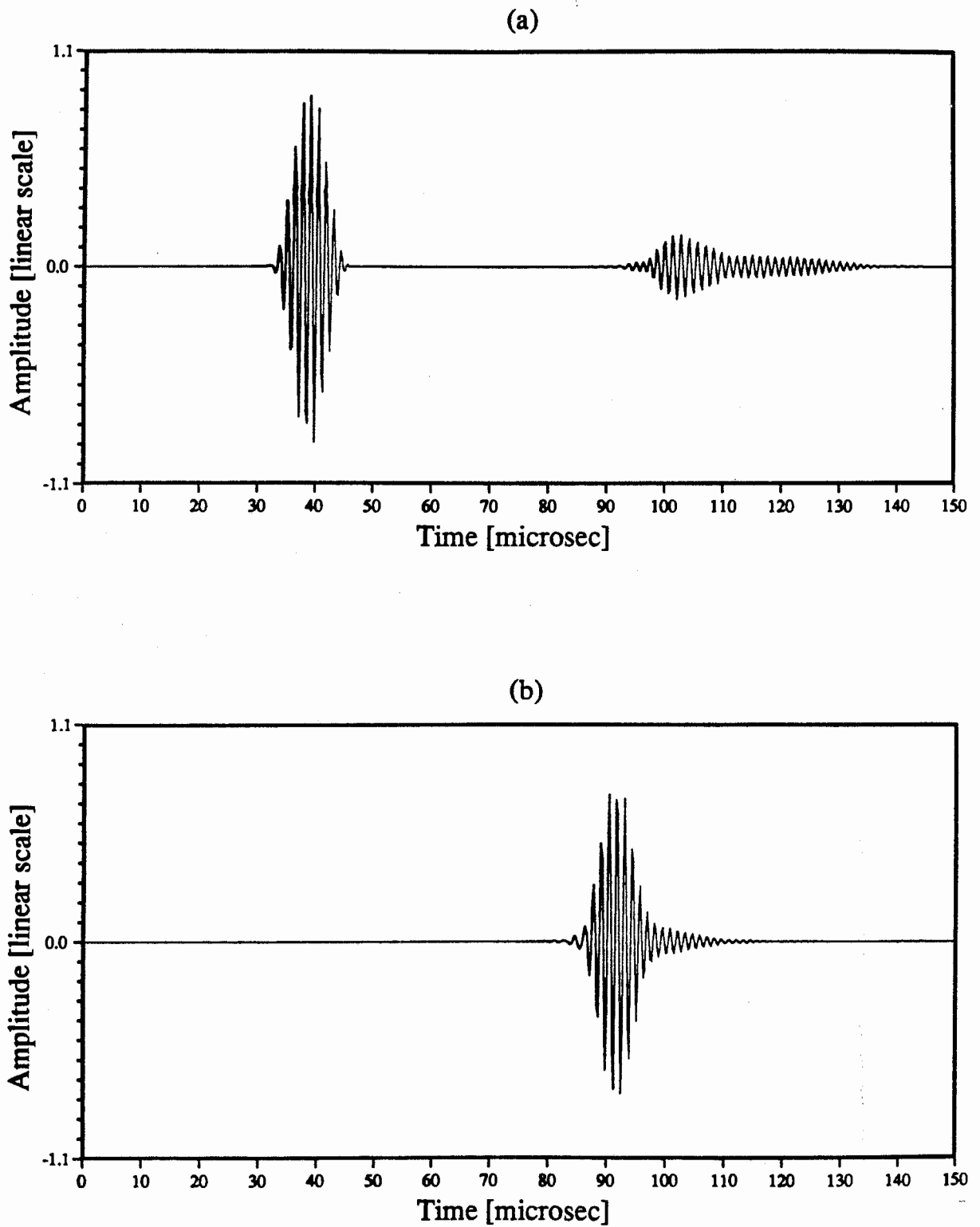


Figure 5.17 (a) Predicted time history in a 3.0 mm thick plate 105 mm before the 0.5 mm deep notch, when the centre frequency of the input tone burst was 0.75 MHz and was designed to excite only a_0 . (b) at 65 mm after the notch.

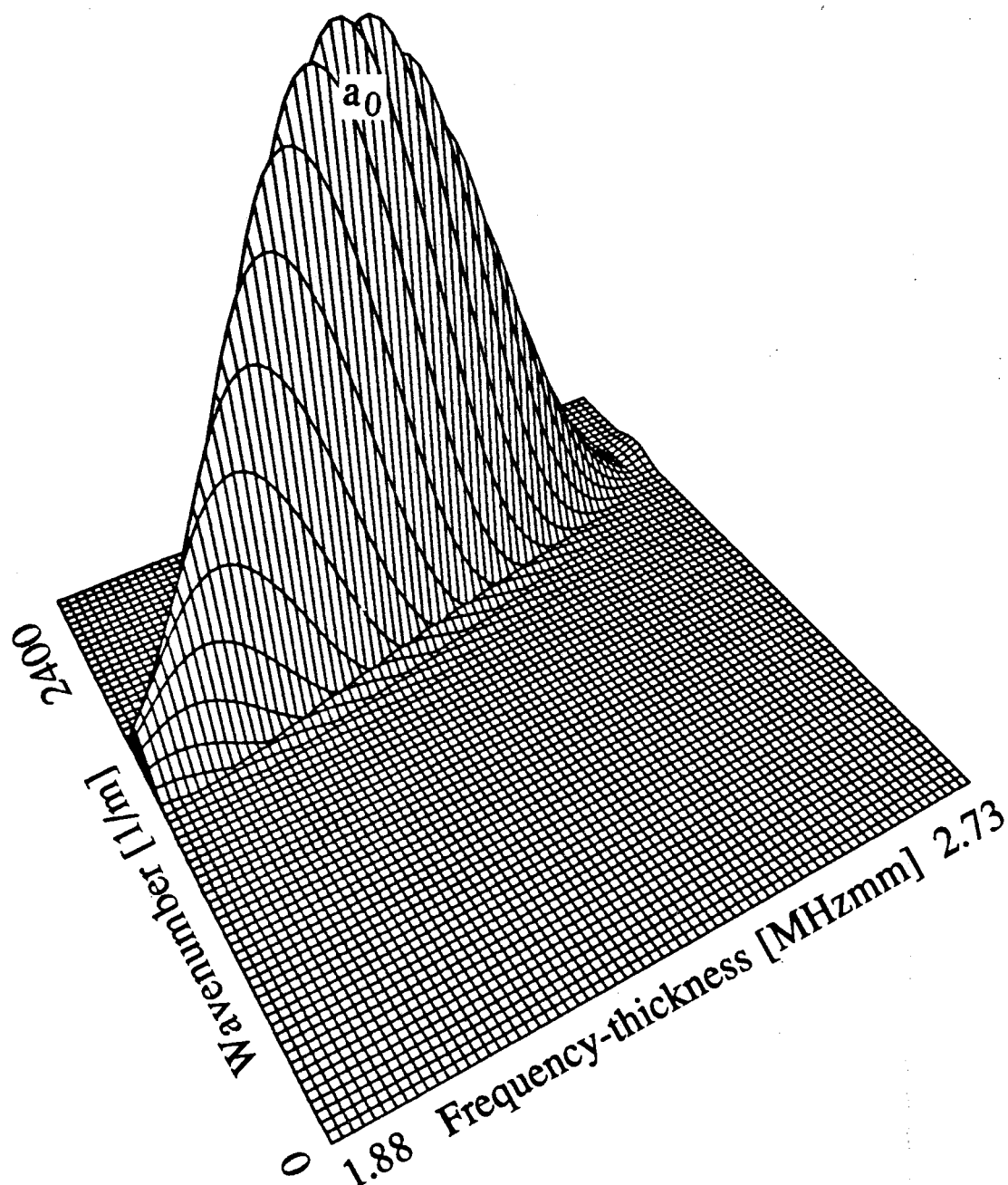


Figure 5.18 Normalised 3-D plot of the 2-D FFT results of the case given in Fig. 5.17(a) when the signal reflected from the notch was gated out, showing a single propagating mode, a_0 .

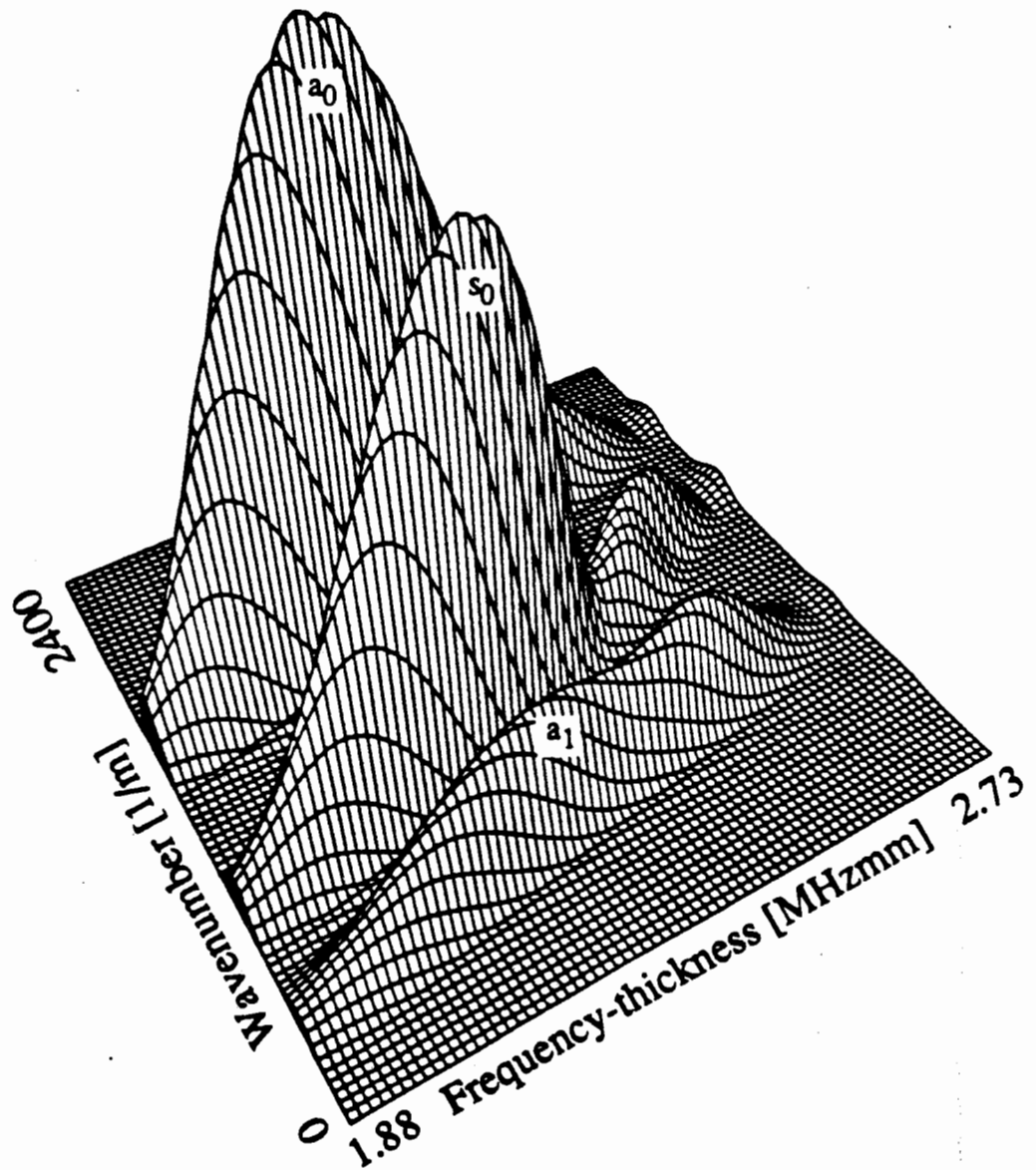


Figure 5.19 Normalised 3-D plot of the 2-D FFT results of the case shown in Fig. 5.17(a) when the incident wave ($t \leq 70 \mu\text{s}$) was gated out. It shows that the signal reflected from the notch contains three propagating modes a_1 , s_0 and a_0 .

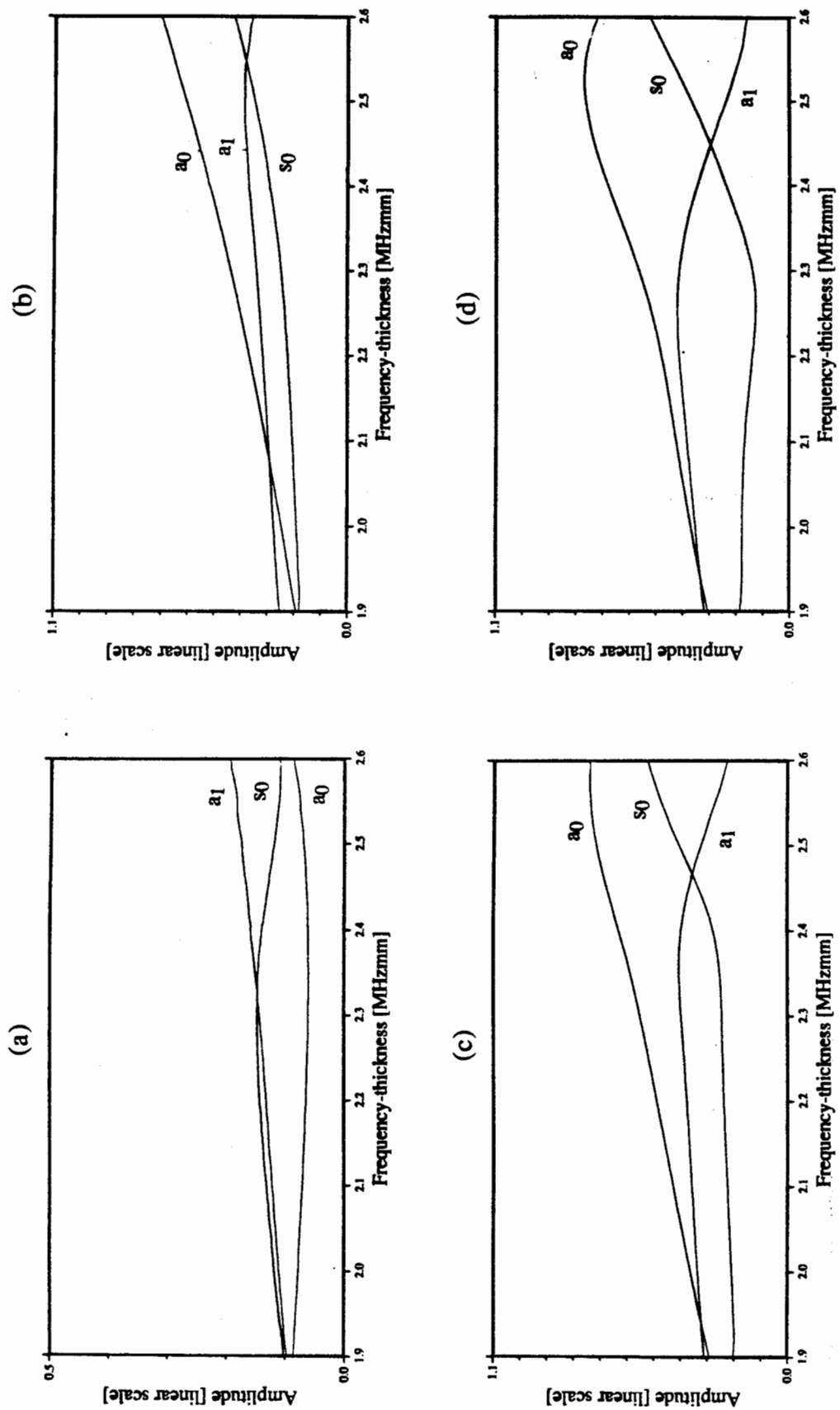


Figure 5.20 Predicted reflection ratio of the a_0 mode as a function of frequency-thickness in the 3.0 mm thick plate after interaction with (a) the 0.5 mm deep notch, (b) the 1.0 mm notch, (c) the 1.5 mm notch, (d) the 2.0 mm notch.

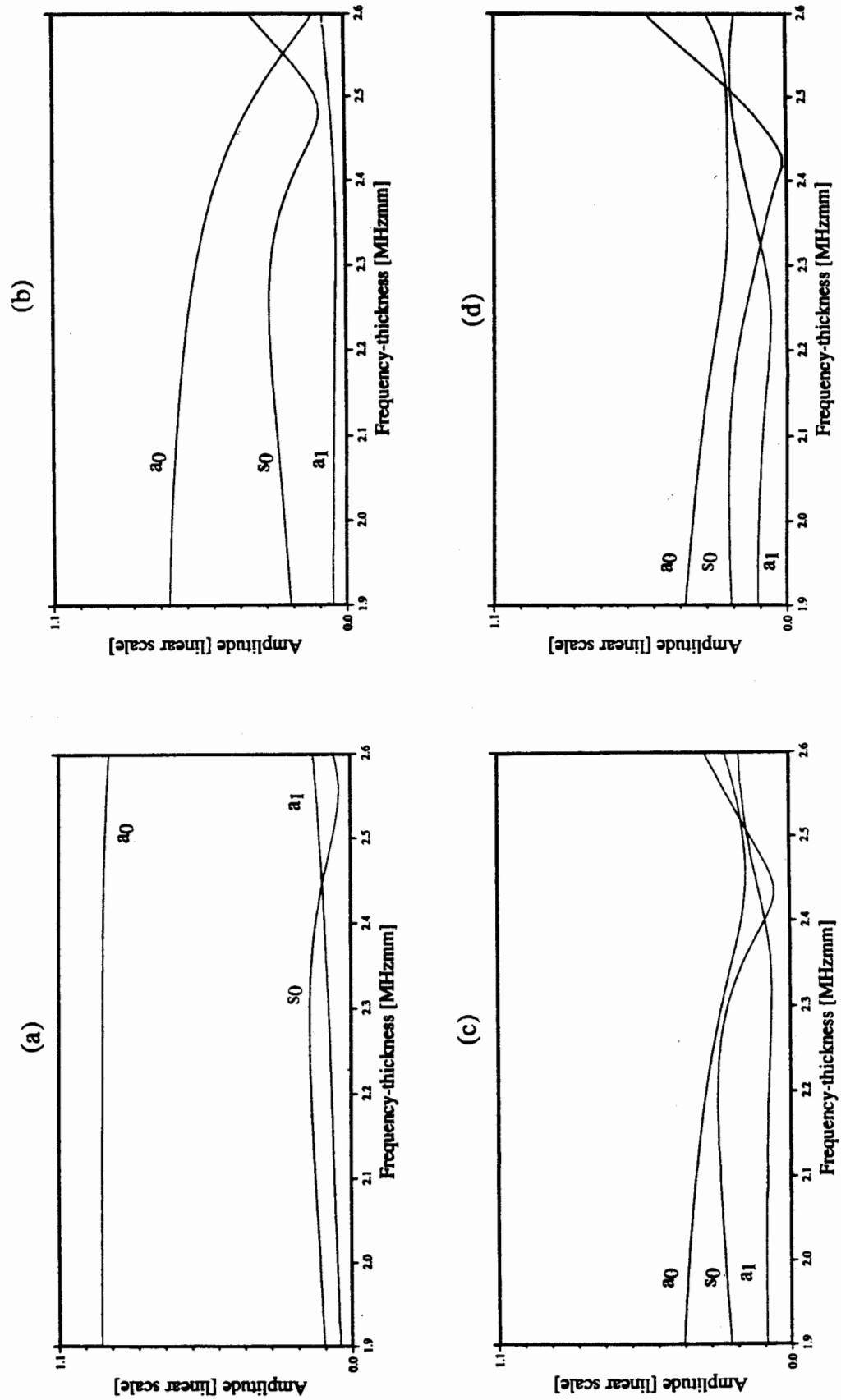


Figure 5.21 Predicted transmission ratio of the a_0 mode as a function of frequency-thickness in the 3.0 mm thick plate after interaction with (a) the 0.5 mm deep notch, (b) the 1.0 mm notch, (c) the 1.5 mm notch, (d) the 2.0 mm notch.

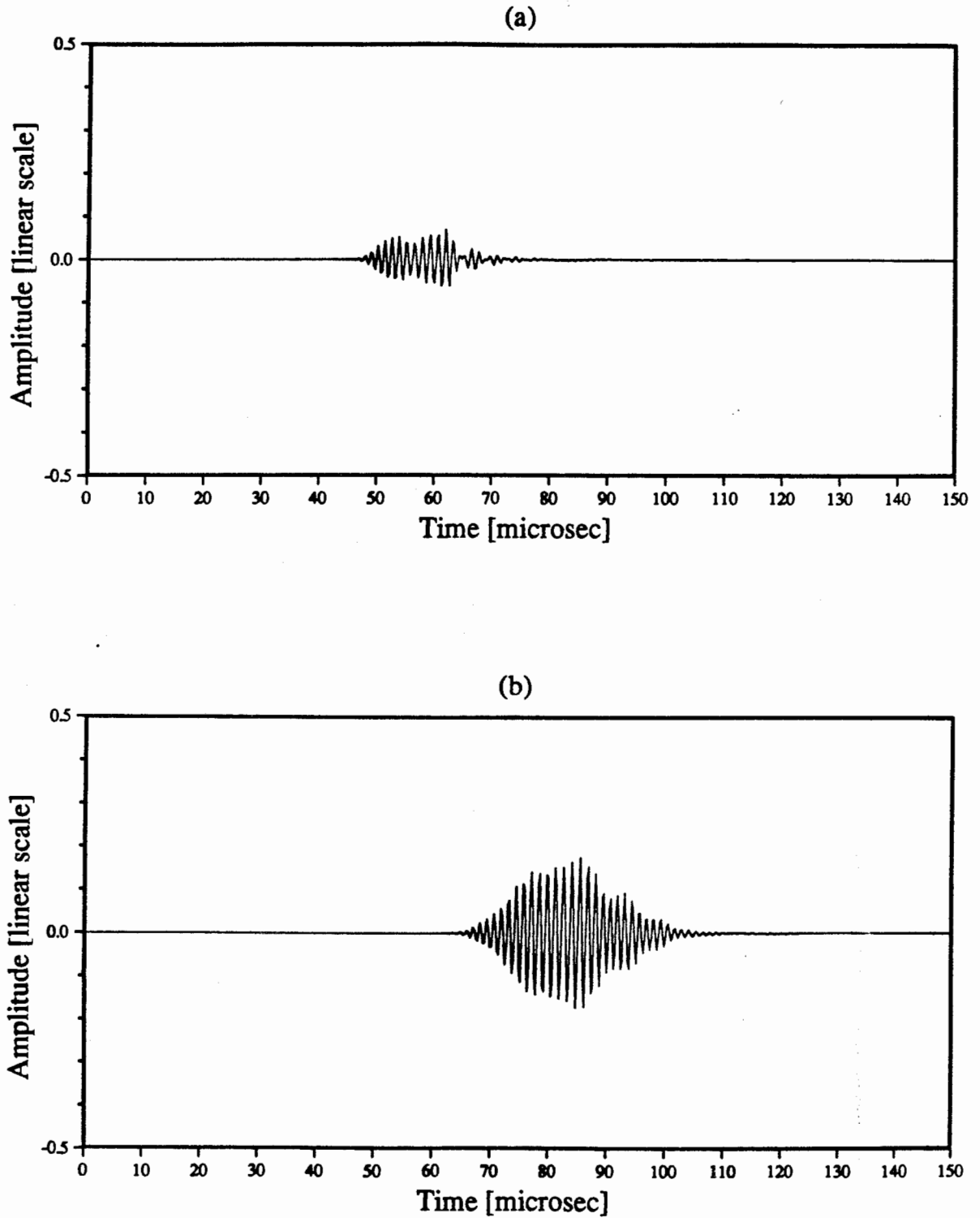


Figure 5.22 (a) Predicted time history in a 3.0 mm thick plate 5 mm after the 0.5 mm deep notch, when the centre frequency of the input tone burst was 0.75 MHz and was designed to excite only a_1 . (b) at 70 mm after the notch.

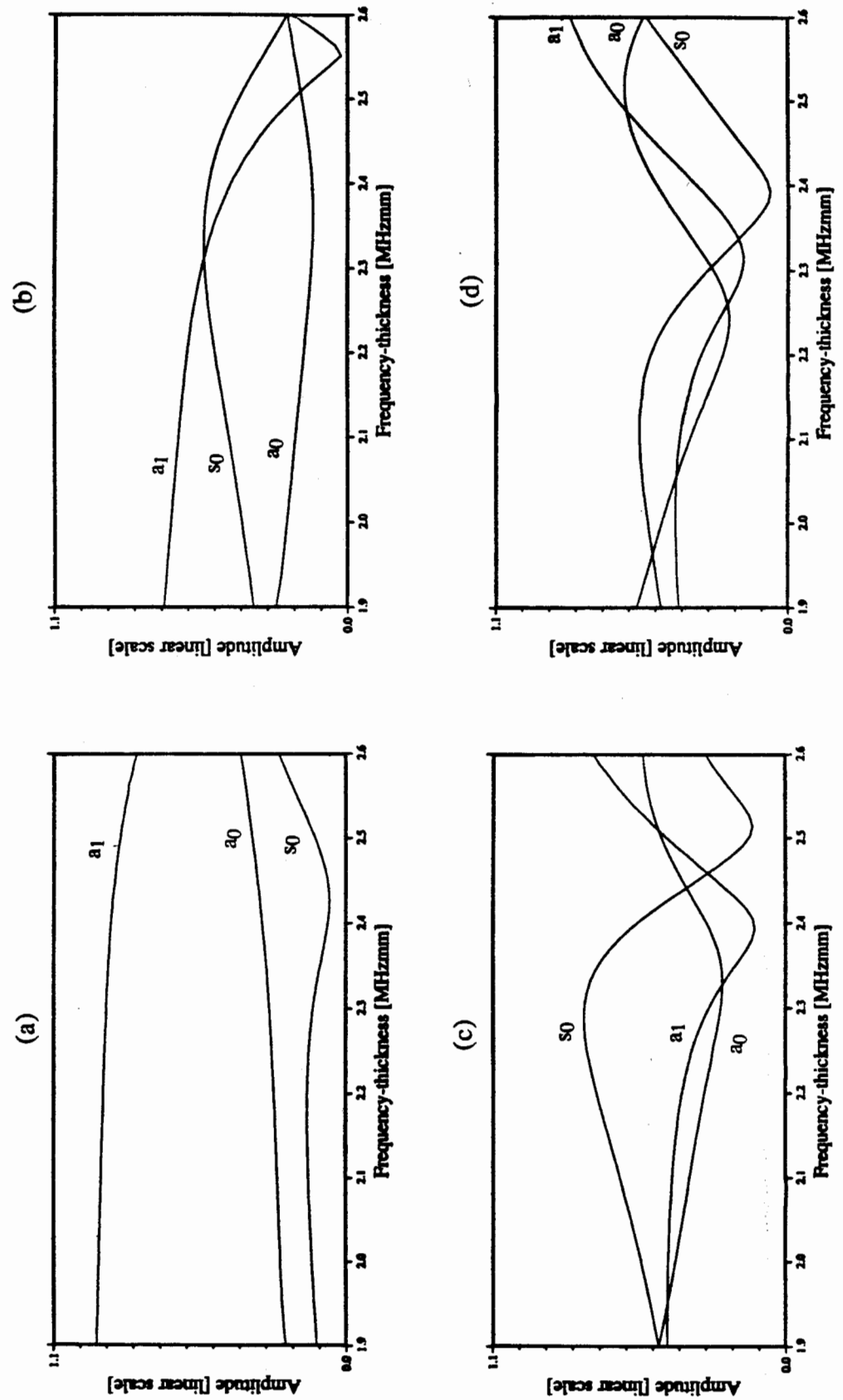


Figure 5.23 Predicted transmission ratio of the a_1 mode as a function of frequency-thickness in the 3.0 mm thick plate after interaction with (a) the 0.5 mm deep notch, (b) the 1.0 mm notch, (c) the 1.5 mm notch, (d) the 2.0 mm notch.

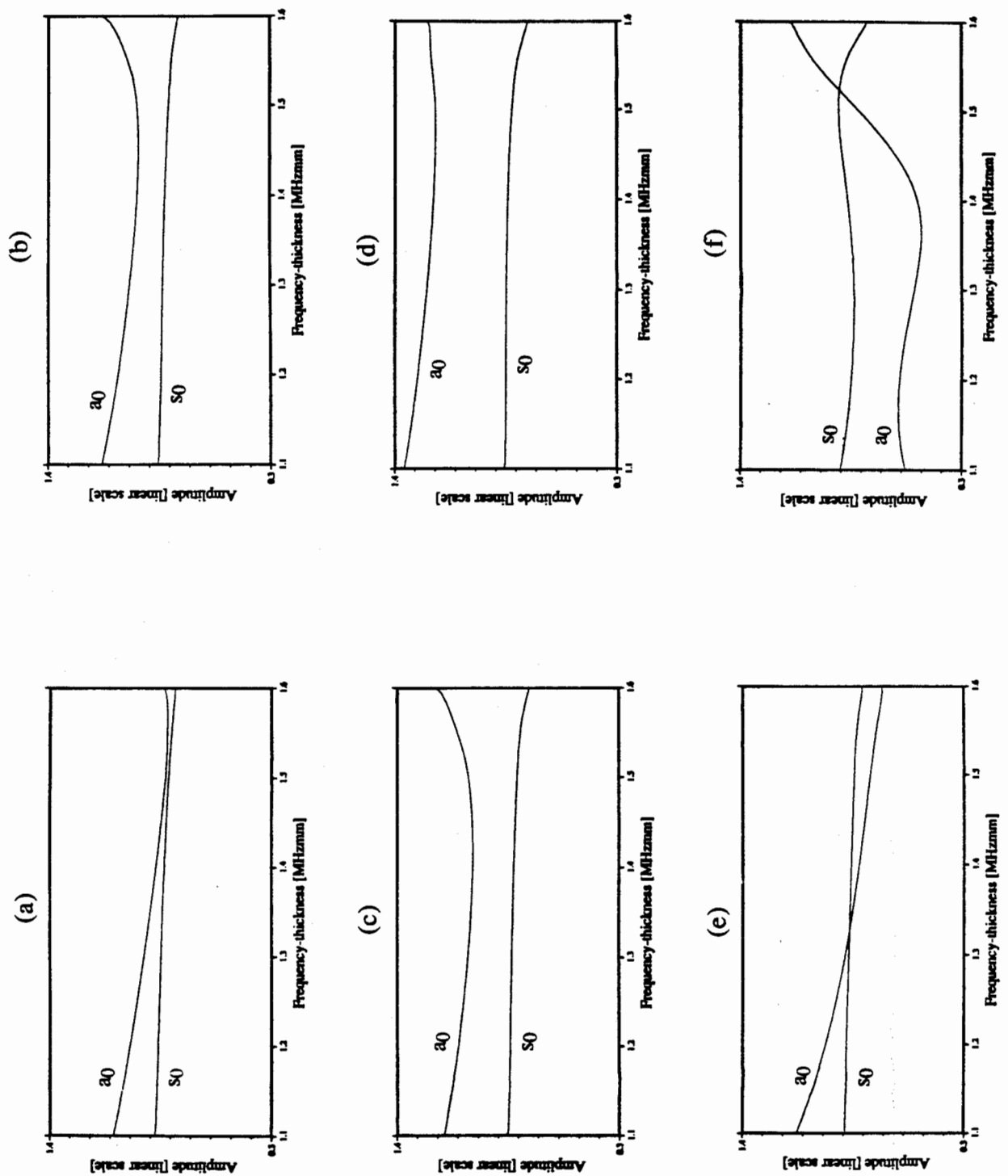


Figure 5.24 Predicted transmission ratio of the s_0 mode as a function of frequency-thickness in the 3.0 mm thick plate after interaction with a 0.5 mm deep notch which was (a) 0.25 mm wide notch; (b) 0.5 mm wide, (c) 0.75 mm wide, (d) 1.0 mm wide, (e) 2.0 mm wide, (f) 4.0 mm wide notch.

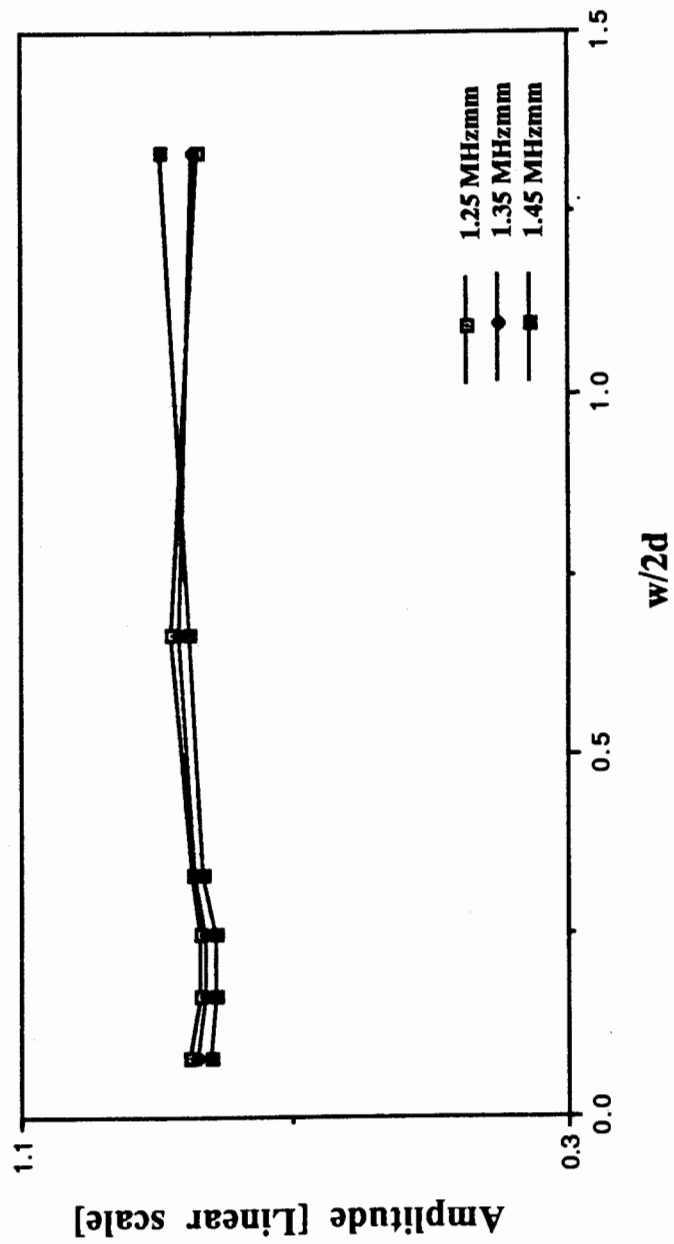


Figure 5.25 Predicted transmission ratio of the s_0 mode as a function of $w/2d$ at 1.25, 1.35 and 1.45 MHzmm.

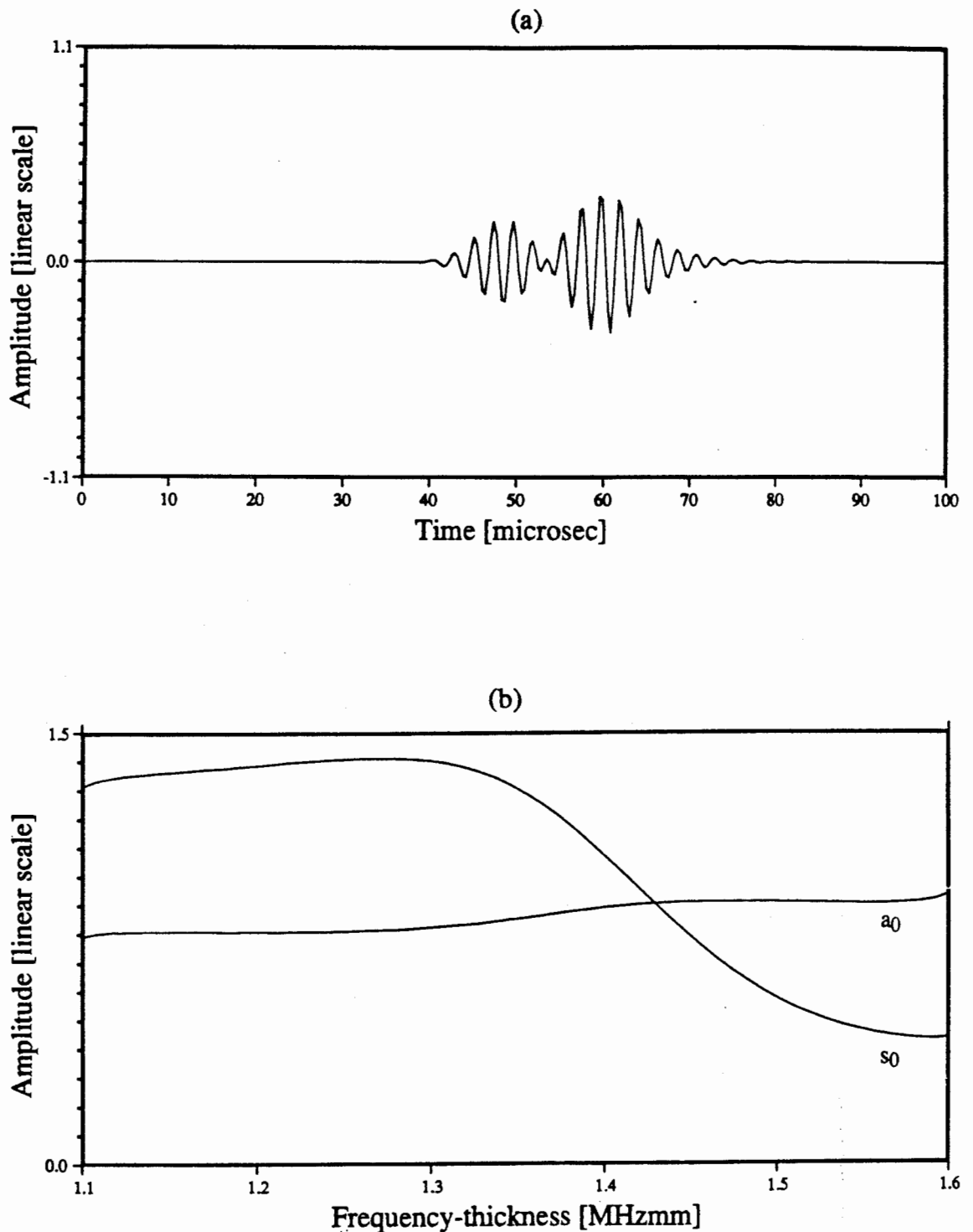


Figure 5.26 (a) Predicted time history in a 3.0 mm thick plate 60 mm after the angled (45° to the plate surface) 1.0 mm deep notch, when the centre frequency of the input tone burst was 0.45 MHz and was designed to excite only s_0 . (b) Predicted transmission ratio of the s_0 mode as a function of frequency-thickness for the case given in (a).

CHAPTER 6

The measurement of propagating Lamb waves in plates

6.1 Introduction

The propagation velocity of individual Lamb waves, once known, may be used as a means of identifying them. However, the measurement of velocity is generally made difficult by the dispersive, multi-mode nature of Lamb waves when excited by commercially available ultrasonic probes.

The aim of the experimental investigations reported in this chapter was to excite a single Lamb wave and to study its propagation. The experimental equipment and the practical methods which were used to excite and receive Lamb waves are discussed. Then the results of the measurement of the properties of propagating Lamb waves using time and frequency domain techniques, and the 2-D FFT method are presented.

6.2 Experimental procedure and equipment

The instrumentation used is shown schematically in Fig. 6.1. A pulse from the pulse generator was used to simultaneously trigger the oscilloscope and a function generator which delivered a tone burst to the power amplifier. The function generator delivered tone bursts of an integer number of cycles. However, in some tests an arbitrary function generator was used, which delivered a tone burst modified by a Hanning window function. The power amplifier delivered the input signal to the transmitting transducer with a gain of 50 dB. The ultrasonic waves excited by the transmitting transducer propagated along the plate and were received by the receiving transducer, the received signal being amplified and transferred to the oscilloscope for digital capture and display. The signals from the oscilloscope were transferred to the computer via the GPIB bus to be edited and then transferred to the spectrum analyser, which was used to carry out the digital Fourier transformation. The resulting transformed data was then transferred back to the computer for redisplaying and editing.

In order to increase the signal-to-noise ratio, successive response signals captured by the digital oscilloscope may be averaged. This was achieved by repeating the input signal, by re-triggering the system once the response of the plate to the previous input had decayed to zero, and averaging the successive responses of the plate.

When more than one spatial record was required, a dial gauge measured the movement of the receiving transducer to obtain an accurate spatial sampling interval. The resolution in positioning the transducer in the experiments was better than ± 0.02 mm.

The steel plates used in the experimental investigations were approximately 300 mm wide and 1 m long, and the propagation distance was restricted to under 400 mm in order to keep the signal-to-noise ratio high. Individual Lamb waves were selectively excited by applying the coincidence principle. The angle of incidence, θ , required for the excitation of the desired mode was calculated using eqn 2.61.

6.3 Practical methods of exciting and receiving Lamb waves

Lamb waves can be excited conveniently by a variety of methods. However, as in the case of bulk waves it is preferable to excite only the Lamb waves which are to be used in the NDT investigation. This not only simplifies the analysis of the data received from the testpiece, but also increases the resolution and sensitivity of the ultrasonic NDT technique.

Many workers in the field including Böttger *et al* (1987) have reported exciting Lamb waves using Electro-Magnetic-Acoustic-Transducers (EMATs). The main advantage of EMATs is the elimination of the need for a liquid couplant. But, as they work by producing eddy currents in the testpiece they are generally limited to NDT applications in metals. Also the distance between the EMAT and the surface of the testpiece has to be accurately controlled to maintain constant electromagnetic coupling conditions.

In the work reported here Lamb waves were excited and received using the coincidence principle. Firestone and Ling (1951), Worlton (1957), Lockett (1973), Perdijon (1985) and many others have applied this technique to excite Lamb waves for NDT purposes. The angle at which maximum transmission and reception of acoustic energy occurs at any particular frequency-thickness product may be obtained from eqn. 2.61 (see Fig. 2.9 for coupling in water).

Standard immersion coupling was not employed because propagation distances are greatly reduced due to the continual leakage of energy to the surrounding fluid. This effect is more pronounced the greater the z component of displacement at the surface of the plate (see Fig. 2.7(a)-(f)).

The standard way of exciting Lamb waves using piezoelectric transducers is to employ a variable angle probe such as those shown in Fig. 6.2(a) and 6.2(b). In the direct wedge method shown schematically in Fig. 6.2(a), the transducer is usually mounted in a block of perspex, which is generally coupled to the plate by the thin film method. The angle of incidence of the transducer element can be varied by sliding it around a curved block (see Hall 1977). The indirect wedge method shown schematically in Fig. 6.2(b) substitutes a liquid for the perspex wedge, (see Hall 1977), immersion coupling enabling the acoustic energy to be transferred from the transducer to the plate. Again the angle of the transducer relative to the plate may be varied, allowing the appropriate coincidence angle to be obtained.

In almost all practical NDT applications it is the surface motion which is important as this is detected by the transducers. The displacement mode shapes (Fig. 2.7) have x and z components, which are dependent on whether the Lamb wave is symmetric or antisymmetric, its mode order and the frequency-thickness product. Any coupling method which employ fluids only measures the z component of the displacement of the Lamb waves at the plate surface ($z = \pm d$). Therefore, if a Lamb wave has very little displacement in the z direction at the plate surface, for example, s_0 at 0.5 MHzmm, it will be more difficult to excite and measure than a mode in which z direction displacements at the surface are large, for example, a_0 at 0.5 MHzmm.

The variable angle, constant emission point broadband transducer used during the experimental investigation and shown schematically in Fig. 6.3(a), incorporated a damping wedge at the front of the probe body to attenuate the face reflection from the base of the transducer body. The transducer element was 10 mm in diameter and was mounted in a small perspex holder which was clamped to the probe body, which was also made of perspex. Grease coupling (thin film layers, typically less than 0.1 mm thick) enabled acoustic transmission between the transducer element and its housing, and between the transducer holder and the probe body. Therefore, a wave going to or coming from the transducer has to propagate through three thin film coupling layers, shown schematically in Fig. 6.3(b), where the layers are highlighted for clarity.

The response of the variable angle probe in air when excited by a broad band pulse is shown in Fig. 6.4(a), and the spectrum of the probe response is shown in Fig. 6.4(b). The multiple interfaces cause serious disadvantages in this type of probe design. From Fig. 6.4(a) it can be

seen that two large face reflections are observed, (labelled B1 and B2 respectively in Fig. 6.4(a)). The reflection labelled B1 was from the base of the perspex transducer body and the reflection labelled B2 was a reverberation of this reflection. From the spectrum of the response shown in Fig. 6.4(b) it may be seen that the available acoustic energy is in the frequency range between 0.5 MHz and 5 MHz, (20 dB down points). The reflection from the transducer element holder (labelled B2 in Fig. 6.4(a)) causes the undulations in the amplitude spectrum. Fig. 6.4(a) and (b) have shown using the simple case of a non-dispersive compression wave, where the two reflections B1 and B2 are separate and may be easily deconvolved from one another in the time domain that the response of direct wedge probes invariably contains reverberations (multiples of the response signal), which are produced within the probe body. In Lamb wave testing where in general the response of the plate is dispersive and more than one mode is present, it is not usually possible separate these reverberations in the time domain and they cause the response of the plate to be further complicated.

The advantage of the indirect wedge method (see Fig. 6.2(b)) or immersion coupling methods over the direct wedge method is that there are no interfaces between the testpiece and the transducer element (see Fig. 6.2(b)). Any reverberation within the coupling fluid may be easily decoupled from the response signal by increasing the delay by moving the transducer element further from the testpiece. Therefore, it is simpler to carry out Lamb wave testing by employing the indirect wedge method using standard immersion transducers.

The Lamb wave test rig shown in Fig. 6.5 was built to overcome the problems encountered in Lamb wave testing when using the 'direct wedge' variable angle probes. In operation the rig was clamped to the surface of the plate and the transducers held in place in the holders, which were filled with water. The orientation angle of the transducers was finely adjusted by slightly moving the transducers by hand until the response of the plate was maximised.

The rig was designed to use immersion transducers up to 33 mm in diameter. It is basically a frame that holds two transducer holders in line with one another, one holder being fixed, and the other moveable. The transducer holders are essentially a block of aluminium with a 33 mm diameter hole drilled through at 16° to the normal. On the under faces of the holders there is a 43 mm diameter groove which locates a 3.5 mm diameter o-ring. A column of water in the transducer holders allowed acoustic energy transfer between the transducer and the plate. Because there is only one interface at the water testpiece boundary, multiple reflections of the response signal do not occur. Spring loading on the moveable transducer holder was incorporated to obtain a water tight seal between the plate and the transducers, the o-rings on the base of the transducer holders providing the water tight seal. The immersion coupling area was localised in the transducer holders (the coupling area was less than 0.001 m^2). Hence,

only a small part of the plate is immersed. Attenuation due to leakage into the coupling fluid, which is the major objection to using immersion coupling was therefore kept to a minimum.

Fixed angle transducer holders were incorporated because they simplified the design of the rig and reduced the size of the coupling area. However, there is no reason why the transducer holders could not incorporate a mechanism which would allow the transducer incidence angle to be adjusted. A 16° angle was chosen because from Fig. 2.6 and 2.9 it may be seen that around 16° the group velocities of all the modes except a_0 is a maximum, dispersion is minimised and the propagation distances are therefore maximised. The four immersion transducers (two matched pairs) used in the experimental investigations were standard off-the-shelf items. The pair of 0.5 MHz immersion transducers were 31.5 mm in diameter and a spectrum of the face reflection when the transducer was excited by a broad band pulse is shown in Fig. 6.6 It may be seen that the energy is spread over the frequency range 0.25 MHz to 0.8 MHz (20 dB down points). The 1 MHz immersion transducers are 25.5 mm in diameter. A spectrum of the face reflection when the transducer was excited by a broad band pulse is shown in Fig. 6.7 from which it may be seen that the energy is spread over the frequency range 0.5 MHz to 1.5 MHz (20 dB down points). The diameter of the immersion transducers was large in order to reduce the angular bandwidth of the excitation signal. However, from Fig. 2.10 it can be seen that the 1.0 MHz and the 0.5 MHz transducers will deliver energy over an angular bandwidth of approximately $\pm 6^\circ$ and $\pm 12^\circ$ respectively. (The small difference in diameter between the 0.5 MHz and 1.0 MHz transducers does effect the angular spread of energy so the angular bandwidth of the 1.0 MHz transducer will not be exactly half that of the 0.5 MHz transducer). Hence, efficient excitation and reception could be achieved from 10° to 22° with the 1.0 MHz transducer and from 4° to 28° with the 0.5 MHz transducer. This is sufficient in many Lamb NDT applications where testing is usually carried out in regions of maximum group velocity, where the coincidence angle in water is always between 10° and 22° (except for the a_0 mode).

The major advantage of fluid coupling is that only longitudinal waves exist in fluids, therefore, irrespective of the coincidence angle, only displacement components associated with re-radiated longitudinal waves will be incident at the face of the transducer. When the direct wedge type probe was used, the re-radiated signal incident on the face of the transducer element is in general due to both longitudinal and shear waves in the perspex wedge since shear waves are generated by mode conversion at the surface of the perspex. This is a disadvantage as it further complicates the transducer response signal. The coupling conditions at the interface between the perspex wedge and the plate is also very sensitive to variations in the applied pressure and the thickness of the thin film layer; therefore, when the probe is indexed in the x direction it is difficult to maintain constant coupling conditions and the quality of the coupling between the transducer and the plate probably varied, which introduced errors

in the 2-D FFT analysis. In the Lamb wave test rig, the water column ensured constant coupling conditions even when the moveable probe was indexed in the x direction.

6.3.1 Pulse excitation

Pulse excitation is not generally used with Lamb waves because many modes tend to be excited. For example, the 10 mm diameter variable angle probe shown in Fig. 6.3(a) delivers most of its energy between 0.5 MHz and 5 MHz (see Fig. 6.4(b)) and within $\pm 15^\circ$ of the angle of incidence of the transducer the frequency-thickness range being controlled by the frequency response characteristics of the transducer and measurement system, and the angular range being controlled by the physical dimensions of the transducer. If the plate is 1 mm thick and the coincidence angle in the perspex is 30° all the Lamb waves in the rectangular region in Fig. 6.8 will be excited. This plot was obtained by combining a graph similar to that of Fig. 2.10 for a 10 mm diameter transducer and Fig. 6.4(b) with the dispersion curves. Such wideband excitation generally results in low signal-to-noise ratios because of the multi-mode dispersive nature of Lamb waves. The resulting time domain signal at 100 mm from the transmitter shown in Fig. 6.9(a) is complicated and is strongly dependent on the propagation distance. The amplitude spectrum shown in Fig. 6.9(b) was derived from Fig. 6.9(a) and shows that there is significant frequency content of the response of the 1 mm thick steel plate up to around 5 MHz. In practice if the excitation signal delivers energy over a wide frequency-thickness range, which includes many propagating modes then the signal-to-noise ratio will be reduced to an unacceptable level over any significant propagation distance.

Since propagation distances greater than 150 mm were required in the tests reported here, pulse excitation methods were not used.

6.3.2 Tone burst excitation

The initial response of a plate to an incident wave is transient, all the Lamb waves possible in the plate being excited as in the case of pulse excitation. If tone bursts of suitable duration, which depends on the attenuation rate of the excited Lamb waves, are tuned to a particular frequency-thickness, this will cause the amplitude of a particular Lamb wave to build up with time provided the angular bandwidth of the excitation is narrow (see Fig. 6.8), which assumes the transducers are very large. The amplitudes of the other modes excited will either be very small, or decay exponentially with time, as very little or none of the incident wave

energy will be available to them. Hence, the most important factor when exciting Lamb waves using tone bursts is to maintain the correct excitation frequency, for a sufficient time. This enables the amplitude of the Lamb wave to build up to a steady-state value, and the amplitude of the other modes excited initially to have sufficient time to be attenuated.

This suggests that the most effective way of increasing the signal-to-noise ratio is to reduce the angular and/or frequency bandwidth of the excitation signal. In practice reduction of the frequency bandwidth is usually achieved by using tone burst excitation signals of an integer number of sinusoids. The bandwidth may be further reduced by smoothing the tone burst, by for example, applying a Hanning window function.

6.4 Time domain measurements of Lamb wave velocities

Initial tests with variable angle probe in perspex block

Before the Lamb wave rig shown in Fig. 6.5 was built, initial tests were carried out using two variable angle transducers shown in Fig. 6.3(a), as the transmitter and the receiver (see Fig. 6.1), the transmitter being driven by the 5 cycle tone burst shown in Fig. 6.10(a) at a pre-selected frequency. In all the tests the incidence angle of the variable angle probes was 28° , which was appropriate to excite s_0 and a_1 in different frequency-thickness regions.

Fig. 6.10(b) shows the response of a 0.5 mm thick steel plate at 200 mm from the transmitter, where the frequency of the excitation tone burst was 1.2 MHz and the incidence angle of the variable angle probes was appropriate to excite and receive s_0 . The incident angle required for the efficient excitation and reception of a_0 at this frequency-thickness product is about 80° , so by the coincidence principle it was only very weakly excited and received. Fig. 6.10(c) shows the amplitude spectrum of the response 200 mm from the transmitter. The sidelobes in the spectrum are due to the excitation signal applied to the exciting transducer which was a simple five cycle tone burst from the function generator. The amplitudes of the sidelobes are significant only up to a frequency of around 3 MHz, so the excitation signal did not have significant energy above 1.63 MHzmm (the cut-off frequency of a_1). Therefore, since a_0 is only very weakly excited and received, s_0 should be the only mode observed and its group velocity measured using the time of flight between two points was found to be 5.35 km/s.

The normalised response of a 2 mm thick steel plate 200 mm from the transmitter when the excitation was a five cycle 1 MHz tone burst from the function generator, is shown in Fig.

6.11. Again, the input signal was intended to excite only s_0 . The amplitudes of the sidelobes in this case were significant up to a frequency-thickness product of around 4 MHzmm, so it was possible for the excitation signal to excite higher order modes (see Fig. 6.8). The time history of the response of the 2.0 mm thick plate indicates that the propagating Lamb wave signals are multi-mode and/or dispersive. Hence, the duration of the response signal is long and from measurements at two points it is difficult to determine anything but a maximum group velocity of 5.1 km/s, which corresponds to the s_0 mode in this frequency-thickness range. It is difficult to determine whether more than one propagating mode is present from the time history plot. However, it can be seen that the lower frequency components of the response signal are at the front of the signal, indicating that their group velocities are larger.

Fig. 6.12 shows the time history of the response of a 3 mm thick steel plate 200 mm from the transmitter. The frequency of the five cycle tone burst from the function generator was 1 MHz, which was intended to excite only a_1 . In this case the amplitudes of the sidelobes were significant up to a frequency-thickness product of around 6 MHzmm, so again it was possible for the excitation signal to excite higher order mode (see Fig. 6.8). The shape of the response signal indicates that there is gross dispersion and more than one propagating mode is present. However, a discrete wave packet with a large amplitude is present and its group velocity of 3.8 km/s indicates that it is the a_1 mode.

Tests with immersion probe and arbitrary function generator

These tests were carried out using the Lamb wave test rig described previously and shown in Fig. 6.5 and 0.5 mm and 3.0 mm thick steel plates.

The first test was carried out on a 0.5 mm thick steel plate using the Lamb wave test rig with the pair of 1 MHz immersion transducers. The input signal from the arbitrary function generator was a five cycle tone burst modified by a Hanning window function and is shown in Fig. 6.13(a). The measured time history of the response of the 0.5 mm thick steel plate at 200 mm from the transmitter is shown in Fig. 6.13(b). As in Fig. 6.10 the frequency of the tone burst was 1.2 MHz and the transducer angle was appropriate to excite and receive only s_0 . The amplitude spectrum shown in Fig. 6.13 (c) was derived from Fig. 6.13(b). It may be seen that the bandwidth of the response is substantially less than in Fig. 6.10(c), the sidelobes in Fig. 6.10(c) being effectively eliminated by using an excitation tone burst which was modified by an applied Hanning window. Comparing the time domain responses it may also be seen that the shape of the response in Fig. 6.13(b) closely resembles the shape of the input

signal (see Fig. 6.13(a)), indicating that the wave is essentially nondispersive over the angular and frequency bandwidths of the input signal.

In all the remaining time domain tests, the bandwidth of the input signal was further reduced by using a twelve cycle tone burst from the arbitrary function generator smoothed by a Hanning window.

Fig. 6.14(a) shows the response of a 0.5 mm thick steel plate at 150 mm from the transmitter, where the transducer angle of 16° was appropriate to excite and receive only s_0 . The frequency of the excitation tone burst was 1 MHz. The incident angle required for the efficient excitation and reception of a_0 at this frequency-thickness product is about 40° in water, so it was only very weakly excited and received. The receiving transducer was then indexed 100 mm, and Fig. 6.14(b) shows the response 250 mm from the transmitter. Comparing the two time domain responses it may be seen that the shape of the response does not change, showing that the wave is effectively nondispersive. Fig. 6.14(a) and 6.14(b) are summed in Fig. 6.14(c), where the time it takes the Lamb wave to travel between the two transducer positions (marked T in the diagram), may be used to determine group velocity. The group velocity measured using the time of flight between the two points was 5.35 km/s.

Fig. 6.15(a) shows the response of a 3 mm thick steel plate at 150 mm from the transmitter, where the incident angle of 16° was appropriate to excite and receive only s_0 . The frequency of the excitation tone burst was 0.45 MHz. The incident angle required for the efficient excitation and reception of a_0 at this frequency-thickness product is about 36° in water, so it was only very weakly excited and received. The receiving transducer was then indexed 100 mm, and Fig. 6.15(b) shows the response 250 mm from the transmitter. Comparing the two time domain responses it may be seen that the shape of the response envelope does not change greatly. However, there is some change between the two signals. For example, the peak of the wave packet (labelled R in Fig. 6.15(a)) is significantly higher than the amplitude of the two adjacent peaks. However, in Fig. 6.15(b) there are two adjacent cycles with very similar peak values. This indicates that a small amount of dispersion is present. The group velocity measured using the time of flight between the two maximum points was 5.15 km/s. However, this is an approximate group velocity as the shape of the wave packet is changing.

Fig. 6.16(a) shows the response of a 3 mm thick steel plate at 150 mm from the transmitter, where the incident angle of 16° was appropriate to excite and receive only s_0 . The frequency of the excitation tone burst was 0.6 MHz. The incident angle required for the efficient excitation and reception of a_0 at this frequency-thickness product is about 32° , so again it was only very weakly excited and received. The receiving transducer was then indexed 100 mm and Fig. 6.16(b) shows the response 250 mm from the transmitter. Comparing the two time

domain responses it may be seen that the duration of the response signal has increased appreciably in Fig. 6.16(b), changing the shape of the response envelope. This indicates that dispersion is present. The maximum group velocity measured, using the time of flight between the two points of first arrival, was 4.5 km/s. However, it is not feasible in a single test to measure the variation of velocity with frequency using time domain data only

Fig. 6.17(a) shows the response of a 3 mm thick steel plate at 150 mm from the transmitter, where the incident angle of the wave was appropriate to excite and receive s_0 . The frequency of the excitation tone burst was 0.75 MHz. The incident angle required for the efficient excitation and reception of a_0 at this frequency-thickness product is about 30° , so again it was only weakly excited and received. The receiving transducer was then indexed 100 mm, and Fig. 6.17(b) shows the response 250 mm from the transmitter. The two response signals both exhibit gross dispersion and the maximum group velocity, measured using the time of flight from the leading edge of the signal was 3.7 km/s.

Fig. 6.18(a) shows the response of a 3 mm thick steel plate at 150 mm from the transmitter when the frequency of the excitation tone burst was 1 MHz. The angular bandwidth of the input signal was appropriate for the s_1 , a_1 and s_0 modes in the frequency-thickness range of the excitation signal. The receiving transducer was then indexed 100 mm and Fig. 6.18(b) shows the response 250 mm from the transmitter. The two response signals both indicate that there is more than one propagating mode. Gross dispersion is present and beating between the different modes is taking place. As in Fig. 6.12 a discrete wave packet with a large amplitude is present, and its group velocity measured using the time of flight between the points of maximum amplitude was 3.8 km/s indicating that it is a_1 .

The time domain measurements have shown that the Lamb wave velocities and amplitudes may be measured readily if the wave is essentially nondispersive and can be decoupled from other propagating modes. The other modes can be removed either by gating out the unwanted signals in cases where the modes of interest have significantly different group velocities from the other modes, or by using the coincidence principle to reduce the amplitude of the signals in the unwanted modes. However, the coincidence effect requires the angular bandwidth of the transducers to be small and the phase velocities of the modes to be significantly different. Therefore, in practical applications using commercially available transducers, the dispersive multi-mode nature of Lamb waves, usually restricts the use of time domain methods to low frequency-thickness products where only a_0 and s_0 may propagate.

6.5 Frequency domain measurements of Lamb wave velocities

Tests were carried out using the amplitude and phase spectrum methods discussed previously in chapter 3 to measure the velocity of propagating Lamb waves in the 0.5 mm and 3 mm thick steel plates. The excitation signal was a five cycle tone burst modified by a Hanning window function and the pair of 0.5 MHz immersion transducers were used unless otherwise stated.

As an example of a nondispersive frequency-thickness region, the velocity of s_0 around 0.5 MHzmm was measured using both the phase and amplitude spectrum methods. The response of the steel plate at 200 mm from the transmitter is shown in Fig. 6.13(b). If the response of the plate at 250 mm is captured, the response at 200 mm inverted, and then the two responses summed, Fig. 6.19(a) will be obtained. The amplitude spectrum shown in Fig. 6.19(b) was obtained by Fourier transforming Fig. 6.19(a). The dips in the spectrum occur at frequencies where eqn 3.1 is satisfied. The velocity of the s_0 mode was calculated using the mode numbers shown in Fig. 6.19(b). The signal in Fig. 6.13(b) was inverted in order to produce minima in Fig. 6.19(b) rather than maxima. This was because it is easier to read the discrete frequencies of minima. For further discussions of this, see Pialucha *et al* (1989).

Fig. 6.20 shows the results of measuring the velocity of s_0 at 0.5 MHz in the 0.5 mm thick plate using the phase spectrum method (the continuous line). The responses of the plate at 200 mm and 250 mm from the transmitter were Fourier transformed separately in this case, and then eqn 3.2 was used to calculate the wave velocity. The amplitude spectrum results discussed above are denoted by squares in Fig. 6.20. It may be seen that the agreement is excellent, the error between the two methods being less than 1%.

As an example of a dispersive mode, the velocity of s_0 at 0.6 MHz in the 3 mm thick plate was measured using both the phase and amplitude methods. The summed responses of the plate at 200 mm and 250 mm from the transmitter is shown in Fig. 6.21(a). Carrying out a Fourier transform of Fig. 6.21(a) gives the amplitude spectrum shown in Fig. 6.21(b). Again the response at 200 mm was inverted and the dips in the spectrum were used to calculate the velocity from eqn 3.1.

Again, the velocity calculated using the amplitude spectrum method were compared with those obtained using the phase spectrum method. Fig. 6.22 shows that the agreement is excellent the error between the two methods being less than 1%.

In order to show the effect of using one-dimensional spectral methods when more than one mode is present, the amplitude spectrum method was applied at 1 MHz in the 3 mm thick plate using the pair of 1 MHz immersion transducers. The summed responses of the 3 mm thick steel plate at 200 mm and 250 mm from the transmitter is shown in Fig. 6.23(a) the response at 200 mm being inverted. Fig. 6.23(b) was obtained by carrying out a Fourier transformation of Fig. 6.23(a). The dips in the spectrum correspond to the frequencies where eqn 3.1 was satisfied. However, in this case the results are not clear because more than one mode is present and the mode number associated with each dip is difficult to determine.

The results shown in Fig. 6.20 and 6.22 demonstrated that one-dimensional spectral methods (phase and amplitude spectrum) may be used to measure the velocity of Lamb waves when dispersion is present. However, because they implicitly assume that only one propagating mode is present they are not reliable when more than one mode is propagating. For more details on the use of one-dimensional spectral methods of measuring velocity see for example, Pialucha *et al* (1989).

6.6 The measurement of propagating Lamb waves using the 2-D FFT method

In this section the results of measuring the properties of propagating Lamb waves in 0.5 mm, 2 mm and 3 mm thick steel plates using the 2-D FFT method will be presented. Results using both the variable angle probe and the Lamb wave test rig will be presented.

Tests with variable angle probes

These tests were carried out using the variable angle probes and the simple 5 cycle excitation tone bursts that was not modified by a Hanning window (see Fig. 6.13(a)), from the function generator.

Fig. 6.24 shows the normalised three-dimensional view of the amplitude-wavenumber-frequency information, which was obtained by carrying out a two-dimensional Fourier transformation of the time histories from 64 equally spaced positions between $x = 175$ mm and $x = 238$ mm on the 0.5 mm thick steel plate. The time history at $x = 200$ mm was shown previously in Fig. 6.10(b). The spatial sampling interval was 1 mm and a_0 was decoupled by the coincidence angle. This is essential, as a_0 has a low wavelength which would result in

spatial aliasing for the above spatial sampling interval. The maximum amplitude of the response of the plate is between 0.8 MHz and 1.8 MHz. At each discrete frequency in Fig. 6.24 the wavenumber at which the amplitude is a maximum corresponds to the s_0 mode, and no other peak is evident confirming that only the s_0 mode is observed. The dips in the amplitude of the wavenumber-frequency information seen in Fig. 6.24 are due to two effects. The deep dips (which may be seen more clearly in Fig. 6.10(c)), are due to the abrupt nature of the tone burst employed. The shallow dips are caused by the reflection B2, (see Fig. 6.3), from the transducer holder of the variable angle probe.

The amplitude of the excitation signal, the spatial pressure distribution of the transducer, and the modal properties of s_0 , which are functions of frequency, all contribute to the determination of the proportion of energy available to excite the mode at a particular frequency. The mode shape and phase velocity of s_0 are almost constant in the frequency-thickness range of the excitation, so the amplitude of the mode is effectively only a function of the frequency content of the excitation signal as can be deduced from Fig. 6.24.

Fig. 6.25 shows the normalised two-dimensional view of the amplitude wavenumber-frequency information for the 2 mm steel plate, where the response at $x = 200$ mm was shown previously in Fig. 6.11. Fig. 6.26 was obtained by carrying out a two-dimensional Fourier transformation of the time histories of 64 equally spaced positions between $x = 175$ and 222.25 mm. Two modes, s_0 and a_1 , are present in Fig. 6.25; s_0 is the dominant mode and has its maximum amplitude at a frequency of 1 MHz, the centre frequency of the excitation. The response reduces rapidly away from this frequency, and side lobes similar to those of Fig. 6.10(c) are seen. The s_0 mode is seen over a much narrower frequency range in Fig. 6.25 than in Fig. 6.24 because the frequency-thickness value is higher and the phase velocity of s_0 (and hence the coincidence angle) varies rapidly with frequency-thickness in this range (see Fig. 2.9). Therefore, the excitation signal is only appropriate over a narrow range of frequencies where the wavenumbers of the incident beam and the Lamb waves being excited are matched. The a_1 mode observed at higher frequencies has been excited mainly by the sidelobes of the excitation signal. The duration of the response in Fig. 6.11 was very long due to the dispersive nature of s_0 in this frequency-thickness range and the 'ridge' parallel to the wavenumber axis at 1 MHz in Fig. 6.25 was due to truncation of the time domain signals after 200 μ s (see Fig. 6.11). In order to calculate the true amplitudes of the two modes present, the frequency content of the input signal, the pressure distribution of the transducer, the method of coupling and the mode shapes on the plate surface must be considered.

Fig. 6.26 shows the normalised three-dimensional view of the amplitude-wavenumber-frequency information for the 3 mm plate, where the response at $x = 200$ mm was shown previously in Fig. 6.12. Fig. 6.26 was obtained by carrying out a two-dimensional Fourier

transformation of the time histories of 64 equally spaced positions between $x = 175$ mm and $x = 222.25$ mm. Three modes, s_0 , s_1 , and a_1 are present. The different modes are observed in the frequency-thickness regions where their wavenumbers and mode shapes are appropriate for their excitation and reception; a_1 dominates the response of the plate, its maximum amplitude being measured at 1 MHz, the centre frequency of the excitation. The s_0 mode is seen only at frequencies below 1 MHz while s_1 is seen at higher frequencies; both modes have been excited by the sidelobes of the excitation signal.

A comparison of the 2-D FFT results and the theoretically predicted wavenumber dispersion curve for s_0 is shown in Fig. 6.27. The 2-D FFT results are represented by squares and are the wavenumber-frequency points at which the amplitudes in Fig. 6.24 are a maximum. From Fig. 6.27 it may be seen that the agreement between the theoretical predictions and experimental results was excellent, the maximum difference between the measured results and the theoretical predictions being less than 1%.

Fig. 6.28 shows a comparison of the theoretically predicted wavenumber dispersion curves for s_0 and a_1 , with experimental results obtained by locating the wavenumber(s) at particular frequencies at which the amplitude shown in Fig. 6.25 reaches a maximum. Again the agreement between the theoretical and experimental results is seen to be excellent, the maximum difference between the measured results and the theoretical predictions being less than 1%.

Test with immersion probes and arbitrary function generator

In this test the Lamb wave rig was used and the excitation was a five cycle 1.2 MHz tone burst modified by a Hanning window, from the arbitrary function generator.

Fig. 6.29 shows the normalised three-dimensional view of the amplitude-wavenumber-frequency information for the 0.5 mm thick steel plate, where the time history at $x = 200$ mm was shown previously in Fig. 6.13(b). Fig. 6.29 was obtained by carrying out a two-dimensional Fourier transformation of the time histories from 64 equally spaced positions, between $x = 200$ mm and 263 mm where the spatial sampling interval was 1 mm. The maximum amplitude of the response of the plate is at 1 MHz, and the single peak indicates that only one propagating mode, s_0 , is present. There are no large dips present in Fig. 6.29 (unlike in Fig. 6.24), because the sidelobes of the bandwidth of the excitation signal has been significantly reduced by the application of the Hanning window. The shallow dips due to the

reverberations in the transducer holder block shown in Fig. 6.24 have also been eliminated by using the water column coupling in the Lamb wave test rig.

Since use of immersion transducers and the arbitrary function generator produce more satisfactory signals, this system was used in the subsequent tests on the interaction of Lamb waves with defects which are presented in chapter 7.

6.7 Conclusions.

Localised immersion coupling, using a water column and standard immersion probes has been shown to be more satisfactory for the generation of single Lamb modes than standard variable angle probes. This is because it eliminates reverberations and shear waves in the coupling media, which are commonly encountered when using standard variable angle probes.

However, even using the localised immersion Lamb wave test rig, the results have shown that it is very difficult to obtain a pure mode using transducers of finite dimensions because the plate is excited over a range of frequencies and wavenumbers, the frequency range being mainly dependent on the number of cycles in the excitation tone burst and on whether a smoothing window is applied. The wavenumber range is mainly dependent on the angle required and on the size of the transducers.

Time domain methods can be used to measure the group velocity of Lamb waves. These methods are simple to implement and require minimal signal processing, but they can only be applied in restricted frequency-thickness regions due to the dispersive multi-mode nature of Lamb waves.

The amplitude and phase spectrum methods have been used to measure the phase velocity of s_0 at low frequency-thickness products, where it could be decoupled from other modes. It has been shown that these one-dimensional spectral methods can cope with dispersive signals, but they may only be used reliably when there is one propagating mode.

The 2-D FFT method has been used to measure the amplitudes and velocities of propagating Lamb waves over a range of frequencies and phase velocities in a single test. It has been shown that this technique may be used when there is multi-mode propagation and/or dispersion. The experimental and numerical results are in excellent agreement with theoretical predictions, the maximum difference in wavenumber being 1%. Although the results presented here have been for Lamb waves, the technique is equally applicable to the

measurement of other propagating waves, for example, a mixture of longitudinal and shear waves.

The 2-D FFT method can be used with any Lamb wave propagation distance, subject to signal-to-noise ratio considerations. Multi-element array transducers are now available, which will greatly simplify the experimental implementation of the method. This makes the method very attractive for many NDT applications where Lamb waves are used.

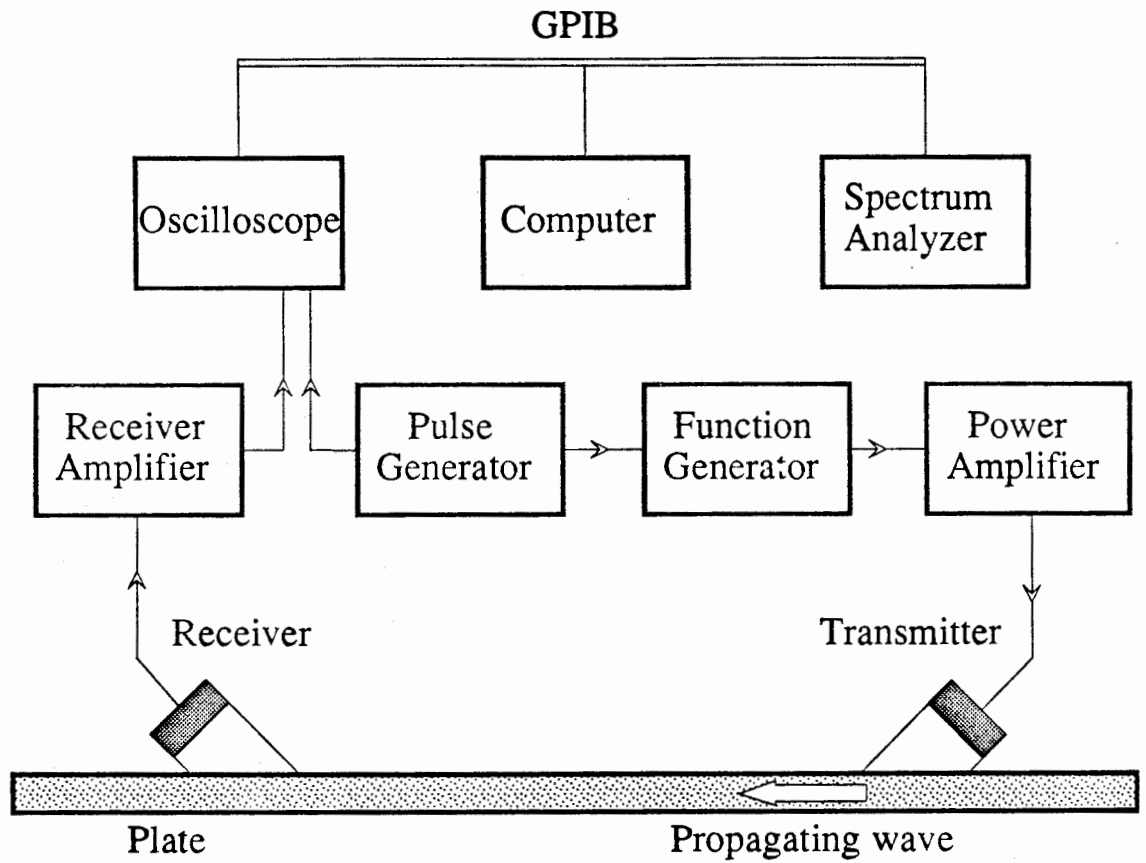


Figure 6.1 Schematic representation of experimental setup.

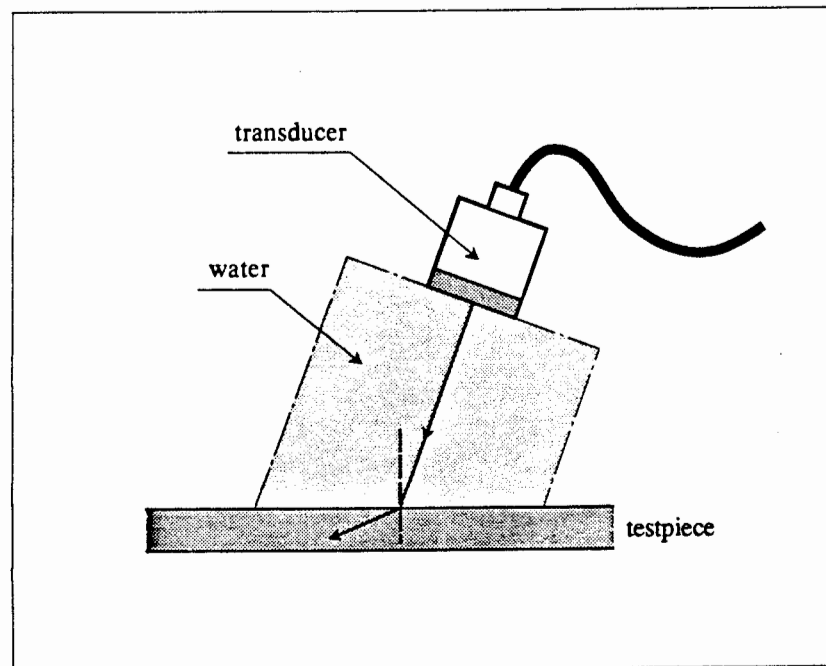
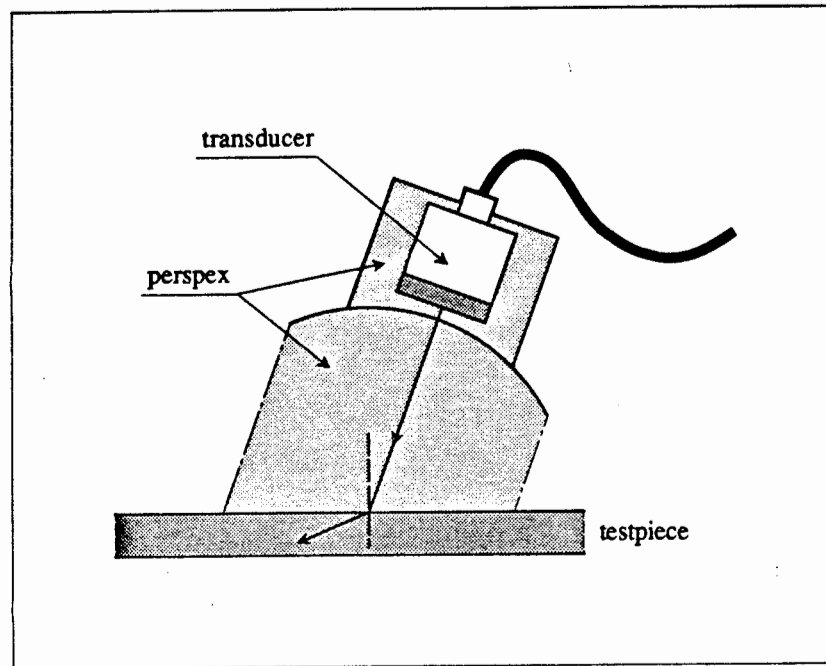


Figure 6.2 Schematic representation of (a) the direct 'wedge' method and (b) the indirect 'wedge' method.

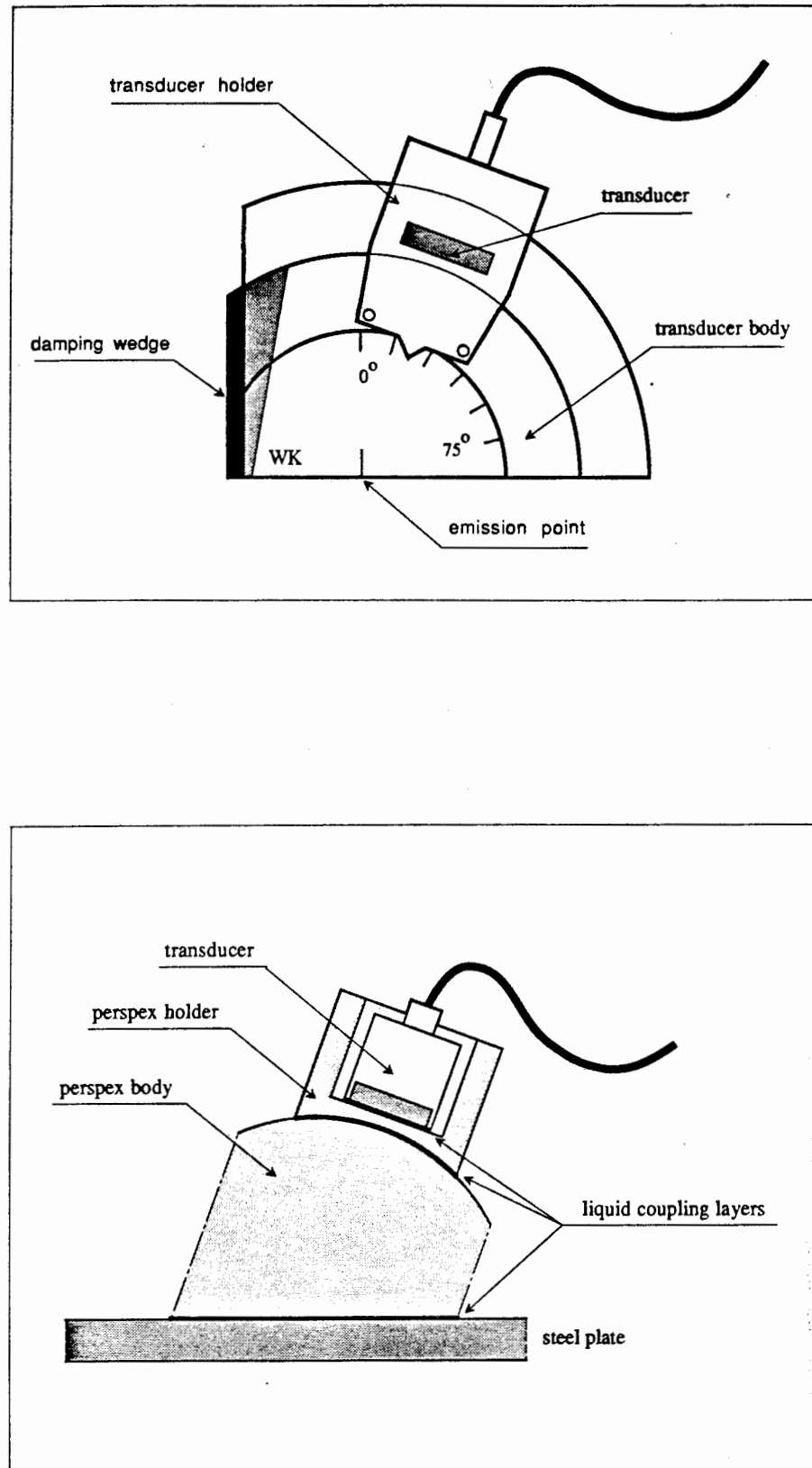


Figure 6.3 Schematic representation of (a) the variable angle probe and (b) the interfaces of the variable angle probe shown in (a).

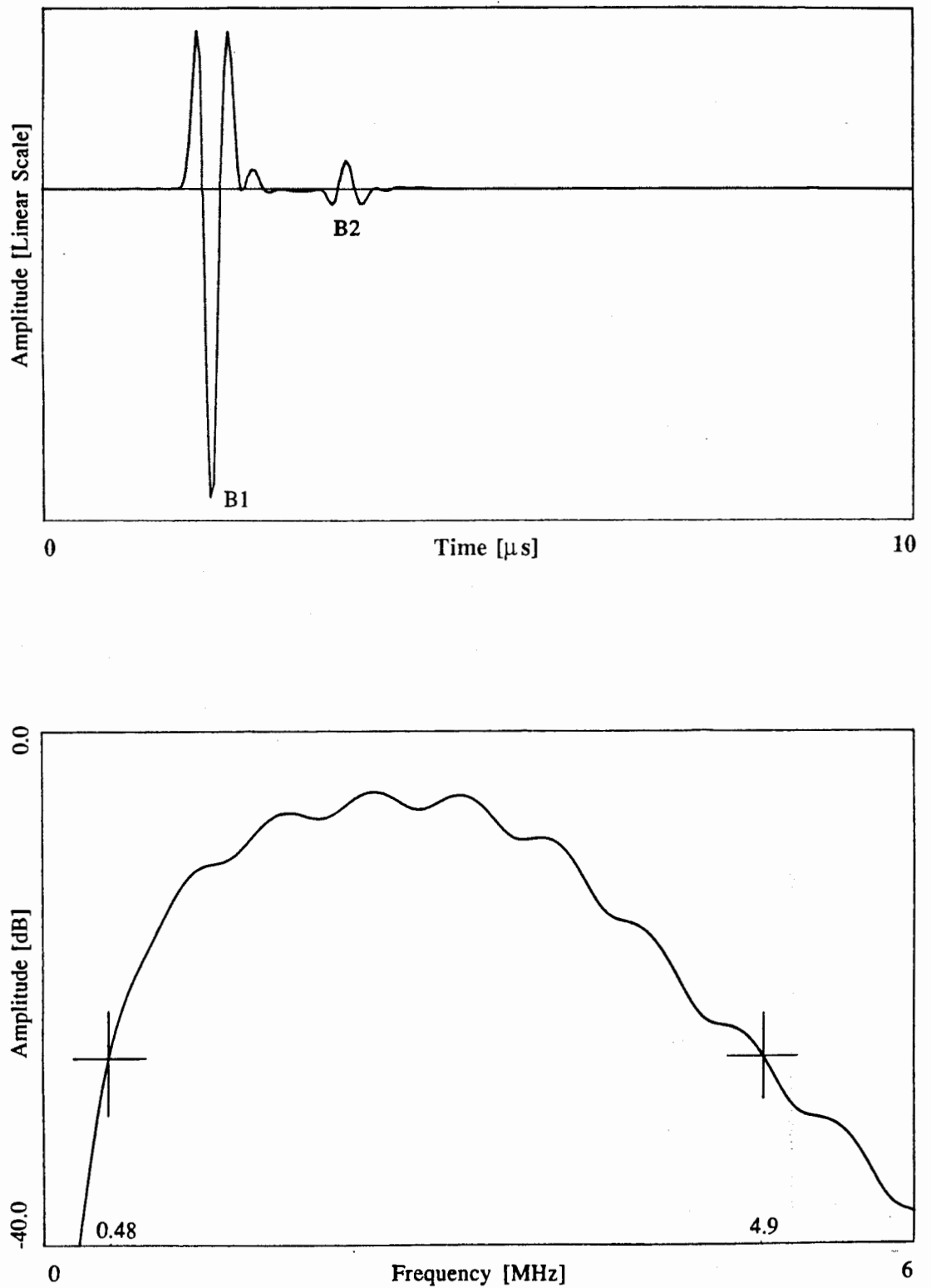


Figure 6.4 (a) Normalised time history of the response of the variable angle probe in air when excited by a broad band signal. (b) Amplitude spectrum of the time history shown in (a).

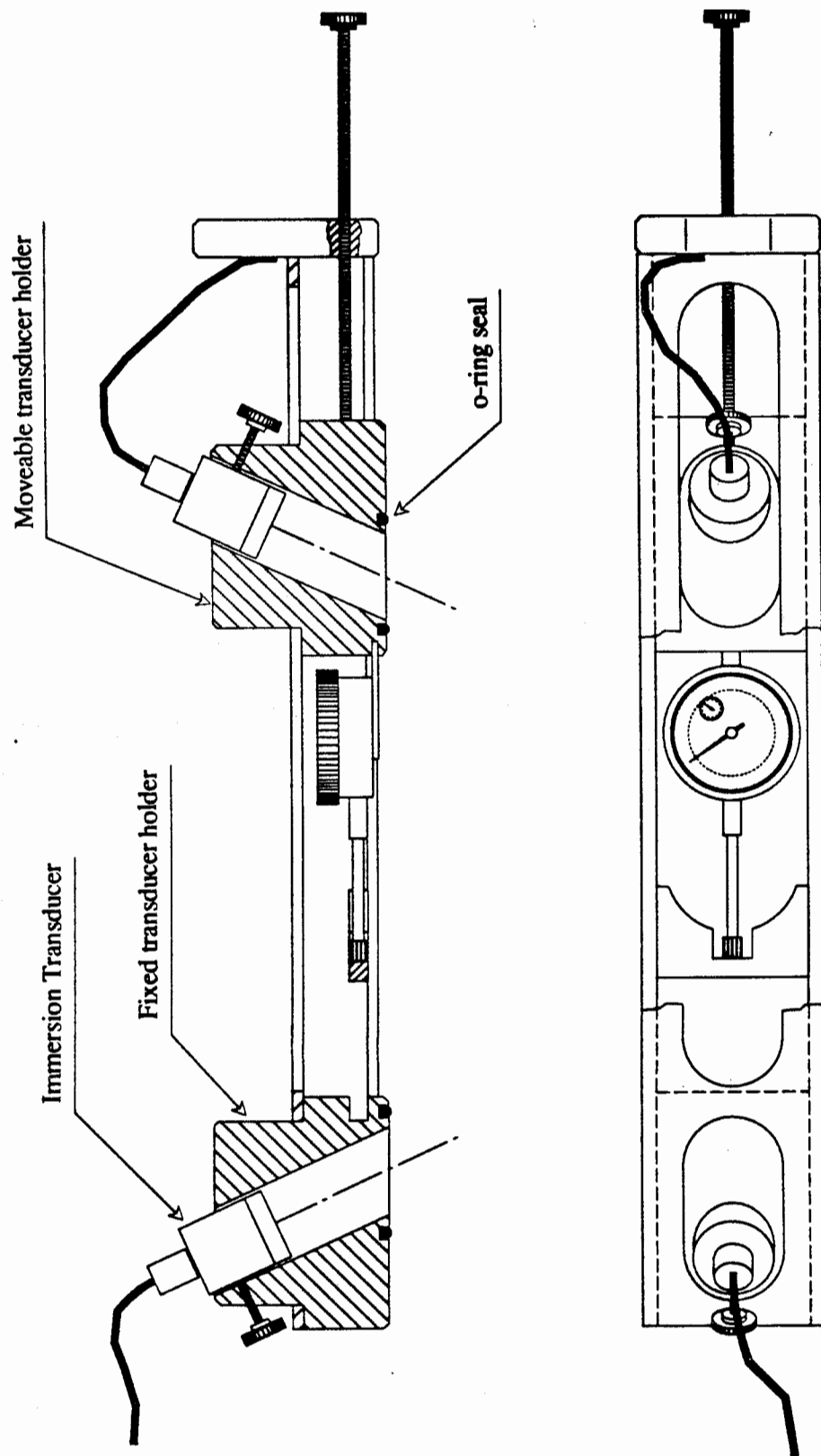


Figure 6.5 Schematic representation of the Lamb wave test rig.

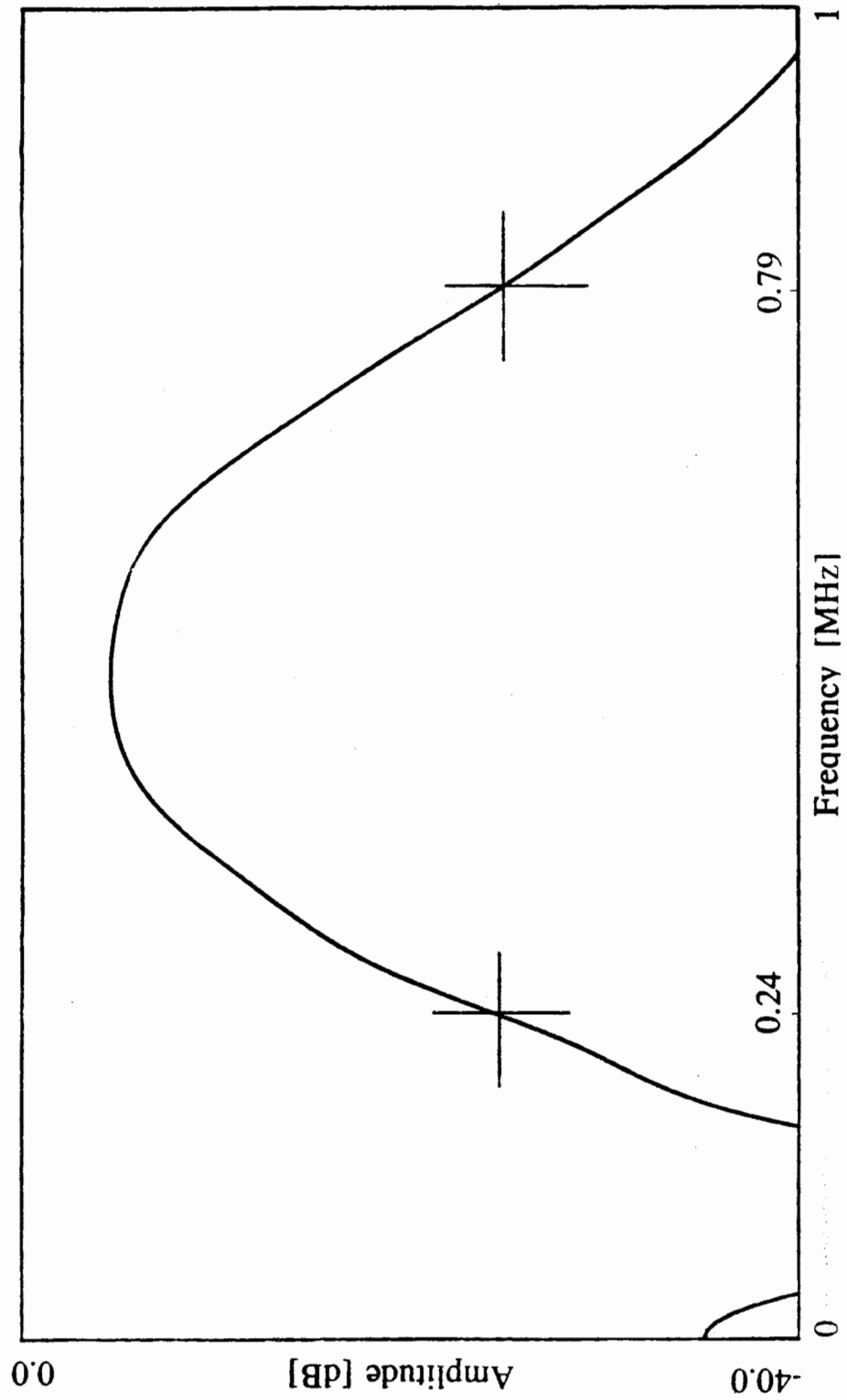


Figure 6.6 Amplitude spectrum of the response of the 0.5 MHz immersion probe when excited by a broad band signal.

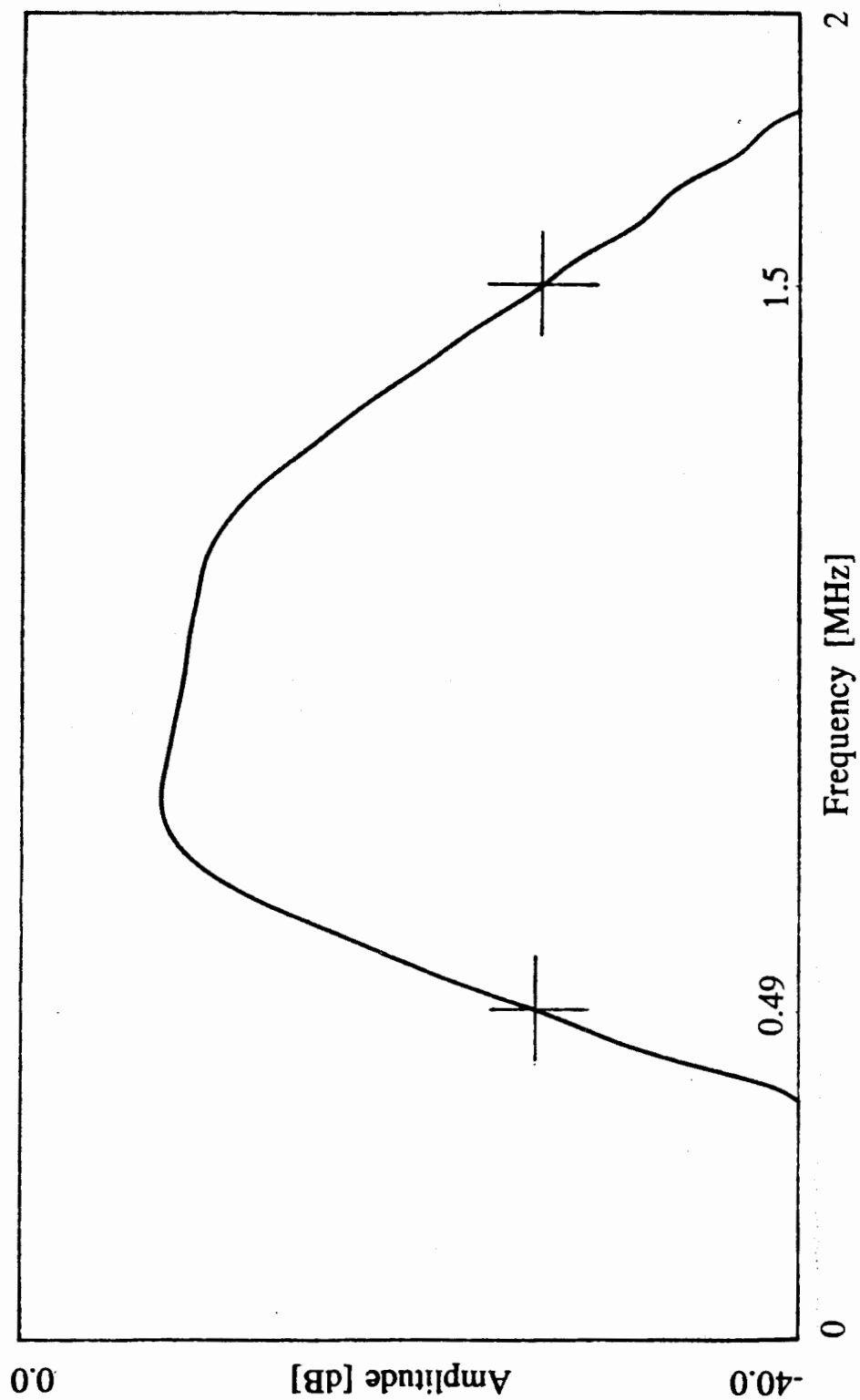


Figure 6.7 Amplitude spectrum of the response of the 1.0 MHz immersion probe when excited by a broad band signal.

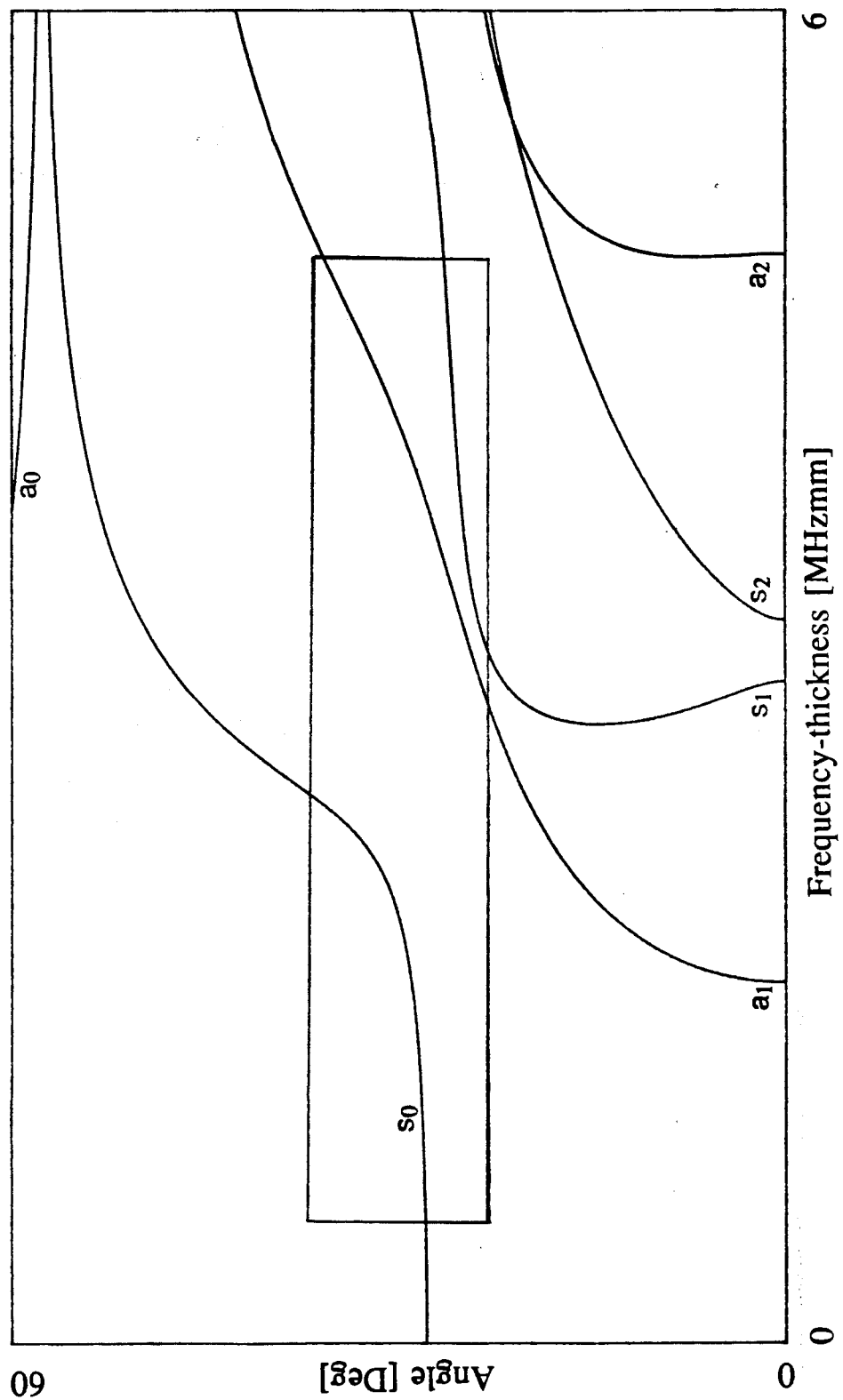


Figure 6.8 Lamb wave coincidence angle dispersion curve for steel for a variable angle probe mounted in a perspex block (perspex $c_L = 2550$ m/s). The rectangle shows the region of excitation for the variable angle probes used in the initial experiments with pulse excitation.

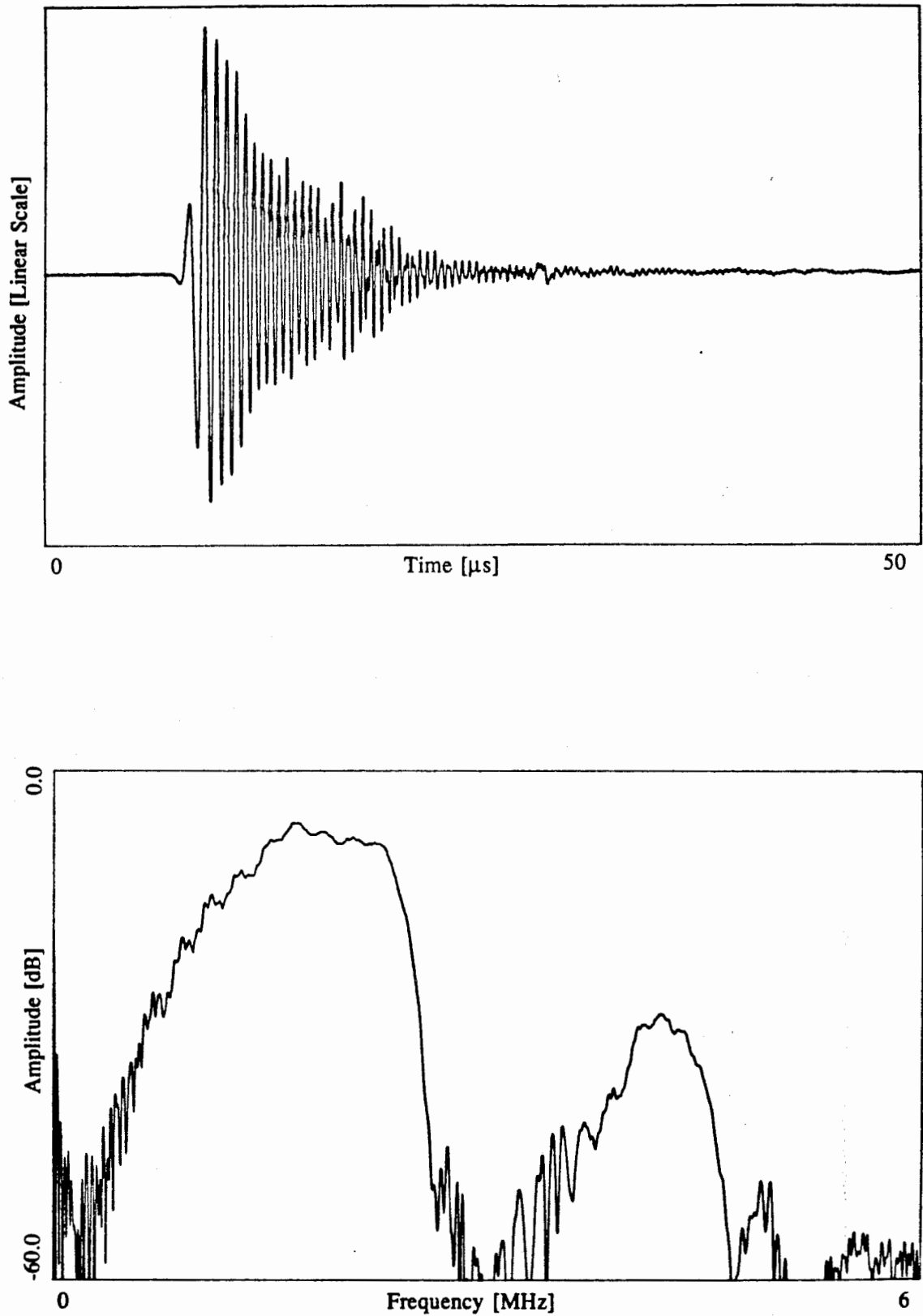


Figure 6.9 (a) Normalised time history of the measured response at $x = 100$ mm in a 1.0 mm thick plate when broad band pulsed excitation was used. (b) Amplitude spectrum of the time history shown in (a)

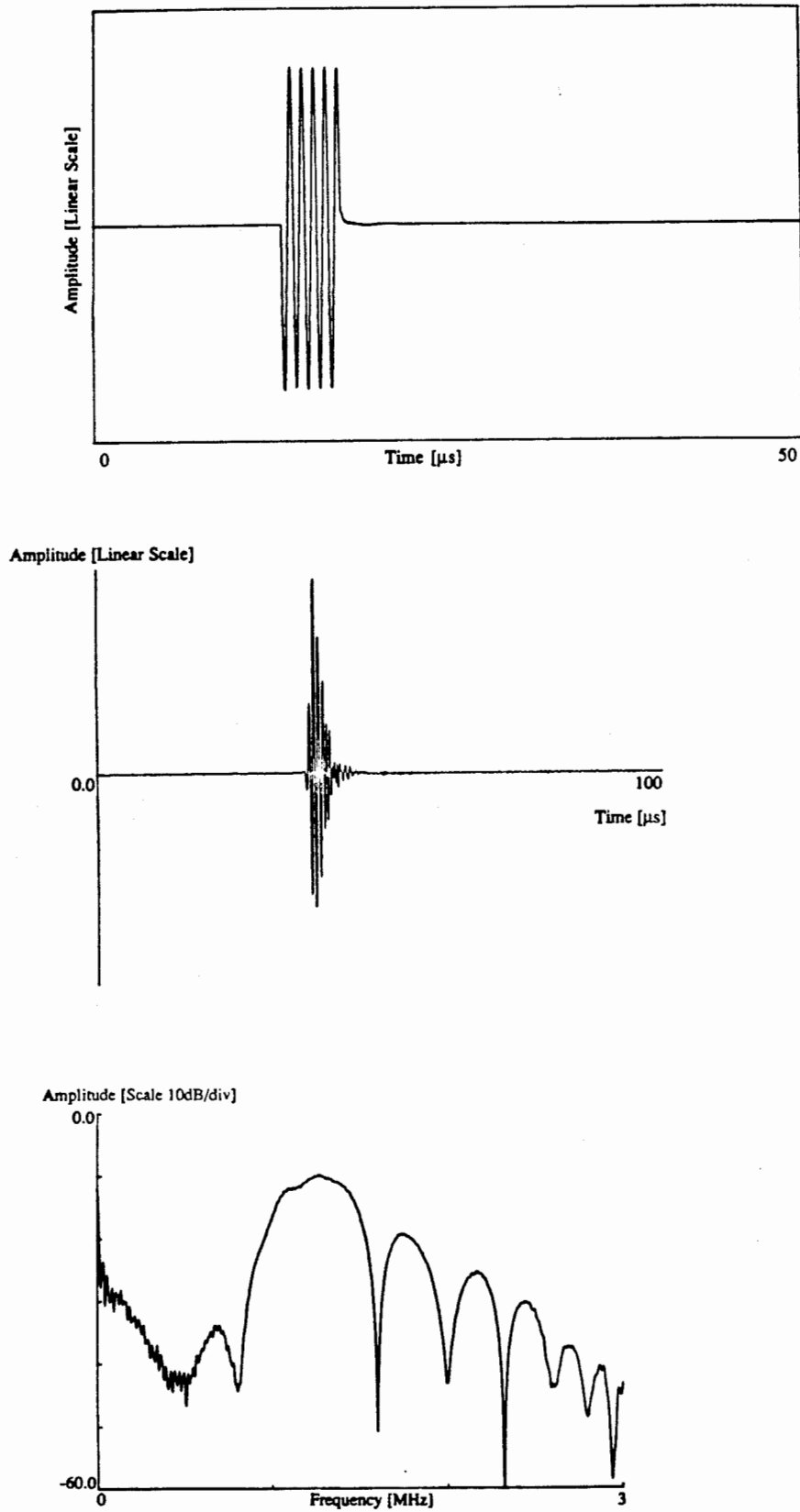


Figure 6.10 (a) Normalised time history of a simple 5 cycle excitation tone burst at 1.2 MHz. (b) Measured response at $x = 200$ mm in a 0.5 mm thick plate when the excitation signal shown in (a) was appropriate for s_0 . (c) Amplitude spectrum of the time history shown in (b).

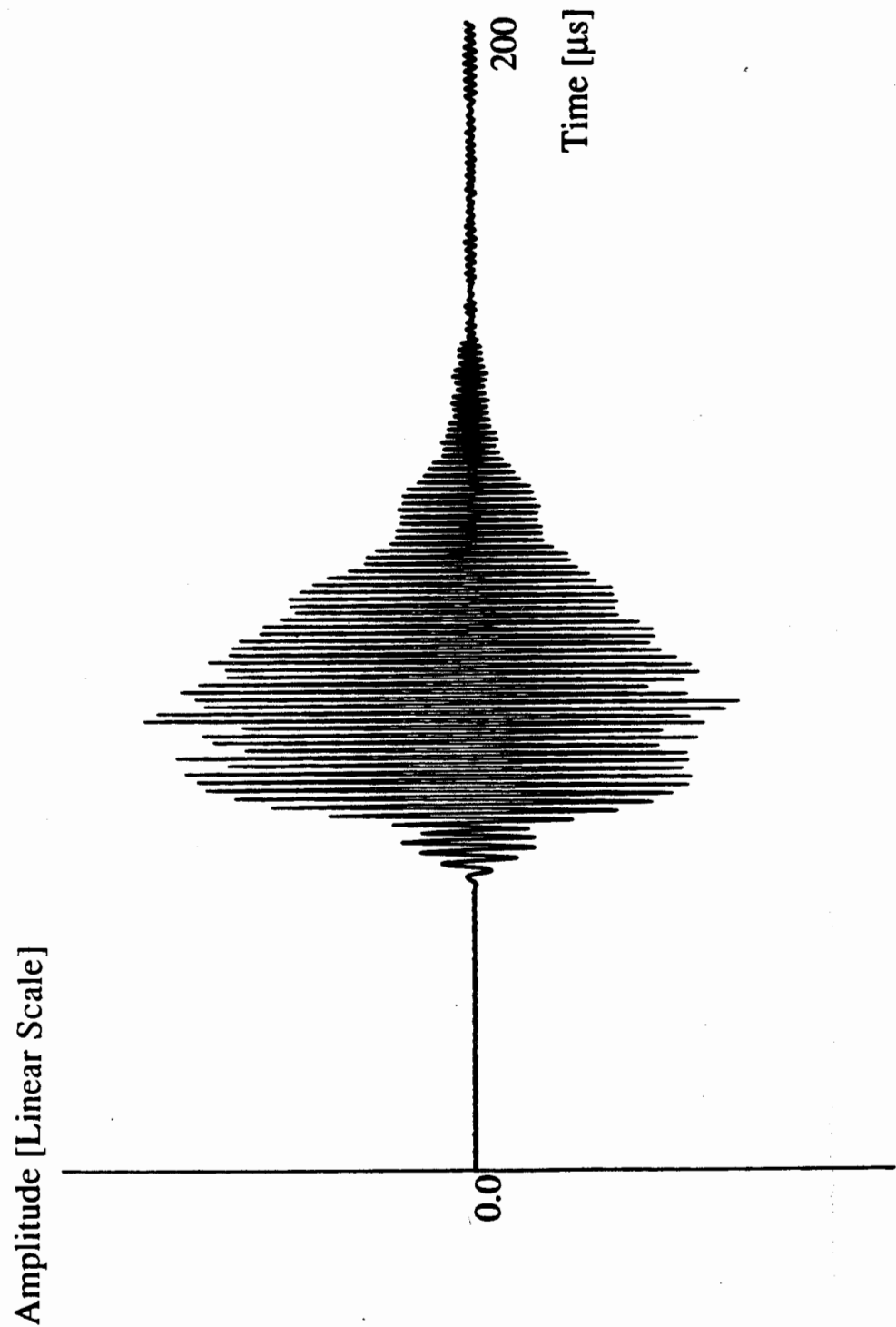


Figure 6.11 Normalised time history of the measured response at $x = 200$ mm in a 2 mm thick plate when the frequency of the excitation signal shown in Fig. 6.10(a) was 1.0 MHz and was appropriate for s_0 .

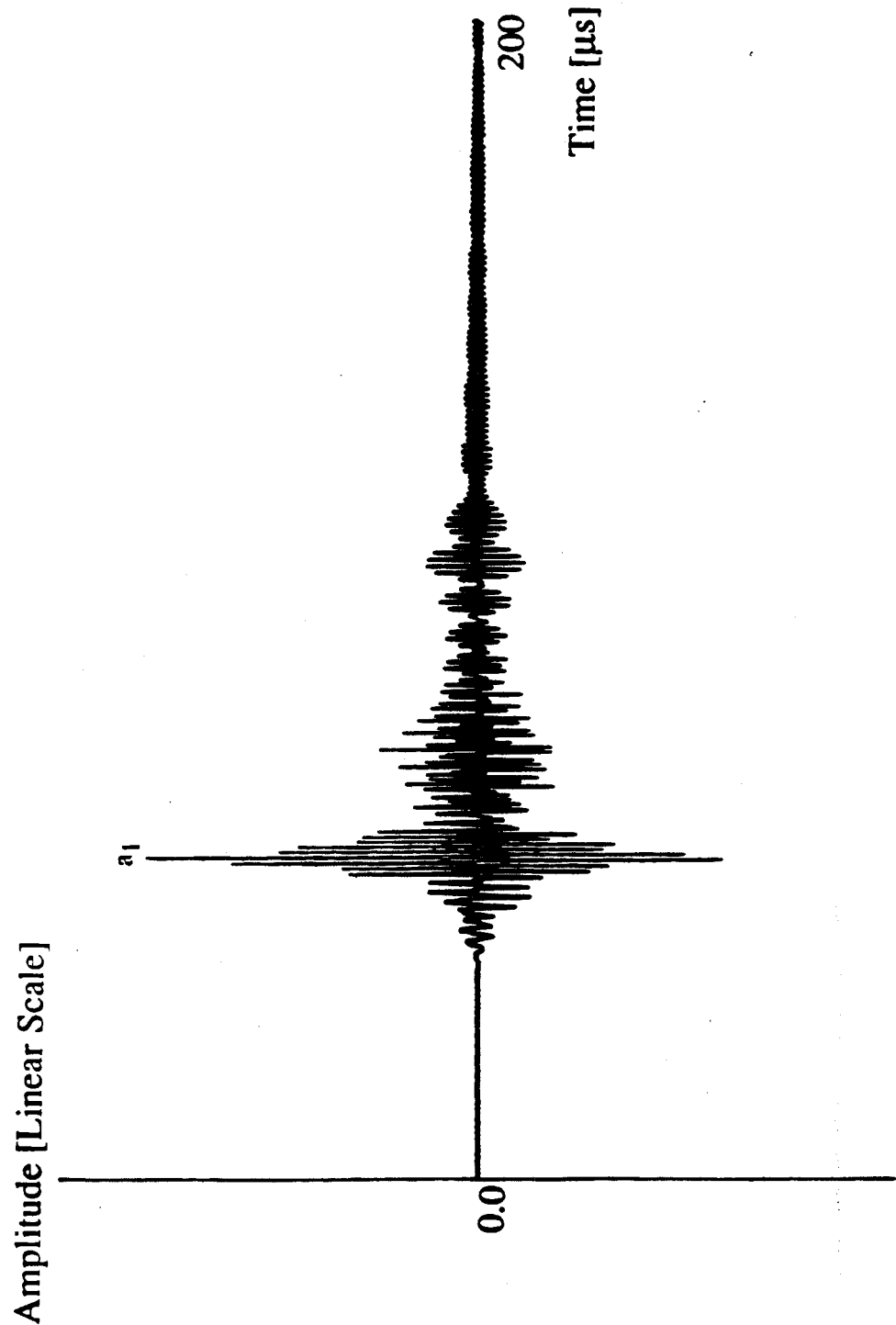


Figure 6.12 Normalised time history of the measured response at $x = 200$ mm in a 3 mm thick plate when the frequency of the excitation signal shown in Fig. 6.10(a) was 1.0 MHz and was appropriate for a_1 .

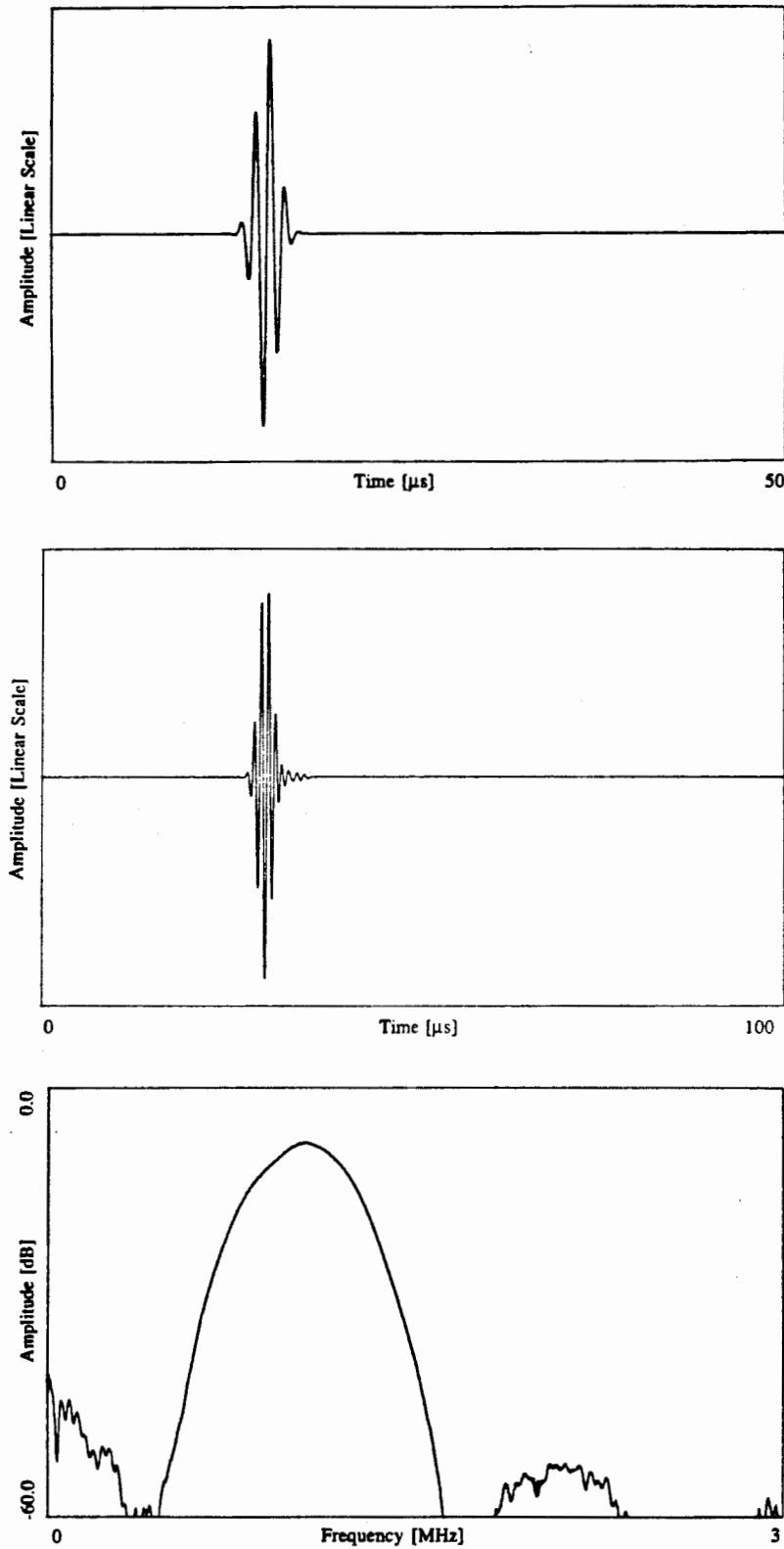


Figure 6.13 (a) Normalised time history of the 5 cycle 1.2 MHz excitation tone burst modified by a Hanning window. (b) Measured response at $x = 200$ mm in a 0.5 mm thick plate when the excitation signal shown in (a) was appropriate for s_0 . (c) Amplitude spectrum of the time history shown in (b).

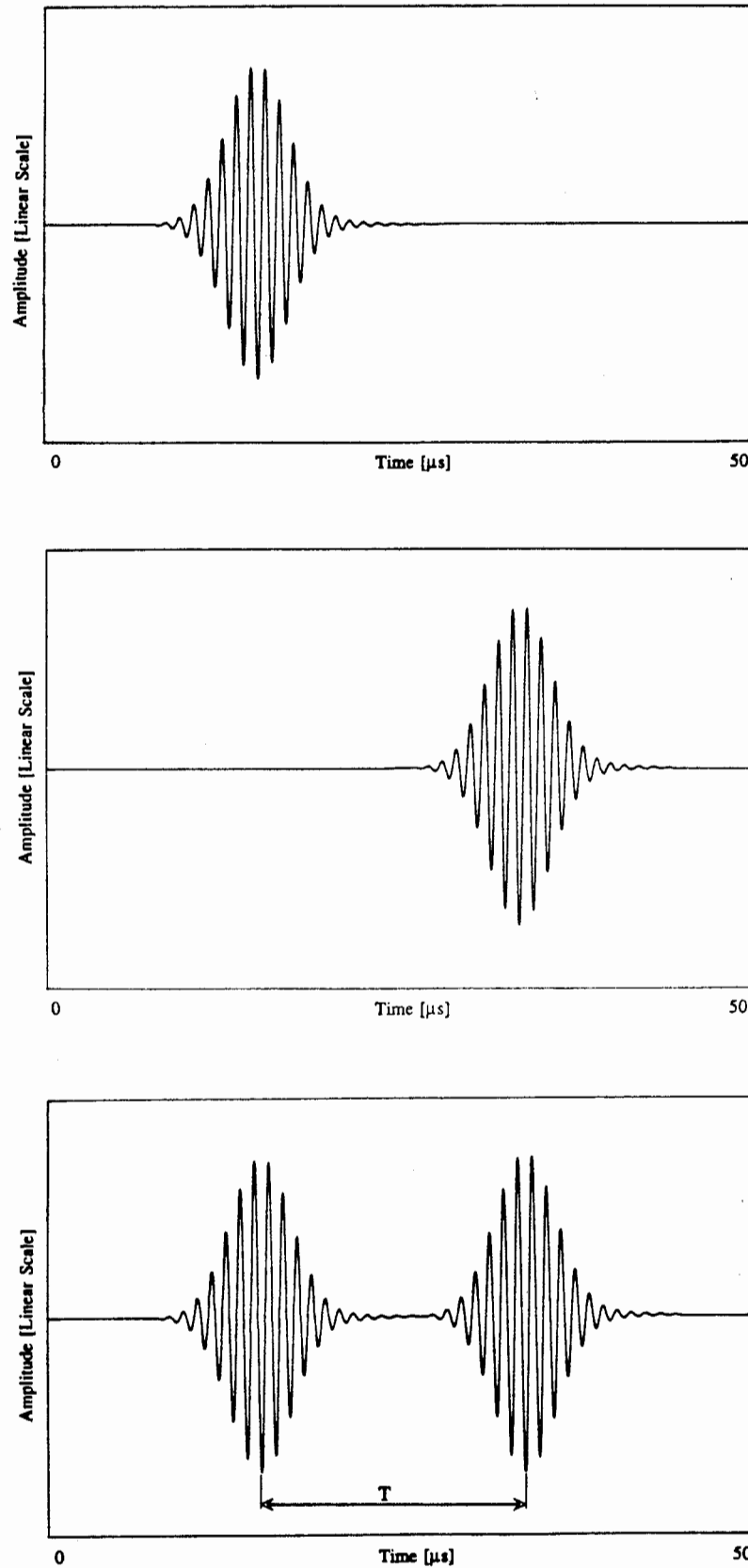


Figure 6.14 (a) Normalised time history of the measured response at $x = 150$ mm in a 0.5 mm thick plate when the excitation signal was a 12 cycle 1.0 MHz tone burst in a Hanning window and the angle was appropriate for s_0 ; (b) at $x = 250$ mm and (c) the sum of the time histories shown in (a) and (b).

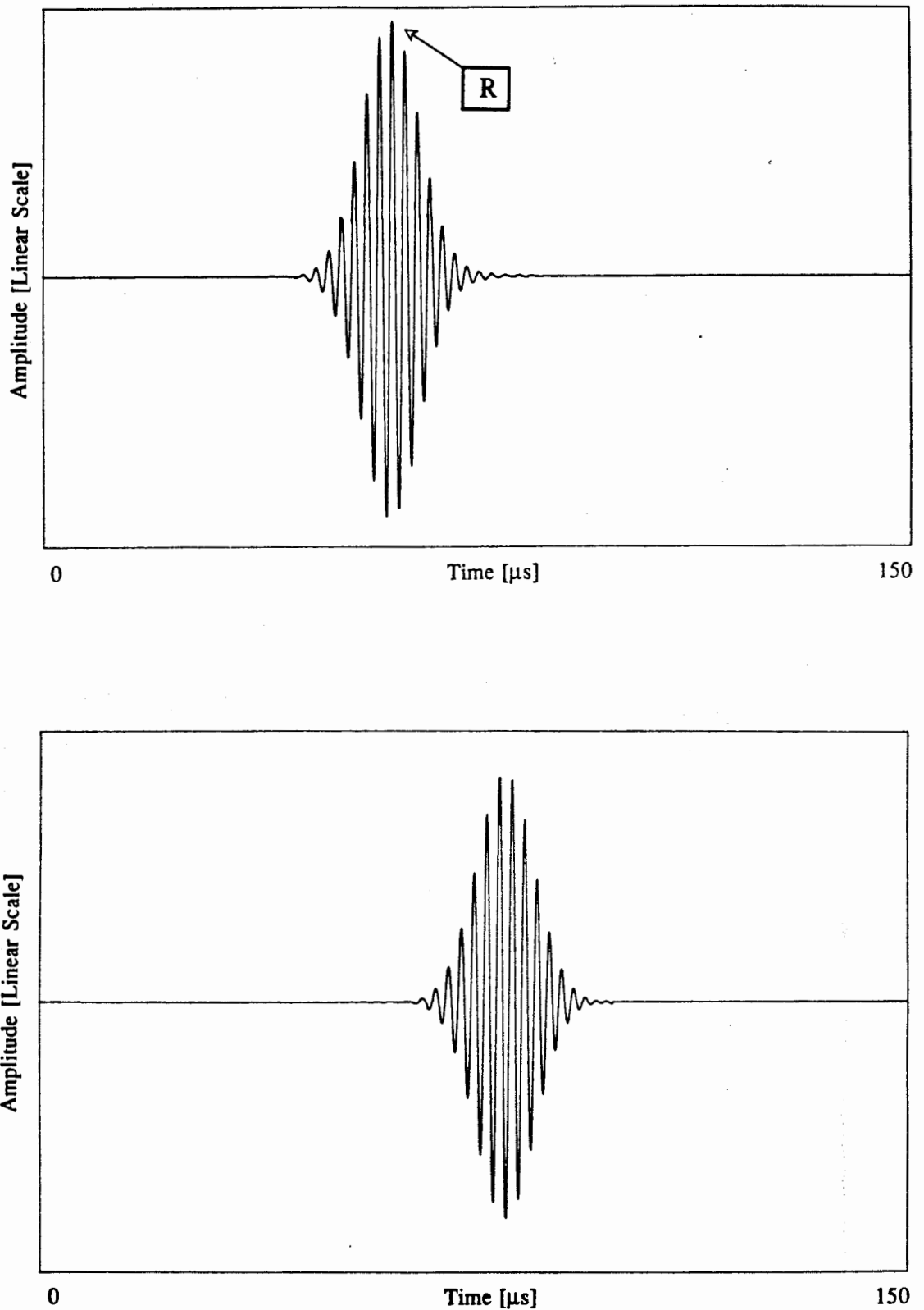


Figure 6.15 (a) Normalised time history of the measured response at $x = 150$ mm in a 3.0 mm thick plate when the excitation signal was a 12 cycle 0.45 MHz tone burst in a Hanning window and the angle was appropriate for s_0 ; (b) at $x = 250$ mm.

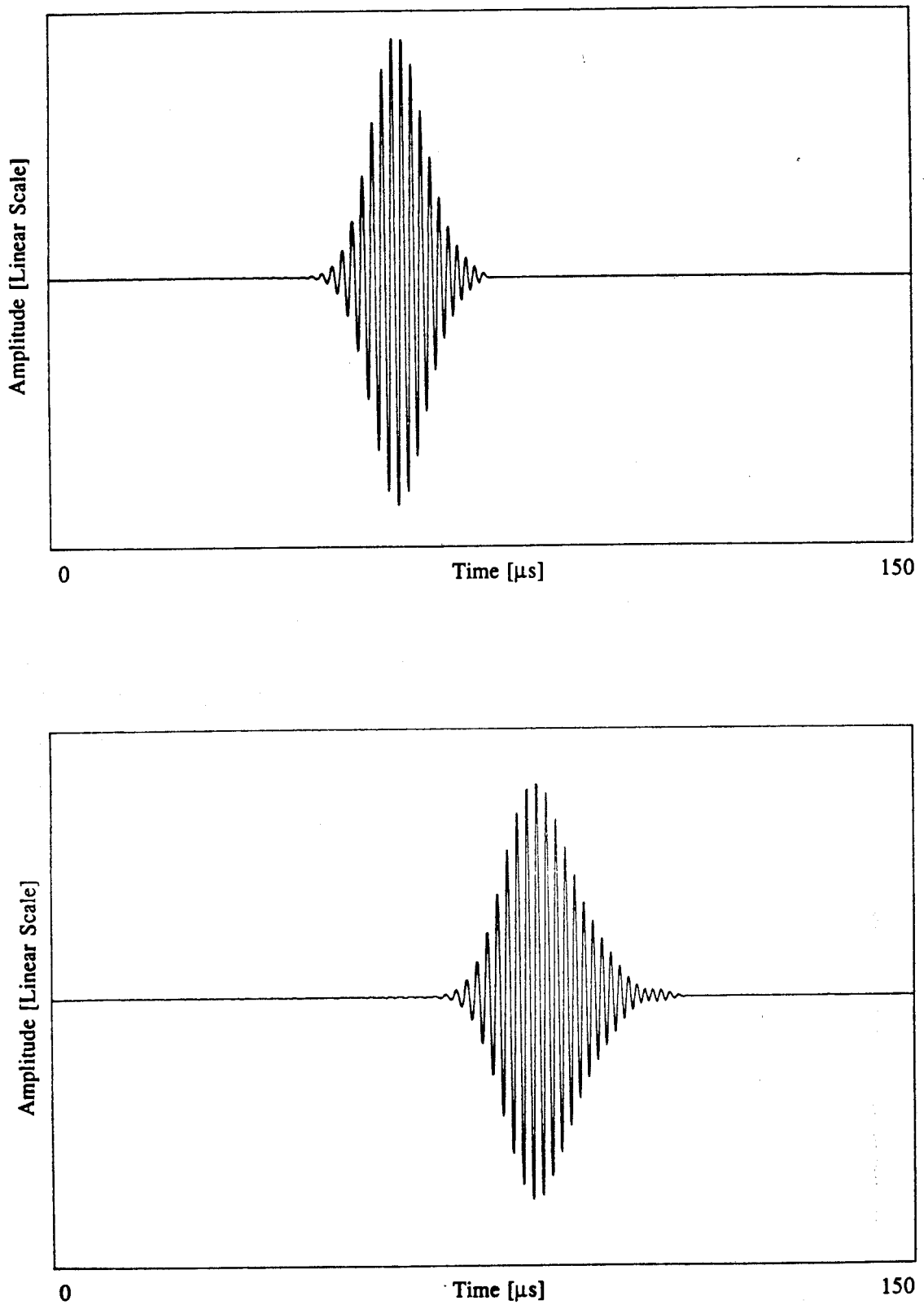


Figure 6.16 (a) Normalised time history of the measured response at $x = 150$ mm in a 3.0 mm thick plate when the excitation signal was a 12 cycle 0.6 MHz tone burst in a Hanning window and the angle was appropriate for s_0 ; (b) at $x = 250$ mm.

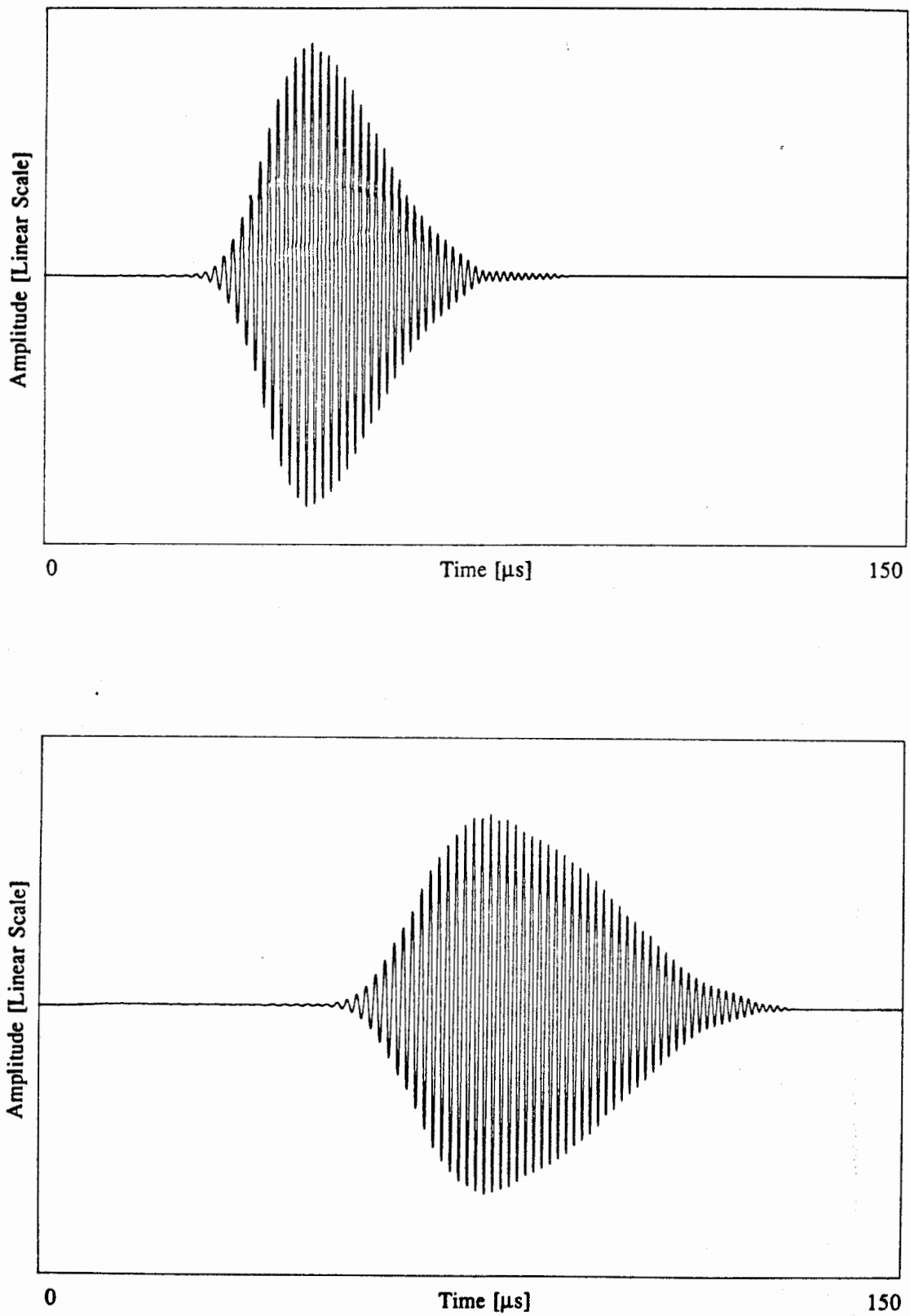


Figure 6.17 (a) Normalised time history of the measured response at $x = 150$ mm in a 3.0 mm thick plate when the excitation signal was a 12 cycle 0.75 MHz tone burst in a Hanning window and the angle was appropriate for s_0 ; (b) at $x = 250$ mm.

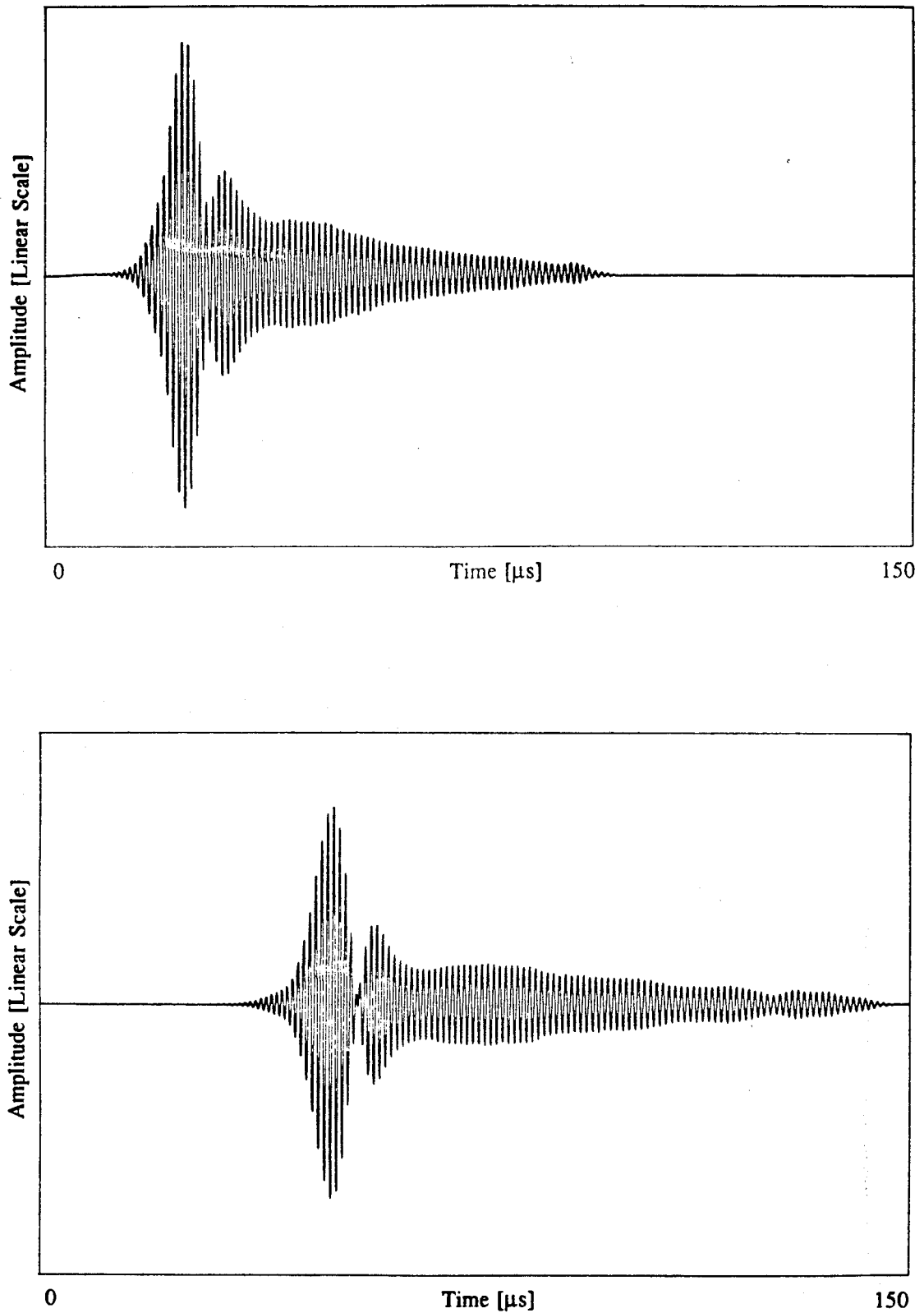


Figure 6.18 (a) Normalised time history of the measured response at $x = 150$ mm in a 3.0 mm thick plate when the excitation signal was a 12 cycle 1.0 MHz tone burst in a Hanning window and the angle was appropriate for s_1 , a_1 , and s_0 ; (b) at $x = 250$ mm.

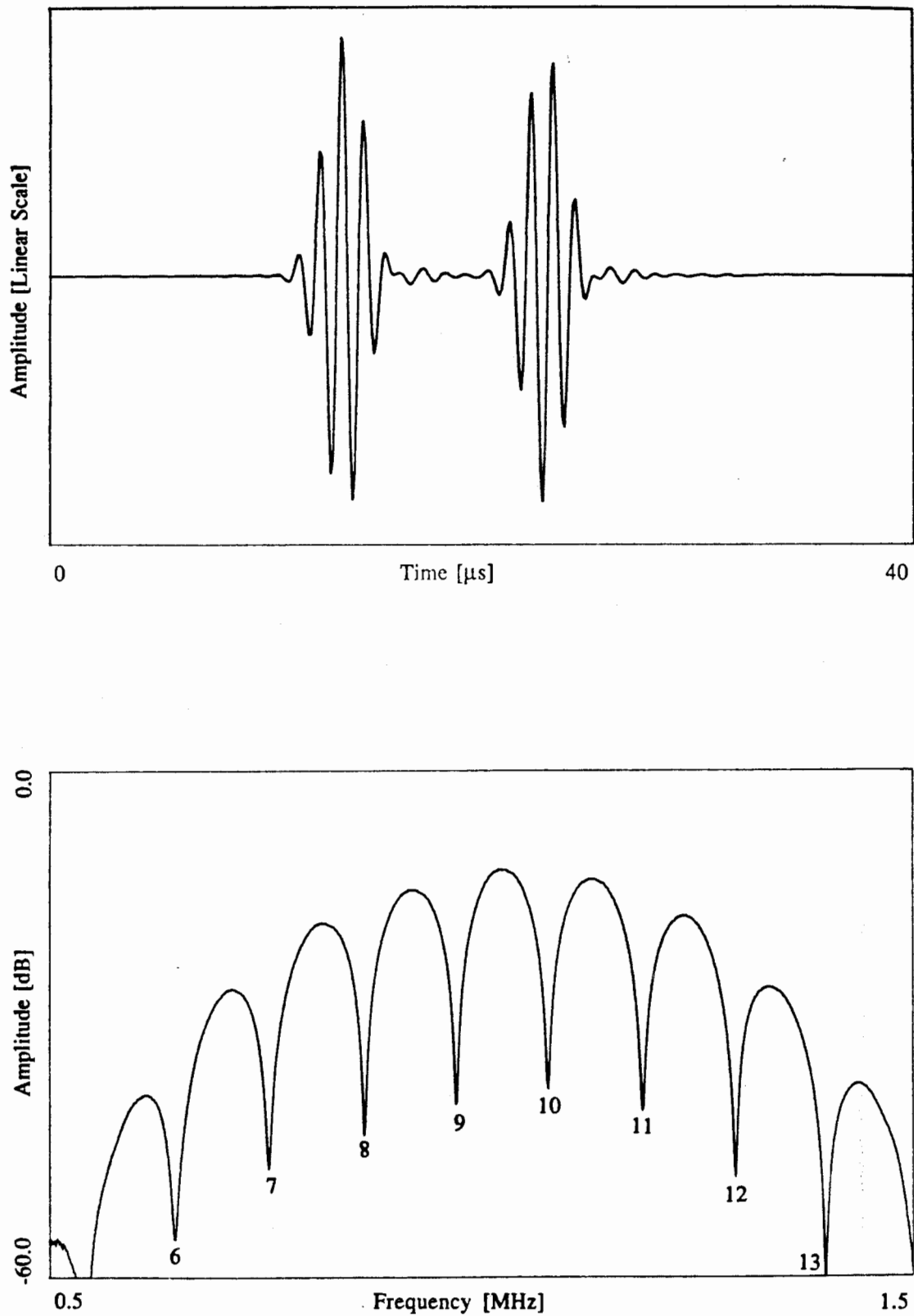


Figure 6.19 (a) Normalised time history of the measured summed responses at $x = 200$ mm and $x = 250$ mm in a 0.5 mm thick plate when the excitation signal was a 5 cycle 1 MHz tone burst in a Hanning window and the angle was appropriate for s_0 ; (b) Amplitude spectrum of the time history shown in (a).

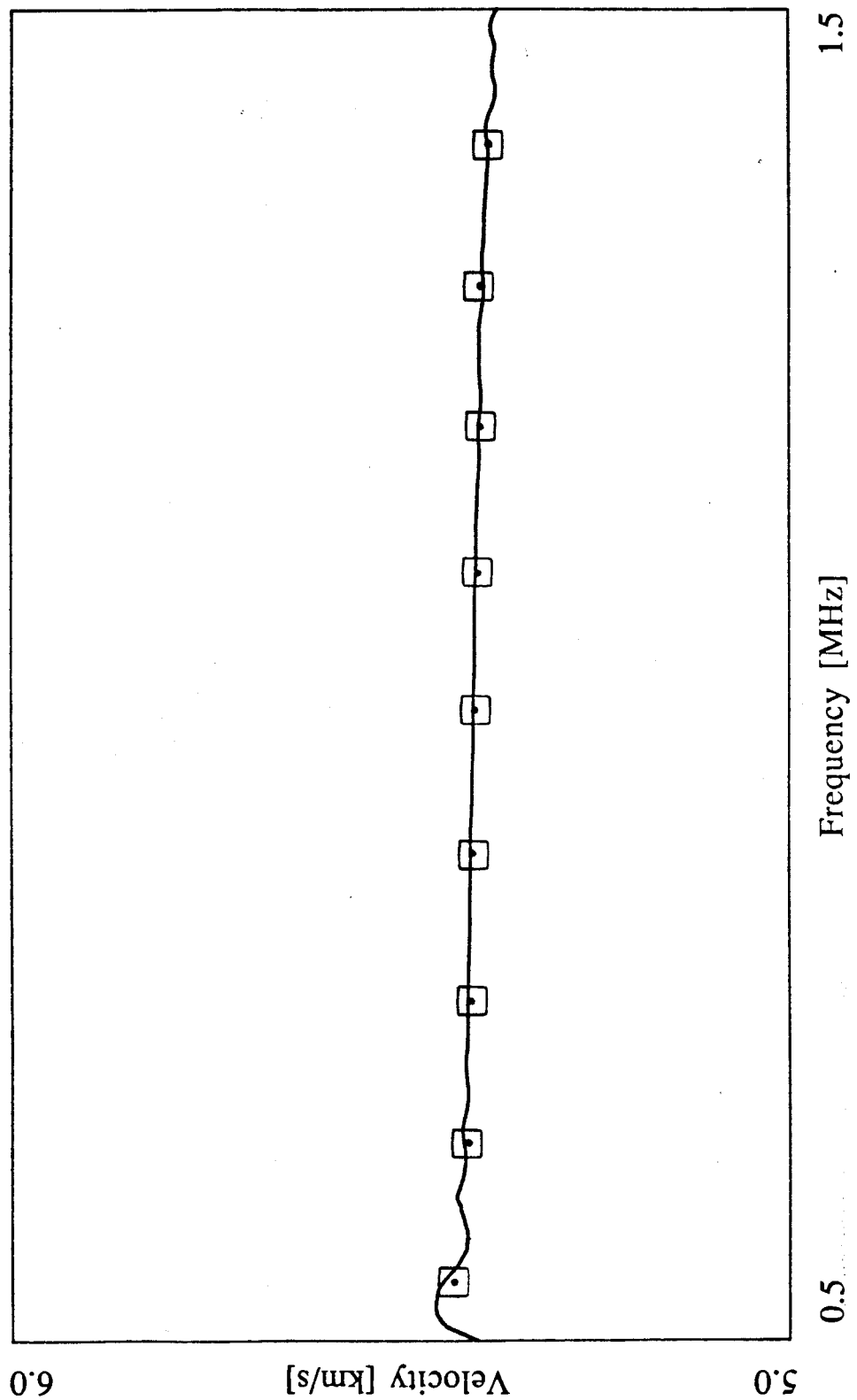


Figure 6.20 A comparison of the phase and amplitude spectrum results obtained from the time record shown in Fig. 6.19, where the amplitude spectrum results are denoted by squares.

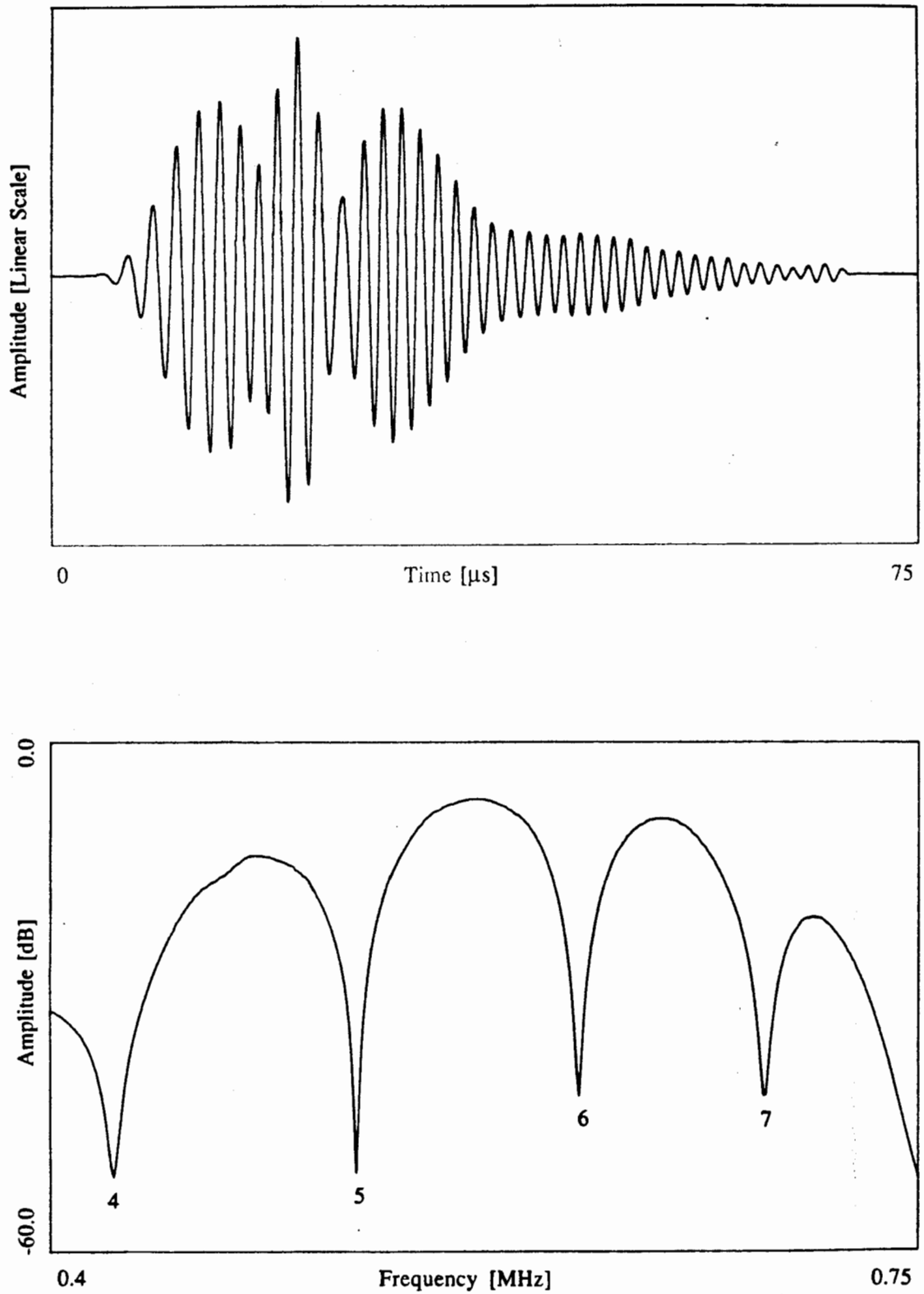


Figure 6.21 (a) Normalised time history of the measured summed responses at $x = 200$ mm and $x = 250$ mm in a 3.0 mm thick plate when the excitation signal was a 5 cycle 0.6 MHz tone burst in a Hanning window and the angle was appropriate for s_0 ; (b) Amplitude spectrum of the time history shown in (a).

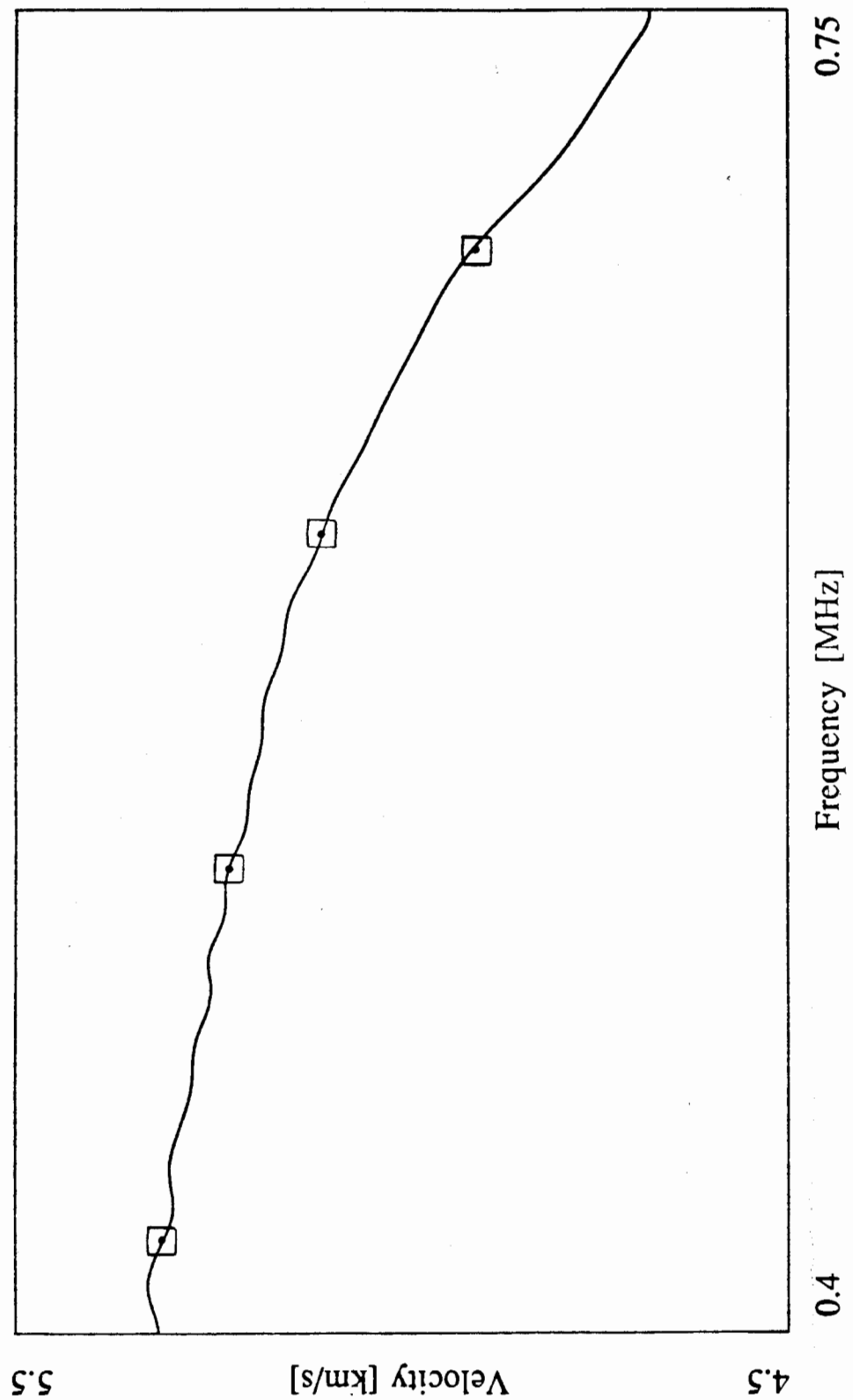


Figure 6.22 A comparison of the phase and amplitude spectrum results obtained from the time record shown in Fig. 6.21, where the amplitude spectrum results are denoted by squares.

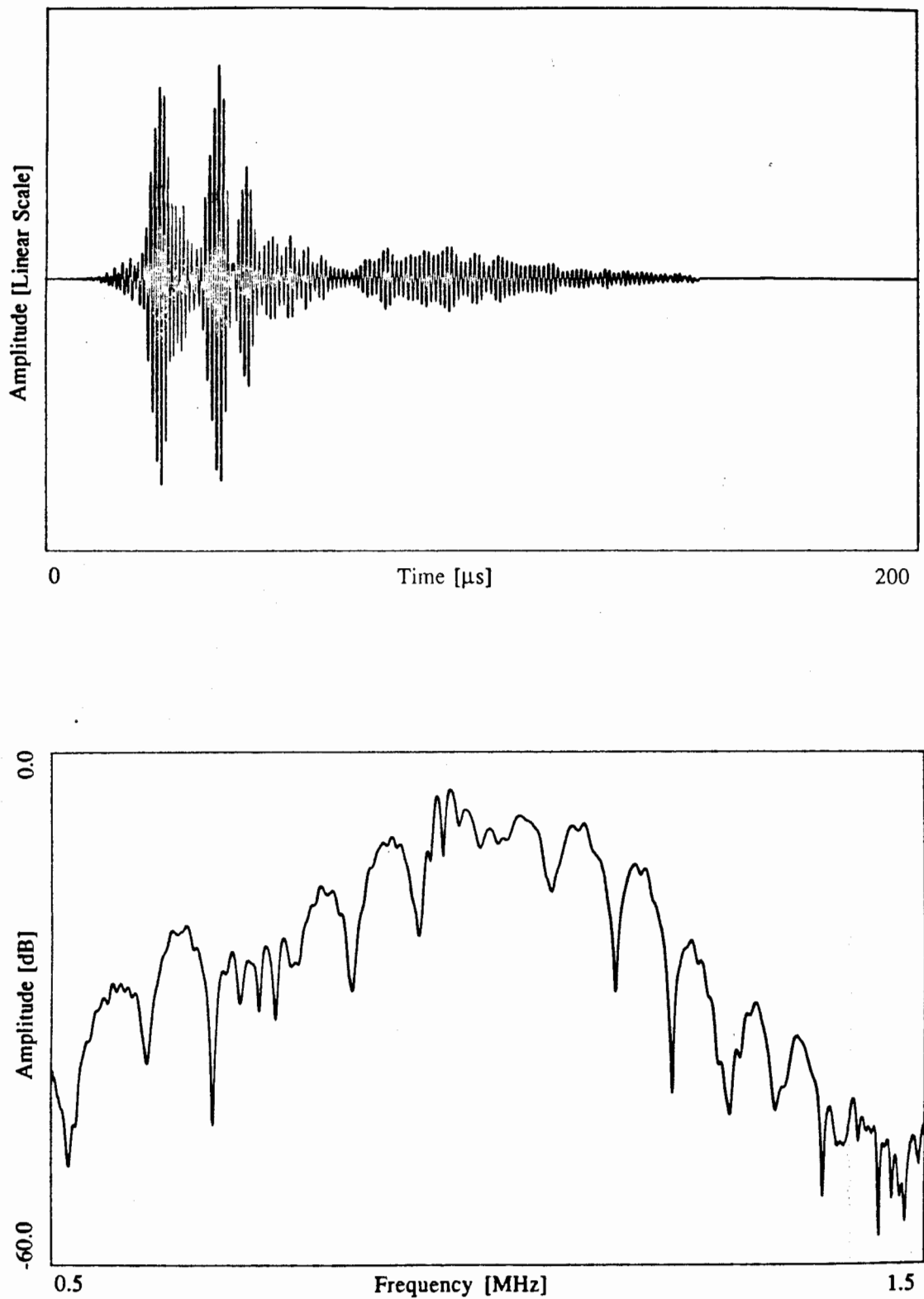


Figure 6.23 (a) Normalised time history of the measured summed responses at $x = 200$ mm and $x = 250$ mm in a 3.0 mm thick plate when the excitation signal was a 5 cycle 1.0 MHz tone burst in a Hanning window and the angle was appropriate for s_1 , a_1 , and s_0 ; (b) Amplitude spectrum of the time history shown in (a).

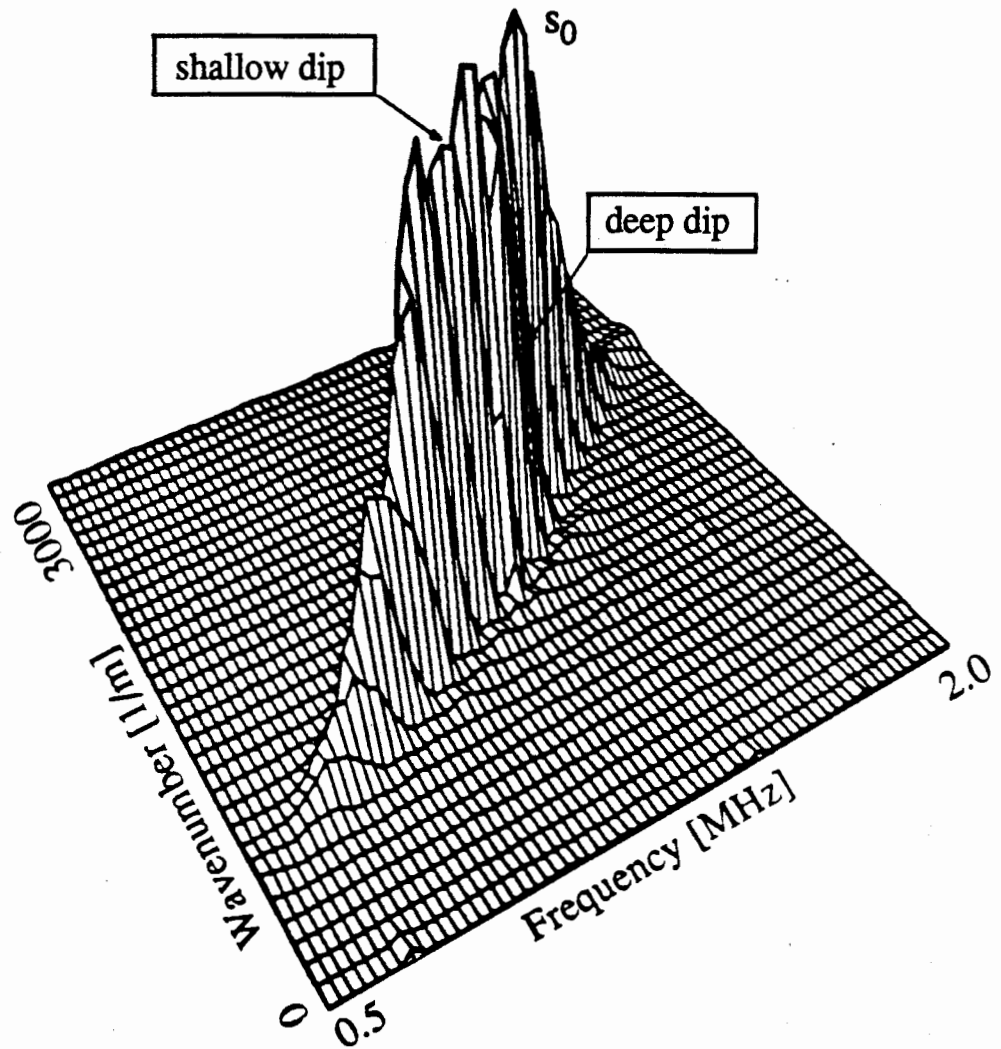


Figure 6.24 Normalised 3-D plot of the 2-D FFT results for the case of Fig. 6.10(b).

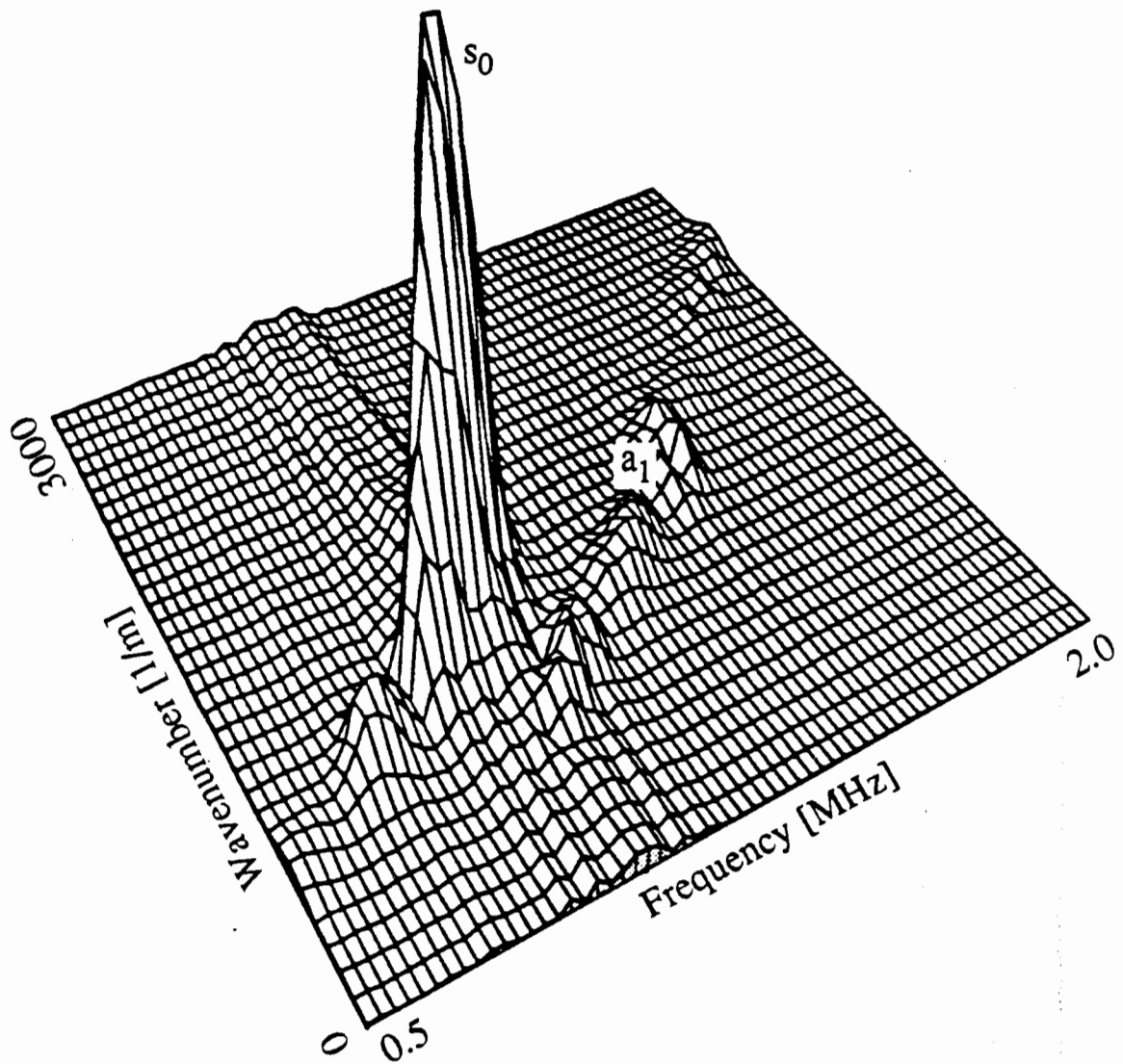


Figure 6.25 Normalised 3-D plot of the 2-D FFT results for the case of Fig. 6.11.

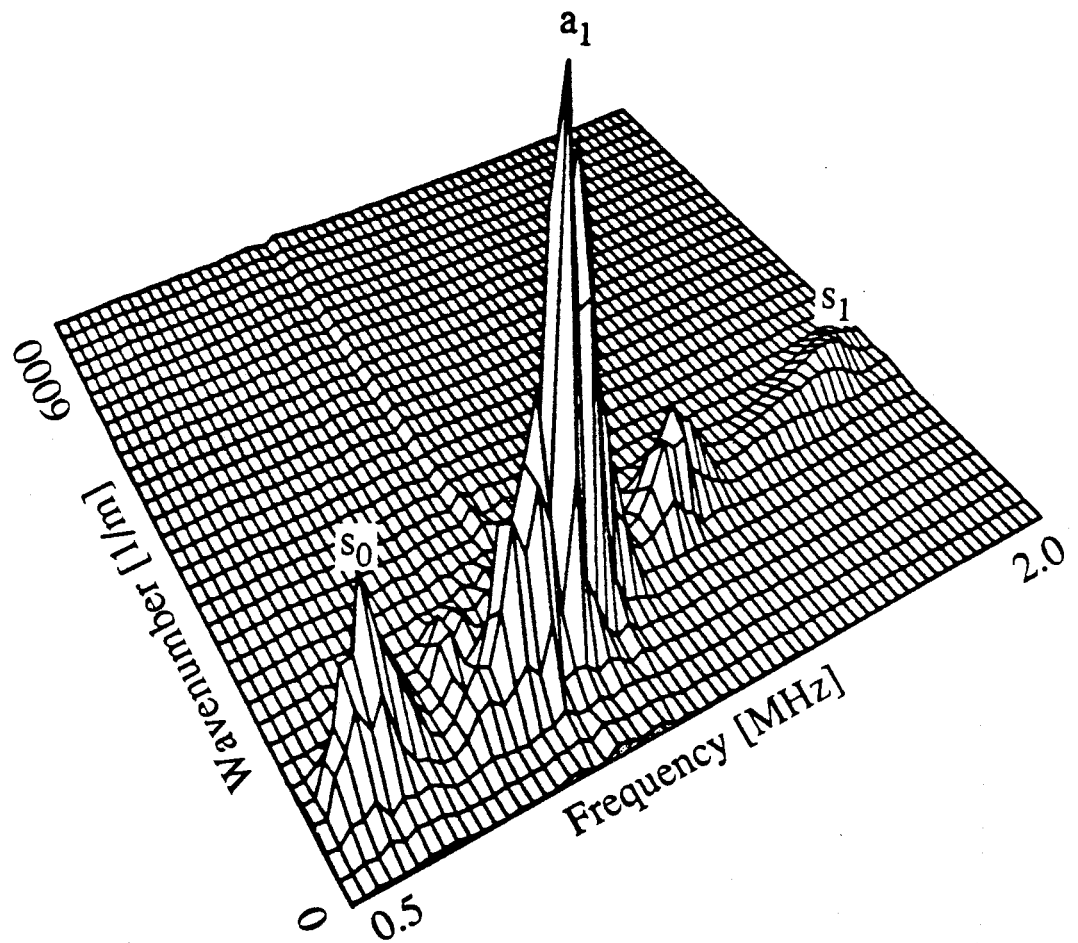


Figure 6.26 Normalised 3-D plot of the 2-D FFT results for the case of Fig. 6.12.

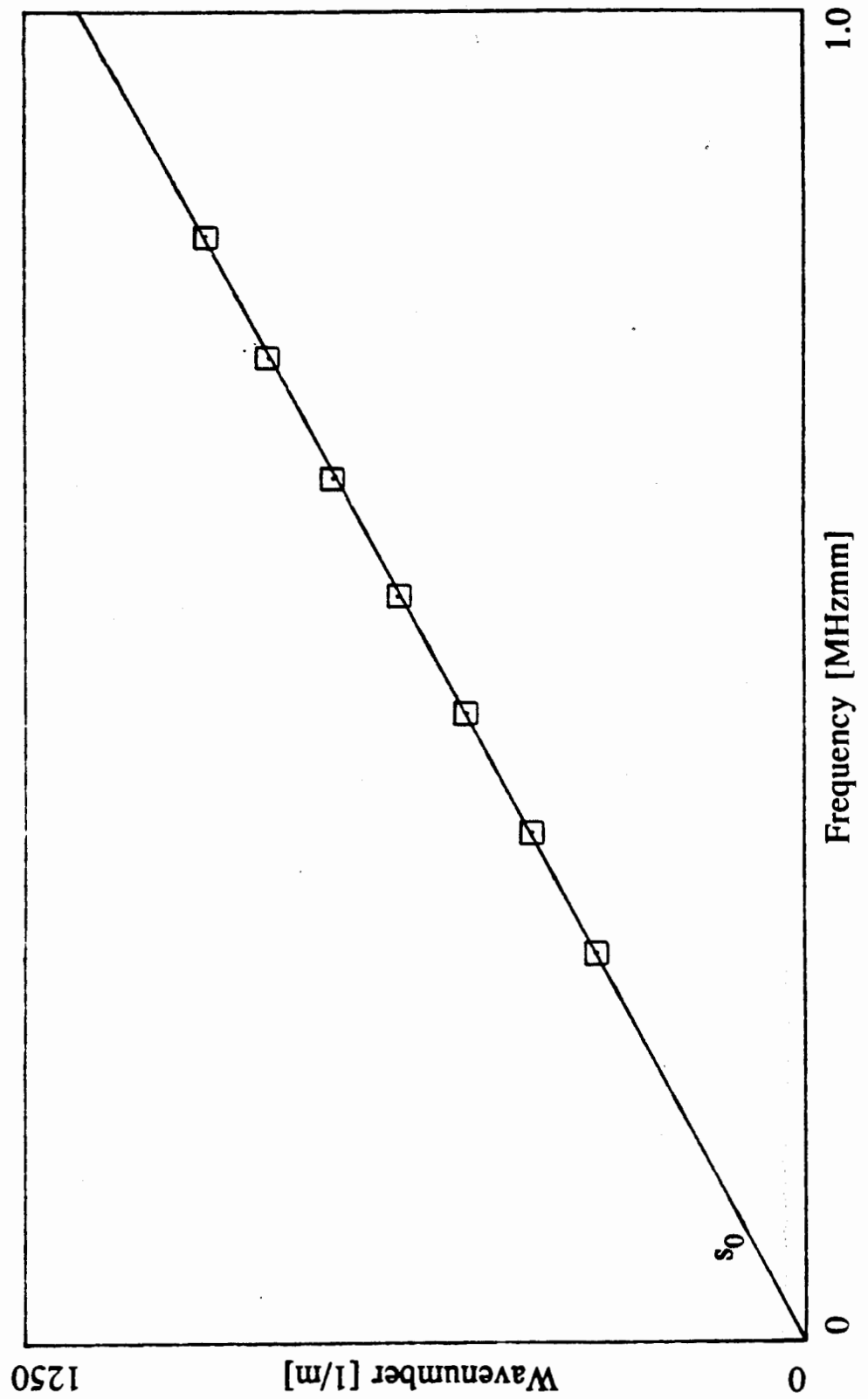


Figure 6.27 A comparison of the experimental results (□) obtained from Fig. 6.24 with the analytically generated dispersion curve for s_0 .

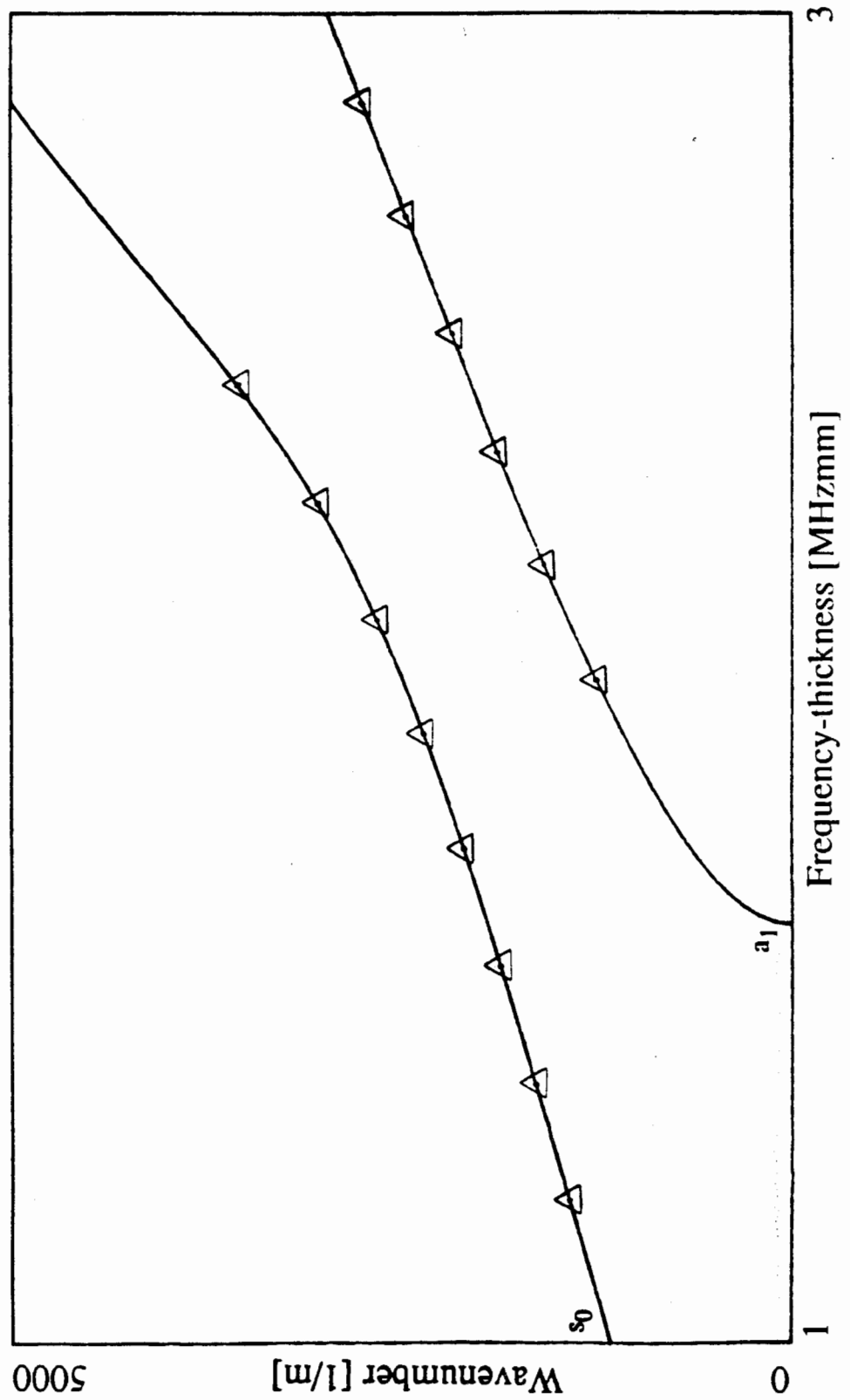


Figure 6.28 A comparison of the experimental results (Δ) obtained from Fig. 6.25 with the analytically generated dispersion curve s_0 .

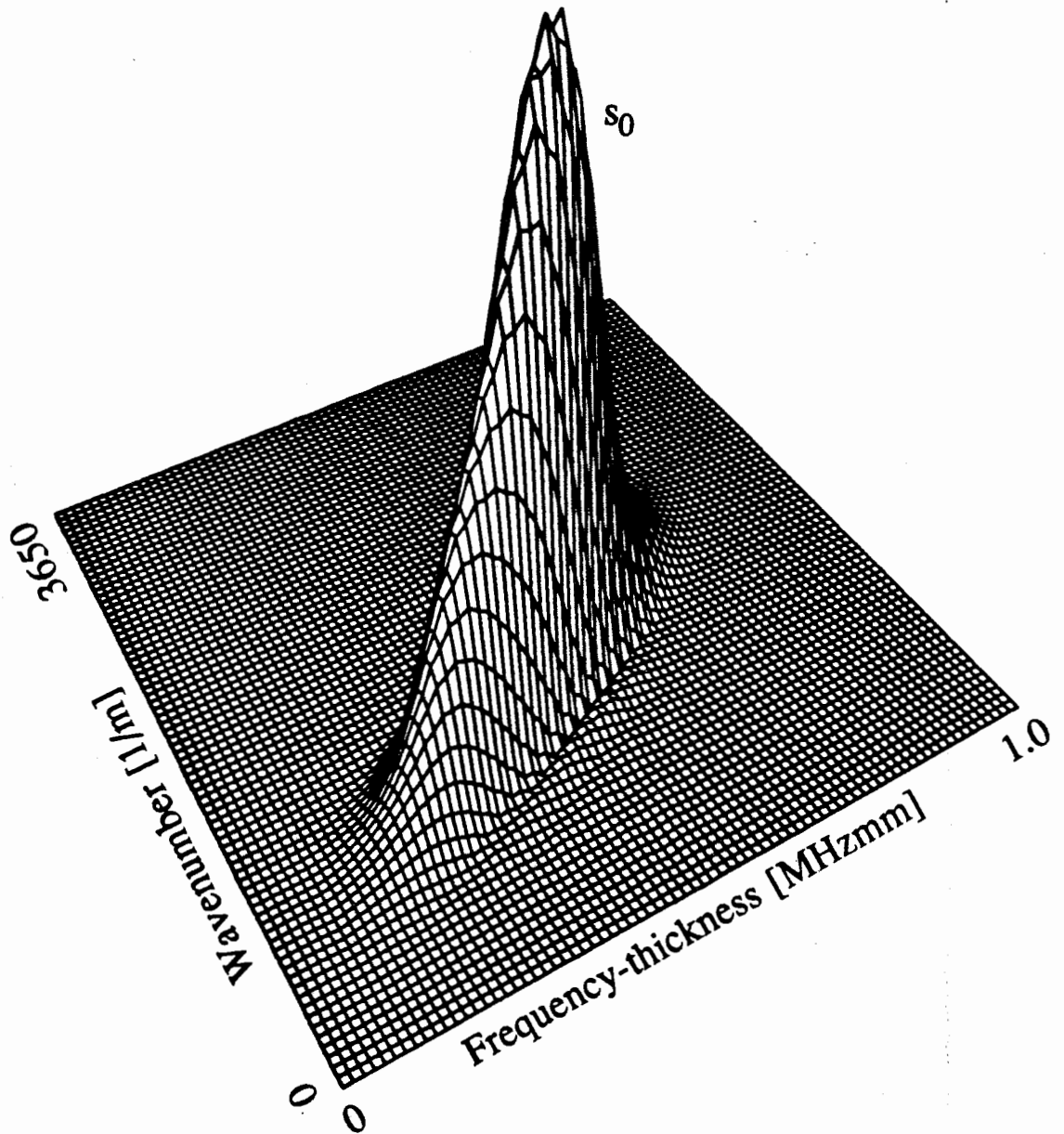


Figure 6.29 Normalised 3-D plot of the 2-D FFT results for the case of Fig. 6.13(b).

CHAPTER 7

The measurement of Lamb wave interaction with notches

7.1 Introduction

The major objective of the experimental program reported in this chapter was to validate the finite element (FE) predictions presented in chapter 5. This was achieved by exciting an individual Lamb wave and measuring its amplitude after it had interacted with straight sided notches of varying depths in 3.0 mm thick steel plates. The experimental testing procedure when the 2-D FFT method was used is shown schematically in Fig. 7.1(a) and (b), where in (a) the reference 2-D FFT was obtained over a region of the plate without a notch. The transmission ratios were then obtained by dividing the 2-D FFT of the response of the plate after the Lamb wave had propagated through the notch, see Fig. 7.1(b), by the reference 2-D FFT.

The cold rolled mild steel plates used in the 2-D FFT tests were approximately 300 mm wide and 1 m long. The individual Lamb waves were selectively excited by applying the coincidence principle described previously. The experimental procedure, testing equipment and Lamb wave test rig described in chapter 5, were used throughout. In all the tests the coincidence angle of the transmitter and the receiver was 16° . In the 2-D FFT tests, the receiver was indexed from 350 to 413 mm from the transmitter, and at least 100 successively captured signals were averaged to keep the signal-to-noise ratio high. The sampling frequency was 5 MHz and a 1024 by 1024 (1k) point two-dimensional FFT was used (the 64 spatial points were padded with 960 zeros). The tests were carried out approximately in the middle of the plate so that any reflections from the edge of the plate were not included in the captured signals.

The measured properties of the plates used in the experiments are given in Table 7.1. The bulk velocities were measured using the amplitude spectrum method discussed in chapter 3 and 6 and in both cases the measurement accuracy was about $\pm 0.2\%$. The density value was obtained from measurements of the weight and volume of the plates, where the measurement accuracy was of the order of about $\pm 0.5\%$. Poisson's ratio was calculated from the measured

values for c_1 and c_2 using eqn 2.19. Comparing the values given in Table 7.1 with those used in the FE studies ($c_1 = 5960$ m/s, $c_2 = 3260$ m/s and $\rho = 8000$ kg/m³) it may be seen that the values used for c_1 , c_2 and ν in the FE studies are almost the same as those obtained from the steel plates, but that there is a difference of 2.4% in the density values. This was because majority of the FE modelling was carried out before the experimental investigation and the values given by Krautkrämer and Krautkrämer (1983) were used.

ρ [kg/m ³]	ν	c_1 [m/s]	c_2 [m/s]
7810	0.2839	5927	3256

Table 7.1 Measured properties of the steel plates

The first part of this chapter presents the experimental results of the transmission ratios of the Lamb waves s_0 and a_1 to notches in different frequency-thickness regions (shown previously in chapter 5, see Fig. 5.2), and the experimental results are then compared with the numerical predictions presented in chapter 5. Finally the results of qualitative tests carried out to determine the presence of defects in the weld region of a butt welded plate are presented.

7.2 Measurements of Lamb wave interaction with straight sided notches

The tests reported in this section were carried out to measure the sensitivity of the symmetric and antisymmetric Lamb waves s_0 and a_1 in regions 1 and 2 (see Fig. 5.2) respectively, to notches of varying depths.

The response of the 3.0 mm thick steel plate at 350 mm from the transmitter is shown in Fig. 7.2(a), when the centre frequency of the 12 cycle excitation tone burst modified by a Hanning window was 0.48 MHz, which was appropriate to excite only the s_0 mode. The amplitude spectrum shown in Fig. 7.2(b) was obtained from the time history shown in (a) and shows that the signal is narrow band, the working range being from 0.41 MHz to 0.55 MHz, (20dB down points). The wave packet seen in Fig. 7.2(a) was identified as the s_0 mode from a measurement of its group velocity using the time of flight method. The shape of the response wave packet indicates that very little dispersion is present over the frequency-thickness interval of the input signal.

Fig. 7.3(a) to (d) show the response of the plate at 350 mm from the transmitter after interaction with 0.5, 1.0, 1.5 and 2.0 mm deep notches respectively, which were located 250

mm from the transmitter, when the excitation was the same as in Fig. 7.2. The signals in Fig. 7.3(a) to (d) are dominated by the s_0 mode, though some evidence of a_0 is seen, particularly with the deeper notches. The predictions of chapter 5 indicated that significant amplitudes of a_0 could be generated by mode conversion. However, the observed amplitudes are small because the coincidence angle for a_0 is 36° in this frequency-thickness region so it is ineffectively received by the transducer oriented at 16° . The a_0 mode is therefore partially 'decoupled' by the orientation of the receiving transducer. The transmission ratios given in Table 7.2 were obtained by dividing the maximum amplitudes of the signals shown in Fig. 7.3 by the maximum amplitude of the reference signal shown in Fig. 7.2(a).

$h/2d$	1/6	1/3	1/2	2/3
FE predictions	0.97	0.81	0.57	0.36
Time domain	0.98	0.82	0.59	0.39
2-D FFT	0.98	0.82	0.58	0.37

Table 7.2 Measured transmission ratio of s_0 at 1.45 MHzmm

The FE predictions have been included for comparison purposes and it may be seen that the agreement between them and the time domain measurements is very good, the maximum difference being 3%. From Fig. 7.3(b) to (d) it may be seen that the amplitude of the a_0 mode, which has partially separated from s_0 and is seen when $t > 25 \mu\text{s}$ is significant. Therefore, the difference between the FE predictions and the measured results is probably due to the measured s_0 signal containing some of the a_0 mode which was mode converted from s_0 when it interacts with the notch.

The reference 2-D FFT shown in Fig. 7.4(a) was obtained by carrying out a two-dimensional Fourier transform on the response of the plate at 64 equally spaced positions, when the receiving transducer was indexed from 350 to 413 mm from the transmitter. Fig. 7.4(b) shows the result of carrying out a 2-D FFT on the response of the plate over the same propagation distances after interaction with the 1.0 mm deep notch located 250 mm from the transmitter. In both cases the maximum amplitude of the response is at 0.48 MHz. However, at each discrete frequency in Fig. 7.4(b) there are 2 wavenumbers relating to the incident s_0 mode and the a_0 mode, which was caused by mode conversion at the notch, at which the amplitude is a maximum. The wavenumber of a_0 is greater than that of the s_0 mode so it is partially hidden in the 3-D plot. Here, as in the time domain responses presented in Fig. 7.3, the magnitude of the a_0 mode is very small when compared with the FE predictions presented in Fig. 5.13(b) due to the decoupling effect discussed above. In Fig. 7.5 the measured amplitude versus wavenumber information from the 2-D FFT results at 1.35, 1.45 and 1.55

MHz is given. From these two-dimensional plots the variation of the amplitude with wavenumber may be clearly shown and it is possible to measure the relative amplitude of the s_0 mode after it has propagated through the notch. In Fig. 7.5 the curve that reaches the largest amplitude at the wavenumber relating to the s_0 mode was obtained from the 2-D FFT results of the reference signal, which was a pure s_0 mode. The other curves are from the 2-D FFT results after the s_0 mode had propagated through one of the notches, the results relating to each of the 4 notches being labelled in Fig. 7.5. It may be seen that, as expected from Fig. 2.4, the wavenumber at which the amplitude is a maximum changes with frequency and in this particular case, the amplitude of the s_0 mode decreases monotonically with increasing $h/2d$ as predicted in the FE results. From table 7.2 it may be seen that at 1.45 MHzmm the 2-D FFT results are in excellent agreement with the FE predictions. Comparisons of the results at 1.35 and 1.55 MHzmm with the FE predictions in Fig. 5.13 showed that these measurements are also in excellent agreement with the theoretical predictions.

Fig 7.6(a) shows the response of the 3.0 mm thick steel plate at 350 mm from the transmitter when the centre frequency of the excitation tone burst was 0.83 MHz. The wave packet was identified as the a_1 mode by measuring the time of flight of the leading edge of the signal. A 25 cycle excitation tone burst modified by a Hanning window was used because the a_1 mode is very dispersive in this frequency-thickness region, see Fig. 2.5. The amplitude spectrum of Fig. 7.6(a) is shown in Fig. 7.6(b), from which it may be seen that acoustic energy is available in the frequency range between 0.78 MHz and 0.88 MHz, (20dB down points). Fig. 7.6(c) shows the response of the plate at 350 mm from the transmitter after interaction with a 1.0 mm deep notch, which was located 250 mm from the transmitter, when the excitation was the same as in Fig. 7.6(a). In this frequency-thickness range three propagating modes (a_1 , a_0 and s_0) are possible, and the incidence angle of the receiving transducer was appropriate for the a_1 mode although small components of the s_0 and a_0 modes will also be measured. The shape of the response time history in Fig. 7.6(c) indicates that Lamb waves with similar group velocities (the wave packets have not separated) are present. Therefore, it is not possible to measure the amplitude of the a_1 mode in the time domain unless the propagation distance (after the notch) is considerably increased so that the modes can separate.

Fig. 7.7 show the transmission amplitudes of the a_1 , s_0 and a_0 modes versus wavenumber at 2.5 MHzmm. In Fig. 7.7 the curve that reaches the largest amplitude at the wavenumber relating to the a_1 mode was obtained from the 2-D FFT result of the reference signal, which was a pure a_1 mode. The other curves are from the 2-D FFT results after the a_1 mode had propagated through one of the notches, the results relating to each of the 4 notches being labelled in Fig. 7.7. The 3-D plots of the 2-D FFT results are not presented because the amplitudes of the s_0 and a_0 modes, which are caused by mode conversion at the notch and are small due to their coincidence angle not being correct, and in the plot they are hidden behind the much larger amplitude of the a_1 mode, which has the smallest wavenumber (see, Fig.

7.7). In fig. 7.7 it may be seen that the transmission ratios are non-monotonic with respect to notch depth. For example, the transmission amplitude is greater after interaction with the 2 mm notch than after interaction with the 1.5 mm notch.

Fig. 7.8(a) to (d) show the transmission ratios of the a_1 mode obtained from the 2-D FFT results as a function of the frequency-thickness product after interaction with the 0.5, 1.0, 1.5 and 2.0 mm deep notches respectively. The measured transmission amplitude ratios are represented by squares and the numerical predictions are represented by a continuous line and are included for comparison purposes. It may be seen that the trend of the experimental results follow the FE predictions very well, but that the FE predictions are shifted to the right (to higher frequency-thicknesses). This shift represents a 2% change in frequency or thickness (about 0.05 MHzmm) and is probably due to the properties of the FE model not exactly matching the steel plates used in the experimental investigations. It is particularly interesting to note that the minimum in the transmission curves predicted in Fig. 7.8(b) is reproduced in the experiments, confirming that this effect is readily measurable and so could be used for defect sizing. The minima predicted in the other curves are not seen because after allowing for the 2% shift in frequency-thickness, these occurred outside the measurement bandwidth.

frequency-thickness [MHzmm]	h/2d			
	1/6	1/3	1/2	2/3
2.35	0.90	0.38	0.19	0.38
2.45	0.84	0.19	0.50	0.69
2.55	0.76	0.20	0.79	0.82

Table 7.3 Measured transmission ratio of the a_1 mode

The transmission ratio of the a_1 mode is presented in Table 7.3 as a function of h/2d at various frequency-thickness values. It may be seen that the transmission ratio does not decrease monotonically with increasing h/2d, as, for example, s_0 does around 1.45 MHzmm (see Table 7.2), but is a non-monotonic function as predicted in the FE results in Table 5.4.

7.2.1 Discussion

The experimental results are in excellent agreement with the numerical predictions presented in chapter 5 and have shown how the 2-D FFT method may be used to quantify Lamb wave defect interactions. At 1.45 MHzmm the results obtained using a time domain approach and

the 2-D FFT method were in good agreement. The results have indicated that even below the cut-off frequency-thickness product of the a_1 mode (1.63 MHzmm for steel), when the amplitude of the mode converted wave is significant (see Fig. 7.3(b) to (d)), it is not generally possible to completely decouple it from the incident wave or vice versa using the coincidence principle, therefore the propagation distance after the defect must be sufficient to allow the modes to separate spatially if time domain methods are to be applied. This is a restrictive limitation to using time domain methods in quantitative NDT because in general a defect can be located anywhere along the propagation path. Moreover, in region 1 (see Fig. 5.2) for grease or liquid coupled transducers which measure only the z component of displacement, the a_0 mode is strongly coupled because its motion in the z direction at the surface is around 93% of the maximum motion (which also occurs in the z direction just below the surface, see Fig. 5.3(a)), whereas for the s_0 mode, the motion in the z direction at the surface is only around 37% of the maximum motion. Therefore, the measuring system is effectively biased towards measuring the a_0 mode in this frequency-thickness range.

The results relating to the transmission ratio of the a_1 mode have verified the FE predictions of local minima in the transmission ratios, which are a function of frequency-thickness. They have also indicated that when more than 2 propagating modes are present and their group velocities are similar, which is usually the case, see Fig. 2.6, the wave packets of each mode will not be separated unless the propagation distance (after the notch) is considerable. Therefore, if a quantitative analysis is required the 2-D FFT method must be used.

The form of the experimental measurements and the FE predictions of the transmission of the a_1 mode through notches of varying depth at around 2.5 MHzmm where the predicted ratios are non-monotonic and a strong function of frequency-thickness have been in very good agreement, though the experimental results are shifted by about 0.05 MHzmm (2%) on the frequency-thickness axis. This is approximately the difference between the density used in the model and that of the plates used in the experiments. Another possible cause of the difference in the results is that the plates were cold rolled mild steel, in which c_1 and c_2 in the plane of the plate (the rolling direction) are different to c_1 and c_2 normal to the plane of the plate. However, measurements of the velocities c_1 and c_2 to the degree of accuracy required in the plane of the plate are extremely difficult, so the values from measurements normal to the plate were used. These errors are not seen in the results for the transmission of the s_0 mode in region 1, because the transmission ratios are almost constant for all the notches over the frequency-thickness range tested so the shift would not be seen.

7.3 Defects in a butt welded plate

These tests were carried out to demonstrate that Lamb waves can be used as a quick and simple qualitative inspection method, the shape of the response signal being used to detect the presence of defects. A schematic representation of the butt welded 3.12 mm thick steel plate and the positions of the transmitting and receiving transducers relative to the butt weld region is shown in Fig. 7.9. In all the tests the input signal was a 0.325 MHz 10 cycle tone burst modified by a Hanning window. The propagation distance was 250 mm and the weld region was 125 mm from the transmitter. The frequency-thickness region (1 MHzmm) was chosen because both the a_0 and s_0 modes are effectively nondispersive and their group velocities differ by a considerable amount. At around 1 MHzmm the wavelength of the s_0 is approximately 16 mm. Many workers, for example, Duncumb and Keighley (1987) have reported using the s_0 mode below 1.63 MHzmm in steels and being able to detect defects with dimensions of the order of 25% of the plate thickness. In this case we would like the Lamb wave to be sensitive to defects of a significant depth (greater than 20% of the plate thickness) in the weld region, but insensitive to the small changes in thickness and material properties in the weld region. The plate thickness increased by up to around 1 mm over the 7 mm length of the weld region. This change in thickness is of the same order as the predicted detection threshold for notches using the s_0 or the a_0 mode in low frequency-thickness regions. Hence, a good weld would be expected to have little effect on the propagation of these modes.

This is confirmed in Fig 7.10(a) which shows the response of a good region of the plate at 250 mm from the transmitter. The first and second wave packets in Fig. 7.10(a) were identified as the s_0 and a_0 modes, respectively, from measurements of the time of flight of the leading edge of the individual wave packets. Both modes are excited by the excitation transducer (confirmed by the arrival time of the individual wave packets in Fig. 7.10(a)) because of the finite size of the transducers (see section 2.12). Therefore, if mode conversion occurred at the weld, which was equidistant from the two transducers, the a_0 mode produced by s_0 at the defect in the weld region and the s_0 mode produced by the incident a_0 mode would arrive at the receiver at the same time. Fig. 7.10(b) to (d) show the response of the plate at 250 mm from the transmitter after interaction with defective butt welds where the defects in the weld region were approximately 30%, 40% and 60% of the plate thickness respectively and the excitation signal was the same as in Fig. 7.10(a). The a_0 and s_0 modes, caused by mode conversion in the butt welded region can clearly be seen at the trailing edge of the s_0 wave packet in Fig. 7.10(b), (c) and (d) and have changed the shape of the response signals considerably. From the time histories of the measured responses shown in Fig. 7.10 it may be seen that the shape of the Lamb wave response signal at low frequency-thicknesses, where only a_0 and s_0 are possible may readily be used to determine the presence of defects in the butt welded region when the defect depth is of the order of 30% or more of the plate thickness.

Although the Lamb wave testing rig was used in the experiments reported in this section, similar results (the reference response signal would not be as good) may be obtained using the variable angle probes. The variable angle probes are well suited for use in qualitative methods because they are easy to use especially when dealing with practical problems such as uneven surfaces, restrictive access and obstacles in the propagation path, for example ribs and stiffeners on plates.

7.4 Conclusions

The experimental results have validated the finite element predictions presented in chapter 5, the agreement between the measured and the FE predictions of the transmission ratios being very good in the series of tests carried out around 1.45 MHzmm to determine the sensitivity of the s_0 mode to notches. The experimental investigations have shown that at frequency-thickness products below the cut off value of the a_1 mode it is possible to decouple the a_0 and s_0 modes so that the amplitudes of individual wave packets can be measured in the time domain.

The 2-D FFT method has been used to determine the transmission ratio of the a_1 mode in a frequency-thickness region where the wave is dispersive and more than one other mode is possible. At around 2.5 MHzmm the form of the experimental results and the FE predictions of the transmission of the a_1 mode through notches of varying depth, where the predicted ratios are non-monotonic and are strong function of frequency-thickness, have been in very good agreement. The experimental results have validated the FE predictions which indicated the presence of minima in the amplitude of the transmission ratios at particular frequency-thickness products, although the experimental results have been shifted by about 0.05 MHzmm (2%) on the frequency-thickness axis.

The tests on the butt welded steel plates have shown that fast, qualitative inspections may be carried out using Lamb waves by simply monitoring the change in shape of the response signal.

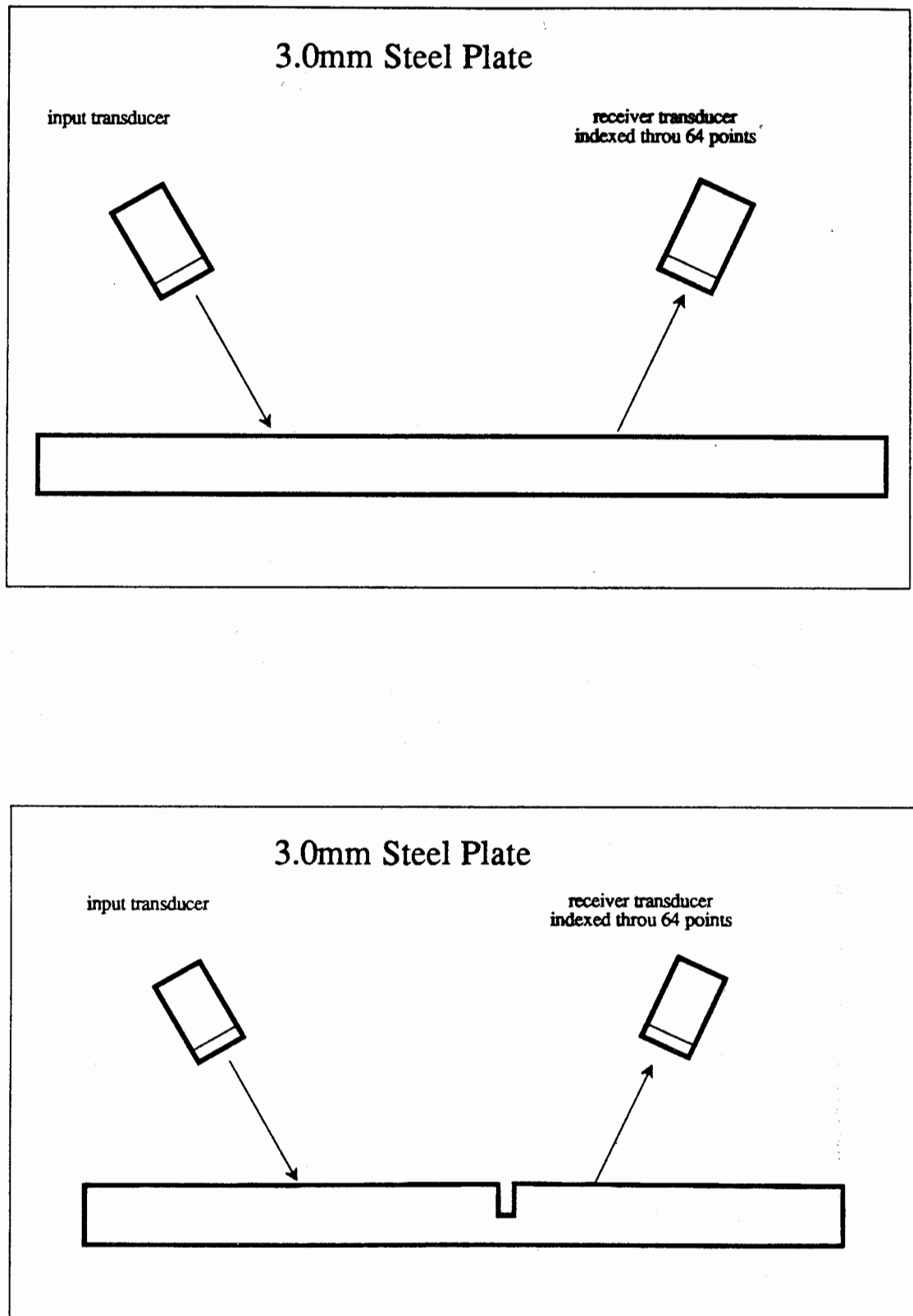


Figure 7.1 Schematic representation of experimental procedure; (a) to obtain reference 2-D FFT; (b) to obtain 2-D FFT after interaction with a notch.

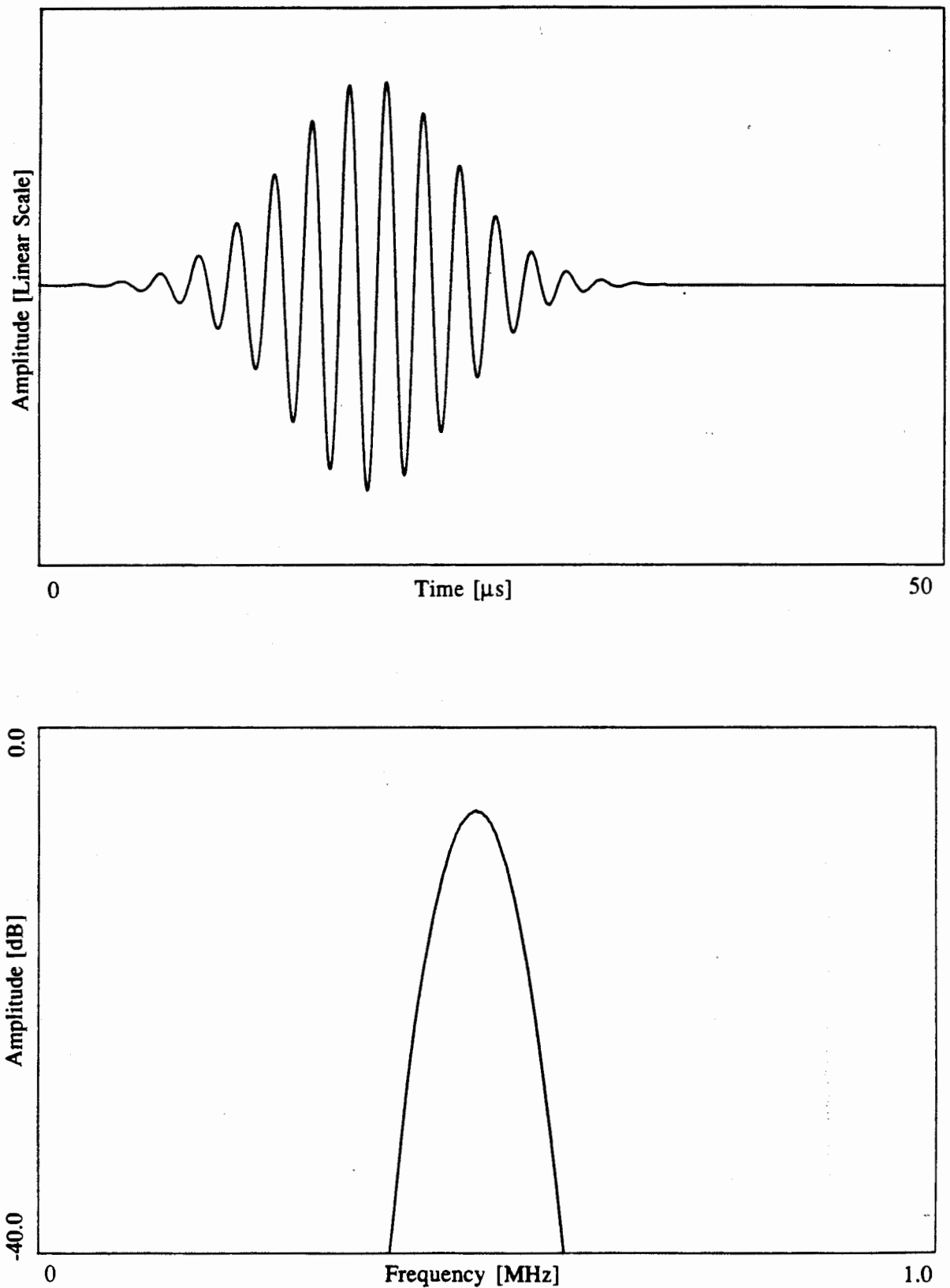


Figure 7.2 (a) The time history of the measured response at $x = 350$ mm from the transmitter in a 3.0 mm thick steel plate, when the excitation was appropriate for s_0 . (b) Amplitude spectrum of the time history shown in (a).

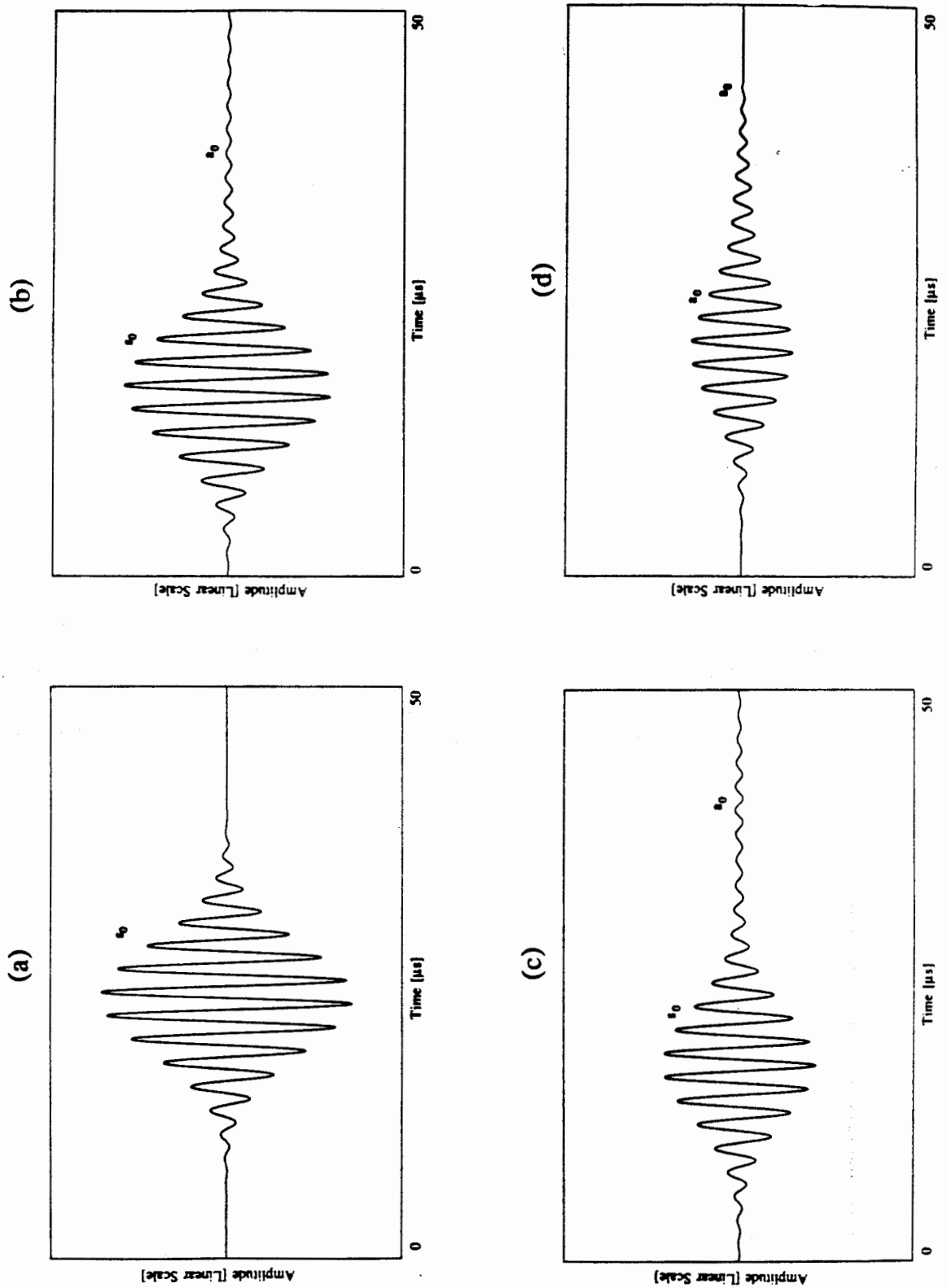


Figure 7.3 (a) The time history of the measured response at $x = 350$ mm from the transmitter in a 3.0 mm thick steel plate, when the excitation was appropriate for s_0 and a 0.5 mm deep notch was located at $x = 250$ mm; (b) a 1.0 mm notch; (c) a 1.5 mm notch; (d) a 2.0 mm notch.

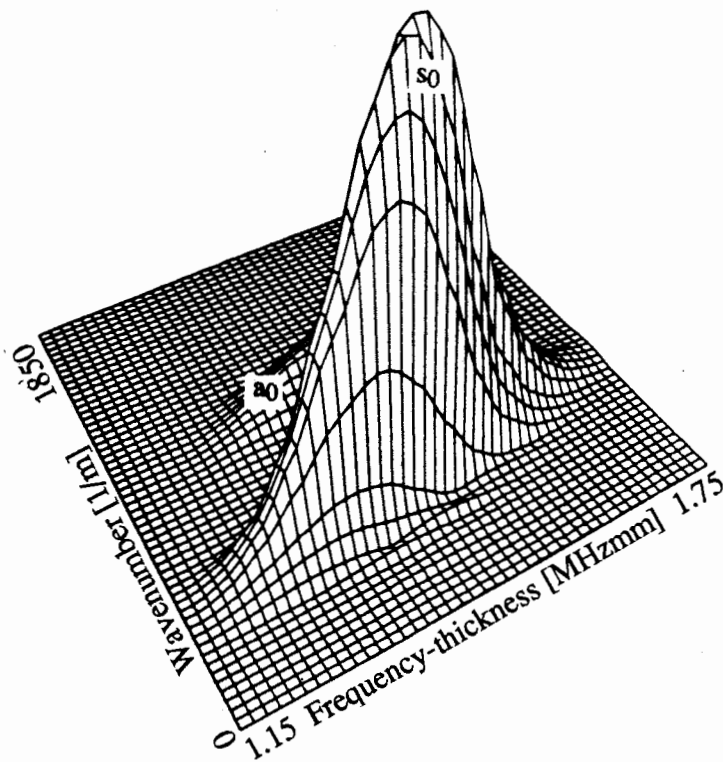
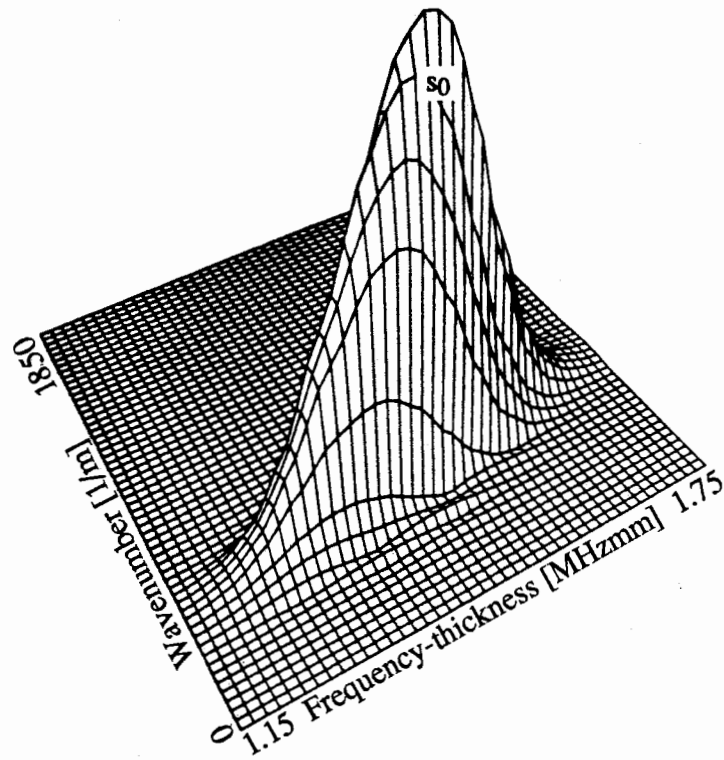


Figure 7.4 (a) Normalised 3-D plot of the reference 2-D FFT results for the case of Figure 7.2(a). (b) Normalised 3-D plot of the 2-D FFT results after the s₀ mode had interacted with the 2.0 mm deep notch.

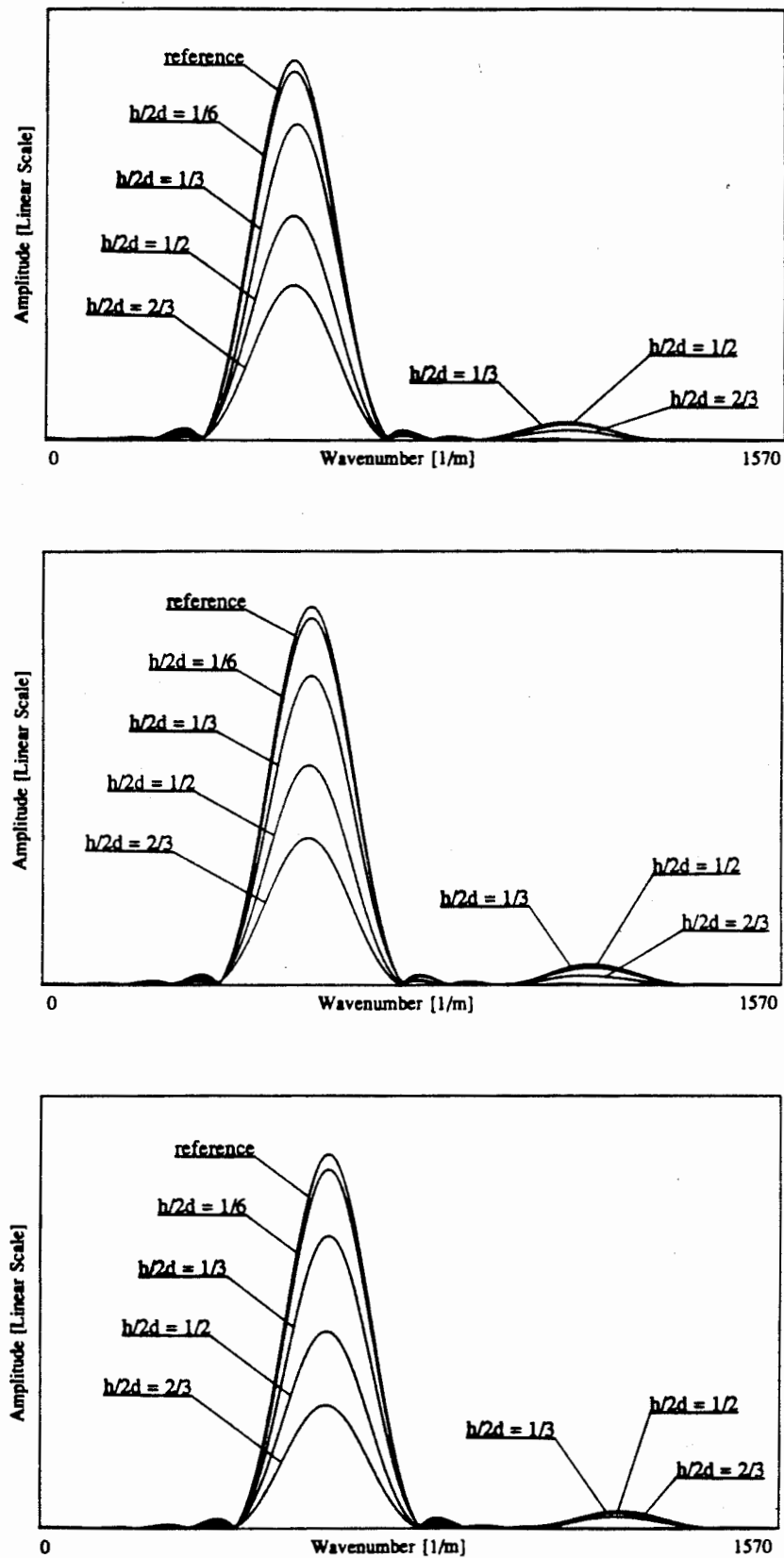


Figure 7.5 Normalised plot of the measured amplitude versus wavenumber information from the 2-D FFT results, obtained after the transmission of s_0 across notches of different depths; (a) at 1.35 MHzmm, (b) at 1.45 MHzmm and (c) 1.55 MHzmm.

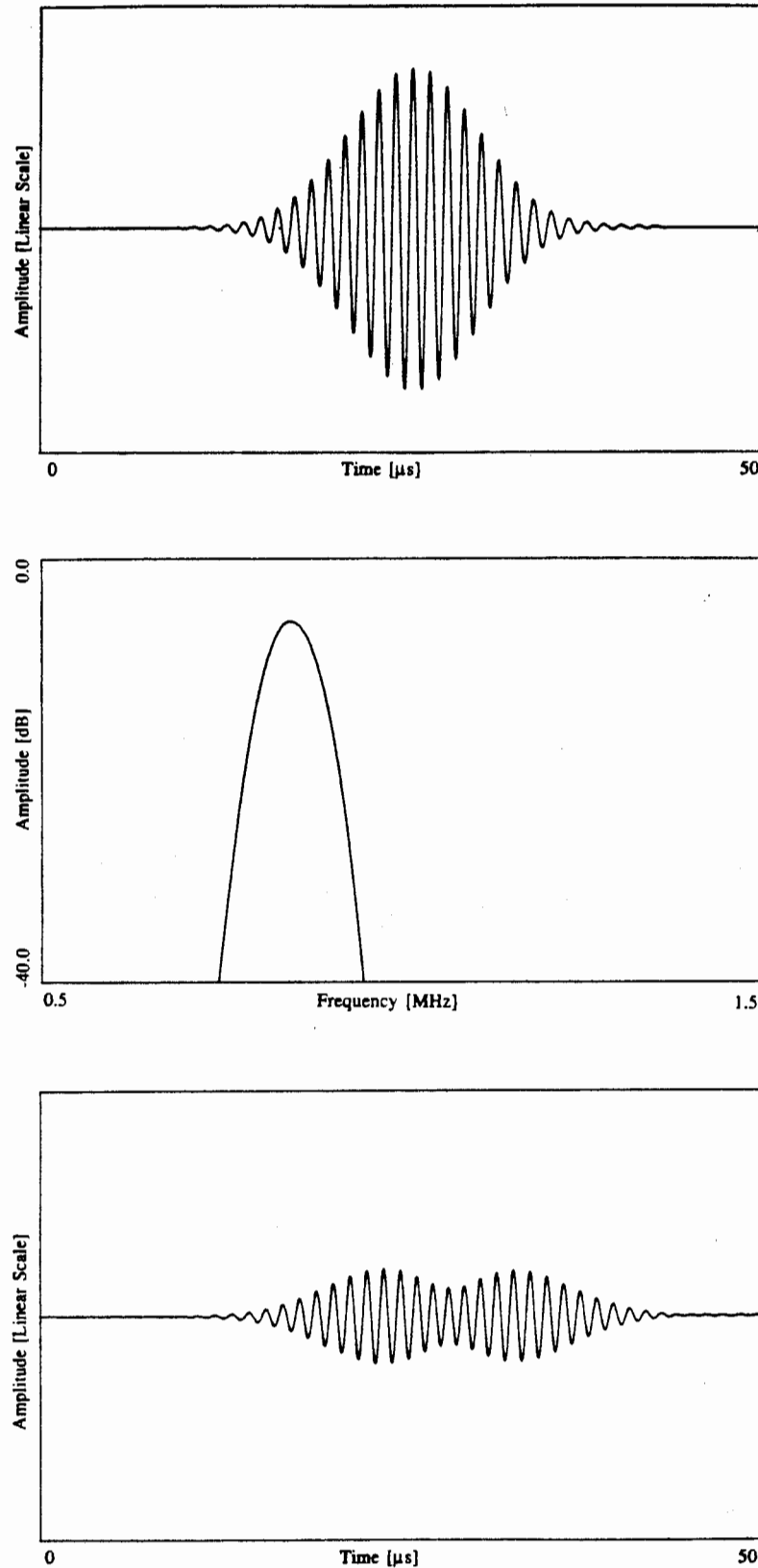


Figure 7.6 (a) The time history of the measured response at $x = 350$ mm from the transmitter in a 3.0 mm thick steel plate, when the excitation was appropriate for a_1 . (b) Amplitude spectrum of the time history shown in (a). (c) Time history of the response when a 1.0 mm deep notch was located at $x = 250$ mm and the excitation was the same as in (a).

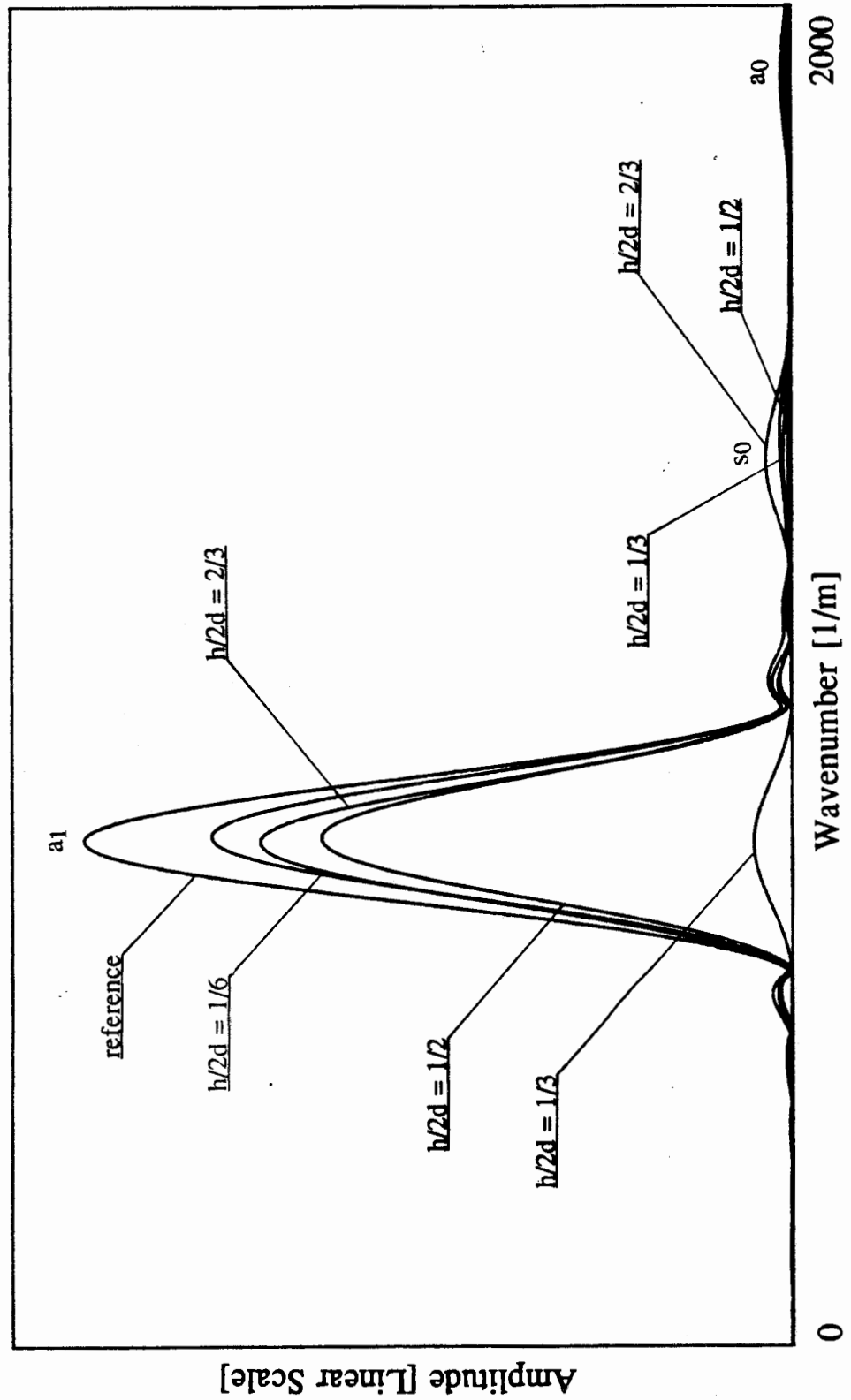


Figure 7.7 Normalised plot of the measured amplitude versus wavenumber information from the 2-D FFT results, obtained after the transmission of a_1 across notches of different depths at 2.5 MHzmm.

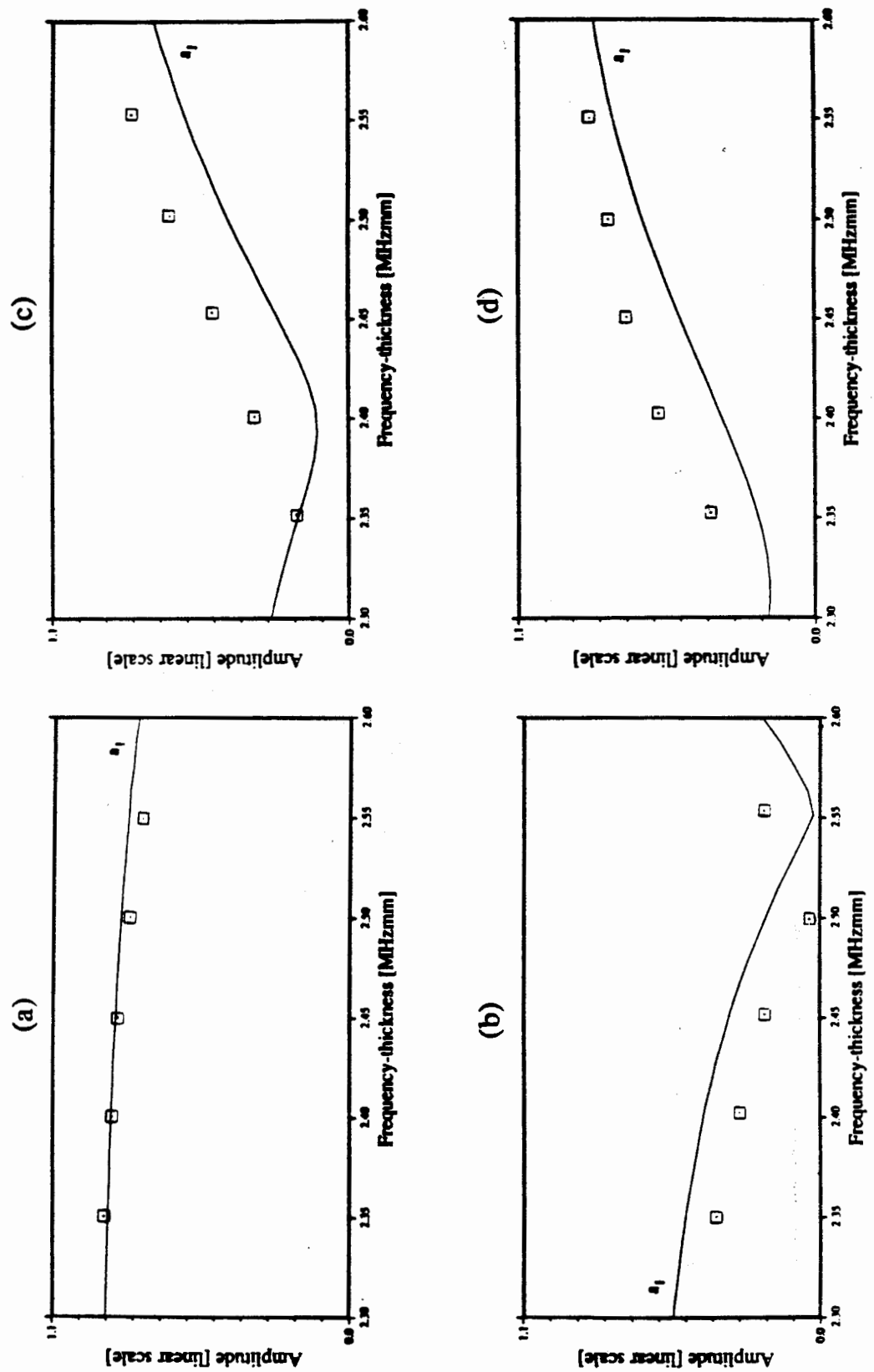


Figure 7.8 Transmission ratio of the a_1 mode as a function of frequency-thickness after interaction with (a) the 0.5 deep notch, (b) the 1.0 mm notch, (c) the 1.5 mm notch and (d) the 2.0 mm notch.

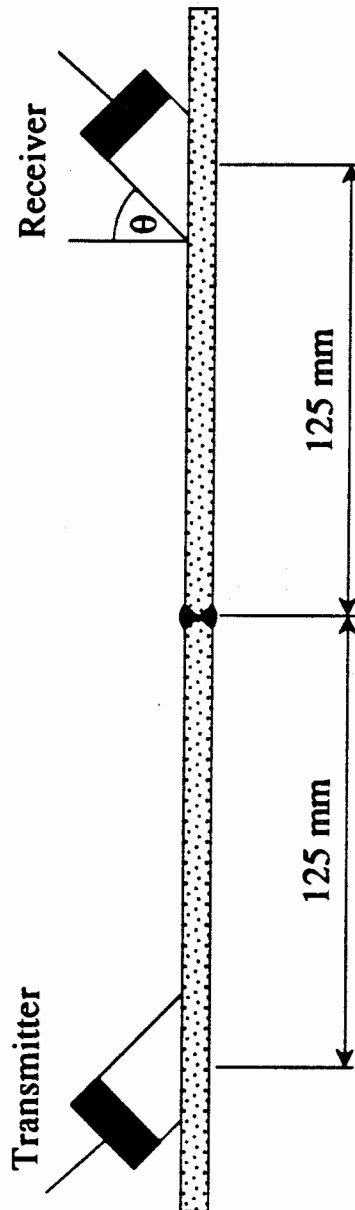


Figure 7.9 Schematic representation of a 3.12 mm thick 350 mm long butt welded steel plate.

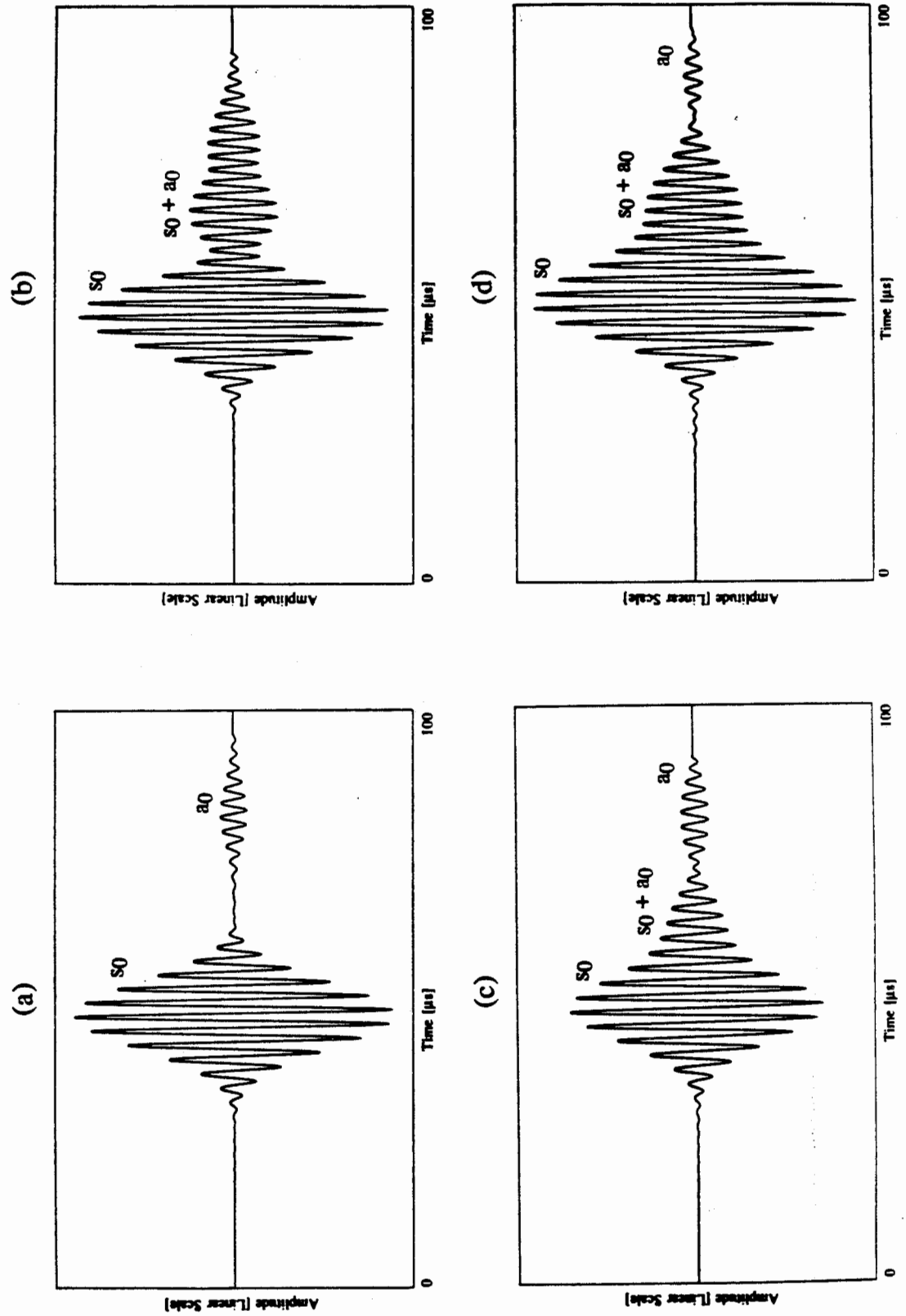


Figure 7.10 Normalised time history of the measured response at $x = 500$ mm from the transmitter in a 3.12 mm thick butt welded steel plate, when the excitation was appropriate for s_0 and the weld region was located at $x = 250$ mm. (a) good weld (b) poor weld (c) bad weld and (d) very bad weld.

CHAPTER 8

The practical implementation of Lamb waves in standard NDT methods

8.1 General

Since Worlton (1957) used Lamb waves to non-destructively test plates there has been a great deal of interest in the application of Lamb waves in nondestructive testing and monitoring and for the evaluation of material properties, especially non-metals. Much of the early work in the field relied as much on empirical experience gained through experimental investigations as on scientifically based ideas. However, in the last few years the potential of Lamb wave methods has been broadened considerably by the introduction of cheap and fast personal computers and workstations coupled with the availability of electronic devices and instrumentation, for example, digital oscilloscopes and arbitrary function generators.

The major practical advantages of using Lamb waves in NDT and monitoring applications are firstly that they are two-dimensional (a stress field is produced throughout the plate thickness, although stress nodes are generally present and have to be considered). Therefore, the entire thickness of the plate may be interrogated. This is an important advantage, as in many NDT and monitoring applications coverage of the entire thickness of the plate is required in order to find defects which may be initiated at either surface or internal sites, for example, fatigue cracks. Secondly and more importantly, information about the integrity of the plate along the propagation path of the Lamb wave, rather than at a single point as is the case in standard ultrasonic NDT using bulk waves, is obtained. This allows us to carry out fast long range two-dimensional scanning of large plates; the same approach may be used in pipe inspection when the wall thickness to pipe diameter is less than 0.1 (see Harker 1988). Fast, long range testing is generally less sensitive than standard high frequency ultrasonic NDT, but it has great potential in the routine inspection of large, defect-tolerant structures, for example, oil rigs and pipe lines where NDT inspections have to be carried out periodically.

The multi-mode dispersive nature of Lamb wave means that measurement of their amplitudes and velocities over significant propagation distances is the key problem in NDT applications.

Therefore, most NDT using Lamb waves in frequency-thickness regions above the cut-off value of the a_1 mode has been qualitative and in the majority of cases the Lamb wave(s) signal is simply compared in the time or frequency domains with a reference or 'good' signal; any difference between the two may then be used to identify the presence of a defect. These NDT and monitoring systems can hence be thought of in terms of simple "GO/NO GO" tests, the simplicity of these techniques being their biggest advantage. The dispersive multi-mode nature of Lamb waves means that in practice the response signal is very complicated. Dispersion, the presence of many propagating modes and their interaction with boundaries or other features which are not of interest generally mean that the duration of the time domain signal is also very large. Hence, these comparison methods usually have to store a very large amount of data (see Bartle 1987) if a significant duration of the response is to be compared with the reference. This is costly in terms of hardware and the testing process is generally slow. These restrictions have ensured that comparison methods have not been developed for NDT applications where on line results are required, but instead have concentrated on nondestructive monitoring applications. A further restriction of comparison techniques is that the response signal is very sensitive to changes in the testing conditions, especially propagation distance and coupling.

This chapter will deal with the practical difficulties associated with using Lamb waves in NDT and ways in which these problems may be circumvented. In particular, a comparison method in which the signal-to-noise ratio is maximised is presented, together with preliminary finite element predictions and experimental results to demonstrate its use.

8.2 Signal-to-noise considerations

8.2.1 Standard techniques for maximising the signal-to-noise ratio

Lamb waves are usually dispersive so the response signal of a mode will spread out spatially as it propagates along the plate, and the change in shape of the response signal will be a function of the degree of dispersion of the wave. This results in a reduction of the maximum amplitude of the signal and, after a short propagation distance, the maximum amplitude may reduce towards the noise level.

The simplest way of improving the signal-to-noise ratio over any given distance is to increase the amplitude of the excitation signal by, for example, using a power amplifier, or by reducing the bandwidth of the excitation signal. This is generally achieved by increasing the number of cycles in the excitation tone burst. The signal-to-noise ratio may also be improved by using

the coincidence principle to preferentially excite a single mode, and hence to minimise the amount of energy distributed among other modes which are not of interest (especially if they are highly dispersive). The signal-to-noise ratio may be further enhanced by exciting individual modes in frequency-thickness regions where dispersion is a minimum, which in most cases correspond to regions in which the group velocity is a maximum. Recently, with the widespread introduction of digital capture systems, the signal-to-noise ratio is usually improved by averaging successive response signals.

Many workers, for example, Bartle (1987) and others at The Welding Institute and Rose *et al* (1983) have tried to overcome signal-to-noise problems by using long duration tone burst excitation signals and bonding piezoelectric elements to the testpiece to maximise the transfer of acoustic energy. However, they have been unable to report obtaining good results in frequency-thickness regions above the cut-off value of the a_1 mode.

In the next section a novel qualitative comparison approach in which the signal-to-noise ratio is maximised is presented. The results of finite element (FE) predictions to check the validity of the method will be presented, as will the results of a preliminary experimental investigation.

8.2.2 Signal regeneration

Background

The fundamental idea of the method described here is to launch a signal that by superposition of its frequency components will recombine to form a signal with a simple shape (a pulse or tone burst) at the measurement position. A major benefit of employing this method is the analysis may be carried out in the time domain, where signal processing is kept to a minimum.

Suppose, for example, that a simple windowed tone burst of the type shown in Fig. 8.2(a) is used to excite a dispersive Lamb mode. Due to dispersion the signal received at a remote position along the plate will have a different shape and will in general have a lower peak amplitude (see, for example, Fig. 8.2(b)). Therefore the frequency components of the signal corresponding to the highest group velocities will be at the front of the signal, the slower components appearing later. If the received signal is reversed in time and is used to excite the transmitter, the new received signal should then be of the same form as the original excitation.

The advantage of this method is not only that the comparison of the reference and the response signal is made trivial, but the signal-to-noise ratio is maximised at the measurement position.

This is because at the measuring point the wave is focussed spatially, the maximum amplitude there being greater than at the excitation position, and as resolution (the ability to separate signals at closely spaced positions, eg a defect close to a boundary) is a function of the spatial extent of the ultrasound, this is also maximised. This method is therefore akin to using focussed probes in standard ultrasonic NDT to improve the signal-to-noise ratio and enhance resolution.

General theory

Let the excitation signal of the plate at a location defined as $x = 0$ be given by

$$[F(\omega)]_{x=0} = \int_{-\infty}^{+\infty} f(t) e^{-i\omega t} dt \quad (8.1)$$

If damping is negligible the response signal at a position $x = L$ is

$$[F(\omega)]_{x=L} = \int_{-\infty}^{+\infty} f(t) e^{-i(\omega t - kL)} dt \quad (8.2)$$

where the wavenumber $k = \omega/c$ is a function of ω . These two functions are related by the transfer function $H(\omega)$, where

$$H(\omega) = \frac{[F(\omega)]_{x=L}}{[F(\omega)]_{x=0}} \quad (8.3)$$

Suppose we wish to obtain a signal $g(t)$, whose Fourier transform is $G(\omega)$, at $x = L$. Then from eqn 8.3 the required input, $I(\omega)$, at $x = 0$ is given by

$$I(\omega) = \frac{G(\omega)}{H(\omega)} = G(\omega) [H(\omega)]^{-1} \quad (8.4)$$

The time domain signal $I(t)$, which must be applied at $x = 0$ to obtain $G(\omega)$ at $x = L$, may be obtained by inverse Fourier transforming eqn (8.4), ie

$$I(t) = \frac{1}{2\pi} \int_{-\infty}^{+\infty} \frac{G(\omega)}{H(\omega)} e^{i\omega t} d\omega \quad (8.5)$$

In the simple case when a single wave packet is present

$$[H(\omega)]^{-1} = e^{-ikL} = e^{-i\omega L/c} \quad (8.6)$$

and

$$I(t) = \frac{1}{2\pi} \int_{-\infty}^{+\infty} G(\omega) e^{-i\omega(L/c - t)} d\omega \quad (8.7)$$

If the time domain signal $g(t)$ is applied at $x = 0$ then the response, $I^*(t)$, at $x = L$ is

$$I^*(t) = \frac{1}{2\pi} \int_{-\infty}^{+\infty} G(\omega) e^{i\omega(L/c + t)} d\omega \quad (8.8)$$

The proposed technique is to use the reverse of the signal $I^*(t)$ as the excitation signal. The function $I^*(-t)$ has the desired property that the components of $I^*(t)$ which arrive at the tail of the signal will be present at the front of $I^*(-t)$. Now,

$$I^*(-t) = \frac{1}{2\pi} \int_{-\infty}^{+\infty} G(\omega) e^{i\omega(L/c - t)} d\omega \quad (8.9)$$

and by comparing eqn 8.7 and 8.9 it may readily be shown that in this simple case $I(t)$ is equal to $I^*(-t)$ if $G(\omega)$ is even. Therefore, if the desired signal $g(t)$ is symmetrical, the simple signal reversal approach is valid. This class of signal, for example, a tone burst comprising an integer number of cycles enclosed in a window function was used in the most of the experimental and numerical tests presented in this thesis.

Numerical study

A finite element and experimental study was carried out by Décobert (1990) to investigate the validity of the signal regeneration method and to determine if it could be used as a reliable method of detecting defects using the Lamb mode a_0 at very low frequency-thickness products.

The finite element results reported in this section are from Décobert (1990), where the a_0 was launched from the edge of a 2 mm thick plate at $x = 0$ by applying a 3 cycle 60 kHz tone burst excitation signal, $f(t)$, modulated by a Hanning window function to limit the bandwidth. The amplitude of the x and z displacement components at each node at the plate edge may be calculated from

$$f(0,t) = \sum_j \Phi_j(z) A_j e^{i\omega_j t - ik_j L} \quad (8.10)$$

which was obtained from eqn 4.24, where $\Phi_j(z)$ and A_j were defined in chapter 4, $L = 340$ mm and k is the frequency dependent wavenumber of the a_0 mode (see Fig. 2.4). In the case reported here, the mode shape, $\Phi(z)$, of a_0 is effectively independent of frequency and the z direction through-thickness displacement components are constant, therefore eqn 8.10 was simplified to

$$f(0,t) = \sum_j A_j e^{i\omega_j t - ik_j L} \quad (8.11)$$

The time domain input signal $f(0,t)$, was applied at the edge of the plate in the z direction only since in this frequency-thickness region a_0 is the only antisymmetric mode and a pure a_0 mode may be excited by applying an input signal which is symmetric in the z direction with respect to the middle of the plate.

Fig. 8.1(a) to (d) from Décobert (1990) show the normalised time histories of the response of the top surface of the plate in the z direction at $x = 0, 200, 260$ and 340 mm respectively, when the signal applied at $x = 0$ was appropriate to excite only a_0 and to recombine into the 3 cycle tone burst at $x = 340$ mm. From (a) it may be seen that the input is distorted and its duration is increased in comparison to a 3 cycle tone burst, the lower frequency components are at the front of the signal and the higher frequency components are at the tail. In (b) and (c) it may be seen that the signal is progressively recombining into the 3 cycle tone burst; and in (d) at $x = 340$ mm it may be seen that the response is a 3 cycle tone burst modified by a Hanning window function. The result of the summation at $x = 340$ mm is that all of the frequency components of the excitation signal spread out at $x = 0$ in Fig. 8.1(a)) arrive in phase at the monitoring position $x = 340$ mm. The spatial extent of the response at this position is a minimum; therefore, the signal-to-noise ratio is a maximum and as can be seen in Fig. 8.1(d) the maximum amplitude at $x = 340$ mm is greater than at $x = 0$, (Fig. 8.1(a)) where the wave was launched.

Experimental results

The aim of the experimental investigation was to excite s_0 in a dispersive region, capture the response signal, reverse the response and then excite the system with the resulting signal and see if the new response was of the same form as the original input signal shown in Fig. 8.2(a). This would test the feasibility of the signal regeneration method under experimental conditions. The instrumentation used was shown previously in Fig. 6.1, where a digital arbitrary function generator was used to apply the reversed response signal.

The excitation signal shown in Fig. 8.2(a) was a 12 cycle 0.65 MHz tone burst modified by a Hanning window. Fig. 8.2(b) shows the response of the 3.0 mm thick steel plate at $x = 200$ mm from the transmitter, where the incident angle at $x = 0$ was appropriate to excite only s_0 . The change in shape of the time history indicates that the s_0 mode is dispersive in this frequency-thickness region (see Fig. 2.6). Fig. 8.3(a) shows the result of reversing the response signal shown in Fig. 8.2(b). The response of the 3.0 mm thick steel plate at $x = 200$ mm from the transmitter is shown in Fig. 8.3(b), when the excitation at $x = 0$ was the reversed response signal shown in Fig. 8.3(a), from which it may be seen that the response in this case is of the same form as the tone burst shown in Fig. 8.2(a).

Fig. 8.4 shows the response of the 3.0 mm thick steel plate at 200 mm from the transmitter, when the excitation at $x = 0$ was shown in Fig. 8.3(a). However, in this case there was a 1.0 mm deep and 0.5 mm wide straight sided notch, normal to the plate surface (see, Fig. 5.1(a)) at $x = 100$ mm. Comparing the responses in Fig. 8.4 and 8.3(b) it may be seen that there has been a discernible change in the shape of the response in Fig. 8.4, which is caused by the presence of the notch. The mode conversion of the incident wave, s_0 , to a_0 after interaction with the notch has significantly increased the duration of the response signal in Fig. 8.4 and has also changed its shape.

The FE and experimental results reported here and by Décobert (1990) have shown that the signal regeneration method enables us to use grossly dispersive Lamb waves in NDT applications without the signal-to-noise being reduced to an unacceptable level after small propagation distances.

8.3 Transducers, coupling and excitation signals

8.3.1 Transducers

Here, the excitation and reception of Lamb waves will be considered separately and comments on the effects of the size and orientation of the transducer will be given.

Excitation transducer

In the past, the standard way of exciting and/or receiving Lamb waves has been to use piezoelectric elements and some variation of the 'direct wedge' type of probe design. However, in chapter 6 it was shown that the 'direct wedge' transducer invariably causes the measured signal to be complicated by the convolution of the response of the plate with the response of the transducer. In general, multiple reverberations may take place within the body of the probe where shear, longitudinal and Rayleigh waves may exist. This can be overcome by using immersion transducers.

To excite a pure Lamb mode using finite piezoelectric transducers the input must not only be at the correct frequency-thickness product (this being controlled by the excitation signal), but must also be appropriate so that only the surface displacement pattern (ie phase velocity or wavelength) of the mode required is imposed. Other modes may be decoupled by reducing the angular bandwidth of the excitation signal. This may be achieved by using a large transducer and by orienting the transducer to the coincidence angle of the required mode.

In array element transducers such as those used by for example, Jitsumori *et al* (1986), selective excitation of individual modes is achieved when the element spacing is equal to the Lamb mode wavelength, each element acting as a piston source. The wavelength of the excitation signal is constant because the element spacing is fixed, and transducers that use this principle are inflexible as individual transducers have to be manufactured for different wavelength ranges. However, in array transducers with large numbers of active elements it is possible to modify the phase of the excitation signal to each element in order to change the wavelength of the excitation signal.

Some investigators, notably Böttger *et al* (1987), have employed Electro-Magnetic-Acoustic-Transducers (EMATs) in Lamb wave NDT applications on metal tubes. The major advantage of using these transducers is that they are non contacting. However, lift-off (variation of the

distance between the EMAT and the surface of the testpiece), is a major problem and the transducers tend to be very large compared to piezoelectric transducers and the output is in general lower than that of piezoelectric transducers. EMATs are also inflexible in that they will only excite Lamb waves over a fixed range of wavelengths

When EMATs or array element transducers are used, the spatial bandwidth of the excitation signal is reduced by increasing the size of the transducer.

Reception transducer

The requirements of reception and excitation are very similar, but obviously if two transducers are employed (see Fig. 6.1) the receiver transducer has to be aligned with the excitation transducer. When piezoelectric transducers are used the coincidence angle of the receiving transducer is opposite to the excitation angle (see Fig. 6.1). The advantage of having a separate receiving transducer in Lamb wave testing is that it may be focussed (using the coincidence principle) on a mode which is not (strongly) excited but which is produced by mode conversion at the defects; as the finite element results presented previously indicate that in some cases defect sensitivity may be substantially improved by measuring the amplitude of modes produced at the defect. Practical implementation of the 2-D FFT method requires the use of array element transducer where each element may act as a point receiver.

8.3.2 Coupling

Although Luukala and Merilainen (1973) have excited Lamb waves using air coupling, for efficient acoustic energy transfer between the plate and a piezoelectric transducer, a couplant is required or the transducer has to be bonded to the plate surface. However, when the transducer is bonded to the plate surface it is difficult to obtain a single mode so coupling is usually achieved through a plastic wedge (usually perspex) or a water path.

Immersion coupling is generally not used in long range applications because of the large amount of leakage of energy from the Lamb wave to the surrounding fluid that takes place and thin film grease coupling is generally employed. However, problems are invariably encountered when the probes are moved as it is difficult to maintain constant coupling conditions. Localised coupling using a fluid column offers the constant and reliable coupling conditions of immersion coupling but avoids the disadvantage of the rapid reduction in the signal-to-noise ratio caused by the surrounding fluid. The results from the Lamb wave testing

rig (see Fig. 6.5) developed during the project has shown the advantages of using localised immersion coupling methods, where standard off-the-shelf broad band immersion transducers were used.

The main advantage of using EMATs is the elimination of the need for a couplant, which is sometimes necessary in special applications, for example, when testing very hot components or components where surface contamination is a problem.

8.3.3 Excitation signals

In all NDT applications, efficient methods of exciting Lamb waves are crucial. This not only simplifies the analysis of the data received from the test piece, but it also increases the resolution and sensitivity of the ultrasonic NDT technique. The amplitude of the excitation signal, the spatial distribution of the pressure field and the modal properties of the mode required, which are all functions of frequency, contribute to the determination of the proportion of energy available to excite the required mode at that frequency.

When pulsed excitation signals are used it is very difficult to obtain a single mode and the signal-to-noise ratio is reduced towards the noise level over short propagation distances. Tone bursts reduce the bandwidth of the excitation signal and make the excitation of individual modes easier. However, as was shown in chapter 6, tone burst excitation signals modified by a smoothing window function (in all the tests reported in this thesis a Hanning window was used) further reduce the bandwidth of the excitation signal by eliminating the high and low frequency content of simple sinusoidal tone bursts. This enables individual modes to be excited more efficiently. In practice, windowed tone burst excitation signals may be applied using an arbitrary function generator.

8.4 Decoupling boundaries and other impedance mismatches

The best way of decoupling unwanted signals is to gate out the unwanted response signal(s) in the time and frequency domains. In the time domain this is only possible if one mode is propagating or the individual Lamb modes have separated, which requires that dispersion is a minimum. Frequency domain gating is possible if the frequency content of the mode required may be separated from other propagating modes. Therefore, in the past it has not usually been possible to isolate the wave packets of individual Lamb modes in frequency-thickness regions above the cut-off value of the a_1 mode. However, the availability of arbitrary function

generators, which allow the input signal to be specially tailored to selectively excite individual modes more efficiently means that it is possible to reduce the bandwidth (frequency domain) and to excite Lamb waves in regions where time domain gating may be possible (ie regions of maximum group velocity where the fastest modes (generally the the symmetric modes) will separate out quickly (see Fig. 2.6).

8.5 The implementation of the 2-D FFT method

The implementation of the 2-D FFT method is more costly than using time or frequency domain techniques as it requires a digital oscilloscope, a computer and an array transducer (the tests reported here were carried out by indexing a standard transducer, but this would not be practical in industrial NDT and initial tests carried out using a multi-element array transducer have indicated the applicability of these transducers as receivers). However, the method may be used to measure the amplitudes and velocities of Lamb waves in frequency-thickness regions where many propagating modes are possible. Crucially, the 2-D FFT method may be used with any propagation distances subject to signal-to-noise considerations and the location of the defect relative to the measuring transducer is not important. Therefore, fast, long range, quantitative Lamb wave testing or monitoring may be carried out using the 2-D FFT method.

8.6 Choice of time or frequency domain methods or the 2-D FFT method

Conventional quantitative NDT methods use the amplitude and the velocity of bulk waves to determine the size and location of a defect. These methods, as mentioned briefly in chapter 1, are generally relatively easy to apply and require a minimum of signal processing, for example, the setting of time gates and amplitude thresholds in C-scanning. The complicated nature of Lamb wave signals in high frequency-thickness regions, where more than two modes are possible has meant that very little quantitative NDT using Lamb waves has been carried out in frequency-thickness regions where more than two modes may propagate. Practically, this is a serious restriction; for example, if a 12 mm thick steel plate was being tested the excitation signal would have to be less than 136 kHz, the cut-off frequency of a_1 .

Lamb wave testing may be carried out in low frequency-thickness regions, where the only propagating modes are a_0 and s_0 which may be easily decoupled from one another, using standard ultrasonic testing time domain techniques. The analysis may be carried out by measuring the time lag or amplitude of the wave packet, or by comparing the shape of the response signal with a reference signal. Use of the signal regeneration method described in

section 8.2.1 can simplify the comparison method significantly and the availability of digital devices, such as arbitrary function generators and oscilloscopes make the implementation of this method practically feasible. An important advantage of this method is that it maximises the signal-to-noise ratio of the signal at the measurement position and it also allows Lamb wave testing to be carried out in the time domain when a dispersive mode is used.

One-dimensional spectral methods involving the Fourier analysis of the response of a single point may sometimes give more accurate measurements of the velocity of propagating Lamb waves than simple time domain techniques, and they may also be used to filter out some modes if the frequency content of the mode required may be separated from the other propagating modes. However, they do not allow the amplitudes of modes at a particular frequency to be measured.

Defect detectability is related to mode order, type and frequency-thickness product, but in general defect detectability is improved by increasing the frequency-thickness product. Therefore, it would be advantageous to carry out Lamb wave testing in frequency-thickness regions above the cut-off value of the a_1 mode. However, in these frequency-thickness regions standard time domain methods may not generally be used. A variety of comparison methods have been developed in order to overcome this problem, but they have generally been unsuccessful. Therefore, in general the 2-D FFT method must be used to carry out quantitative NDT analysis at frequency-thicknesses above the cut-off value of the a_1 mode. As stated previously the computational requirements of the 2-D FFT method are quite modest and can be easily handled by a fast microcomputer or workstation. It should be noted that the resolution in the temporal FFT's does not have to be good, and in reality, spatial FFT's will only be required at a few discrete frequencies, since when tone burst excitation is used, the bandwidth of the excitation signal is fairly narrow. This means that a full two-dimensional Fourier transform algorithm need not be implemented and the analysis could be carried out in real time. This gives the method great potential, particularly in fast, long range Lamb wave testing or monitoring applications.

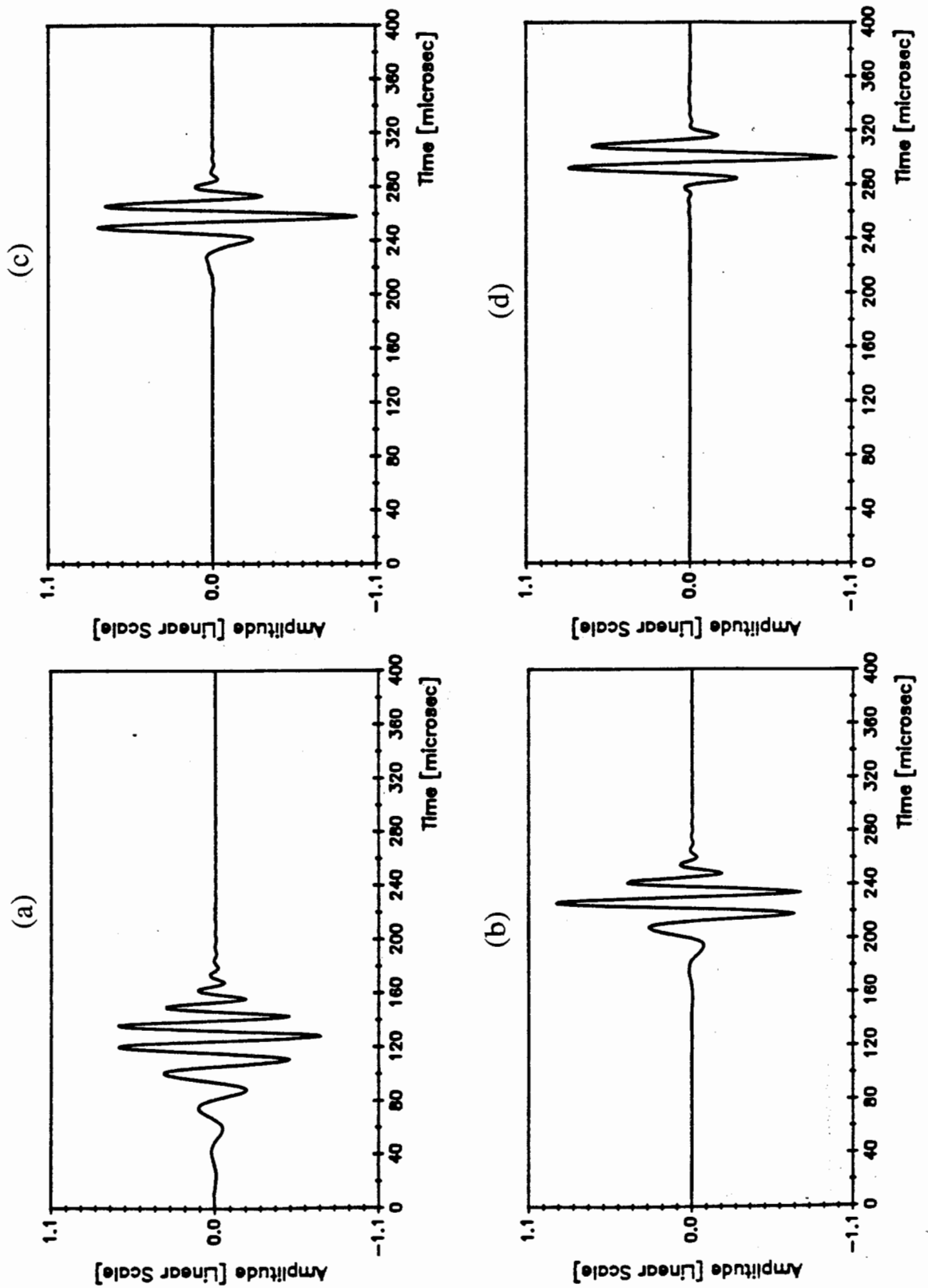


Figure 8.1 (a) Predicted time history at $x = 150$ mm in a 2.0 mm thick plate, when the excitation signal was a 3 cycle 60 kHz tone burst modified by a Hanning window and was designed to excite only a_0 and recombine at $x = 340$ mm to form the 3 cycle tone burst. (b) at 200 mm, (c) at 260 mm and (d) at 340 mm.

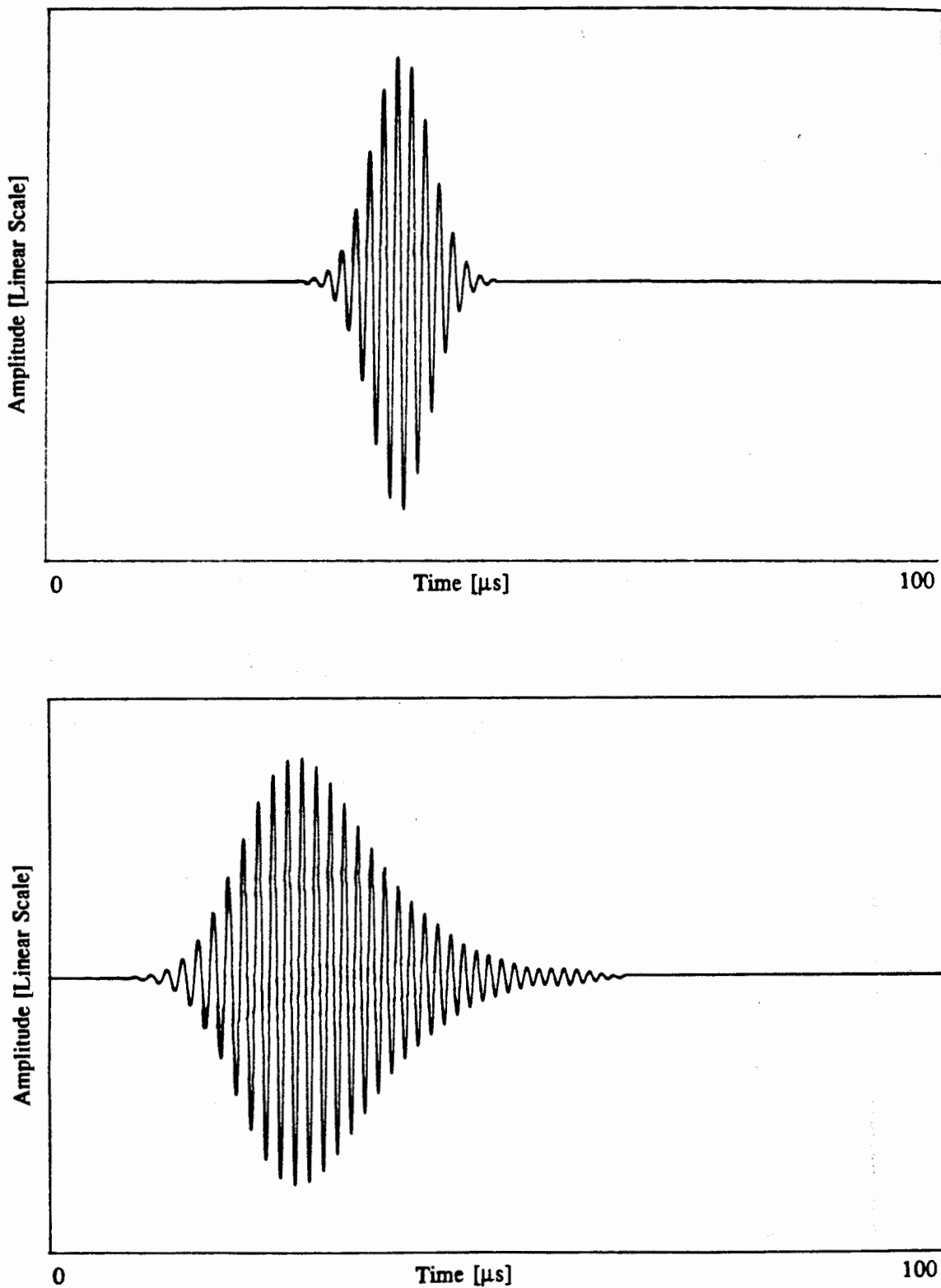


Figure 8.2 (a) Time history of the 12 cycle 0.65 MHz tone burst in a Hanning window excitation signal applied to the transmitter. (b) Normalised time history of the measured response at $x = 200$ mm in a 3.0 mm thick plate when the excitation signal was shown in (a).

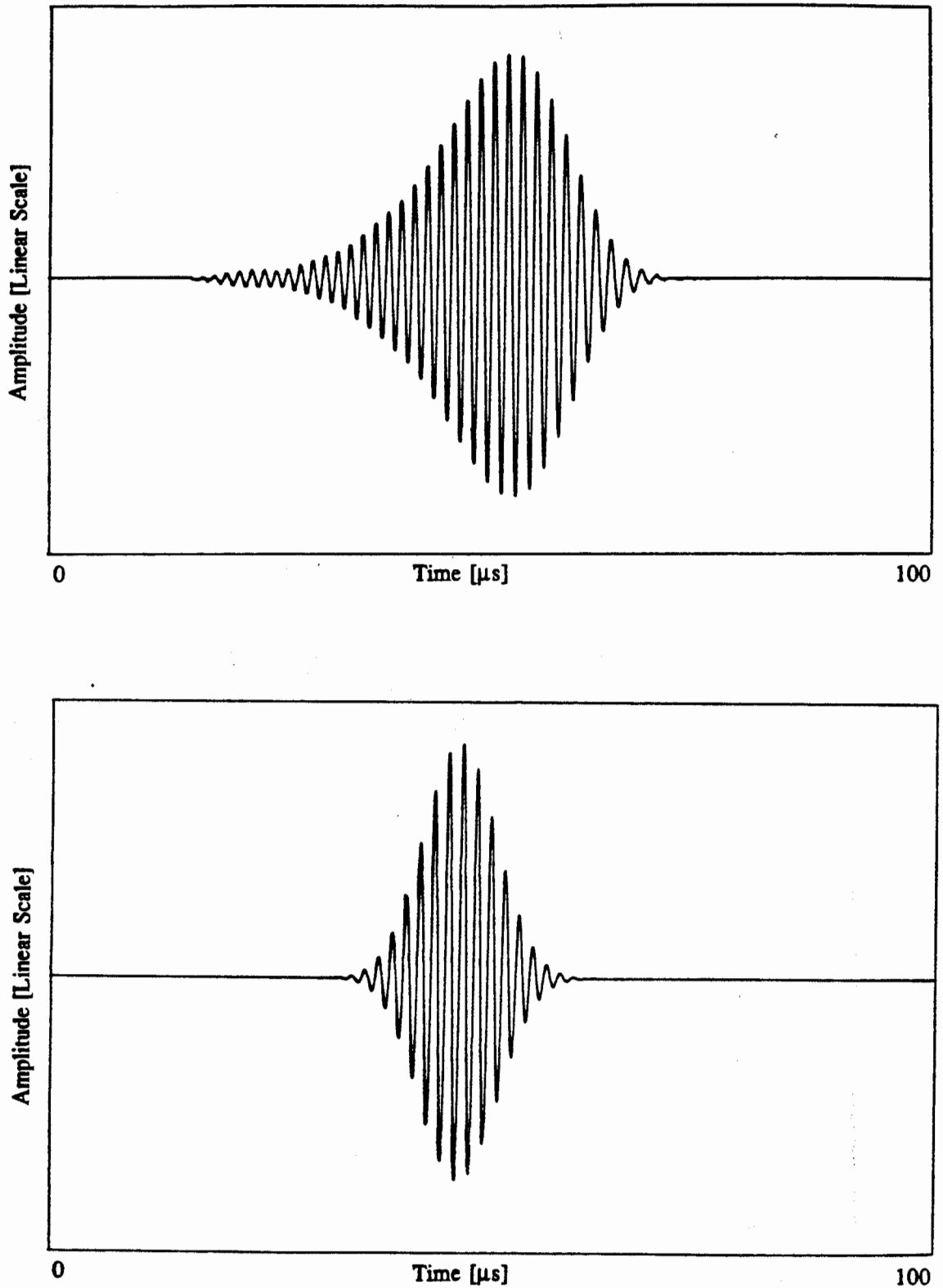


Figure 8.3 (a) The reverse of the response signal shown in Fig. 8.2(b) used as the excitation signal. (b) The time history of the measured response at $x = 200$ mm from the transmitter in a 3.0 mm thick steel plate, when the excitation signal was shown in (a).

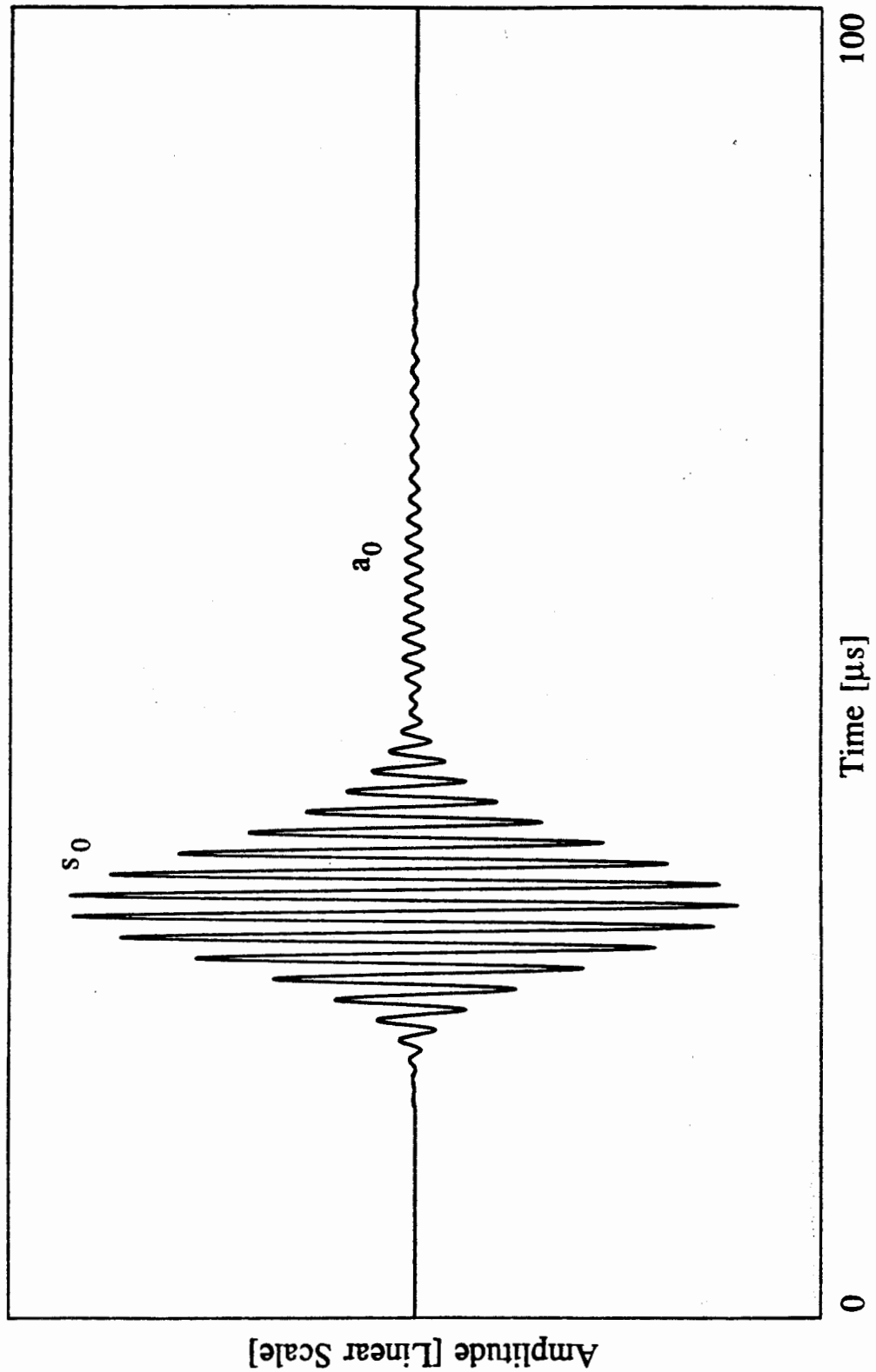


Figure 8.4 (a) The time history of the measured response at 200 mm from the transmitter in a 3.0 mm thick steel plate, when the excitation was shown in Fig. 8.3(a) and a 1.0 mm deep and 0.5 mm wide notch was located at 100 mm from the transmitter.

CHAPTER 9

Conclusions

9.1 General

The main conclusion of the thesis is that Lamb waves may be used very successfully for the NDT of plates or plate-like structures. Since they produce stresses throughout the thickness of the plate (in some cases there may be stress nodes which must be carefully considered), the entire thickness of the plate is interrogated. This means that it is possible to find defects that are initiated at either surface or at internal locations. However, the behaviour of Lamb waves on interaction with defects is very complicated and in general defect sensitivity is a function of mode type, mode order and the frequency-thickness product, and is not simply wavelength dependent.

There are two distinct areas where propagating Lamb waves may be applied in NDT applications. In localised, detailed NDT applications, the detectability of a defect may be optimised by choosing the most suitable mode at the appropriate frequency-thickness product. In these cases the propagation distances are small so in most frequency-thickness regions dispersion does not cause the signal-to-noise ratio to deteriorate to an unacceptable level. Testing may therefore be carried out in almost any region using immersion coupling. In the long range NDT of plates and plate-like structures, a fast, coarse inspection may be carried out. Here, the two-dimensional nature of Lamb waves means that in maximum group velocity regions they may be propagated further than bulk waves. In these cases maximising the propagation distance is generally more important than optimising defect detectability. Therefore, immersion coupling methods should be avoided as energy is continually leaked to the surrounding fluid and localised coupling methods in which energy leakage is minimised are preferable.

9.2 Signal processing

The complicated multi-mode dispersive nature of Lamb wave signals means that the major problem when using them in NDT applications has been signal interpretation. The major achievement of the thesis was the development of quantitative methods of applying Lamb waves in industrial nondestructive testing (NDT). The key problem of measuring the amplitudes and velocities of individual Lamb waves when more than one mode is present at any given frequency has been solved by the development of a method which uses a two-dimensional Fourier transformation. This has made possible the interpretation and quantitative measurement of the complicated Lamb wave signals which are commonly found in NDT applications when plates are excited by commercially available transducers.

Although the 2-D FFT method has been used here to measure the properties of Lamb waves, the technique is equally applicable to the measurement of other two-dimensional modes, for example, a mixture of longitudinal and shear waves. The computational requirements of the 2-D FFT method are fairly modest and it is anticipated that the method could readily be implemented on a microcomputer interfaced to a data capture system. The multi-element transducers which are now available make the implementation of the 2-D FFT method feasible in industrial NDT applications.

9.3 Numerical modelling

Finite element modelling of Lamb wave propagation in a variety of frequency-thickness regions has been carried out successfully. A method has been developed to launch a single Lamb mode in a finite element model using broadband input signals. This facilitated the quantitative modelling of the interaction of individual Lamb waves with notches in steel plates, and the 2-D FFT method could then be used to measure the amplitudes of the different propagating Lamb waves.

A major finding from the finite element predictions and experimental results has been that Lamb wave techniques may be used to find notches with depths of around 8% of the plate thickness (assuming a 5% change in amplitude can be detected). This is substantially better than reported previously by other researchers. The finite element tests have shown that the transmission and reflection coefficients of Lamb waves when they interact with notches are non-monotonic and are a strong function of the notch depth, mode type and order and the frequency-thickness product. The potential of using the frequency-thickness locations of

the minima and maxima in the amplitude of the reflection and transmission ratios for sizing purposes has been highlighted.

The numerical tests have indicated that the implementation of quantitative Lamb wave techniques where the amplitude(s) of modes caused by mode conversion are measured can increase the sensitivity of these techniques considerably.

9.4 Practical applications

Efficient methods of selectively exciting Lamb waves are essential if meaningful results are to be obtained in frequency-thickness regions above the cut-off value of the first non zero order mode, a_1 . This usually requires that the frequency and angular bandwidths of the excitation signal should be tightly controlled. The first requirement may be met by using an arbitrary function generator to produce long duration tone bursts modified by suitable smoothing window functions (for example, a Hanning window). The second requirement may be achieved by using large transducers and orienting them using the coincidence angle to decouple unwanted modes. In order to minimise the spatial extent of the signal (maximise signal-to-noise) and to obtain the reasonable propagation distance Lamb wave testing is carried out in frequency-thickness regions away from the cut-off values.

An experimental test rig incorporating localised immersion coupling which use standard immersion transducers, which are driven by an arbitrary function generator has been manufactured and procedures have been developed to validate the finite element predictions. The results of investigations on a variety of plates with straight sided notches have been in excellent agreement with the numerical predictions.

Standard time or frequency domain qualitative or quantitative methods can be applied in low frequency-thickness product regions, where the only propagating modes are a_0 and s_0 , as they may be easily decoupled from one another by gating in the time domain or by transducer orientation. Time domain tests carried out on a butt-welded steel plate have shown that fast qualitative inspections in which the shape of the response wave packet at low frequency-thickness values is monitored may be used.

A signal regeneration method has been developed which maximises the signal-to-noise ratio of a Lamb wave response signal at the measurement position. The adoption of this method potentially allows dispersive Lamb waves (especially the a_0 mode at low frequency-thicknesses) to be used in long range testing applications.

In higher frequency-thickness regions, application of the 2-D FFT method allows quantitative results to be obtained. However the excitation signal must be controlled so that, for example, unwanted signals from boundaries or other impedance changes not of interest may be gated out or decoupled. The computational requirements of the method are reasonably modest and in most situations may be readily handled by a PC or workstation computer interfaced to a digital data capture system.

References

- Alsop, L. E., and Goodman, A. S. (1972). "Finite difference formulas for Neumann conditions on irregularly shaped boundaries," *IBM J. Res. and Dev.* 16 pp365-371.
- Alterman, Z. (1968). "Finite difference solutions to geophysical problems," *J Phys. Earth* vol 16 pp113-128.
- Alterman, Z., and Loewenthal, D. (1972). "Computer generated seismograms," *methods in computational physics* vol 12.
- Auld, B. A. (1973). *Acoustic Fields and Waves in Solids* (Wiley-Interscience, New York).
- Auld, B. A., and Tsao, E. M. (1977). "A variational analysis of edge resonance in a semi-infinite plate," *IEEE transaction on sonics and ultrasonics*, vol. SU-24, 1977, pp317-326.
- Avioli, M. J. (1988). "Lamb wave inspection for large cracks in centrifugally cast stainless steel," EPRI report RP2405-23, Georgetown University.
- Ball, D. F., and Shewring, D. (1976). "Some problems in the use of Lamb waves for the inspection of cold-rolled steel sheet coil," *Nondestructive testing* 6 (3) pp138-145.
- Bartle, P. M. (1985). "Acoustic pulsing-some questions answered," The Welding Institute, Abington, Cambridge.
- Bartle, P. M. (1987). "Acoustic pulsing monitoring: principles operational requirements and potential," The Welding Institute, Abington, Cambridge.
- Bathe, H-J. (1982). *Finite element procedures in engineering analysis* (Prentice-Hall Inc., New York).
- Bertholf, L. D. (1967). "Numerical solutions to two-dimensional elastic wave propagation in finite bars," *J. Appl. Mech.* vol 34 pp725-734.
- Blake, R. J. (1988). "Numerical models of Rayleigh wave scattering from surface features," Ph.D. thesis, Dept. of Electronic and Electrical Eng, University of London (University College).
- Blake, R. J., and Bond, L. J. (1989). "A general model for Rayleigh wave-surface feature scattering problems," in *Rev. Prog. Quant. NDE* 9A pp77-84.
- Bond, L. J. (1982). "Methods for the computer modelling of ultrasonic waves in solids," *Research techniques in NDT*, vol 6 pp107-150.
- Bond, L. J., Punjani, M., and Saffari, N. (1984). "Review of some recent advances in quantitative ultrasonic NDT," *IEEE Proc.* Vol 131, Pt. A, No. 4 pp265-274.
- Boness, K. D. (1981). "Ultrasonic verification of weld signatures," Report AERE-M3223 UKAEA, Harwell, England.
- Böttger, W., Schneider, H., and Weingarten, W. (1987). "Prototype EMAT system for tube inspection with guided ultrasonic waves," *Nuclear Eng. and Design* 102 pp356-376.
- Brekhovskikh, L. M. (1980). *Waves in Layered Media* (Academic Press, New York).

- Burger, C. P., Hughes, R. G., Miskioglu, I., Waskey, J., and Neal, S. (1982). "Improved ultrasonic evaluation of surface defects through photoelastic visualisation of elastic waves," Techn. Advances in Eng. and their impact on detection, diagnosis and prognosis methods, pp39-44, Scottsdale, Ariz., USA.
- Burmistrov, V. V., Kononova, O. M., and Treshchalin, M. A. (1978). "Ultrasonic inspection of small-diameter ribbed-bore pipe," Sov. J. NDT vol 14 (2) pp182-184.
- Chimenti, D. E., and Bar-Cohen, Y. (1985). "Signal analysis of leaky lamb wave spectra for NDE of composites," in Proc. IEEE Ultrasonic Sym., vol 2 pp1028-1031.
- Chimenti, D. E., and Nayfeh, A. H. (1985). "Leaky Lamb waves in fibrous composite laminates," J. Appl. Phys. vol 58 pp4531-4538.
- Conn, D. L., and Jackson, J. F. (1971). "In-line ultrasonic inspection of colded rolled strip," Material Evaluation vol 29 (2).
- Cooper, J. A., Dewhurst, R. J., and Palmer, S. B. (1986). "Characterization of surface-breaking defects in metals with the use of laser-generated ultrasound," Philos. Trans. R. Soc. A 320 (1554), pp319-328.
- Courant, R., Friedrichs, K., and Lewy, H. (1967). "On the partial differential equations of Mathematical physics," IBM J. Res. and Dev. 11 pp215-234.
- Cremer, L. (1942). "Theorie der schalldammung dunner wande bei schragem einfall," Akustische Zeitschrift 7, pp81-104.
- Datta, S. K., and Shah, A. H. (1987). "Ultrasonic scattering by planar and non-planar cracks," in Rev. Prog. Quant. NDE 6 pp69-78.
- Décobert, F. (1990). "Use of flexural waves for the detection of cracks in large structures," B. Sc Thesis, Mech. Dept., Imperial College, London.
- Derkacs, T., and Matay, I. M. (1979). "Ultrasonic detections of surface flaws in gas turbine ceramics," in Rev. Prog. Quant. NDE La Jolla, Calif., pp691-699.
- Doyle, P. A. (1978). "Crack depth measurement by ultrasonics: A review," Ultrasonics vol 16 (4) pp164-170.
- Duncan, D. B. (1985). "Computer simulation of ultrasonic testing," in Proc. 5th Canadian Conf. NDT, pp345-355.
- Duncumb, A. C., and Keighley, D. M. (1987). "Inspection of titanium tubing using ultrasonic Lamb waves generated by an electromagnetic acoustic transducer," in Proc. 4th Euro. Conf. NDT, vol 4 pp2228-2236.
- Ensminger, D. (1973). *Ultrasonics The Low-and High-Intensity Applications* (Marcel Dekker, Inc. New York).
- Ergin, K. (1952). "Energy ratio of the seismic waves reflected and refracted at a rock-water boundary," Bull. Seim. Soc. Am., vol 42, pp349-372.
- Finch, R. D, and Bray, D. E. (1973). "Acoustic flaw detection in railway wheels," in Proc Ultrasonics Int. Conf., pp194-198.
- Firestone, F. A. (1940). "Flaw detection device and measuring instrument," U.S. Pat. 2,280,130.

- Firestone, F. A., and Ling, D. S. (1951). "Methods and means of generating and utilizing vibrational waves in plates," U.S. Pat. 2,536,128.
- Fitting, D. W., and Adler, L. (1982). "Frequency dependent interaction of ultrasonic waves with surface-breaking cracks," *New Procedures in NDT*, pp203-212, Saarbrucken, Germany.
- Freedman, A. (1978). "Reflectivity and Transmittivity of Elastic Plates, 1: Comparison of Exact and Approximate Theories", 65 Mount Pleasant Av., Weymouth, Dorset, England.
- Freedman, A. (1981). "On The Overlapping Resonances Concepts of Acoustic Transmission Through An Elastic Plate, 1: Examination of Properties", 65 Mount Pleasant Av., Weymouth, Dorset, England.
- Gazis, D. C., and Mindlin, R. D. (1960). 1960, "Extensional vibrations and waves in a circular disk and a semi-infinite plate", *J. Appl. Mech.* vol 27, pp541-547.
- Georgiou and Bond (1985). "Studies in ultrasonic wave-defect interaction," in *Proc. 4th Int. Sym. offshore Mech. and Arctic Eng.* (1985) vol 2 pp451-460.
- Graff, K. F., (1975). *Wave motion in Elastic Solids* (Clarendon Press, Oxford).
- Guyott, C. C. H. (1986), "The non-destructive testing of adhesively bonded structures," Ph. D Thesis, Mech. Dept., Imperial College, London.
- Hall, K. G. (1976). "Crack depth measurement in rail steel by Rayleigh waves aided by photoelastic visualization," *Nondestructive Testing* vol 9 (3) pp121-126.
- Hall, K. G. (1977). "A Qualitative evaluation of the variable-angle ultrasonic transducers by the photoelastic visualization method," *Ultrasonics* pp245-252.
- Harker, A. H. (1985). "Numerical modelling of the scattering of elastic waves in plates," *J. NDE* vol 4 pp89-106.
- Harker, A. J. (1989). *Elastic Waves in Solids With Applications to NDT of Pipelines* (Grosvenor Press, Portsmouth).
- Harumi, K., Suzuki, F., and Saito, T. (1973). "Computer simulation of nearfield for elastic wave in a solid half-space," *J. Acoust. Soc. Am.* vol 53, pp600-664.
- Hayashi, N., and Naoe, M. (1986). "Plate Wave detection of aluminium sheet," *Sumitomo Light Met. Tech. Rep.* 27, (1), pp10-17.
- Hitchings, D. (1987). "FE77 user manual," Imperial College internal report.
- Jitsumori, A., Inoue, S., Maekawa, T., and Inari, T. (1986). "Generation of Lamb waves using linear array probe and its application to flaw detection," *Jap. J. of Appl. Phys. Supp. Proc.* 6th symposium ultrasonic electronics Tokyo vol 25, pp200-202.
- Kinra, V. K., and Vu, B. Q. (1983). "Diffraction of Rayleigh waves by an edge crack," *SESA Spring conference*, Cleveland, Ohio, pp187-189.
- Kline, R. A., and Hashemi, D. (1987). "Ultrasonic guided-wave monitoring of fatigue damage development in bonded joints," *Materials Evaluation* vol 45.

- Klein, A., and Salzburger, H. J. (1982). "Characterization of surface defects by Rayleigh waves," *New Procedures in NDT*, pp193-202, Saarbrucken, Germany.
- Kolsky, H. (1963). *Stress waves in solids* (Dover Publ., New York).
- Krautkrämer, S., and Krautkrämer, H., (1983), *Ultrasonic Testing of Materials* (Springer-Verlag, Berlin).
- Krieg, R. D., and Key, S. W. (1973). "Transient shell response by numerical time integration," *Int. J. Num. Meth. Eng.* vol 7, pp273-286.
- Kriz, R. D., and Gary, J. M. (1989). "Numerical simulation and visualization models of stress wave propagation graphite/epoxy composites," in *Rev. Prog. Quant.NDE 9A* pp125-132.
- Lamb, H., (1917). "On waves in an elastic plate," *Poc. Roy. Soc. London, Ser. A*,
- Lehfeldt, W. (1962), "Ultrasonic inspection of sheets by means of Lamb Waves," *Materialpruf 4 (9)* pp331-337
- Lockett, K. T. (1973). "Lamb and torsional waves and their use in flaw detection in tubes," *Ultrasonics* vol 11 (1) pp31-37.
- Ludwig, R., Moore, D., Langenberg, K. J., and Lord, W. (1988). "Analytical and numerical predictions of short pulsed elastic waves on a half space," in *Rev. Prog. Quant. NDE 8A* pp165-171.
- Luukkala, M., and Merilainen, P. (1973). "Metal Plate Testing Using Airborne Ultrasound," *Ultrasonics*.
- Lyon, R. H. (1955). "Response of An Elastic Plate to Localized Driving Forces," *J. Acoust. Soc. Am.*, vol 27 (2).
- Mal, A. K., Yin, C.-C., and Bar-Cohen, Y. (1988). "The influence of the material dissipation and imperfect bonding on acoustic wave reflection from layered solids," in *Rev. Prog. Quant. NDE 7B* pp927-934.
- Mal, A. K., and Bar-Cohen, Y. (1990). "Characterization of composite using combined LLW and PBS methods," in *Rev. Prog. Quant. NDE 10A*.
- Mansfield, T. L. (1975). "Lamb wave inspection of aluminium sheet," *Material Evaluation* pp96-100.
- Merkulov, L. G., and Rokhlin, S. I. (1970). "Passage of Lamb waves through a region of a plate with a stratification," *Sov. J. NDT* vol 3 pp256-264.
- Moore, D., Ludwig, R., and Lord, W. (1988). "A 3-D finite element formulation for ultrasonic NDT phenomena," in *Rev. Prog. Quant. NDE 8A* pp103-108.
- Nayfeh, A. H., and Chimenti (1988). "Propagation of guided waves in fluid-coupled plates of fibre-reinforced composites," *J. Acoust. Soc. Am.*, vol 83 (5).
- Newland, D. E. (1984). *Random vibrations and spectral analysis* (Longman Inc, New York).
- Nickell, R. E. (1973). "Direct integration methods in structural dynamics," in *Proc. ASCE EM2* pp303-317.

- Numerich, S. K., Dale, N., and Dragonette, L. R. (1984). "Generation and exploitation of plate waves in submerged shell structures", *Advan. in fluid struct. interaction ASME (AMD vol 64)* pp59-74.
- Okada, K. (1986). "Ultrasonic Measurement of Anisotropy in Rolled Materials Using Surface Wave," *Jpn. J. Appl. Phys.* 1 25 (suppl. 25-1), pp. 197-199.
- Perdijon, J. (1985). "La Transmission d'Energie Par Couplage Resonnant Entre Une Onde Libre et Un Onde Guidee," *Revue Phys. Appl.* 20 pp173
- Pialucha, T. (1991). "The Reflection Coefficient From Interface Layers in NDT of Adhesive Joints," Ph. D Thesis, Mech. Dept., Imperial College, London.
- Pialucha, T., Guyott, C. C. H., and Cawley, P. (1989). "An amplitude spectrum method for the measurement of phase velocity," *Ultrasonics* vol 27 pp270-279.
- Plona, T. J., Behraves, M. and Mayer, W. G. (1975). "Rayleigh and Lamb Waves at Liquid-Solid Boundaries," *Ultrasonics* vol 13, pp171-174
- Press, W. H., Flannery, B. P., Teukolsky, S. A., and Vetterling, W. T. (1988). *Numerical Recipes: The Art of Scientific Computing* (Cambridge University Press, Cambridge).
- Randall, R. B. (1987). *Frequency analysis* (Bruel and Kjaer, Naerum, Denmark).
- Rayleigh, Lord (1885). "On Waves Propagating Along The Plane Surfaces of An Elastic Solid," *Proc. London Math. Soc.*, 17 pp4-11.
- Redwood, M. (1960). *Mechanical Waveguides* (Pergomon Press, Oxford).
- Reinhardt, H. W., and Dally, J. W. (1970). "Some Characteristics of Rayleigh Wave Interaction With Surface Flaws," *Materials Evaluation* vol 28 (10) pp213-220.
- Reissner, H. (1938). "Der senkrechte und schrage durchtritt einer in einem flussigen medium erzeugten ebenen dilatation-(longitudinal)-welle durch eine in diesem medium befindliche planparallele feste platte," *Helv Phys. Acta* vol 11.
- Rokhlin, S. I. (1979). "Interaction of Lamb Waves With Elongated Delaminations in Thin Sheets," *International Advances in NDT*, vol 6, pp263-285.
- Rokhlin, S. I. (1986) "Interface properties characterization by ultrasonic surface and interface wave," *Adhesive Joint-Formation, characteristics, and testing* Ed., K. L., Mittal (Plenum Press, New York).
- Rokhlin, S. I., and Bendec, F. (1983). "Coupling of Lamb waves with the aperture between two elastic sheets," *J. Acoust. Soc. Am.*, vol 73.
- Rokhlin, S. I., Mayhan, R. J., and Adler, L. (1984). "On-Line Ultrasonic Lamb Wave Monitoring of Spot Welds," *Am. Soc. of NDT*.
- Rose, J. L., Fuller, M. C., Nestleroth, J. B., and Jeong, V. H. (1983). "An ultrasonic global inspection technique for an offshore K-Joint," *Soc. of Petro. Eng. J.* vol 23 pp358-364.
- Rothe, A. (1986). "Excitation of Lamb Waves in a Thin Plate with Short Ultrasonic Pulses," M. Sc Thesis, Mech. Dept., Imperial College, London.
- Rowland, R. R., and Lichodziejewski, W. (1973). "Lamb Wave Bond Inspection," *Material Evaluation* vol 31 (2).

- Sache, W., and Pao, Y-H., (1978). "On determination of phase and group velocities of dispersive waves in solids," J. Appl. Phys. vol 49 pp4320-4327.
- Saffari, N. and Bond, L. J. (1983). "Mode-conversion phenomena at surface breaking cracks for defect characterisation," in Proc. IEEE Ultrasonics Symp., pp960-964.
- Silk, M. G., and Bainton, K. F. (1979). "The propagation in metal tubing of ultrasonic wave modes equivalence to Lamb waves," Ultrasonics vol 17 (1) pp11-19.
- Singh, G. P., and Singh, A. (1981). "A technique for notch depth determination using pulse-echo Rayleigh waves," Materials Evaluation vol 39 (13) pp1232-1236.
- Smith, W. D. (1975). "The application of finite element analysis to body wave propagation problems," Geophys. J. R. A. S. vol 42 pp747-768.
- Smith, G. D. (1985). *Numerical Solution of Partial Differential Equations: Finite Difference methods* (Oxford University Press).
- Szilard, J. (1982). *Ultrasonic Testing* (John Wiley).
- Temple, J. A. G. (1988). "Modelling the propagation and scattering of elastic waves in inhomogeneous anisotropic media," J. Phys. D: Appl. Phys. vol 21 pp857-874.
- Timoshenko, S. P. (1982). *Theory of Elasticity 3rd Ed.* (McGraw-Hill).
- Torvik, J. P. (1967). "Reflection of wave trains in semi-infinite plates," J. Acoust. Soc. Am., vol 41 pp346-353.
- Viktorov, I. A. (1965). "Ultrasonic Lamb Waves," Akust. Zh. Vol 11 pp1-15
- Viktorov, I. A. (1970). *Rayleigh and Lamb Waves* (Plenum Press New York).
- Worlton, D. C. (1957). "Ultrasonic Testing With Lamb Waves," Non-Destructive Testing, 15 14 pp218-222.
- Worlton, D. C. (1961). "Experimental Confirmation of Lamb Waves Megacycle Frequencies," J. Appl. Phys., vol 32 (32), pp967-971.
- You, Z., and Lord, W. (1988). "Finite element study of elastic waves interaction with cracks," in Rev. Prog. Quant. NDE 8A pp109-116.
- Zelik, J. A., and Reinhardt, W. W. (1972). "Application of Lamb Wave Techniques to Space Cabin Structures," Material Evaluation vol 30 (9).
- Zhang Shou-yu, Zhang Sheng-yong, and Ying, C. F. (1985). "Study of the Lamb Wave by the Photoelastic Visualization Technique," in Proc. 11th World Conference on NDT, Las Vegas, pp1003-1007.
- Zhang, S. Y., Shen, J. Z., and Ying, C. F. (1988). "The reflection of the Lamb wave by a free plate edge: Visualization and theory," Materials Evaluation vol 46 pp638-641.
- Zienkiewicz, O. C. (1971). *The finite element method in engineering science* (McGraw-Hill, New York).